



Cardiff  
Catalysis Institute

---

Sefydliad Catalysis  
Caerdydd

# **Metal Oxide Preparation for Heterogeneous Catalysis**

Thesis Submitted in accordance with the requirement of Cardiff University for  
the degree of Doctor of Philosophy (PhD)

**William Wallace**

**2019**

## Abstract

The preparation method of a heterogeneous catalyst is one of the most fundamental aspects that can determine its morphology, surface area, phases present, elemental mixing and of course ultimately its catalytic activity. Currently there are a large number of different ways of preparing metal oxide catalysts such as co-precipitation or sol gel but over the last 20-30 years there has been a large number of solvent systems that have been used to develop alternative synthesis techniques such as supercritical solvents, ionic liquids, deep eutectic solvents and switchable solvents. These systems contain interesting properties that are not found in conventional solvent systems which could be utilised to synthesise metal oxide or metal oxide precursors that have unique properties that gives them an advantage over the metal oxide catalysts prepared by conventional methods.

The aim of this thesis was to investigate the potential for these novel systems and adapt them for the application of metal oxide catalyst preparation and to see how these techniques compare with more established methods. In order to assess these systems three catalytic reactions were chosen to use as a model to see how metal oxide catalyst prepared by these methods compare with methods such as co-precipitation or supercritical anti-solvent. 1) the use of  $\text{Co}_3\text{O}_4$ ,  $\text{Mn}_2\text{O}_3$  and  $\text{Fe}_2\text{O}_3$  for the total oxidation of propane to  $\text{CO}_2$ . 2) the use of copper-manganese oxide (hopcalite) for low temperature carbon monoxide oxidation and 3) Cu/ZnO catalyst for methanol synthesis from  $\text{CO}_2$  and  $\text{H}_2$ .

Cobalt oxalate, manganese oxalate and iron oxalate were prepared using choline chloride-oxalic acid based deep eutectic solvent with a water or water-alcohol anti-solvent. It was found the for cobalt and iron precursors a rod shape morphology could be achieved and this morphology was retained after calcination although the precipitated manganese did not form rods. Varying the anti-solvent mixture changed morphology and surface area of the cobalt oxide and iron oxide catalysts. Mixed cobalt manganese oxide and

iron manganese oxide prepared using deep eutectic solvents were also shown to form rod like morphologies similar to the single cobalt oxide and iron oxide catalysts. These catalysts that were tested for propane total oxidation method and did show some variations in activity between the different preparation methods but there was no significant improvement over the reference catalysts.

The use of hydrothermal synthesis to make a crednerite phase  $\text{CuMnO}_2$  as a precursor to the spinel phase copper-manganese oxide was found to produce spinel copper-manganese oxide catalysts with properties that differed from co-precipitated equivalents. These catalysts demonstrated lower deactivation during the first 30 minutes of CO oxidation despite having generally having lower a surface area, although these catalysts showed deactivation after temperature ramp to 50 °C. Characterisation on the crednerite derived spinel showed that they differed from the regular co-precipitated hopcalite with XPS showing a higher  $\text{Cu}^+:\text{Cu}^{2+}$  at lower temperature heat treatment which may indicate greater Cu-Mn integration.

The use of a switchable solvent system was demonstrated for the preparation of carbonate precursors to copper manganese oxides CO oxidation catalysts which were shown to have high surface areas and excellent CO conversion comparable to copper-manganese oxide catalysts prepared by supercritical anti-solvent methods, presenting a less energy intensive method of making metal oxide catalysts to supercritical anti-solvent precipitation.

The use of choline chloride-urea deep eutectic solvents to prepare copper-zinc oxide methanol synthesis catalysts was shown to be an ineffective method, with the MP-AES showing loss of zinc at higher copper loadings and XPS showing large amounts of surface chlorine present after calcination resulting in inactive catalysts. An initial study using switchable solvents to prepare Cu/ZnO catalysts was shown to produce catalysts that were active for methanol synthesis and presents a promising potential for future development.

## Acknowledgements

I want to thank many people who all have been helpful through the project with good advice, guidance and training as well as great support. I have found the Cardiff Catalysis Institute to be a very welcoming and supporting environment.

I would firstly like to thank my supervisor Dr Jonathan Bartley and Professor Graham Hutchings for the guidance on the project and my PhD throughout the years and for given me the chance to undertake this work.

Secondly, I would like to thank my postdocs; Dr Simon Kondrat who gave me very good help and training in the early days of my PhD, Dr James Hayward who also gave me good help and training and who also performed the methanol synthesis data presented in this thesis. Dr Mark Douthwait Dr Samuel Patterson and Dr James Carter who gave help throughout the course. I would like to also acknowledge Dr Dave Morgan who performed the XPS experiments for this work and gave guidance on XPS analysis and Dr Tom Davis who help with some of the SEM images also presented in this work.

Of course, I would like to give a big thanks to the technicians and workshop: Chris Morgan, Dr Greg Shaw, Dr Michal Perdjon, Steve Morris, Lee Wescombe and Julian Young who have been great support and have help keep the labs in an organised and well-maintained condition. I would also like to thank my fellow PhD especially those who started at the same time as me (October 2015) in no order; Nia Richards, Parag Shan, Luke Parker, Simon Dawson, Emilia and Jerry who thought out the PhD have been good friends and given the CCI a very good atmosphere and made it an enjoyable place to work.

Finally, I would like to give thanks to my parents who have given me support throughout these years.

## Abbreviations

Abbreviations	Definition
ATR	Attenuated total reflectance
A.U	Arbitrary units
BET	Brunauer Emmet Teller (surface area analysis)
BPR	Back pressure regulator
ChCl	Choline Chloride
DBU	1,8 Diazobicyclo [5.4.0] undec-7-ene
DES	Deep eutectic solvent
DSC	Differential scanning calorimetry
EDX	Energy dispersive X-ray
FID	Flame Ionisation detector
FTIR	Fourier Transformed Infrared spectroscopy
GAS	Gas anti-solvent
GC	Gas Chromatography
GHSV	Gas Hourly space velocity
IL	Ionic liquid
MFC	Mass Flow Controler
mins	Minutes
MP-AES	Microwave Plasma Atomic Emission Spectroscopy
PPM	Parts per million
S.A	Surface area

SAS	Supercritical anti-solvent
scCO <sub>2</sub>	Supercritical CO <sub>2</sub>
scH <sub>2</sub> O	Supercritical water
SEM	Scanning electron microscopy
SCF	Supercritical fluids
SHS	Switchable hydrophobic solvent
SPS	Switchable polar solvent
T <sub>10</sub> /T <sub>50</sub> / T <sub>90</sub>	Temperature of 10% 50% or 90% conversion
TCD	Thermal conductivity detector
TEA / N <sub>222</sub>	Triethylamine
TEM	Transmission electron microscopy
TGA	Thermal Gravimetric analysis
TPR	Temperature programmed Reduction
VOC	Volatile organic compounds
XPS	X-ray photoelectron spectroscopy
XRD	(powder) X-ray diffraction

# Contents

Abstract .....	i
Acknowledgements.....	iii
Abbreviations.....	iv
Chapter 1 Introduction and Literature Review .....	1
1.1 Catalysis .....	1
1.2 Overview of metal oxides in heterogeneous catalysis .....	5
1.3 Current methods of preparing metal oxide precursors and catalysts .....	7
1.3.1 Co-precipitation .....	8
1.3.2 Sol gel synthesis .....	11
1.3.3 Hydrothermal and solvothermal techniques.....	12
1.4 Application of metal oxide as catalysts .....	15
1.4.1 Metal oxides catalyst for total oxidation of volatile organic compounds ..	15
1.4.2 Hopcalite .....	18
1.4.3 Copper/zinc Oxides based catalyst for methanol synthesis .....	23
1.5 Supercritical fluids for metal oxide preparation.....	26
1.5.1 Supercritical fluids .....	26
1.5.2 Type of supercritical fluid process .....	27
1.5.3 Supercritical anti-solvent process for heterogeneous catalyst preparation .....	28
1.6 Ionic liquids and deep eutectic solvents .....	30
1.6.1 Ionic liquids .....	30
1.6.2 Deep eutectic solvents .....	33
1.6.3 Solubility of metal salts in deep eutectic solvents .....	35
1.6.4 Anti-solvent processes using ionic liquids and deep eutectic solvents ....	37
1.6.5 Ionothermal synthesis of metal oxide .....	38
1.7 Switchable solvents .....	39
1.8 Discussion: green processes for making metal oxide catalysts .....	43

1.9 Aims of the Thesis .....	46
1.10 Chapter 1 References .....	47
Chapter 2 Experimental .....	57
2.1 Introduction .....	57
2.1.1 Chemicals list .....	57
2.2 Catalyst preparation .....	59
2.2.1 Deep eutectic solvents .....	59
2.2.2 Oxalate gel method for cobalt oxide preparation .....	61
2.2.3 Supercritical anti-solvent process .....	61
2.2.4 Preparation of crednerite and spinel derivatives by hydrothermal synthesis .....	64
2.2.5 Preparation of copper manganese oxides by co-precipitation .....	64
2.2.6 Switchable solvent experiment for metal oxide preparation .....	65
2.3 Catalyst characterisation: theory and methods .....	66
2.3.1 Powder X-ray diffraction .....	66
2.3.2 X-ray photoelectron spectroscopy .....	69
2.3.3 Electron microscopy .....	72
2.3.4 Thermal gravimetric analysis and differential scanning calorimetry .....	75
2.3.5 Temperature programmed reduction .....	76
2.3.6 Surface area analysis .....	77
2.3.7 Infra-red spectroscopy .....	79
2.3.8 Microwave plasma atomic emission spectroscopy .....	81
2.4 Catalysts testing .....	83
2.4.1 Gas chromatography .....	83
2.4.2 Carbon monoxide oxidation reaction .....	87
2.4.3 Propane oxidation .....	89
2.4.4 Methanol synthesis testing .....	91
2.5 Chapter 2 References .....	93
Chapter 3 Choline Chloride-Oxalic Acid Based Deep Eutectic Solvents for the Preparation of Metal Oxalate Precursors for Metal Oxide Catalyst .....	95

3.1 Introduction .....	95
3.1.1 Background on deep eutectic solvents and metal oxalates.....	95
3.1.2 Overview of the preparation method for cobalt, manganese and iron oxalate .....	97
3.1.3 Aims of the chapter .....	99
3.2 Cobalt oxalate .....	99
3.2.1 Synthesis of cobalt oxalate and cobalt oxide and comparison to standard .....	99
3.2.2 Effect of heat treatment .....	108
3.2.3 Effect of anti-solvent mixtures and rate of addition of anti-solvent .....	112
3.3 Iron oxalate .....	124
3.4 Manganese oxalate.....	130
3.5 The preparation of mixed metal oxides using DES-oxalate method.....	135
3.5.1 Cobalt manganese oxalate.....	136
3.5.2 Iron manganese oxalate.....	140
3.5.3 Mixed oxide catalyst testing.....	143
3.6 Chapter 3 Conclusions.....	145
3.7 Chapter 3 Future work .....	146
3.8 Chapter 3 References .....	147
Chapter 4 Evaluation of Delafossite Phase Copper-Manganese Oxides and Spinel Derivatives for CO Oxidation.....	149
4.1 Introduction .....	149
4.1.1 Background on delafossite materials.....	149
4.1.2 Aims of Chapter 4 .....	151
4.2 Crednerite synthesis .....	151
4.2.1 Hydrothermal synthesis of crednerite .....	151
4.2.2 Spinel oxides derived from crednerite .....	152
4.2.3 Hopcalite prepared by co-precipitation .....	153
4.3 Characterisation of crednerite and its spinel derivatives and comparison with co-precipitated hopcalite .....	153

4.4 Crednerite and spinel derivatives as catalyst for CO oxidation .....	175
4.4.1 Carbon monoxide conversion activity of crednerite and spinel derivatives in comparison with co-precipitated hopcalite. ....	175
4.4.2 Discussion on surface area normalised rates .....	179
4.4.3 The effect of airflow heat treatment methodology on the activity on the CO oxidation activity .....	180
4.4.4 Catalyst deactivation and stability.....	181
4.5 Chapter 4 Conclusions.....	184
4.6 Chapter 4 Future Work.....	185
4.7 Chapter 4 References .....	186
Chapter 5 Switchable Solvents for The Preparation of Copper Manganese Oxide Catalysts.....	188
5.1 Introduction.....	188
5.1.1 Background on switchable solvents.....	188
5.1.2: Choosing the switchable solvent and overview on the switching process for metal carbonate preparation .....	189
5.1.3 Aims of Chapter 5 .....	191
5.2 Switchable solvent for single metal carbonate preparation: copper and manganese carbonates .....	191
5.3 Switchable solvent for copper-manganese preparation.....	197
5.3.1 Switchable solvent to prepare hopcalite precursor and comparison to SAS and co-precipitated hopcalite .....	198
5.3.2 Change in precursor salt and precipitation atmosphere.....	205
5.3.3 Effect of varying the amount of triethylamine.....	214
5.3.4 Effect of aging time and atmosphere .....	222
5.4 Chapter 5 Conclusions.....	238
5.5 Chapter 5 Future work .....	239
5.6 Chapter 5 References .....	240
Chapter 6 Deep Eutectic Solvent and Switchable Solvents for The Preparation of Copper-Zinc Oxides.....	242
6.1 Introduction.....	242

6.1.1 Background.....	242
6.1.2 Aims of chapter .....	244
6.2 Deep eutectic solvent preparation.....	245
6.2.1 Effect of the Cu:Zn ratio .....	245
6.2.2 Effect of the rate of precipitation and the precursor salt.....	252
6.2.3 Catalytic testing.....	259
6.3 Switchable solvent preparation .....	260
6.3.1 Characterisation .....	261
6.3.2 Catalyst testing.....	267
6.4 Chapter 6 Conclusions.....	269
6.5 Chapter 6 Future work .....	270
6.6 Chapter 6 Reference.....	271
Chapter 7 Overall Conclusions and Future Work .....	273
7.1 Conclusions .....	273
7.1.1 Deep eutectic solvents for metal oxide preparation .....	273
7.1.2 Crednerite as a hopcalite precursor.....	275
7.1.3 Switchable solvents for hopcalite and copper zinc oxide .....	276
7.1.4 Overall conclusions .....	277
7.2 Future work expansion of deep eutectic solvent, hydrothermal and switchable solvent systems .....	279
7.3 Chapter 7 References .....	281

# Chapter 1 Introduction and Literature Review

## 1.1 Catalysis

A catalyst is most commonly defined as “a substance that increases the rate of a reaction but does not get changed itself”<sup>1</sup> but this is a simplified explanation of an area of science that is fundamental in chemical industry, and in fact even in nature since without enzymes, biological catalysts, life could not occur<sup>2</sup>. Catalysts are categorised into three main areas 1) biocatalysis: the use of biological catalyst (enzymes), 2) homogeneous catalysis: when the catalyst is in the same phase as the substrate (for example an organometallic complex dissolved in a solvent) and 3) heterogeneous catalysis: the use of a catalyst that is a different phase to the reactants or products. Heterogeneous catalysts are usually solids that catalyse reactants that are either in the gas phase (such as the oxidation of carbon monoxide to carbon dioxide) or liquid phase (such as the Meerwien Ponndorf Verley, catalytic reduction of carbonyls to alcohols<sup>3</sup>).

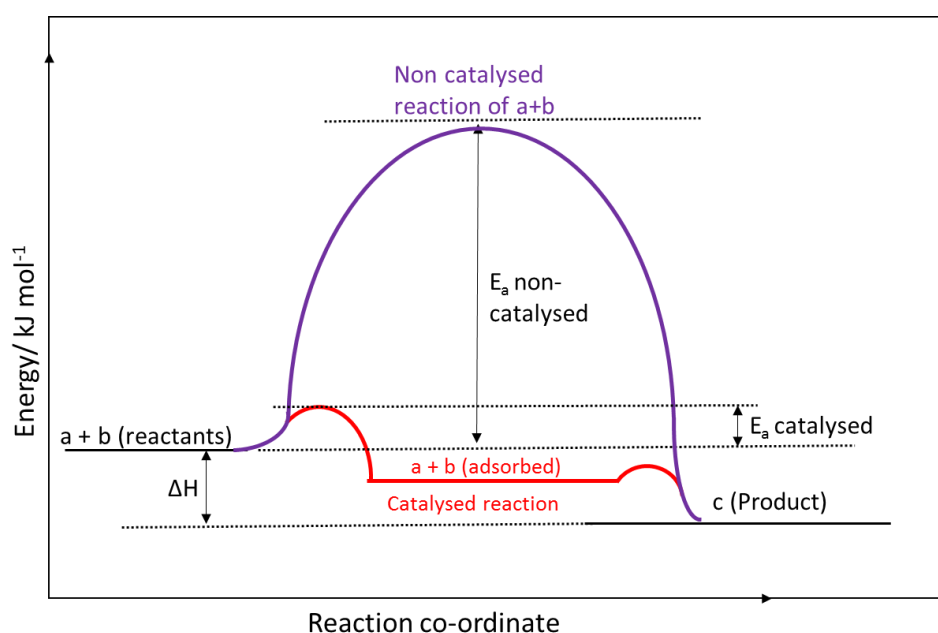
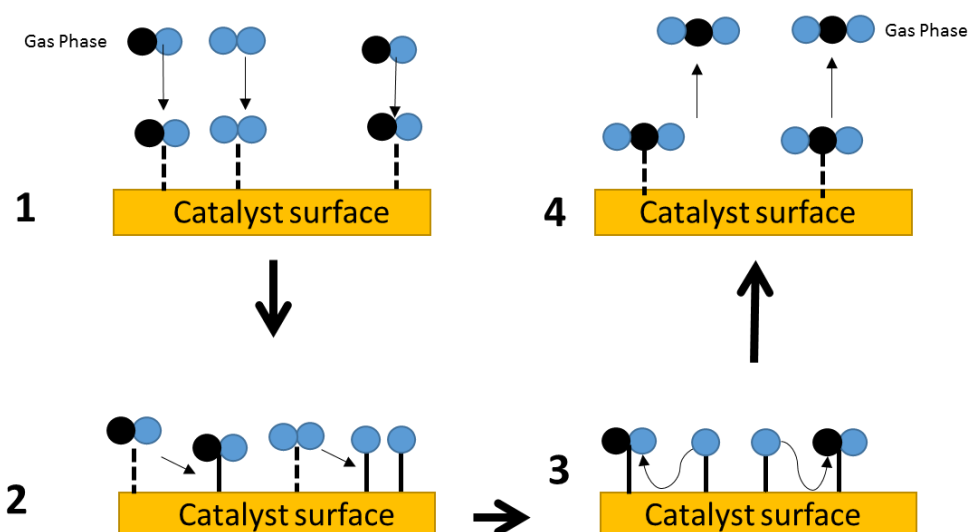


Figure 1.1: Energy diagram showing the difference in activation energy between a non-catalysed reaction and a catalysed reaction on a heterogeneous catalyst surface<sup>2</sup>.

The catalyst achieves the increase in the rate at which the reaction proceeds to equilibrium by allowing the reaction to proceed via a pathway with activation energy ( $E_a$ ) that is significantly lower than it would be if there was no catalyst<sup>4, 5</sup>. For example, under ambient conditions oxidation of carbon monoxide with oxygen to form carbon dioxide would need at least  $494 \text{ kJ mol}^{-1}$  to break the O-O bond<sup>1</sup>, but in the presence of a catalyst (for example gold nanoparticles on a metal oxide support) the oxygen can adsorb and disassociate on the surface and lower the activation energy to as little as  $20\text{-}44 \text{ kJ mol}^{-1}$ <sup>6</sup> (as shown in **Figure 1.2**). The lowering of the activation energy means it is more likely that the CO will react with the oxygen (on the surface), thereby increasing the rate at which CO oxidises to  $\text{CO}_2$ .

Heterogeneous catalysis has many favourable factors that has led to wide spread applications. These include their thermal stability, less complex preparations and easier handling than homogeneous catalysts and as such have been applied in many reactions, such as the three way catalyst<sup>7</sup> in car exhausts but also in many important industrial applications such as the synthesis of methanol from carbon dioxide and hydrogen<sup>8</sup> (which is a feedstock be used to make other organic products)<sup>2</sup> or the Fischer Tropsch reaction<sup>9, 10</sup>.



**Figure 1.2:** A Langmuir Hinshelwood type mechanism 1) physisorption onto surface 2) chemisorption and disassociation 3) reaction on surface and 4) desorption of product from surface

In heterogeneous catalysis the reaction occurs on the surface of the catalyst whether a bulk metal oxide, supported metal catalyst or in some cases the interface between the supported metal catalyst and the support. The reactants interact with the solid catalyst in two ways 1) physisorption, where the molecules are bound to the surface with weak Van De Waals forces and chemisorption where the molecules form a chemical bond with the catalyst surface and the molecule disassociates. When the reactants are adsorbed onto the surface the molecules react before the exothermic reaction causes desorption of the product from the surface of the catalyst<sup>2,4</sup>.

There are a variety of mechanisms that occur with heterogeneous catalysts but the three main mechanisms in heterogeneous catalysis are Langmuir Hinshelwood, Eley Rideal and Mars Van Krevelen<sup>11</sup>. In the Langmuir Hinshelwood mechanism (**Figure 1.2**), the reactants (a) and (b) adsorb onto the surface of the catalyst, then the reactants disassociate (on the surface) before (a) and (b) react to form product (c) which desorbs from the surface.

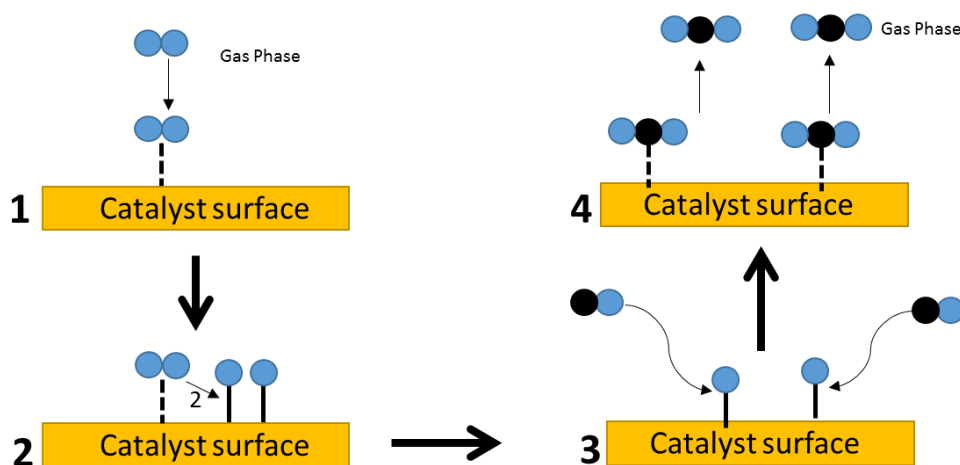


**Figure 1.3: Eley Rideal Mechanism 1) (a) is adsorbed onto the surface 2) disassociates on surface, 3) (b) in gas phase reacts with the adsorbed (a) to forms (c) and 4) (c) disassociated from the surface**

In Eley Rideal (**Figure 1.3**) only (a) absorbs onto the surface and (b) remains in the gas or liquid phase reacting with (a) to form (c) which then desorbs from the surface. Mars Van Krevelen (**Figure 1.4**) is another mechanism pathway that occurs with metal oxide catalysts. In this mechanism the reactant (a) is adsorbed onto the surface, (a) then reacts with the surface (b) of the catalyst to form (c) and the catalyst is then regenerated by reacting

with (b) from the atmosphere. An example of this would CO oxidation where CO is oxidised by surface oxygen of a metal oxide and atmospheric oxygen would then react with the catalyst to regenerate the metal oxide site<sup>12</sup>.

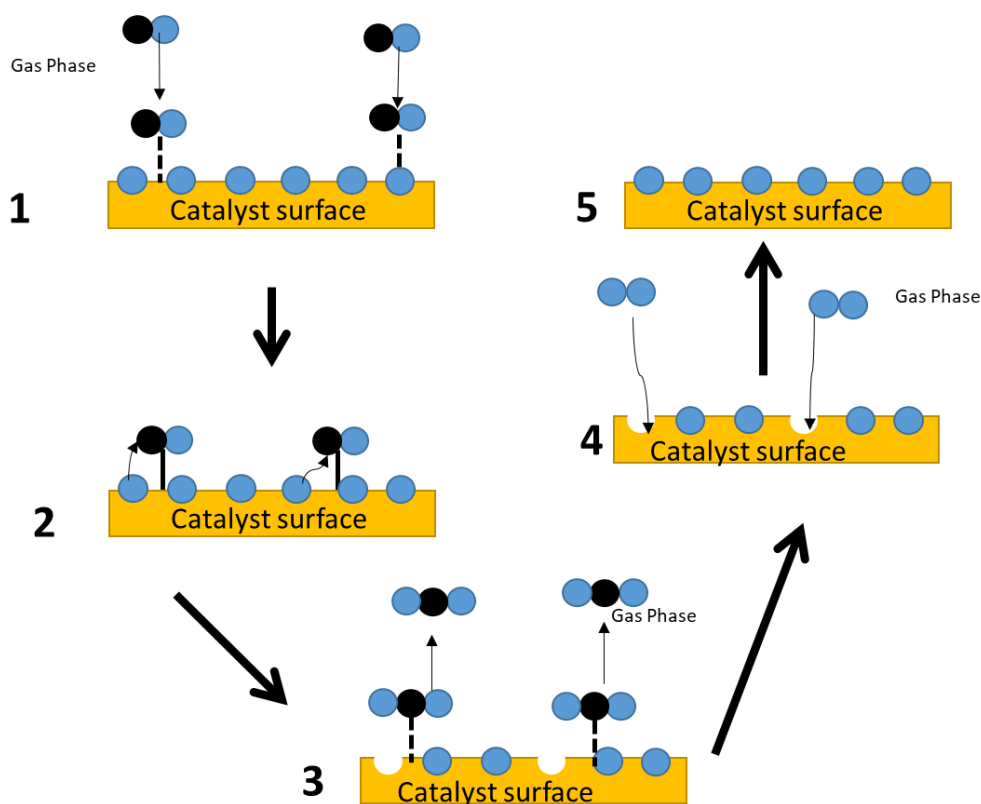


**Figure 1.4: The Mars Van Krevelen mechanism 1) (a) is adsorbed onto the surface, 2) lattice oxygen (b) of the catalyst reacts with (a) to form (c), 3) (c) disassociate from surface, 4) atmospheric oxygen (b) reacts with the catalyst surface to regenerate the oxide (5).**

Sometimes catalysts may, proceed with two (or more) of these mechanisms, for example hopcalite as a CO oxidation catalyst was found to catalyse the oxidation of CO to CO<sub>2</sub> via both the Langmuir Hinshelwood and Mars Van Krevelen mechanisms (see Section 1.4.2 Hopcalite)<sup>12</sup>.

Heterogeneous catalysis is a highly important area, not just in industry but its contribution to the way we live, and provides solutions to many of the problems we face today including utilisation of captured CO<sub>2</sub><sup>13</sup>, reduction of harmful emissions<sup>14</sup>, and the production of ammonia for use in fertiliser for food production<sup>2, 15</sup>. The most common heterogeneous catalysts are either bulk catalysts with metal oxides being the most common or supported metal catalyst such as gold nanoparticles supported on an metal oxide support<sup>16</sup>.

The choice of catalyst used is generally dependent on the reaction which it is being used for, with factor such as desired products, selectivity and activity (the rate of conversion) being the most important. However there are other factors that have to be considered such as the cost-benefit of the catalyst for that certain reaction (i.e. using  $\text{Co}_3\text{O}_4$  or  $\text{Pt}/\text{Al}_2\text{O}_3$  as a VOC oxidation catalysts<sup>17</sup>), whether or not the catalyst deactivates in short or long term, although all catalyst eventually deactivate<sup>18</sup>, and its resistance to poisoning from impurities in the gas feed such as sulphur or water vapour.

## 1.2 Overview of metal oxides in heterogeneous catalysis

For a large number of reactions involving heterogeneous catalysts, metal oxides are heavily used either as bulk catalyst or as a support<sup>19</sup>. Metal oxide are used as bulk heterogeneous catalysts for a variety of reactions such as total oxidation (e.g. carbon monoxide<sup>20</sup> or volatile organic compounds (VOC)<sup>21</sup> to  $\text{CO}_2$ ), selective oxidation<sup>22</sup> and dehydrogenation<sup>23</sup>, among many others process<sup>24</sup>.

The reasons for the use of metal oxides in these reactions varies with the application, as low-cost alternatives to supported noble metal catalysts or for other factors such as oxygen mobility. This makes the study of metal oxides in the field of heterogeneous catalysis is a highly important one. Metal oxide catalysts can be used as either a single metal oxide with examples including  $\text{Co}_3\text{O}_4$ ,  $\text{Mn}_3\text{O}_4$ <sup>17, 21</sup> and  $\text{CeO}_2$ <sup>7, 17</sup> or as mixed metal oxide comprising of two or more metal elements such as  $\text{CuMn}_2\text{O}_4$ ,  $\text{LaMnO}_3$ <sup>25</sup> or mixed  $\text{CeO-MnO}$ <sup>26</sup>.

The phase of a metal oxide whether a single or mixed element oxide, plays an important role in its properties such as oxygen mobility<sup>27</sup>, thermal stability<sup>27</sup>, redox behaviour<sup>28</sup> and acid-base properties<sup>29</sup> and can influence the catalytic activity and selectivity of that metal oxide. Common examples of metal oxide phases that are commonly used as catalysts include corundum  $\text{Al}_2\text{O}_3$  (single metal), spinel ( $\text{AB}_2\text{O}_4$ ) (single or mixed)<sup>29</sup> and perovskite  $\text{ABO}_3$  (mixed metals)<sup>30</sup> although there are many others including fluorite and delafossite<sup>31</sup>.

Spinel phase oxide materials are bulk oxides with the formula  $AB_2O_4$  where A is a +2 metal in a tetrahedral co-ordinated to four oxygens in  $AO_4$  and B is a +3 metal co-ordinated in a octahedral arrangement to 6 oxygens in the form of  $BO_6$ <sup>1, 22</sup>. Spinel oxides can be present as either a mixed metal oxide such as  $CuCr_2O_4$ <sup>32</sup> or  $CuMn_2O_4$ <sup>33</sup> or as a single metal oxide materials such as  $Co_3O_4$  or  $Mn_3O_4$  (which would comprise of  $Mn^{2+}(Mn^{3+})_2O_4$ )<sup>1, 22, 34</sup>. There are some cases where an inverted spinel can exist, i.e. where the +2 is in the octahedral B site and the +3 are in the tetrahedral A-site<sup>35, 36</sup>. Although spinel phase oxides in the bulk comprise of both the octahedral (A) site and the tetrahedral (B) site in the bulk in reality, on the surface, the structure is different and in the case of spinel it has been found that the surface is populated by octahedral sites with studies showing little presence of tetrahedral sites<sup>22</sup>. Spinel phase materials are studied as heterogeneous catalysts and in other fields due to their properties such as chemical and thermal stability, low cost of materials, ease of preparation and their redox cycling<sup>37, 38</sup>. These properties of spinel phase metal oxides makes them suitable for applications in high temperature, gas phase reactions such as the total oxidation of VOCs<sup>14</sup>.

Although single and mixed metal oxides as catalysts (not supports) have advantages it should be noted that they also have disadvantages compared to supported (noble) metal catalysts, the main one being that metal oxides are mostly less active than supported metal catalysts<sup>16</sup>. However, there are also a variety of other reasons that make metal oxides less favourable, notably that some metal oxides deactivate quicker and are more prone to (non-selective) poisons such as  $SO_2$  or atmospheric water<sup>39, 40</sup>.

A notable example of this is with CO oxidation. Haruta in the late 1980s demonstrated that supporting gold onto metal oxide was able to catalyse the conversion of CO to  $CO_2$  with 100% conversion of CO<sup>41, 42</sup> even in the presence of water in the gas feed. In comparison  $Co_3O_4$  is also a highly active CO oxidation catalysts showing 100% CO conversion at sub ambient temperatures, but  $Co_3O_4$  was only highly active for CO oxidation under ultra-dry conditions. The presence of atmospheric water reduces its catalytic activity due to water binding to the active site ( $Co^{3+}$ )<sup>43</sup>.

The cost and increased scarcity of noble metals, as well as competition with other applications, has made it more difficult to scale up their application on an industrial level and as a result, research in the field of heterogeneous catalysts for several processes in recent years has seen the shift of focus (back) to the use of metal oxide catalysts<sup>38, 44, 45</sup>. As a result, there is a focus on finding ways of improving the activity of metal oxide catalysts to a level that is nearer to supported noble metal catalysts. In order to improve the performances of metal oxide catalysts research groups try to improve factors such as the total surface area, reducing potential catalyst poisoning, increased phase integration and exploring the metal oxides particle shape/morphology<sup>46-48</sup>. There are various ways in which these factors can be improved, but the most common and important is how the metal oxide catalyst is prepared<sup>28, 49</sup>.

### **1.3 Current methods of preparing metal oxide precursors and catalysts**

One of the main strategies of improving the catalytic activity of metal oxide to levels comparable with supported metal catalysts is through the method by which these catalysts are prepared.

One strategy of making metal oxides with higher surface area is through the decomposition of a precursor material; a metal salt, that under heating degrades to the oxide. For example, manganese oxide can be prepared through the decomposition a manganese precursor (such as manganese carbonate or manganese oxalate)<sup>50</sup> at temperatures >200 °C. Preparing a metal oxide catalyst through thermal decomposition of a metal salt has several advantages. Firstly, the controlled thermal decomposition of the metal salt can determine which phase is formed. For example, manganese oxalate can form  $Mn_3O_4$ ,  $Mn_2O_3$  or  $MnO$  depending on the atmosphere the manganese oxalate is calcined under<sup>51</sup>. The second advantage is that the precursor salt can act as a soft template for the resulting oxide to form both

single and mixed oxides with a higher surface area. A third advantage is that the templating can give better mixing of elements at lower temperatures than a solid-state reaction of two oxides.

There are a wide variety of preparation technique for metal oxides, with the established methods such as co-precipitation, sol gel and hydrothermal synthesis being the more common approaches<sup>46, 52, 53</sup>. The different preparation techniques and precursors, as well as the heat treatment, can rapidly change the properties of catalysts such as surface area, elemental mixing, morphology and phase of the final material<sup>28, 54</sup>.

While some of the research focuses on improving and understanding more established methods such as co-precipitation and sol gel chemistry. The use of more novel techniques such as supercritical anti-solvent precipitation or ionothermal synthesis (the use of a deep eutectic solvent or ionic liquid under hydrothermal conditions<sup>55</sup>) has in recent years received increased attention as a method of preparing materials with increased surface area and better elemental mixing as well as lower calcination temperatures<sup>56</sup>.

### 1.3.1 Co-precipitation

The most established and refined method of making mixed metal oxides is via the co-precipitation method<sup>57</sup>. Precipitation is simply the formation of an insoluble solid or precipitate from a solvent and co-precipitation is when two or more components are simultaneously precipitated<sup>58</sup>. This is achieved by dissolving a metal salt in water then adding an agent that reacts with the dissolved species (metal ions) to form an insoluble species<sup>58</sup>. For metal oxide catalysts (**Figure 1.5**) typically the metal salts would be dissolved in water (with metal nitrates being the most common salts due to their high solubility), then using a base, such as sodium carbonate, a metal carbonate is formed and precipitates out of the solution<sup>59</sup>. The metals then undergo an aging process in the solution, before filtration, washing (to remove any residual precipitating agents, nitrates and sodium) and dried before calcination to form the oxide<sup>60, 61</sup>.

Co-precipitation remains one of the most widely used methods for preparing catalysts in industry since the process is relatively simple, reproducible and can be easily scaled up compared to other techniques<sup>62</sup>. The co-precipitation method has had the advantage of being heavily studied and refined over many years with aspects of the techniques including, pH, concentration of metal salt and precipitating agent and the aging of the precursor in the solution all being studied and optimised<sup>61, 63</sup>.

Aging, the time the precursor is left in the solution mixture, has often been cited as a highly important aspect of co-precipitation of metal oxide catalyst<sup>64</sup>. The aging of a catalyst precursor can have a variety of effects on the precursor such as morphology, surface area of the precursor final metal oxide formed and the catalytic activity of the final metal oxide.

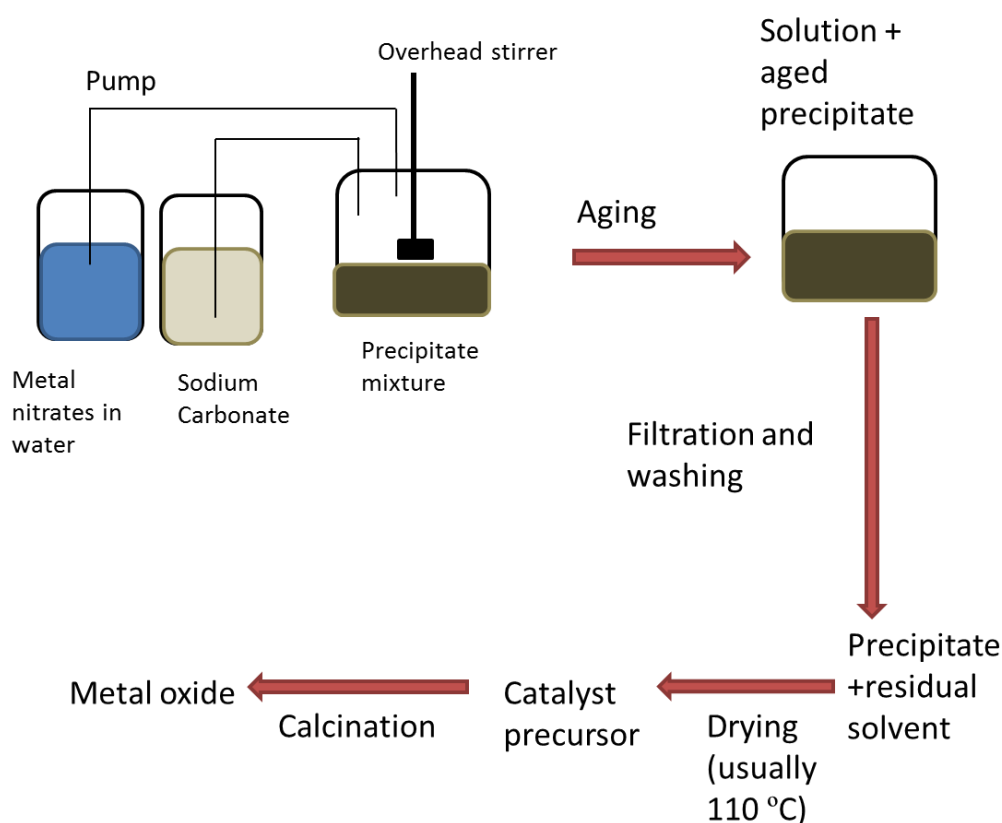


**Figure 1.5: The steps of making a metal oxide catalyst using co-precipitation**

There are many aspects of aging itself that can affect the final material such as the temperature<sup>64</sup> and pH<sup>57</sup> of the solution that the precursor is being aged in, as well other factors such as continued addition of metal nitrate and

sodium carbonate after the initial addition and the atmosphere that the solution is being aged under<sup>65</sup>.

Many studies on aging of copper-zinc oxide precursors have shown the effect of aging on the Cu/Zn hydroxyl carbonate precursor, with the non-aged sample forming a more amorphous phase while the aging allows the formation of crystalline Cu/Zn hydroxyl carbonate<sup>66</sup>. Aging of hopcalite catalysts (see section 1.4.2) was found to have an impact on their performance with the catalysts aged for 30 minutes shown to be the most active compare to those that were aged longer<sup>47</sup>.

There are other aspects of the aging environment that may affect the catalysts. Mirzaei *et al.* looked into the effect of aging on CuO/ZnO CO oxidation catalysts under different atmospheres; air, hydrogen, nitrogen and carbon dioxide<sup>65</sup>. This showed that for all atmospheres surface area increased with aging time, but the CO oxidation activity of the catalyst varied with different aging atmospheres. The catalyst aged under air showed the highest conversion while those aged under carbon dioxide showed the lowest activity<sup>65</sup>.

The pH of the solution during the precipitation and aging is also very important, since changing the pH can greatly affect the phase formation of the catalyst for example with Cu/ZnO a higher pH can cause the formation of crystalline CuO<sup>67</sup>.

Refinement of these aspects of co-precipitation (especially aging, temperature and pH) has resulted in co-precipitation being one of the most widely used methods of preparing mixed metal oxides and still is activity researched as well as remaining an industrial favourite for the preparation of several catalysts such as Cu/ZnO/Al<sub>2</sub>O<sub>3</sub><sup>59</sup>.

### 1.3.2 Sol gel synthesis

Sol gel synthesis is another widely used method for the preparation of single and mixed metal oxides. As with co-precipitation the use of sol gel chemistry to make metal oxides has been utilised for a long time but is still widely studied in the field of inorganic synthesis, not just being limited to metal oxides and heterogeneous catalysts<sup>53</sup>.

Although there are many different sol gel synthesis methods, the basic steps are as follows<sup>53, 58, 68, 69</sup>. The process starts off with the formation of a metal alkoxide in solution. This metal alkoxide then hydrolyses to form a dispersed colloid called a “sol”. This sol undergoes polycondensation to form the “gel” which is made up of a network of bridged metal species<sup>68, 69</sup>. The solvent is removed and the gel is dried to remove any solvent resulting in the formation of a porous gel such as xerogel or aerogel (aerogel being formed when the solvent inside the pores is replaced with gas without structure collapse through techniques such as supercritical drying<sup>53, 70, 71</sup>). The gel is then calcined to form the metal oxide.

The use of the sol gel technique has many advantages. Notably, it is a very good technique for forming mixed metal oxides since the gel process bridges different elements resulting in a near perfect elemental distribution and also sol gel materials generally have high surface areas<sup>20</sup>. As such the method has been used to make mixed metal oxide catalysts such as cobalt manganese oxide<sup>72</sup>, copper manganese oxide<sup>20</sup> and lanthanum based perovskites<sup>73</sup> as well as being used to prepare Cu/ZnO/Al<sub>2</sub>O<sub>3</sub> catalysts for methanol synthesis through a xerogel or aerogel (polymer gels) precursors<sup>70</sup>.

However one of the disadvantages of sol gel synthesis is that it utilises larger chelating agents such as citric acid, which can undergo exothermic combustion during the calcination process<sup>53, 70</sup>. While this does create high surface areas it can also create residual carbon on the surface and cause sintering of the material reducing the surface area.

### 1.3.3 Hydrothermal and solvothermal techniques

#### 1.3.3.1 Overview on hydrothermal and solvothermal techniques

Solvothermal techniques in simple terms are a chemical reaction/synthesis in a solvent under a pressurised system at a temperature near or higher than the solvents boiling point<sup>52</sup>. This is usually between 1-15 bar and 100-270 °C for water, but can vary depending on the solvent used<sup>74-76</sup>. The process of using solvothermal synthesis dates as far back as the 19<sup>th</sup> century, but the method is still utilised in many fields including metal oxide preparations<sup>75, 76</sup>. Solvothermal reactions are usually performed in a high-pressure autoclave such as the one presented in **Figure 1.6**. The solvent is contained in a non-reactive liner to protect the autoclave reactor from any corrosive substances.

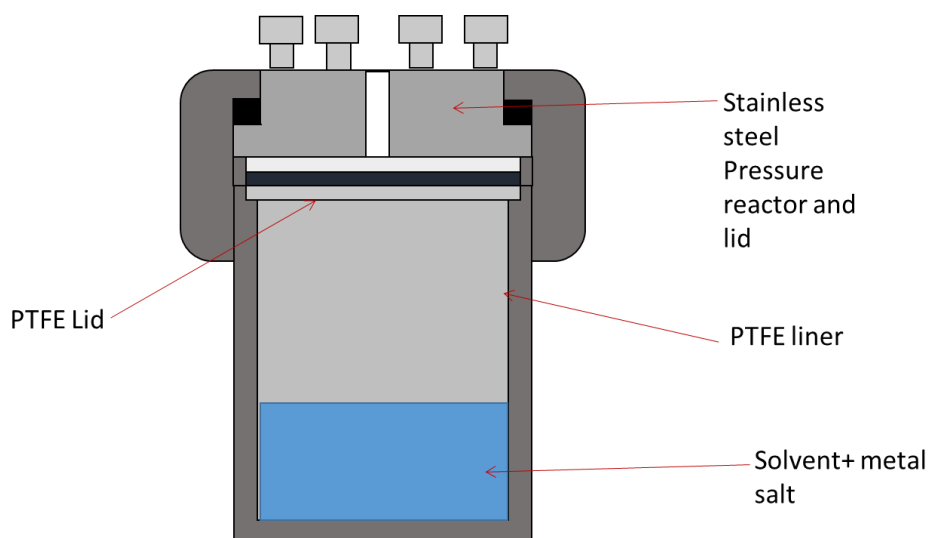


**Figure 1.6: A pressurised autoclave used for a solvothermal method**

Hydrothermal, is the use of water as the solvent and the term solvothermal usually applied when the technique is used with non-aqueous solvent such as ethanol is used<sup>76</sup>. Another type of solvothermal technique is ionothermal; the use of an ionic liquid or deep eutectic solvent as the solvent<sup>77</sup>.

During hydrothermal/ solvothermal synthesis, the greater pressure allows reaction mixture to remain in the liquid phase at much greater temperatures

than could be achieved under atmospheric conditions, allowing transportation of the metal ions to occur easily compared to lower temperature liquid phase or high temperature solid state equivalents<sup>77</sup>. The pressure of the reaction at a given temperature can be controlled by the volume of the solvent in the vessel<sup>74</sup>.

One factor that makes solvothermal/hydrothermal synthesis attractive is that it can be used to make kinetic controlled and metastable materials, which under the high temperatures, required for solid state reactions or calcination of a precursor salt, would not form in favour of a more thermally stable material<sup>52, 58, 77</sup>. Varying the pressure and temperature as well as any additives can rapidly change how the particles grow, thereby allowing a method that can tailor the morphology and size of the metal oxide nanoparticles<sup>76</sup>. Hydrothermal techniques can also be used to dissolve oxides in water under pressure that would usually be insoluble under atmospheric pressure<sup>78</sup>.

### **1.3.3.2 Hydrothermal synthesis for metal oxide preparation**

Hydrothermal, solvothermal and ionothermal methods have been used in a wide range of reactions and synthesis; however, the focus here will be on the preparation of metal oxides (ionothermal is discussed in Section 1.6.5).

Hydrothermal synthesis has been widely used for the preparation of metal oxides, most famously zeolites<sup>75</sup> but also a variety of single metal oxides (for example  $\text{Mn}_3\text{O}_4$  and  $\text{Fe}_2\text{O}_3$ <sup>79</sup>) and mixed metal oxide phases including spinels<sup>32, 80</sup> and perovskites<sup>81, 82</sup>. Hydrothermal synthesis presents a number of advantages over solid state reactions or calcination of metal salts. Firstly, although high temperatures and pressure above 100 °C and 1 bar are required, the conditions are lower than that of the solid state equivalent<sup>77</sup>. An example of this would be delafossite phase materials which have the form  $\text{ABO}_2$  such as  $\text{CuFeO}_2$  or  $\text{CuMnO}_2$  (where the A site is +1 metal such as  $\text{Cu}^+$  or  $\text{Ag}^+$  and B site is a +3 metal such as  $\text{Mn}^{3+}$  or  $\text{Fe}^{3+}$ ). Delafossite are formed through solid state preparation under an inert atmosphere at 860-1150 °C<sup>83</sup>

but can easily be formed at temperatures <200 °C under hydrothermal conditions<sup>31, 52</sup>.

Likewise, forming a metal oxide from a precursor such as a metal oxalate or metal carbonate<sup>66</sup> through co-precipitation or sol gel requires a calcination step with temperatures of 270-500 °C to break down the precursor metal salt into the metal oxide. This can cause several potential problems, notably sintering<sup>84</sup> of the metal oxide catalyst as well as residual carbon forming on the surface of the metal oxide, potentially blocking active sites and reducing catalytic activity. However, because most hydrothermal synthesis makes the metal oxide, rather than a precursor salt, this step is essentially eliminated.

Another advantage of solvothermal/ hydrothermal synthesis for metal oxide preparation is that it is a tailorable method and different oxide morphologies can be achieved by changing parameters such as the volume of solvent, the temperature and reaction time<sup>85</sup>. For example, Zheng *et al* reported that manganese acetate in ethanol (with no other additive, although under an inert atmosphere) under solvothermal conditions (200 °C) would form dispersed round particle after 3-6 hours that would grow into 1-dimensional rods after 12 hours<sup>85</sup>.

Hydrothermal synthesis has another advantage over in that it is essentially a one-pot and one step process, forming both single and mixed metal oxides without the need for a calcination step<sup>32</sup>, although some do require washing steps as hydrothermal synthesis involve the use of additives such or bases (e.g. NaOH), to form a precursor that would then form the desired oxide phase during the hydrothermal process<sup>86</sup>.

## 1.4 Application of metal oxide as catalysts

### 1.4.1 Metal oxides catalyst for total oxidation of volatile organic compounds

Volatile organic compounds are defined as organic compounds that have a high vapour pressure and are low boiling<sup>87</sup>, examples including alcohols, hydrocarbons (such as propane, n-hexane) and ketones. Industry is under increased legislation to reduce emissions of these compounds<sup>88</sup>, and one of the strategies of achieving this is through total oxidation of these compounds to CO<sub>2</sub><sup>89</sup>.

Supported metal catalysts have shown excellent activity towards VOC oxidation with examples including platinum or palladium supported on Al<sub>2</sub>O<sub>3</sub><sup>17</sup>, but as stated in Section 1.2 the expense of noble metal catalysts has seen several groups focus on metal oxide alternatives such as Mn<sub>2</sub>O<sub>3</sub>, Mn<sub>3</sub>O<sub>4</sub> and Co<sub>3</sub>O<sub>4</sub> or mixed phase as CoMnO<sub>x</sub> and CuMn<sub>2</sub>O<sub>4</sub><sup>90</sup>. Spinel phase metal oxides are notably one of the most common alternatives<sup>91</sup> as are perovskite phase oxides such as LaMnO<sub>3</sub> or LaCoO<sub>3</sub>. However perovskites require a more energy intensive approach such as higher calcination conditions to form (up to 800 °C)<sup>92</sup> which can result in heavy sintering and reduced surface area. In comparison, spinel phase materials often require a calcination temperature of 300-500 °C to form the phase<sup>37</sup>. On the whole the use of spinel phase oxides the oxidation of VOCs is still a popular area of research<sup>14</sup>.

Examples of single metal spinel oxides that have been used as VOC oxidation catalysts include Co<sub>3</sub>O<sub>4</sub> and Mn<sub>3</sub>O<sub>4</sub><sup>93, 94</sup>. In the case of Mn<sub>3</sub>O<sub>4</sub>, it was noted to have superior propane conversion over other manganese oxides such as Mn<sub>2</sub>O<sub>3</sub> and MnO<sub>2</sub> owing to its oxygen mobility which helps increase the oxidation performance at lower temperatures<sup>94</sup>. Oxygen mobility is an important factor since many of these metal oxides oxidise VOCs via the Mars Van Krevelen mechanism<sup>38</sup>.

$\text{Co}_3\text{O}_4$  is another spinel phase material of particular interest due its high catalytic activity compared to similar spinel oxides such as  $\text{Mn}_3\text{O}_4$  or  $\text{Fe}_3\text{O}_4$  for both VOC oxidation and low temperature CO oxidation<sup>17, 95</sup>. One of the key factors for highly active cobalt oxide catalysts is the crystallite size with  $\text{Co}_3\text{O}_4$  that have a smaller crystallite size being more active for both CO and propane oxidation<sup>17</sup>. As a result, the main focus of  $\text{Co}_3\text{O}_4$  was to form nanocrystalline  $\text{Co}_3\text{O}_4$  while increasing the surface area as well as controlling the morphology and particle shape of these crystallites has also been researched<sup>21, 93</sup>. The reducibility of  $\text{Co}_3\text{O}_4$  has also been noted as another important factor in its catalytic oxidation of VOCs<sup>89</sup>.

There are a variety of techniques that can be used to achieve highly active materials such as hard templating with KIT-6<sup>17</sup>, precipitation in ethylene glycol (at 160 °C)<sup>96</sup> or supercritical anti-solvent precipitation<sup>21</sup>.  $\text{Co}_3\text{O}_4$  prepared by supercritical anti-solvent and by solid state reaction had a lower temperature of total conversion ( $T_{100}$ ) for propane oxidation than the reference Pd/  $\text{Al}_2\text{O}_3$  or Pt / $\text{Al}_2\text{O}_3$ <sup>21, 91</sup>.

Although cobalt oxide had been demonstrated as a very good VOC oxidation catalyst, there have been many developments on mixed spinel oxides, in order to increase their activity for total conversion at lower temperatures. Mixed metal spinel oxides such as cobalt manganese oxide, iron manganese oxide and copper manganese oxide (commonly referred to as hopcalite and explained in more detail in Section 1.4.2) have higher CO and VOC oxidation activity at lower temperatures (lowering their temperature at which they achieve 10% conversion ( $T_{10}$ )) than the single spinel oxide counterparts<sup>14, 97</sup>.

This results from several factors such as change in redox behaviour<sup>38</sup> and increase in reducibility<sup>97</sup>. It has been noted that the  $\text{Co}^{2+}$  in  $\text{Co}_3\text{O}_4$  played a less active role in the reaction than  $\text{Co}^{3+}$  and substituting the tetrahedral site for a more active +2 metal such as  $\text{Cu}^{2+}$  was found to increase its VOC conversion at lower temperatures<sup>98</sup>.

**Table 1.1: Examples of Propane oxidation using a variety of different metal oxides and comparison with supported Pt/Al<sub>2</sub>O<sub>3</sub>. (T<sub>x</sub>= temperature which x% conversion is achieved)**

Catalyst	Preparation methods	Reaction Conditions	Surface area/ m <sup>2</sup> g <sup>-1</sup>	Activity	Ref
Co <sub>3</sub> O <sub>4</sub>	Mixed oxalate formed by precipitation with ammonium oxalate in water	97.8 ml min <sup>-1</sup> 0.4% propane+ 20% O <sub>2</sub> /Ar	60	T <sub>50</sub> ≈ 200 °C. full conversion by 250 °C	95
Co <sub>3</sub> O <sub>4</sub>	Supercritical anti-solvent (scCO <sub>2</sub> ) 10% water Calcined 250 °C	0.5% Propane/air GHSV= 6000 h <sup>-1</sup>	36	T <sub>10</sub> =110 °C T <sub>50</sub> =175 °C 100% conversion at 200 °C	21
Co <sub>3</sub> O <sub>4</sub> Nano crystalline	Solid state reaction with Co(NO <sub>3</sub> ) <sub>2</sub> ·6H <sub>2</sub> O and NH <sub>4</sub> HCO <sub>3</sub> Calcined 300 °C	0.5 % propane/air GHSV= 45000 h <sup>-1</sup>	159	T <sub>10</sub> =145 °C T <sub>50</sub> =165 °C T <sub>100</sub> =200 °C	17
Co <sub>3</sub> O <sub>4</sub>	Templating with KIT-6	0.5% propane.air GHSV= 4800 h <sup>-1</sup>	138	T <sub>10</sub> =170 °C T <sub>50</sub> =250 °C	91
Mn <sub>x</sub> Co <sub>3-x</sub> O	Redox method of Co(NO <sub>3</sub> ) <sub>2</sub> and KMnO <sub>4</sub> on ceramic honeycomb monolith hydrothermal at 95 °C	0.3% propane +10% O <sub>2</sub> with N <sub>2</sub> balance 50 ml min <sup>-1</sup>	35.5 (6:4 Co:Mn)	T <sub>50</sub> =310 °C (6:4 Co:Mn)	99
Cu <sub>1.5</sub> Mn <sub>1.5</sub> O <sub>4</sub> /CuO	Co-precipitation Cu(NO <sub>3</sub> ) <sub>2</sub> , Mn(NO <sub>3</sub> ) <sub>2</sub> Na <sub>2</sub> CO <sub>3</sub> Calcined 500 °C	1% Propane +7% O <sub>2</sub> / He balance 200 ml min <sup>-1</sup>	46	T <sub>50</sub> =292 °C	90
La <sub>0.8</sub> Ce <sub>0.2</sub> MnO <sub>3</sub>	Citric acid gel With nitric acid treatment	0.5% Propane+10% O <sub>2</sub> 100 ml min <sup>-1</sup>	26 112 (acid etching)	T <sub>50</sub> =237°C T <sub>90</sub> =284 °C Acid treatment: T <sub>50</sub> =156°C T <sub>90</sub> =196 °C	100
4.8% Pt/Al <sub>2</sub> O <sub>3</sub>	Impregnation Calcined 300 °C	4% (1:16 propane:O <sub>2</sub> ) Helium balance 30 ml min <sup>-1</sup>	-	100% conversion by 350 °C T <sub>50</sub> =265 °C <sup>87</sup>	101 87

Like the single oxides, researchers have investigated different methods of preparation of mixed oxide phases to increase surface area<sup>95</sup> or control the morphology<sup>102</sup> as well as control the ratios of the two (or more) metal elements<sup>99</sup>. The group of Li *et al.* prepared high surface area Co-Mn spinel oxide (1:1) by annealing a Co-Mn 1,3-propanediol complex, which resulted a porous “coral” like morphology, with a surface area of 99 m<sup>2</sup> g<sup>-1</sup>, higher than the single metal oxides (Co<sub>3</sub>O<sub>4</sub> and Mn<sub>3</sub>O<sub>4</sub>) prepared by the same method. The mixed cobalt manganese oxide had higher catalytic activity for total oxidation of benzene than the single oxide equivalents<sup>38</sup>.

Tang *et al.* used a redox reaction between KMnO<sub>4</sub> and Co(NO<sub>3</sub>)<sub>2</sub> on a ceramic honeycomb to form nanosheets of spinel phase Co-Mn oxides which performed better (T<sub>50</sub> of 310 °C) than Pt/Al<sub>2</sub>O<sub>3</sub> (T<sub>50</sub> of 370 °C) as propane oxidation catalysts<sup>99</sup>. Faure and Alphonso prepared both single manganese oxide, cobalt oxide and mixed cobalt manganese spinel phase oxides by creating oxalate precursors through precipitation of metal nitrates with oxalic acid and forming the oxides through controlled decomposition, using a 4% O<sub>2</sub>/Ar and a mass spectrometer to detect the temperature of CO<sub>2</sub> formation, holding the reaction at that temperature<sup>95</sup>.

#### 1.4.2 Hopcalite

Hopcalite catalysts are mixed copper-manganese spinel phase oxides in the form of Cu<sub>x</sub>Mn<sub>3-x</sub>O<sub>4</sub><sup>61, 103, 104</sup>. CuMn<sub>2</sub>O<sub>4</sub> (Cu:Mn ratio of 1:2) is the most common ratio used as a catalyst since this ratio had been demonstrated as the most active towards CO oxidation<sup>61, 103</sup>, although other Cu:Mn ratios such as Cu<sub>1.5</sub>Mn<sub>1.5</sub>O<sub>4</sub> have also been applied as catalysts<sup>104</sup>. Hopcalite has been used as a heterogeneous catalyst for many process, most commonly for the low temperature oxidation of carbon monoxide to carbon dioxide<sup>105, 106</sup> and total oxidation of VOCs such as propane<sup>90</sup>, toluene<sup>103</sup> or naphthalene<sup>33</sup>. Hopcalite has also been used as catalyst for other processes such as H<sub>2</sub>O<sub>2</sub> decomposition<sup>107</sup> and the water gas shift reaction<sup>108</sup>.

### 1.4.2.1 Hopcalite as a CO Oxidation Catalyst

Hopcalite was used in the early 1920s as a CO oxidation catalyst in breathing masks<sup>109</sup>. It was reported that mixtures of copper oxide or silver oxide on manganese dioxide produced active catalysts that were effective at converting CO to CO<sub>2</sub> at room temperature<sup>109</sup>. Since then the use of mixed copper-manganese oxides continues to be studied, most notably into new ways of preparing hopcalite with better activity and higher surface areas<sup>46, 110</sup>. Even 30 years after Haruta demonstrated that supported gold catalysts had superior CO oxidation activity at sub ambient conditions<sup>16, 42</sup>, hopcalite remains the standard catalyst for CO oxidation in respirators<sup>20, 111</sup>, mostly owing to its lower cost. The publication on supported gold nanoparticles that renewed interest in both fields of CO oxidation and on the preparation of hopcalite in the 1990s<sup>16, 112, 113</sup>.

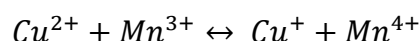


**Figure 1.7: Copper-manganese redox coupling proposed by Schwab et al<sup>107</sup>**

The reaction mechanism of hopcalite (**Figure 1.7**) was proposed by Schwab *et al.* and later confirmed by XPS studies by Veprek *et al.* to involve a redox coupling mechanism between the copper and manganese, with copper cycling between Cu<sup>2+</sup> and Cu<sup>+</sup> and manganese cycling between Mn<sup>3+</sup> and Mn<sup>4+</sup><sup>28, 46, 106, 107</sup>. It is thought that this redox mechanism is responsible for the enhanced catalytic activity of hopcalite towards both CO oxidation at ambient temperatures and VOC oxidation<sup>114</sup>. Veprek *et al.* observed that the deactivation of hopcalite was followed by a shift of the copper to lower binding energy and a decrease in the satellite at 940-943 eV which would suggest a rapid decrease in surface Cu<sup>2+</sup><sup>106</sup>.

Hopcalite has also been used with addition of metals such as gold, silver and cobalt as a catalyst for CO oxidation and propane oxidation<sup>115, 116, 117</sup>. Gold doping on hopcalite was shown to improve the stability of the catalyst during CO oxidation<sup>117</sup>. Studies on hopcalite using a temporal analysis of products reactor (TAP) reactor showed that standard, (non doped) hopcalite, converts CO into CO<sub>2</sub> with both the Mars Van Krevelen and the Langmuir-

Hinshelwood mechanisms<sup>12</sup>. The study also showed that doping gold onto hopcalite promoted the Mars Van Krevelen system over the Langmuir Hinshelwood mechanism and it was believed that doping with gold increased the reducibility of the copper thereby increasing the redox cycling ( $\text{Cu}^{2+}/\text{Cu}^+$  and  $\text{Mn}^{3+}/\text{Mn}^{4+}$ ) and thereby increasing the CO conversion<sup>12, 28</sup>.

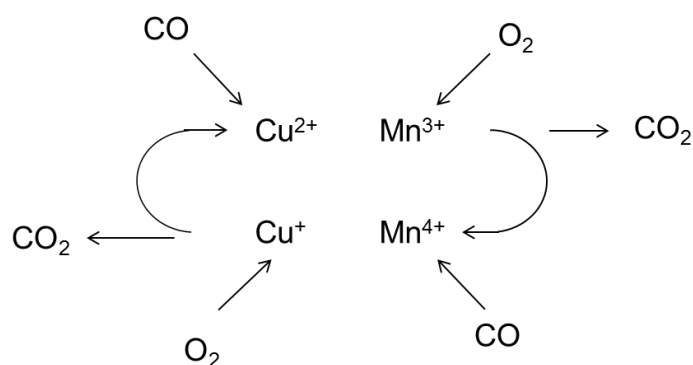


**Figure 1.8: A catalytic cycle of hopcalite during CO oxidation showing the redox coupling between copper and manganese<sup>106</sup>**

Generally most investigations have accepted that for CO oxidation hopcalite is more active in a more disordered state than the crystalline spinel phase<sup>115</sup>. As a result calcination and heat-treatment conditions are usually limited to 200-400 °C. Calcination at or above 500 °C forms highly crystalline  $\text{CuMn}_2\text{O}_4$  and phase separated  $\text{Mn}_2\text{O}_3$ ,  $\text{Mn}_3\text{O}_4$  and  $\text{CuMnO}_2$  resulting in a less active catalyst<sup>46, 107</sup>. The extent of crystallinity and copper-manganese mixing was studied by Kondrat *et al.* showing that phase separated Cu/Mn, formed when hopcalite was calcined under an inert atmosphere, was totally inactive and that hopcalite needed both copper-manganese mixing and some extent of a spinel phase, in order to be an active CO oxidation catalyst<sup>28</sup>.

#### 1.4.2.2 Preparing Hopcalite

The recent research on hopcalite catalysts has been focused on the variations in preparation techniques in order to improve their catalytic preformation and stability<sup>46, 118</sup>. Like many other mixed oxide catalysts, hopcalite is commonly prepared by co-precipitation, typically using copper and manganese nitrates with  $\text{Na}_2\text{CO}_3$  as the precipitating agent<sup>28, 33, 61</sup>.

Hutchings *et al.* carried out several studies into improving co-precipitation in the 1990s demonstrating that factors such as pH, Cu:Mn ratio and aging time dramatically affect the CO oxidation activity of hopcalite<sup>61, 119</sup> In the last decade other methods for preparing had been explored including, but not limited to ball milling<sup>105</sup>, supercritical anti-solvent precipitation (with both supercritical CO<sub>2</sub> and supercritical H<sub>2</sub>O)<sup>46, 120</sup>, sol gel<sup>20</sup> and flame spray pyrolysis<sup>118</sup>.

These routes were investigated for a range of reason but most notably to increase the total surface area, reduce the use of sodium<sup>47</sup>, increase the catalyst stability in particular, towards atmospheric water poisoning<sup>111</sup> and varying Cu:Mn mixing. The reason for improving the first two points are more obvious, since increased surface area will expand the number of surface sites where the reaction can occur, thereby increasing the rate of CO conversion and sodium is a poison that has been shown to reduce the CO oxidation activity of mixed copper-manganese systems<sup>47</sup>. Finding an alternative which reduces or eliminate the use of sodium is desirable. Supercritical anti-solvent, flame spray pyrolysis and ball milling are examples of methodologies that can make hopcalite or its precursors without the use of sodium containing salt as the precipitating agent.

The deactivation by water has been one of greater focus over the last few years<sup>118</sup>. Generally commercial hopcalite is prone to deactivation with the presence of atmospheric water in the gas feed in a relatively short time period<sup>20, 111</sup>.

**Table 1.2: Comparison of copper-manganese oxide CO oxidation catalyst prepared with different methods**

Cu:Mn ratio	Preparation Method	Surface area/ $\text{m}^2 \text{g}^{-1}$	Phase	Reaction conditions	CO conversion	Ref
1:2	Co-precipitation optimum conditions pH 9 aging 12 hours 80 °C	110 (300 °C) 34 (500 °C)	MnCO <sub>3</sub> /CuO (300 °C) CuMn <sub>2</sub> O <sub>4</sub> (500 °C)	5% CO/He 5 ml min + O <sub>2</sub> 50 ml min <sup>-1</sup> 20 °C GHSV 33000 h <sup>-1</sup>	80% (steady state)	61
1:2	Supercritical anti-solvent ethanol (5- 15% water)	65- 175	amorphous	5000 ppm (0.5%) CO/air GHSV 12000 h <sup>-1</sup>	65 % initial 30% steady state (25 mins)	46
1:2	Flame Spray pyrolysis Cu/Mn 2-ethyhexanoate	35-184	Cu <sub>1.5</sub> Mn <sub>1.5</sub> O <sub>4</sub> , Mn <sub>3</sub> O <sub>4</sub>	100 mg 0.67 % CO/ 33.33% O <sub>2</sub> / 66 % N <sub>2</sub> 67 ml min <sup>-1</sup>	80% at 60°C	39
1:2	Ball milling 0.5-72 hours	21-78	CuMn <sub>2</sub> O <sub>4</sub> (72 hours) CuO, Mn <sub>2</sub> O <sub>3</sub>	5000 ppm (0.5%) CO/air GHSV 12000 h <sup>-1</sup>	40% initial 23% steady state (25 mins)	105
1:4	Sol Gel (optimum catalyst): metal nitrates in ethylene glycol-water-nitric acid. Refluxed 105 °C	185 (350 °C)	Amorphous calcined 350 °C Cu <sub>1+x</sub> Mn <sub>2-x</sub> O <sub>4</sub> / Mn <sub>2</sub> O <sub>3</sub>	(pre-treated 1 hour air 5 hours N <sub>2</sub> (200 °C) 10000 ppm (1%) CO/air flow: 50 ml min <sup>-1</sup>	Up to 60 % (2:8)	20

Recently the use of flame spray pyrolysis had been demonstrated to make a hopcalite catalyst that had better atmospheric water resistance than the conventional hopcalite<sup>118</sup>.

The increased research into copper-manganese oxide over the last 20 years has shown that, despite the fact that it has already been an established industrial catalyst for nearly a century and more active alternatives such as supported gold catalysts, the use of copper-manganese oxide catalysts is still relevant and generates interest with new methods of preparation being continually investigated.

### 1.4.3 Copper/zinc Oxides based catalyst for methanol synthesis

Copper-zinc catalysts have been applied for many reactions but the most famous two are water gas shift<sup>121</sup> and methanol synthesis<sup>8</sup> and are made industrially on 5000 ton per year scale<sup>59</sup>. This has caused extensive studies into Cu/ZnO systems for catalysis including different methods of preparation although co-precipitation remains the favourite due to its optimisation, good Cu/Zn mixing and highly studied system. Recent synthetic methods for copper-zinc oxide include sol gel and supercritical anti-solvent process (which would be covered later in section 1.5.3).

Methanol synthesis is a highly important industrial process<sup>122</sup> with an output of up to 50 Mtons per annum<sup>123</sup> and is an area that still attracts attention in academia and industry today<sup>8</sup> using a whole variety of catalysts, but the most widely studied is Cu/ZnO/Al<sub>2</sub>O<sub>3</sub><sup>67, 124</sup>. Cu/ZnO has been applied as methanol synthesis catalyst since the 1960s<sup>122</sup> and their use as methanol synthesis catalysts, and water gas shift, is still ongoing with the focus on both improving Cu/ZnO catalysts and fundamental understanding of this catalyst during the reaction itself. Methanol is synthesised through the hydrogenation of CO<sub>2</sub> (3:1 H<sub>2</sub>:CO<sub>2</sub>) to form methanol and water (**Figure 1.9 a**)<sup>8, 67, 125</sup>, although the reaction is more complex with multiple steps, intermediates, side reactions such as the reverse water gas shift reaction (**Figure 1.9 b**)<sup>125</sup>, as well as the formation of side products such as HCO<sub>2</sub> or H<sub>2</sub>CO<sup>8</sup>. If CO is

present in the gas mixture then it can be hydrogenated (**Figure 1.9 c**) to form methanol as well: some syn gas contains mixtures of both CO and CO<sub>2</sub><sup>67</sup>.

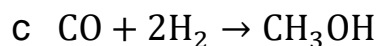
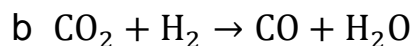
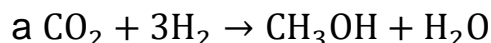


**Figure 1.9: a) Methanol synthesis from CO<sub>2</sub> hydrogenation, b) reverse water gas shift and c) methanol from CO**<sup>125, 126</sup>

The route to methanol is thermodynamically favoured, by high pressure (from around 50 bar to as high as 100 bar<sup>127</sup>) and lower temperatures since it is an exothermic reaction of -49.8 kJ mol<sup>-1</sup> and under Le Chatilier's principle equilibrium towards methanol, is more favoured at lower temperatures<sup>60 128</sup>.

With Cu/ZnO based catalysts the methanol productivity is directly related to the surface area of copper, with an increase in copper surface area generally relating to an increase in methanol production<sup>64</sup> which is also why industrial Cu/ZnO catalysts use a higher Cu:Zn (typically around 70:30)<sup>127</sup>.

However, there have been many studies that demonstrate the ZnO plays an important role in the process. Research carried out into the effect of the copper with other metals such as copper-manganese, copper-magnesium and copper-ceria and had shown that the secondary metal had an effect on the methanol conversion, but also showed that for some catalysts such as Cu-Mg had higher Cu surface area but lower activity suggesting that the ZnO played an influential role in methanol synthesis<sup>67</sup>.

Studies on co-precipitated Cu/ZnO catalysts are extensive with most using Na<sub>2</sub>CO<sub>3</sub> as the precipitating agent<sup>59, 64</sup>. In the initial stages of co-precipitation, the copper-zinc hydroxyl carbonate forms a phase called zincian georgeite (see section 1.5.3) which then, during aging process becomes zincian malachite (higher ratio Cu:Zn), or at lower Cu:Zn ratios aurichalcite or a hydrotalcite like phase. The aging step is essential for these catalysts with a long aging process resulting in a more crystalline material, growth of the Cu/Zn precursor and better copper-zinc distribution<sup>129</sup>. As well

as the aging time, the temperature and pH of the mixture also has an effect on the precursor and productivity of the final catalyst<sup>57, 60</sup>.

Some of the groups focus on improving co-precipitation catalyst such as Prieto *et al.* who tried to eliminate  $\text{Na}_2\text{CO}_3$  (as source of Na poisoning<sup>123</sup>) by using  $\text{NH}_4\text{HCO}_3$  as the precipitating agent<sup>59</sup>. The group also investigated different calcination conditions (such as using 1%  $\text{NO}/\text{N}_2$  atmosphere)<sup>59</sup>. This method also had the advantage of reducing washing steps required to remove the excess sodium.

Other precipitating agents have also been used, notably oxalic acid in a co-precipitated oxalate-gel method with ethanol, which was reported to have formed a highly active and selective methanol synthesis catalyst<sup>130, 131</sup>. Other preparations include direct combustion of Cu and Zn nitrate with citric and oxalic acid<sup>132</sup>, use of a surfactant during precipitation<sup>133</sup> and a sol gel combustion method<sup>134</sup>. While all of these methods have their advantages giving good Cu surface area and methanol production, for various reasons they have been dismissed as potential alternatives to  $\text{Na}_2\text{CO}_3$  based co-precipitation<sup>59</sup>. But in recent years, supercritical anti-solvent, the use of supercritical fluids, such as supercritical carbon dioxide, as an anti-solvent to precipitate a metal precursor had been successfully applied to make Cu/ZnO catalyst precursor (zincian georgeite) which resulted in a highly active Cu/ZnO methanol synthesis catalyst<sup>135</sup>.

## 1.5 Supercritical fluids for metal oxide preparation

### 1.5.1 Supercritical fluids

Supercritical is a state at which a substance above certain temperature and pressure reaches a point where the liquid-gas interface disappears (**Figure 1.10**) and the substance becomes a supercritical fluid<sup>136</sup>. This state is described as having properties of both gas and liquid<sup>56</sup>, with gas properties such as low viscosity<sup>137</sup> and liquid phase properties such as high densities<sup>136, 138</sup>. In this state the supercritical substance such as supercritical carbon dioxide (scCO<sub>2</sub>) can be utilised as a solvent for chemical reactions for example homogeneous catalysed hydrofomylation<sup>139</sup> or as an anti-solvent method for precipitating a dissolved solid out of a solvent<sup>140</sup>.

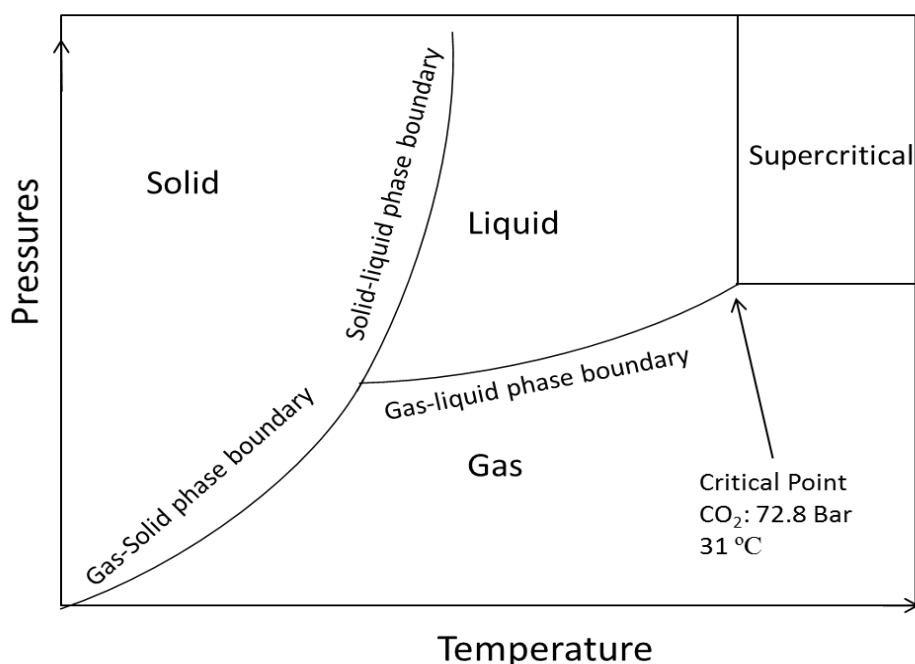


**Figure 1.10: Phase diagram of temperature v.s. pressure showing the point at which a substance becomes "supercritical"** <sup>56, 136, 137</sup>.

There are a wide variety of substances that have been used as supercritical fluids (SCF) such as water (scH<sub>2</sub>O)<sup>120</sup>, carbon dioxide<sup>135</sup>, isopentane<sup>141</sup>, ethanol or ammonia<sup>56</sup>. Carbon dioxide however is the most common and widely applied supercritical fluid as is non-toxic and requires lower temperatures (operating conditions of 31 °C and 72.8 bar) to achieve

supercritical state<sup>138</sup>. Supercritical water has had some applications but mostly avoided due to its corrosive nature making application of supercritical water, especially on an industrial scale, undesirable<sup>142</sup>. However there have been publications into the use of supercritical water to prepare mixed metal oxide catalysts with examples including perovskite phase  $\text{LaMnO}_3$  and hopcalite catalysts<sup>25, 120, 143</sup>.

### 1.5.2 Type of supercritical fluid process

There are a number of ways in which supercritical fluids can be utilised to dissolve or precipitate a precursor material. The application of these techniques varies depending of the field that they are used in. Two examples most commonly used for precipitating solids are discussed below:

Rapid expansion of a supercritical solution (RESS) was one of the earlier developed techniques utilising supercritical fluids<sup>56</sup> and precipitating out solids. It was developed in the 1980s although it had been first discovered as far back as 1879<sup>137, 144</sup>. The technique is relatively simple, dissolving the precursor in a supercritical fluid and then spraying the supercritical fluid into through a heated nozzle into a precipitation vessel. The sudden expansion causes the supercritical fluid to depressurise and revert back to its gas phase, resulting in the rapid nucleation of any dissolved particles in the SCF<sup>145</sup>. The technique was noted for being simpler and cheaper than the anti-solvent methods but had limitations due to the solubility of precursor in supercritical fluids<sup>144</sup>.

The anti-solvent process is the use of supercritical  $\text{CO}_2$  as a way of precipitating a solute from a solvent by using supercritical fluids as a bad solvent i.e. an anti-solvent. The solvent is dissolved into the SCF but the metal salt (such as an acetate) is insoluble and will instantly precipitate in the supercritical fluid and the solvent (for example ethanol) is removed from the precipitate. There are many variations on the use of SCF as anti-solvent but the two main examples are gas anti-solvent (GAS) and supercritical anti-solvent (SAS).

SAS is a flow process, in which, scCO<sub>2</sub> is flowed through the precipitation vessel and the solvent mixture is continually injected into the precipitation vessel through a coaxial nozzle. As the solution mixture exits the nozzle the solvent dissolves into the scCO<sub>2</sub> while any dissolved substance insoluble in scCO<sub>2</sub>, would precipitated instantly and collected on the bottom of the precipitation vessel<sup>56</sup>.

GAS is the use of supercritical CO<sub>2</sub> in a batch type process. The solvent mixture is added to the reactor and the scCO<sub>2</sub> is pumped into the solution until the solution reaches a point at which it is miscible in the supercritical fluid and precipitation would occur<sup>144, 146, 147</sup>. After precipitation the system is opened to a flow anti-solvent system to allow the removal of the solvent as a “washing step”<sup>147</sup>.

SAS is the most common supercritical technique for making metal oxides for the application as catalysts, although the GAS method is applied in situations that might require a batch method like impregnation of a metal or metal oxide onto a support such as the preparation of cobalt and ruthenium on TiO<sub>2</sub> catalyst for the Fischer Tropsch process<sup>9</sup>.

### **1.5.3 Supercritical anti-solvent process for heterogeneous catalyst preparation**

The use of supercritical fluids for the preparation of catalysts and materials in general has greatly expanded over the last 20 years. The earliest examples of SCF for the synthesis of inorganic materials being reported by the group of Reverchon in the 1990s<sup>148</sup> who used supercritical CO<sub>2</sub> to make materials such as Sm<sub>2</sub>O<sub>3</sub> and ZnO. The area expanded in the later 1990s and early 2000s and saw the synthesis mixed oxide such as vanadium phosphates (with isopropanol as the solvent)<sup>149</sup>.

The use of SAS precipitated metal oxides as catalyst had expanded rapidly over the past two decades. Early examples of metal oxide precursors (including applications as catalysts) utilised DMSO or isopropanol<sup>149</sup> as the

solvent<sup>150</sup>. However more recent examples have used ethanol<sup>26</sup> as the solvent due to lower toxicity and lower environmental issues compared to DMSO<sup>46</sup>. The use of SAS to prepare hopcalite (briefly mentioned in Section 1.4.2) had initially used DMSO as the solvent but found that while the precursor had a surface area of  $300 \text{ m}^2 \text{ g}^{-1}$  the resulting catalyst after calcination had a lower surface area of  $10\text{-}50 \text{ m}^2 \text{ g}^{-1}$ <sup>110</sup>. This was later attributed to exothermic decomposition of the acetate salts<sup>46</sup>. When ethanol was used as the solvent the precipitate had a surface area of  $33\text{-}175 \text{ m}^2 \text{ g}^{-1}$ .

It was also found that the addition of water in the alcohol changed the nature of the precipitate (both for hopcalite and other metal acetates)<sup>21, 46</sup>. The acetates that were precipitated from pure ethanol (like DMSO) were found to be predominantly precipitated as metal acetates. However when the water was added to the ethanol/acetate mixture (5-20% volume) the metal precipitates as a metal carbonate<sup>46 66</sup>. The surface area of the precursor as carbonates (with the addition of water) were lower ( $140 \text{ m}^2 \text{ g}^{-1}$ ) than the acetate (when no water was used) ( $264 \text{ m}^2 \text{ g}^{-1}$ ). However after calcination, due to exothermic decomposition of the acetate salts, the catalysts had a low surface area ( $33 \text{ m}^2 \text{ g}^{-1}$ ) whereas the samples that had 5-15 % water/ethanol mixtures were shown to have higher surface area ( $65\text{-}175 \text{ m}^2 \text{ g}^{-1}$ ) in the resulting catalyst. As a result the carbonate precipitates were more active for CO oxidation than the copper-manganese precipitated as acetate<sup>46</sup>. This was also seen with other transition metal oxide catalyst such as cobalt oxide which was reported to show increased surface area and propane oxidation activity with 5-15% water/ethanol content compared to the metal acetates precipitated from pure ethanol<sup>21</sup>.

The most significant example of the advantages of SAS were shown in 2016 when Kondrat *et al.* showed that the SAS technique could be used to make a rare copper-zinc carbonate phase called georgeite<sup>135</sup>. Georgeite and zincian georgeite are amorphous hydroxyl carbonate phases that forms initially during co-precipitation but is unstable and degrades during the aging process to form the more crystalline zincian malachite (2:1 Cu:Zn)<sup>123</sup>. As a result, prior to the supercritical anti-solvent preparation, the study into zincian georgeite as a Cu/ZnO catalyst precursor was rare due to the material

instability<sup>123, 151</sup> but the SAS prepared georgeite/ zincian-georgite (formed from acetate salts in 5-30% water/ethanol solvent) was stable and could be studied in more depth as well being more applied as a Cu/ZnO catalyst precursor.

It was found that the amorphous phase produced a highly dispersed Cu in the ZnO which resulted in a Cu/ZnO catalyst that contained a high Cu surface area<sup>135, 151</sup>. The zincian georgeite derived Cu/ZnO catalyst was found to be an excellent catalyst for both methanol synthesis<sup>135, 151</sup> and water gas shift reactions<sup>152</sup>. When Al (as AlO(OH)) was added it increased the stability of the catalyst without significantly affecting the Cu-Zn dispersion<sup>151</sup>.

The use of supercritical CO<sub>2</sub> to prepare metal oxides is a still expanding area, and although it is yet to be used at an industrial level<sup>60</sup> in the field of catalyst preparation, there is still potential for the method to be scaled up for industrial use.

## 1.6 Ionic liquids and deep eutectic solvents

### 1.6.1 Ionic liquids

Ionic liquids (or more specifically room temperature ionic liquids (RTIL)) are defined as salts which melt at or below 100 °C and form a liquid at room temperature<sup>153</sup>. Most ionic liquids (ILs) are organic based with an organic cation such as an imidazolium, pyridinium or quaternary amide (**Figure 1.11**) and anion which could be either organic or inorganic<sup>154 155</sup>. Although ionic liquids were first discovered in 1914, it is only been with in the last few decades that air and moisture stable ionic liquids have been synthesied<sup>154</sup>.

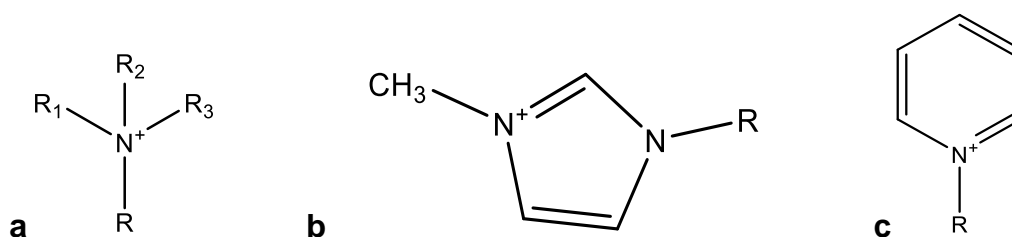


**Figure 1.11: Some of the organic cations used for ionic liquids a) tetra alkyl ammonium b) 1-alkyl-3-methyl imidazolium and c) N-alkyl pyridium<sup>155</sup>**

Ionic liquids have been investigated as alternatives to regular organic solvents<sup>156</sup>, due to various properties such as a very small (almost negligible) vapour pressure<sup>157, 158</sup>, low volatility<sup>159</sup>, stability<sup>160</sup> and easily tuneable properties. As a result, ionic liquids have been applied in many reactions and synthesis, including biological process, catalytic reactions, extraction of metal ions from water, stabilisation of metal nanoparticles and synthesis of inorganic compounds<sup>155, 161-164</sup>. Ionic liquids can have their properties easily modified, for example viscosity, acid-base, electrochemical and solubility, by changing the anion and/or the cation allowing a wide range of applications<sup>163, 165</sup>. Some research groups have also found that ionic liquids can be used not only as a solvent but also as a template and in some cases can act as both a solvent and a template in the same reaction<sup>166</sup>. Many papers on ionic liquids are highly cited, showing the extent the high of interest in the area which is still increasing both academically and industrially<sup>167</sup>. The imidazolium based ionic liquids are the most commonly used although ionic liquids containing other organic cations are also widely used<sup>168</sup>. Imidazolium cations are widely used in ionic liquids since they are commercially widely available and are air stable<sup>169</sup>. Although most imidazolium based ionic liquids are water stable, they are also hygroscopic and would readily add water to the system which may induce precipitation or stop a reaction. The imidazolium based ionic liquids consist of a charged side (with the methyl group) and a non-polar alkyl chain<sup>170</sup>.

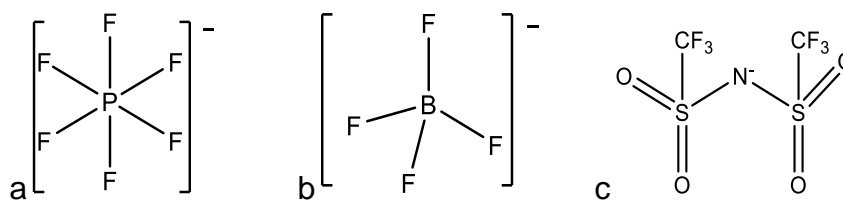


**Figure 1.12: Anions used for ionic liquids a) hexafluorophosphate b) tetrafluoroborate and c) bis-trifluoromethanesulfonylimide**

The length of the alkyl chain has an effect on the ionic liquids properties, most notably its melting point since after a certain chain length ( $C_{10}$ ), the Van de Waals interactions become dominant, increasing the ionic liquids melting point and the ionic liquid starts to form a solid<sup>170, 171</sup>. The length of the alkyl chain has also been an important influence for the stabilisation of nanoparticles in ionic liquid solution, influencing their size distribution<sup>154</sup>.

The choice of anion is also important as it can change the properties of the ionic liquid with the same cation such as solubility in water, the ability to dissolve metal salts and stabilisation of nanoparticles among other properties<sup>156</sup>. Most anions used in ionic liquids are water stable but a few, notably the aluminium chlorates (e.g.  $AlCl_4^-$  and  $Al_2Cl_7^-$ ) decompose when in contact with water<sup>170, 172</sup> and therefore have to be handled in a dry atmosphere. The choice of anion is also important for the water miscibility of the ionic liquid in water with some anions such as chloride and aluminium chloride being water miscible whereas other anions such as  $PF_6^-$ ,  $BF_4^-$  and  $Tf_2N^-$  (**Figure 1.12**) are more water immiscible<sup>172</sup>.

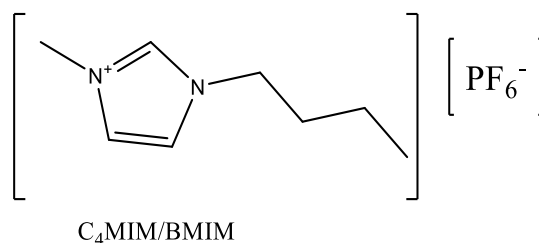


**Figure 1.13: 1-butyl-3-methylimidazolium hexafluorophosphate (BMIm[PF<sub>6</sub>])**

Recently many groups are moving away from the hexafluorophosphate anions as it has been reported to very slowly hydrolyse in excess water, or long term exposure to moisture, to form  $HF$ <sup>168, 173</sup> which makes using these

chemicals hazardous (and consequently defeats the point of using ionic liquids as a green alternative to organic solvents)<sup>174, 175</sup>. As a result, there have been various studies into using the imidazolium cation with alternative anions to  $\text{PF}_6^-$ , although it has been noted that some groups continue with the use of  $\text{PF}_6^-$  despite its disadvantages<sup>168, 174</sup>. Other anions such as bis-trifluoromethanesulfonylimide ( $\text{Tf}_2\text{N}^-$ ) (**Figure 1.12 c**) and trifluoromethanesulfonate are increasingly popular alternatives to hexafluorophosphate and tetrafluoroborate as water immiscible counter ions for the imidazolium based ionic liquids<sup>169</sup>.

There are also a class of ionic liquids termed “task specific ionic liquids” (TSIL) which was first reported by Davis<sup>176</sup>. These are ionic liquids which are based on more common ionic liquids such as imidazolium or quaternary amine, but contain a functional group which modifies the properties of the ionic liquids such as ability to solubilise metal nanoparticles<sup>177</sup>. The functional group of the TSIL interacts with the nanoparticle allowing them to solubilise in the ionic liquid solution<sup>172, 176, 177</sup>.

### 1.6.2 Deep eutectic solvents

Since 2003 there has been a rapid increase in publications on a group of ionic liquids based around quaternary ammonium salts, in particular choline chloride (ChCl) (**Figure 1.14**)<sup>167, 178-181</sup>, which was first developed by the group of Abbott *et al.*<sup>167, 181</sup>. The choline chloride is mixed with a hydrogen bond donor such as urea, oxalic acid, malonic acid and ethylene glycol among others, at various ratios of choline chloride to hydrogen bond donor (for example 1:2 ChCl:urea or 1:1 for ChCl:oxalic acid<sup>182</sup>). When mixed, the choline chloride and the hydrogen bond donor form a single homogenous liquid at a temperature below the melting point of both of the solids, for example a mixture of urea and choline chloride form a liquid at room temperature whereas the melting points of urea and choline chloride (individually) are 135 °C and 302 °C respectively. This type of liquid has been termed a deep eutectic solvent (DES)<sup>167, 178</sup>.

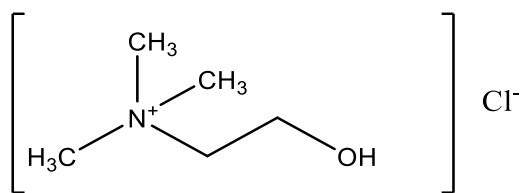


**Figure 1.14: Choline chloride**

A deep eutectic solvent has been defined by most literature as a quaternary amide that interacts with a H-bond donor such as malonic acid, urea or ethylene glycol (**Figure 1.15**) although a review by Smith *et al.*<sup>182</sup> define these as type III DES. The more generic term for the deep eutectic solvent is related to the interaction between acid and bases that causes two solids to form a liquid at a temperature below the melting point of either solid<sup>182</sup>. The other types, (I, II and IV) involves the interaction between a quaternary amide and a metal halide (type I), a metal halide hydrate (type II) or the interaction of a quaternary amide with both an H-bond donor (e.g. urea malonic acid) and a metal halide (type IV)<sup>182</sup>. In this review the term DES would be used for the “type III”.

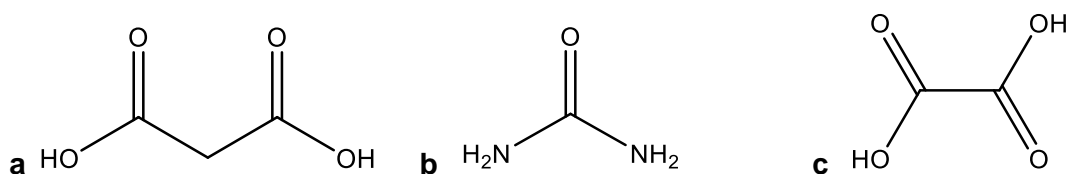


**Figure 1.15: Commonly used H-bond donors used with choline chloride to form the DES a) malonic acid, b) urea and c) oxalic acid**

Deep eutectic solvents have been generally classified and referred in the literature as ionic liquids even though they are not strictly ionic liquids. The definition of an ionic liquid is a room temperature molten salt comprising of anions and cations, whereas deep eutectic solvents are the result of the interaction between choline chloride and hydrogen bond donors<sup>167, 182</sup>. However, the properties, such as low vapour pressure, viscosity and conductivity, of deep eutectic solvents are similar to those of ionic liquids to the extent that deep eutectic solvents are being used as alternatives to ionic

liquids.<sup>183</sup> Deep eutectic solvents have several advantages over ionic liquids<sup>184</sup>. The constituent parts of the DES (choline chloride and H-bond donor) are cheap and readily accessible and the preparation of the DES is relatively simple. In comparison ionic liquids (such as imidazolium) are expensive, require complex synthesis and some pose environmental issues<sup>173, 183, 185</sup>.

These advantages of choline chloride based deep eutectic solvents have led to an increase in their applications and have been as alternatives to both regular organic solvents and ionic liquids. These include the use of DES for the extraction of organic materials (such as lignins and sugars) and/or inorganic material from organic solvent/water<sup>183, 186</sup>, electrochemical deposition<sup>180, 185, 187</sup> and solvents for organic synthesis<sup>188</sup>. Deep eutectic solvents have also been applied as solvents in catalytic reactions, such as the upgrade of crude oil using molybdenum (VI) oxide catalyst in a urea-choline chloride DES<sup>189</sup>. The use of dissolving metals using choline based techniques is currently patented by Abbott<sup>168</sup>.

### 1.6.3 Solubility of metal salts in deep eutectic solvents

The solubility of metal oxides in deep eutectic solvents has been widely studied<sup>178</sup>. The group of Abbott *et al.* carried out a wide range of early research into deep eutectic solvents including their abilities to dissolve metal oxides<sup>187</sup>. In 2005 the group started dissolving metal oxide in choline chloride based deep eutectic solvents. The group focused on dissolving a range of metal oxides (including ZnO, Al<sub>2</sub>O<sub>3</sub> and PbO<sub>2</sub>) in a 1:2 choline chloride-urea deep eutectic solvent and used mass spectrometry, UV-vis and also tested the electrodeposition of the metal oxides from the DES<sup>187</sup>. It was reported that the some metal oxides such as Cu<sub>2</sub>O, PbO<sub>2</sub> and ZnO showed high solubility while other metal oxides such as Al<sub>2</sub>O<sub>3</sub> and CaO showed poor solubility. The paper speculated that this was due to the ability of the metal to complex with the urea and dissolve in the solution. The group noted that

there was a correlation between the solubility of the metal oxide and its melting point; metal oxides with higher melting points, such as  $\text{Al}_2\text{O}_3$  (2045 °C), were less likely to dissolve in the urea/choline chloride DES than metal oxides with lower melting points for example  $\text{MnO}_2$  (493 °C)<sup>187</sup>. However, it should be noted that ZnO does not fit this trend since it has both a high melting point (1975 °C) and a high solubility of 8500 ppm<sup>187</sup>. In 2006 Abbott *et al.* investigated further into dissolving various first row transition metal oxides in choline chloride based DES with malonic acid, urea and ethylene glycol. The group found that the degree of ionic/covalent properties had an effect on the solubility of the metal oxide in the DES, with more ionic oxides dissolving better than more covalent oxides, with zinc oxide and copper oxide being found to be the most soluble oxides and titanium oxide being the least soluble<sup>178</sup>. The group also showed that the oxides were more soluble in the choline chloride-malonic acid DES than the choline chloride-urea or the choline chloride-ethylene glycol<sup>178, 184</sup> (with nearly all metal oxides being the least soluble in the choline-ethylene glycol mixture). The solubility of the metal oxides in the choline chloride DES were also found to be temperature dependent, with ZnO and  $\text{Cu}_2\text{O}$  being noted for temperature dependent<sup>184</sup>.

The group also found that in the choline chloride-malonic acid DES, the metal oxide dissolved and formed a metal chloride whereas in the choline chloride-urea solution the metal oxides formed an oxide-chloride or oxide-urea complex<sup>178</sup>. The group stated that the reason for this was that the metal oxide interaction with the malonic acid was strong enough to accept the oxygen from the metal oxide and thereby forming a metal chloride which increase the metals solubility in the deep eutectic solvent.

Antal *et al.* further investigated  $\text{V}_2\text{O}_5$  in the choline chloride-urea DES focusing what structures formed in the solution<sup>190</sup>. Using <sup>51</sup>V NMR, Infra red spectroscopy and X-ray diffraction the group found that in the DES the vanadium oxide forms a  $[\text{H}_2\text{V}_{10}\text{O}_{28}]^{4-}$  but over a longer time period, due to the hydrogen bonding interactions of the choline chloride-urea DES with the vanadium  $[(\text{CH}_3)_3\text{N}(\text{CH}_2)_2\text{OH}]_4[\text{H}_2\text{V}_{10}\text{O}_{28}].2\text{NH}_2\text{CO}$  forms which has low solubility<sup>190</sup>.

#### 1.6.4 Anti-solvent processes using ionic liquids and deep eutectic solvents

Ionic liquids and deep eutectic solvents have been applied for anti-solvent techniques. A few notable examples focused on re-precipitated zinc oxide from choline chloride into an anti-solvent (mostly water) by the group of Wong *et al.* in 2010<sup>191-193</sup>. The group dissolved zinc oxide into 1:2 choline chloride-urea DES at a concentration of 2400 ppm (at 70°C) for two days<sup>191</sup>. The DES-zinc oxide was injected into different types of anti-solvents (water, 50:50 water ethanol and 10:90 water ethanol) over different time periods. The group found that changing the anti-solvent and the injection time influences the structure, notably injecting over a long time period in water gave 1-D crystals, whereas injecting over a shorter time period gave smaller particles. The group also noted that the ethanol stops or slows the precipitation of ZnO and ZnO structures in 10:90 water ethanol formed more random shapes<sup>191</sup>.

The group further expanded on this in 2011 when they used tri(hydroxymethyl)amino-methane as an additive to induce shape control<sup>192</sup>. It was found that the higher concentrations of the additive gave bigger and more rounded nanoparticles with lower surface area (the surface area with no additive was 52.4 m<sup>2</sup> g<sup>-1</sup> and 15.7 m<sup>2</sup> g<sup>-1</sup> with 500 mM of the additive)<sup>192</sup>.

The group of Hsu *et al.* in 2014 used the zinc oxide anti-solvent method but added copper nitrate to the anti-solvent (50:50 water ethylene glycol)<sup>193</sup>. It was found that the Cu<sup>2+</sup> doped itself onto the ZnO nanoparticles although at higher concentration, the Cu substituted itself into the ZnO structure<sup>193</sup>. The group also found that increasing the amount of Cu<sup>2+</sup> changes the morphology of the nanoparticles to a more rounded morphology. It was also noted that this technique could be used with Ni<sup>2+</sup> as well<sup>193</sup>.

### 1.6.5 Ionothermal synthesis of metal oxide

Ionothermal synthesis, as mentioned earlier (section 1.3.3) is a solvothermal synthesis performed in an ionic liquid or deep eutectic solvent. Ionothermal synthesis is an area that has rapidly expanded over the last few years due to better understanding of deep eutectic solvents and ionic liquids<sup>77</sup>. The method has notably been used for metal oxide preparation including the preparation of  $\text{Co}_3\text{O}_4$ ,  $\text{NiO}$  and  $\alpha\text{-Fe}_2\text{O}_3$ <sup>55, 167, 194</sup> and mixed oxides such as perovskites phase oxides (for example  $\text{Sr}_{1-x}\text{Ba}_x\text{SnO}_3$ )<sup>195</sup>. Ionothermal synthesis has been utilised with both conventional heating and microwave power, the latter being advantageous with ionic liquids due to their high dielectric constant and high polarity allowing them to absorb microwave energy more efficiently than conventional solvents<sup>196, 197</sup>. Choline chloride-urea is one of the most common DES applied but choline chloride-oxalic acid was used with make metal oxalates such as dysprosium and erbium in which the DES acts as both a solvent and a template<sup>198</sup>.

The reasons and the role of DES in ionothermal synthesis varies between different papers and applications with some groups using the DES as a solvent and others using it as a template where the choline chloride-urea breaks down during the process<sup>55</sup>. However, it has been noted that the breaking down of urea (to ammonia and metal carbonate or metal oxide) that occurs in this process (as well as breaking down of other type of DES) is ordered and reproducible<sup>77, 199</sup>. This has led to some groups using DES as a template for metal oxide preparation, with Hammond *et al.* notably in 2017 making ceria with this method, with the group also noting that the addition of water and different temperatures of ionothermal synthesis greatly affected the morphology of the ceria which were shown to have varying CO oxidation activities<sup>55</sup>. The group had also used microwave assisted ionothermal synthesis for the production of iron oxide and found that the temperature influences the phase formed ( $\alpha\text{-Fe}_2\text{O}_3$  or  $\gamma\text{-Fe}_2\text{O}_3$ ) depending on conditions and the addition of water made a difference to the morphology<sup>200</sup>.

As well as being used for metal oxide preparation, DES-ionothermal synthesis has been applied for the preparation of metal oxide precursors (or materials that could be used as metal oxide precursors) including manganese carbonate<sup>201</sup> and a layered double hydroxide of nickel and mixed cobalt-iron as a precursor to the spinel phase oxides<sup>202</sup>. In the case of manganese carbonate, like the ceria, the urea complexes with the manganese, forming a urea manganese chloride which then breaks down under the pressure and temperature of solvothermal conditions to manganese carbonate and ammonium chloride and ammonia<sup>201</sup>. The manganese carbonate formed different morphologies at different temperatures, forming cubic shaped particles at 120 °C and elliptical at 150 °C<sup>201</sup>.

Ionothermal synthesis is rapidly growing area of DES research that has been applied to the preparation of metal oxides (including applications as catalysis). The versatility of DES and ionic liquids with the advantages of using solvothermal conditions that can change the morphology is the reason why there has been such an interest in the area over the last 10-12 years<sup>167</sup>, and probably an area that will see continued development, especially in the application of catalyst preparation.

## 1.7 Switchable solvents

Switchable solvents is a term first used by Jessop in 2005 to describe solvents that can change their properties, e.g. their polarity, under different atmospheres such N<sub>2</sub> to CO<sub>2</sub>, with the atmosphere essentially acting as a switch<sup>203, 204</sup>. Most switchable solvents use CO<sub>2</sub> as the switching gas although other gases such as SO<sub>2</sub> and CS<sub>2</sub> have also been reported<sup>205</sup>. Many switchable solvents are made up from two components for example an amidine-alcohol or an amine-water mixture although single component switchable solvents (such as switchable surfactants) have also been applied<sup>206</sup>.

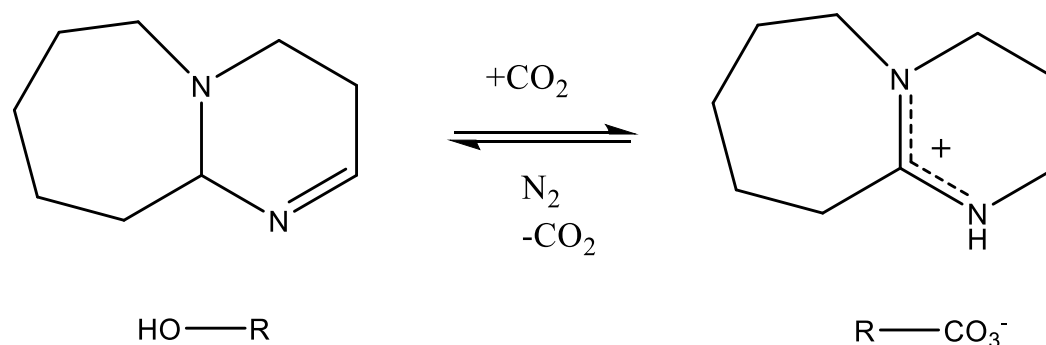


**Figure 1.16: Switching of DBU (left) non polar form (under inert atmosphere) to (right) polar form under carbon dioxide atmosphere<sup>204</sup>**

Early work on switchable solvents focused around the compound 1,8 diazobicyclo[5.4.0]-undec-7-ene commonly referred to as DBU (**Figure 1.16**). When combined with an alcohol, DBU forms an ionic liquid under a carbon dioxide atmosphere which is a highly polar molecule<sup>207</sup>. When heated to 60 °C under nitrogen the carbon dioxide comes off and components revert back to the alcohol and DBU, hence it can be changed back to its original non-polar state under a nitrogen or argon atmosphere. Since then other switchable polar solvent combinations have been discovered<sup>208</sup>. The ability to switch the solvent between non-polar and polar characteristics had been applied as a potential way of reducing the steps and solvents required for synthesis steps, thereby reducing waste<sup>209</sup>. The polarity range of switchable polar solvents (SPS) is different for different amidine/alcohol mixture with some having greater polar change than others<sup>210</sup>.

Although widely used, the DBU/alcohol switchable system is very water sensitive and as a result many SPS system only work under ultra-dry conditions<sup>211</sup>. Any more than 42 ppm of atmospheric water in the system would result in the formation of the solid DBU carbonate<sup>210, 211</sup>, although this process is reversible; 60 °C under inert atmosphere would remove the CO<sub>2</sub> and the mixture switches back to DBU and water<sup>208</sup>. This problem is predominant in most SPS or two component switchable solvents<sup>206</sup>, although Yamanda *et al.* did report that using a primary amine instead of an alcohol with DBU (and other amidines) resulted in a less water sensitive SPS system. However the group also reported that some of these mixtures (including some DBU/primary amine mixture) would still form a bicarbonate

salt in the presence of residual water after several hours<sup>208, 210</sup>. The general water sensitivity of these SPS systems makes them difficult to work with for the preparation of metal oxide precursors, especially if the initial metal salt contains water.

There are a wide variety of switchable systems other than SPS that have been applied, as well as other switchable systems such as switchable hydrophilicity (SHS)<sup>206,209</sup>, switchable surfactants<sup>212</sup> and switchable water; where the additive increases its ionic strength under different atmospheres and can be used to precipitate out compounds<sup>213</sup>.

Switchable hydrophilicity solvents are also widely used. Some of these solvents have a similar, if not higher, polarity range than SPS<sup>138, 210</sup> and these systems have the added advantage that the presence of water is not an issue meaning the ultra-dry conditions are not required. There are a variety of additives (mostly amines) that could be used with water to make SHS, including triethylamine<sup>209</sup>, cyclodimethylamine<sup>214</sup> and N,N,N'-tributylpentanamidine<sup>215</sup> (**Figure 1.17**)

A study by Vanderveen *et al.* into the properties of different amine, amidines and guanidines as SHS showed that the switching ability of these additives was related to the  $pK_{aH}$  (strength of the conjugated acid) and the  $\text{Log } K_{ow}$  (octanol-water partition coefficient). The group reported that an additive with a low  $pK_{aH}$  would result in a mixture that would not react with the  $\text{CO}_2$ , thereby not being able to switch, while a too high  $pK_{aH}$  would remain stable, under ambient temperature, after the  $\text{CO}_2$  addition and will not reverse back under  $\text{N}_2$  atmosphere<sup>138, 209</sup>. Also SHS with a low  $\text{Log } K_{ow}$  would be too hydrophilic and as a result would remain soluble in water and would not form a biphasic system under either atmosphere and likewise a high  $\text{Log } K_{ow}$  would result in a biphasic (hydrophobic) system under both atmospheres<sup>209</sup>. As a result the group concluded SHS that can regularly switch must have a  $\text{Log } K_{ow}$  value of 1.2-2.5 and a  $pK_{aH}$  value of 9.5-13 and even then this can vary with amine: water (volume) ratio<sup>138, 209</sup>

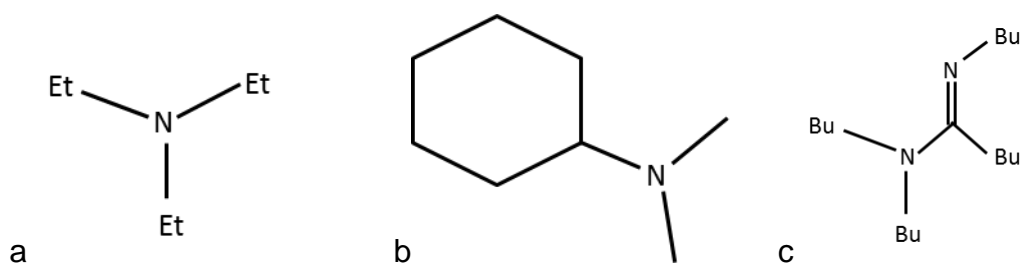


**Figure 1.18: Examples of switchable hydrophilicity solvents a) triethylamine<sup>209</sup> b) cyclodimethylamine<sup>214</sup> and c) N,N,N' tributylpentanamidine<sup>215</sup>**

There are other limitations in the applications of SHS (or any switchable solvent). Triethylamine for example, fits within the parameters that Vanderveen *et al.* reported<sup>209</sup> to make it a good SHS under ambient temperature but it is not always widely used, partially due to its volatility and toxicity.

The method and apparatus used for switchable solvents varies for the different applications. Nanta *et al.* utilised a DBU and ethylene glycol (2:1 ratio) switchable polar solvent mixture (with DMSO) for the dissolution of cellulose but with high pressure CO<sub>2</sub> with a pressure range of 50-100 bar which was near or at supercritical<sup>216</sup>. In fact, the group used a supercritical reactor set up in a SAS like flow system<sup>216, 217</sup> which demonstrates a mixed switchable solvent–supercritical application<sup>216</sup>.

The use of switchable solvents in the field of catalyst preparation is currently rare. However switchable solvents are still a relatively young area of research, compared to the field of ionic liquids or supercritical solvents which have had a more mainstream research and development for at least 20-30 years<sup>218</sup>. Although the area of deep eutectic solvents is not that much older<sup>181</sup> (by 2-3 years) and has already been used as a solvent/method of preparing metal oxides or metal oxide precursors<sup>55, 167</sup>. Switchable solvents have been used for dissolving and re-precipitating metal in the fields of extraction<sup>219, 220</sup> and metal recovery (including copper nitrate and iron nitrate<sup>220</sup>) but not so much in the field of metal oxide/ metal oxide precursor preparation in general. One example of the application of switchable solvents in the field of catalyst preparation was in 2017 by Saunders *et al.* who reported the use of a silylamine based switchable surfactant as an alternative method to deposit

gold nanoparticles onto a support<sup>212</sup>. The use of a switchable surfactant had the advantage that the silylamine would be attached to the gold nanoparticles under a carbon dioxide atmosphere but can be removed by switching to nitrogen thereby removing the need of a post preparation treatment common with other colloids<sup>212</sup>.

## **1.8 Discussion: green processes for making metal oxide catalysts**

The wide variety of different processes used to prepare metal oxides discussed here have each shown their merits and advantages in terms of achieving unique morphologies, higher surface areas and enhanced activities over the more traditional methods (such as co-precipitation). However, the advantages of these techniques should not just be based solely on the enhancement of the catalyst or the perceived relative greenness of the process but the overall energy consumption of the process including the manufacturing of the solvents and the energy consumption of the process and any additional post treatment such (as washing) required which would produce waste solvents.

Although ionic liquids have been classified as green, this is often referred by the fact that this is only based on their very low volatility and ability to retain the solvent after use (unlike organic solvents) but does not consider several major factors: firstly, some ionic liquids can be toxic and secondly the process of making ionic liquid involves various chemical synthesis steps<sup>138</sup>. Seldon referred to this as the E-factor<sup>221</sup>, which is based on the number of chemical steps required to make an ionic liquid from its basic components well as the solvents and yield of each step that are required to make an ionic liquid and the E-factor assess the greenness of ionic liquids based on these factors<sup>138</sup>. This E-factor should also be considered when looking at alternative preparation methods of preparing heterogeneous catalysts.

Deep eutectic solvents often come out well on this basis since their components are relatively abundant, easily purchasable and synthesised and the formation of the eutectic itself does not require complex synthetic steps,

unlike many ionic liquids<sup>221</sup>. As a result, choline chloride based DES are considered green alternatives to ionic liquids.

However one of the misleading facts about DES, that is often ignored, is the assumption of their relatively non-toxic and environmental benign properties<sup>138, 222</sup>. This assumption is based on the fact that their constituent parts such as choline chloride and a carboxylic acid are non-toxic (or a minor hazard), but does not take into consideration that this toxicity changes when they form a DES (just as equally mixing the two solid forms a DES)<sup>222</sup>. This factor is often overlooked in most publications, although most DES such as the choline chloride based sample are highly soluble in water which can easily dissolved and break down the DES<sup>191</sup>.

Another factor which has to be considered in the synthesis of metal oxides for catalysis using novel techniques is the residual species from either the solvent system or any other additives (for example the use of sodium hydroxide or sodium carbonate as base). Often solvents or additives that are added during the process can be retained which could subsequently act as a poison for the catalyst (for example chloride in DES) or create a high exothermic decomposition during calcination making washing steps more essential. In addition, some of these alternative techniques may not be as versatile or understood as co-precipitation<sup>59</sup>.

This factor was often one of the attractive features of the supercritical anti-solvent process since the process involves the removal of the solvent and the drying of the precursor, often eliminating additional steps that would have otherwise be required for solvent base preparation methods. The process also eliminated the need for a sodium containing precipitating agent used for co-precipitation or chelating agents used in sol gel. However the high energy cost of cycling the pressure during the process, even on the lab scale, makes it less suitable for industrial scale up<sup>62</sup>. Despite this, supercritical CO<sub>2</sub> has been used on an industrial scale<sup>138</sup>, and has had many papers citing the advantages of using the process as a way of precipitating precursors but without washing step and a drying step can be performed after the solvent addition under scCO<sub>2</sub><sup>123</sup>.

The greenness of a solvent or preparation method is not only relative to the established solvent, but to the process in general<sup>221</sup> and the clean up afterwards of waste or contaminated water. This is the major problem of co-precipitation in industry since the process produces excess of water containing nitrates and unreacted metals<sup>59, 123</sup>. One of the factors that is in favour of the use of supercritical CO<sub>2</sub> over co-precipitation for metal oxide catalysts preparation is that the process reduced the production of waste water containing metal nitrate and does not require a washing steps<sup>123</sup>.

Overall the continued investigation of alternative and novel preparations of metal oxides for application as catalysts is an area that must and will have continued interest in the future in order to achieve a metal oxide catalyst with greater surface area, morphology control and catalytic activity and to overcome the problems associated with the current preparation methods.

## 1.9 Aims of the Thesis

The work presented in this thesis is part of the UK Catalysis Hub project: Green Catalyst for Green Processes. The title of this thesis is metal oxides for heterogeneous catalysis but the main aim of the Hub project presented here is to find alternative methods of preparing metal oxide or metal oxide precursors to the energy intensive supercritical anti-solvent process. The work will look into some of the solvent systems discussed in the literature review and apply both novel and established techniques to make single and mixed metal oxide for the application as heterogeneous catalysts. The methods chosen for preparation are based on deep eutectic solvents, switchable solvent and hydrothermal synthesis.

Because there is a wide range of different metal oxide catalyst that could be prepared using these methods, this thesis focuses on a few select examples with different chapters investigating different catalysts and/or preparation techniques.

- Chapter 3 investigates the application of choline chloride-oxalic acid based DES for the preparation of iron, cobalt and manganese oxalates as precursors for VOC combustion catalysts.
- Chapter 4 investigates the use of hydrothermal synthesis for the preparation of a delafossite phase  $\text{CuMnO}_2$  (crednerite) as a precursor to spinel phase copper-manganese oxide CO oxidation catalysts
- Chapter 5 investigates the application of switchable solvents to prepare carbonate precursors of copper-manganese oxides as CO oxidation catalysts.
- Chapter 6 investigates the use of both deep eutectic solvents and switchable solvents for the preparation of copper-zinc oxide as catalysts for methanol synthesis.

Each of these catalysts will be compared with a catalyst made by more established/conventional methods such as co-precipitation or sol gel as well as catalyst precursors prepared by supercritical anti-solvent. The catalyst will be compared on the basis of catalytic activity and surface area as well as

difference in morphology and behaviour in comparison to the conventional method. The characterisation and testing will be used to see and determine whether these methods have potential to be a substitute for the more conventional methods, and if using alternative solvent systems such as DES or switchable solvent as well as hydrothermal and SAS have any potential disadvantages.

## 1.10 Chapter 1 References

1. M. Misono, *Heterogeneous Catalysis of Metal Oxides : Perovskites and Heteropoly catalysts*, Elsevier, 2013.
2. M. Bowker, *The Basis and Applications of Heterogeneous Catalysis*, Oxford University Press, 1998.
3. J. R. Ruiz, C. Jimenez-Sanchidrian, J. A. Hidalgo and J. M. Marinas, *Journal of Molecular Catalysis A-Chemical*, 2006, **246**, 190-194.
4. G. C. Bond, *Heterogeneous Catalysis: Principles and Applications*, Clarendon, Second edition, 1987.
5. E. Roduner, *Chemical Society Reviews*, 2014, **43**, 8226-8239
6. M. Haruta, *Gold Bulletin*, 2004, **37**, 27-36.
7. J. Kaspar, P. Fornasiero and M. Graziani, *Catalysis Today*, 1999, **50**, 285-298
8. S. S. Dang, H. Y. Yang, P. Gao, H. Wang, X. P. Li, W. Wei and Y. H. Sun, *Catalysis Today*, 2019, **330**, 61-75.
9. R. P. Marin, S. A. Kondrat, J. R. Gallagher, D. I. Enache, P. Smith, P. Boldrin, T. E. Davies, J. K. Bartley, G. B. Combes, P. B. Williams, S. H. Taylor, J. B. Claridge, M. J. Rosseinsky and G. J. Hutchings, *ACS Catalysis*, 2013, **3**, 764-7.
10. S. Iqbal, T. E. Davies, D. J. Morgan, K. Karim, J. S. Hayward, J. K. Bartley, S. H. Taylor and G. J. Hutchings, *Catalysis Today*, 2016, **275**, 35-39.
11. Y. B. Pan, X. C. Shen, L. B. Yao, A. Bentalib and Z. M. Peng, *Catalysts*, 2018, **8**, 20.
12. K. Morgan, K. J. Cole, A. Goguet, C. Hardacre, G. J. Hutchings, N. Maguire, S. O. Shekhtman and S. H. Taylor, *Journal of Catalysis*, 2010, **276**, 38-48
13. H. Bahruji, M. Bowker, W. Jones, J. Hayward, J. R. Esquiús, D. J. Morgan and G. J. Hutchings, *Faraday Discussions*, 2017, **197**, 309-324.
14. C. He, J. Cheng, X. Zhang, M. Douthwaite, S. Patisson and Z. P. Hao, *Chemical Reviews*, 2019, **119**, 4471-4568.
15. J. R. H. Ross, *Heterogeneous Catalysis: Fundamentals and Applications*, Elsevier Science, 2011.

16. M. Haruta, N. Yamada, T. Kobayashi and S. Iijima, *Journal of Catalysis*, 1989, **115**, 301-309.
17. B. Solsona, I. Vazquez, T. Garcia, T. E. Davies and S. H. Taylor, *Catalysis Letters*, 2007, **116**, 116-121.
18. K. Morgan, A. Goguet and C. Hardacre, *ACS Catalysis*, 2015, **5**, 3430-3445.
19. M. A. Pena and J. L. G. Fierro, *Chemical Reviews*, 2001, **101**, 1981-2017.
20. M. Kramer, T. Schmidt, K. Stowe and W. F. Maier, *Applied Catalysis A-General*, 2006, **302**, 257-263.
21. R. P. Marin, S. A. Kondrat, R. K. Pinnell, T. E. Davies, S. Golunski, J. K. Bartley, G. J. Hutchings and S. H. Taylor, *Applied Catalysis B-Environmental*, 2013, **140**, 671-679.
22. I. E. Wachs and K. Routray, *ACS Catalysis*, 2012, **2**, 1235-1246.
23. S. Royer, D. Duprez, F. Can, X. Courtois, C. Batiot-Dupeyrat, S. Laassiri and H. Alamdari, *Chemical Reviews*, 2014, **114**, 10292-10368.
24. Q. T. Trinh, K. Bholra, P. N. Amaniampong, F. Jerome and S. H. Mushrifl, *Journal of Physical Chemistry C*, 2018, **122**, 22397-22406.
25. W. L. Wang, Q. J. Meng, X. L. Weng and Z. B. Wu, *Catalysis Communications*, 2016, **84**, 167-170.
26. H. Q. Wang, H. X. Jiang, L. Kuang and M. H. Zhang, *Journal of Supercritical Fluids*, 2014, **92**, 84-92.
27. F. Polo-Garzon and Z. L. Wu, *Journal of Materials Chemistry A*, 2018, **6**, 2877-2894.
28. S. A. Kondrat, T. E. Davies, Z. L. Zu, P. Boldrin, J. K. Bartley, A. F. Carley, S. H. Taylor, M. J. Rosseinsky and G. J. Hutchings, *Journal of Catalysis*, 2011, **281**, 279-289.
29. G. Busca, *Physical Chemistry Chemical Physics*, 1999, **1**, 723-736.
30. H. Y. Zhu, P. F. Zhang and S. Dai, *ACS Catalysis*, 2015, **5**, 6370-6385.
31. D. H. Xiong, Q. Q. Zhang, Z. J. Du, S. K. Verma, H. Li and X. J. Zhao, *New Journal of Chemistry*, 2016, **40**, 6498-6504.
32. S. Mobini, F. Meshkani and M. Rezaei, *Journal of Environmental Chemical Engineering*, 2017, **5**, 4906-4916.
33. T. J. Clarke, S. A. Kondrat and S. H. Taylor, *Catalysis Today*, 2015, **258**, 610-615.
34. E. Manova, T. Tsoncheva, C. Estournes, D. Paneva, K. Tenchev, I. Mitov and L. Petrov, *Applied Catalysis A-General*, 2006, **300**, 170-180.
35. D. S. Mathew and R. S. Juang, *Chemical Engineering Journal*, 2007, **129**, 51-65.
36. J. H. Chen, H. Arandiyan, X. Gao and J. H. Li, *Catalysis Surveys from Asia*, 2015, **19**, 140-171.
37. X. L. Zhang, J. H. Ye, J. Yuan, T. Cai, B. Xiao, Z. Liu, K. F. Zhao, L. Yang and D. N. He, *Applied Catalysis A-General*, 2018, **566**, 104-122.
38. Q. Li, T. Odoom-Wubah, Y. P. Zhou, R. Mulka, Y. M. Zheng, J. L. Huang, D. H. Sun and Q. B. Li, *Industrial & Engineering Chemistry Research*, 2019, **58**, 2882-2890.

39. T. Biemelt, K. Wegner, J. Teichert, M. R. Lohe, J. Martin, J. Grothe and S. Kaskel, *Applied Catalysis B-Environmental*, 2016, **184**, 208-215.
40. F. Grillo, M. M. Natile and A. Glisenti, *Applied Catalysis B-Environmental*, 2004, **48**, 267-274.
41. M. Haruta, S. Tsubota, T. Kobayashi, H. Kageyama, M. J. Genet and B. Delmon, *Journal of Catalysis*, 1993, **144**, 175-192.
42. M. Haruta, T. Kobayashi, H. Sano and N. Yamada, *Chemistry Letters*, 1987, 405-408.
43. Y. B. Yu, T. Takei, H. Ohashi, H. He, X. L. Zhang and M. Haruta, *Journal of Catalysis*, 2009, **267**, 121-128.
44. J. Hirayama, I. Orlowski, S. Iqbal, M. Douthwaite, S. Ishikawa, P. J. Miedziak, J. K. Bartley, J. Edwards, Q. He, R. L. Jenkins, T. Murayama, C. Reece, W. Ueda, D. J. Willock and G. J. Hutchings, *Journal of Physical Chemistry C*, 2019, **123**, 7879-7888.
45. D. R. Jones, S. Iqbal, L. Thomas, S. Ishikawa, C. Reece, P. J. Miedziak, D. J. Morgan, J. K. Bartley, D. J. Willock, W. Ueda and G. J. Hutchings, *Catalysis Structure & Reactivity*, 2018, **4**, 12-23.
46. Z. R. Tang, S. A. Kondrat, C. Dickinson, J. K. Bartley, A. F. Carley, S. H. Taylor, T. E. Davies, M. Allix, M. J. Rosseinsky, J. B. Claridge, Z. Xu, S. Romani, M. J. Crudace and G. J. Hutchings, *Catalysis Science & Technology*, 2011, **1**, 740-746
47. A. A. Mirzaei, H. R. Shaterian, R. W. Joyner, M. Stockenhuber, S. H. Taylor and G. J. Hutchings, *Catalysis Communications*, 2003, **4**, 17-20.
48. L. N. Jin, Q. Liu and W. Y. Sun, *Crystengcomm*, 2012, **14**, 7721-7726.
49. I. Luisetto, F. Pepe and E. Bemporad, *Journal of Nanoparticle Research*, 2008, **10**, 59-67.
50. C. C. Yu, L. X. Zhang, J. L. Shi, J. J. Zhao, J. H. Gao and D. S. Yan, *Advanced Functional Materials*, 2008, **18**, 1544-1554.
51. J. Ahmed, T. Ahmad, K. V. Ramanujachary, S. E. Lofland and A. K. Ganguli, *Journal of Colloid and Interface Science*, 2008, **321**, 434-441.
52. W. C. Sheets, E. Mugnier, A. Barnabe, T. J. Marks and K. R. Poepelmeier, *Chemistry of Materials*, 2006, **18**, 7-20.
53. S. Esposito, *Materials*, 2019, **12**, 25.
54. Y. Tanaka, T. Takeguchi, R. Kikuchi and K. Eguchi, *Applied Catalysis A-General*, 2005, **279**, 59-66.
55. O. S. Hammond, K. J. Edler, D. T. Bowron and L. Torrente-Murciano, *Nature Communications*, 2017, **8**, 7.
56. S. A. Kondrat and S. H. Taylor, in *Catalysis*, eds. J. J. Spivey and K. M. Dooley, The Royal Society of Chemistry, 2014, volume 26, pp. 218-248.
57. M. Behrens, D. Brennecke, F. Girgsdies, S. Kissner, A. Trunschke, N. Nasrudin, S. Zakaria, N. F. Idris, S. B. Abd Hamid, B. Kniep, R. Fischer, W. Busser, M. Muhler and R. Schlögl, *Applied Catalysis A-General*, 2011, **392**, 93-102.
58. J. Hu, L. Chen and R. Richards, in *Metal Oxide Catalysis*, eds. S. D. Jackson and J. S. J. Hargreaves, Wiley, 2009, volume 2, chapter 16, pp. 613-664.

59. G. Prieto, K. P. de Jong and P. E. de Jongh, *Catalysis Today*, 2013, **215**, 142-151.
60. M. Behrens and R. Schlogl, *Zeitschrift Fur Anorganische Und Allgemeine Chemie*, 2013, **639**, 2683-2695.
61. G. J. Hutchings, A. A. Mirzaei, R. W. Joyner, M. R. H. Siddiqui and S. H. Taylor, *Applied Catalysis A-General*, 1998, **166**, 143-152.
62. P. Kowalik, K. Antoniak-Jurak, R. Bicki, W. Prochniak, P. Wiercioch and K. Michalska, *International Journal of Hydrogen Energy*, 2019, **44**, 913-922.
63. S. H. Taylor, G. J. Hutchings and A. A. Mirzaei, *Chemical Communications*, 1999, 1373-1374.
64. C. Baltes, S. Vukojevic and F. Schuth, *Journal of Catalysis*, 2008, **258**, 334-344.
65. A. A. Mirzaei, H. R. Shaterian, S. H. Taylor and G. J. Hutchings, *Catalysis Letters*, 2003, **87**, 103-108.
66. P. J. Smith, S. A. Kondrat, J. H. Carter, P. A. Chater, J. K. Bartley, S. H. Taylor, M. S. Spencer and G. J. Hutchings, *ChemCatChem*, 2017, **9**, 1621-1631.
67. J. S. Hayward, P. J. Smith, S. A. Kondrat, M. Bowker and G. J. Hutchings, *ChemCatChem*, 2017, **9**, 1655-1662.
68. B. L. Cushing, V. L. Kolesnichenko and C. J. O'Connor, *Chemical Reviews*, 2004, **104**, 3893-3946.
69. A. E. Danks, S. R. Hall and Z. Schnepp, *Materials Horizons*, 2016, **3**, 91-112.
70. Y. Z. Guo, W. Meyer-Zaika, M. Muhler, S. Vukojevic and M. Epple, *European Journal of Inorganic Chemistry*, 2006, 4774-4781.
71. J. L. Gasser-Ramirez, B. C. Dunn, D. W. Ramirez, E. P. Fillerup, G. C. Turpin, Y. Shi, R. D. Ernst, R. J. Pugmire, E. M. Eyring, K. A. Pettigrew, D. R. Rolison and J. M. Harris, *Journal of Non-Crystalline Solids*, 2008, **354**, 5509-5514.
72. W. B. Li, Y. Lin and Y. Zhang, *Catalysis Today*, 2003, **83**, 239-245.
73. L. Wang, C. Wang, H. K. Xie, W. C. Zhan, Y. L. Guo and Y. Guo, *Catalysis Today*, 2019, **327**, 190-195.
74. A. Rabenau, *Angewandte Chemie-International Edition*, 1985, **24**, 1026-1040.
75. C. S. Cundy and P. A. Cox, *Chemical Reviews*, 2003, **103**, 663-701.
76. K. Byrappa and T. Adschiri, *Progress in Crystal Growth and Characterization of Materials*, 2007, **53**, 117-166.
77. R. E. Morris, *Chemical Communications*, 2009, 2990-2998.
78. L. Smart and E. Moore, *Solid State Chemistry An Introduction*, Taylor & Francis, 2005.
79. N. Torres-Gomez, O. Nava, L. Argueta-Figueroa, R. Garcia-Contreras, A. Baeza-Barrera and A. R. Vilchis-Nestor, *Journal of Nanomaterials*, 2019, 1-15.
80. S. Mobini, F. Meshkani and M. Rezaei, *Process Safety and Environmental Protection*, 2017, **107**, 181-189.
81. A. S. Bhalla, R. Y. Guo and R. Roy, *Materials Research Innovations*, 2000, **4**, 3-26.
82. W. J. Zheng, R. H. Liu, D. K. Peng and G. Y. Meng, *Materials Letters*, 2000, **43**, 19-22.

83. S. Kato, R. Fujimaki, M. Ogasawara, T. Wakabayashi, Y. Nakahara and S. Nakata, *Applied Catalysis B-Environmental*, 2009, **89**, 183-188.
84. J. Hu, W. B. Li and R. F. Liu, *Catalysis Today*, 2018, **314**, 147-153.
85. M. T. Zheng, H. R. Zhang, X. B. Gong, R. C. Xu, Y. Xiao, H. W. Dong, X. T. Liu and Y. L. Liu, *Nanoscale Research Letters*, 2013, **8**, 7.
86. Q. Q. Zhang, D. H. Xiong, H. Li, D. L. Xia, H. Z. Tao and X. J. Zhao, *Journal of Materials Science-Materials in Electronics*, 2015, **26**, 10159-10163.
87. B. Solsona, T. Garcia, G. J. Hutchings, S. H. Taylor and M. Makkee, *Applied Catalysis A-General*, 2009, **365**, 222-230.
88. R. Spinicci, M. Faticanti, P. Marini, S. De Rossi and P. Porta, *Journal of Molecular Catalysis A-Chemical*, 2003, **197**, 147-155.
89. B. Solsona, T. E. Davies, T. Garcia, I. Vazquez, A. Dejoz and S. H. Taylor, *Applied Catalysis B-Environmental*, 2008, **84**, 176-184.
90. M. H. Kim, K. H. Cho, C. H. Shin, S. E. Kang and S. W. Ham, *Korean Journal of Chemical Engineering*, 2011, **28**, 1139-1143
91. B. Solsona, E. Aylon, R. Murillo, A. M. Mastral, A. Monzonis, S. Agouram, T. E. Davies, S. H. Taylor and T. Garcia, *Journal of Hazardous Materials*, 2011, **187**, 544-552.
92. R. Ran, D. Weng, X. D. Wu, J. Fan and L. Qing, *Catalysis Today*, 2007, **126**, 394-399.
93. L. F. Liotta, H. J. Wu, G. Pantaleo and A. M. Venezia, *Catalysis Science & Technology*, 2013, **3**, 3085-3102.
94. S. C. Kim and W. G. Shim, *Applied Catalysis B-Environmental*, 2010, **98**, 180-185.
95. B. Faure and P. Alphonse, *Applied Catalysis B-Environmental*, 2016, **180**, 715-725.
96. X. W. Xie, Y. Li, Z. Q. Liu, M. Haruta and W. J. Shen, *Nature*, 2009, **458**, 746-749.
97. W. X. Tang, X. F. Wu, S. D. Li, W. H. Li and Y. F. Chen, *Catalysis Communications*, 2014, **56**, 134-138.
98. C. Zhang, J. G. Wang, S. F. Yang, H. Liang and Y. Men, *Journal of Colloid and Interface Science*, 2019, **539**, 65-75.
99. W. X. Tang, Z. Ren, X. X. Lu, S. B. Wang, Y. B. Guo, S. Hoang, S. C. Du and P. X. Gao, *ChemCatChem*, 2017, **9**, 4112-4119.
100. B. H. Zhao, R. Ran, L. Sun, Z. S. Yang, X. D. Wu and D. Weng, *Catalysis Communications*, 2018, **105**, 26-30.
101. A. C. Gluhoi, N. Bogdanchikova and B. E. Nieuwenhuys, *Catalysis Today*, 2006, **113**, 178-181.
102. Y. Wang, H. Arandiyani, Y. X. Liu, Y. J. Liang, Y. Peng, S. Bartlett, H. X. Dai, S. Rostamnia and J. H. Li, *ChemCatChem*, 2018, **10**, 3429-3434.
103. Z. Ye, J. M. Giraudon, N. Nuns, P. Simon, N. De Geyter, R. Morent and J. F. Lamonier, *Applied Catalysis B-Environmental*, 2018, **223**, 154-166.
104. T. K. Liu, Y. Y. Yao, L. Q. Wei, Z. F. Shi, L. Y. Han, H. X. Yuan, B. Li, L. H. Dong, F. Wang and C. Z. Sun, *Journal of Physical Chemistry C*, 2017, **121**, 12757-12770.
105. T. J. Clarke, T. E. Davies, S. A. Kondrat and S. H. Taylor, *Applied Catalysis B-Environmental*, 2015, **165**, 222-231.

106. S. Veprek, D. L. Cocke, S. Kehl and H. R. Oswald, *Journal of Catalysis*, 1986, **100**, 250-263.
107. G. M. Schwab and S. B. Kanungo, *Zeitschrift Fur Physikalische Chemie-Frankfurt*, 1977, **107**, 109-120.
108. T. Tabakova, V. Idakiev, G. Avgouropoulos, J. Papavasiliou, M. Manzoli, F. Boccuzzi and T. Ioannides, *Applied Catalysis A-General*, 2013, **451**, 184-191.
109. T. H. Rogers, C. S. Piggot, W. H. Bahlke and J. M. Jennings, *Journal of the American Chemical Society*, 1921, **43**, 1973-1982.
110. Z. R. Tang, C. D. Jones, J. K. W. Aldridge, T. E. Davies, J. K. Bartley, A. F. Carley, S. H. Taylor, M. Allix, C. Dickinson, M. J. Rosseinsky, J. B. Claridge, Z. L. Xu, M. J. Crudace and G. J. Hutchings, *ChemCatChem*, 2009, **1**, 247-251.
111. E. C. Njagi, C. H. Chen, H. Genuino, H. Galindo, H. Huang and S. L. Suib, *Applied Catalysis B-Environmental*, 2010, **99**, 103-110.
112. M. Li, D. H. Wang, X. C. Shi, Z. T. Zhang and T. X. Dong, *Separation and Purification Technology*, 2007, **57**, 147-151.
113. C. Jones, K. J. Cole, S. H. Taylor, M. J. Crudace and G. J. Hutchings, *Journal of Molecular Catalysis A-Chemical*, 2009, **305**, 121-124.
114. K. Li, R. R. Zhang, R. J. Gao, G. Q. Shen, L. Pan, Y. D. Yao, K. H. Yu, X. W. Zhang and J. J. Zou, *Applied Catalysis B-Environmental*, 2019, **244**, 536-545.
115. B. Solsona, G. J. Hutchings, T. Garcia and S. H. Taylor, *New Journal of Chemistry*, 2004, **28**, 708-711.
116. C. Jones, S. H. Taylor, A. Burrows, M. J. Crudace, C. J. Kiely and G. J. Hutchings, *Chemical Communications*, 2008, 1707-1709.
117. K. J. Cole, A. F. Carley, M. J. Crudace, M. Clarke, S. H. Taylor and G. J. Hutchings, *Catalysis Letters*, 2010, **138**, 143-147.
118. K. Wegner, M. Medicus, E. Schade, J. Grothe and S. Kaskel, *ChemCatChem*, 2018, **10**, 3914-3922.
119. G. J. Hutchings, A. A. Mirzaei, R. W. Joyner, M. R. H. Siddiqui and S. H. Taylor, *Catalysis Letters*, 1996, **42**, 21-24.
120. D. Rangappa, S. Ohara, M. Umetsu, T. Naka and T. Adschiri, *Journal of Supercritical Fluids*, 2008, **44**, 441-445.
121. P. Kowalik, K. Antoniak-Jurak, W. Prochniak, P. Wiercioch, M. Konkol, R. Bicki, K. Michalska and M. Walczak, *Catalysis Letters*, 2017, **147**, 1422-1433.
122. M. V. Twigg and M. S. Spencer, *Topics in Catalysis*, 2003, **22**, 191-203.
123. S. A. Kondrat, P. J. Smith, J. H. Carter, J. S. Hayward, G. J. Pudge, G. Shaw, M. S. Spencer, J. K. Bartley, S. H. Taylor and G. J. Hutchings, *Faraday Discussions*, 2017, **197**, 287-307.
124. M. Behrens, *Journal of Catalysis*, 2009, **267**, 24-29.
125. M. Saito, T. Fujitani, M. Takeuchi and T. Watanabe, *Applied Catalysis A-General*, 1996, **138**, 311-318.
126. Y. F. Zhao, Y. Yang, C. Mims, C. H. F. Peden, J. Li and D. H. Mei, *Journal of Catalysis*, 2011, **281**, 199-211.
127. M. Behrens, F. Studt, I. Kasatkin, S. Kuhl, M. Havecker, F. Abild-Pedersen, S. Zander, F. Girgsdies, P. Kurr, B. L. Kniep, M. Tovar, R.

- W. Fischer, J. K. Norskov and R. Schlogl, *Science*, 2012, **336**, 893-897.
128. W. Wang, S. P. Wang, X. B. Ma and J. L. Gong, *Chemical Society Reviews*, 2011, **40**, 3703-3727
129. M. S. Spencer, *Catalysis Letters*, 2000, **66**, 255-257.
130. Y. L. Zhang, Q. Sun, J. F. Deng, D. Wu and S. Y. Chen, *Applied Catalysis A-General*, 1997, **158**, 105-120.
131. W. L. Dai, Q. Sun, J. F. Deng, D. Wu and Y. H. Sun, *Applied Surface Science*, 2001, **177**, 172-179.
132. H. Lei, Z. Y. Hou and J. W. Xie, *Fuel*, 2016, **164**, 191-198.
133. Z. Chu, H. B. Chen, Y. Yu, Q. Wang and D. Y. Fang, *Journal of Molecular Catalysis A-Chemical*, 2013, **366**, 48-53.
134. L. Shi, C. Y. Zeng, Y. Z. Jin, T. J. Wang and N. Tsubaki, *Catalysis Science & Technology*, 2012, **2**, 2569-2577.
135. S. A. Kondrat, P. J. Smith, P. P. Wells, P. A. Chater, J. H. Carter, D. J. Morgan, E. M. Fiordaliso, J. B. Wagner, T. E. Davies, L. Lu, J. K. Bartley, S. H. Taylor, M. S. Spencer, C. J. Kiely, G. J. Kelly, C. W. Park, M. J. Rosseinsky and G. J. Hutchings, *Nature*, 2016, **531**, 83-87.
136. F. Cansell, C. Aymonier and A. Loppinet-Serani, *Current Opinion in Solid State & Materials Science*, 2003, **7**, 331-340.
137. J. A. Darr and M. Poliakoff, *Chemical Reviews*, 1999, **99**, 495-541.
138. C. J. Clarke, W. C. Tu, O. Levers, A. Brohl and J. P. Hallett, *Chemical Reviews*, 2018, **118**, 747-800.
139. P. G. Jessop, *Journal of Synthetic Organic Chemistry Japan*, 2003, **61**, 484-488.
140. G. J. Hutchings, *Journal of Materials Chemistry*, 2009, **19**, 1222-1235.
141. A. Baiker, *Chemical Reviews*, 1999, **99**, 453-473.
142. S. Sarrade, D. Feron, F. Rouillard, S. Perrin, R. Robin, J. C. Ruiz and H. A. Turc, *Journal of Supercritical Fluids*, 2017, **120**, 335-344.
143. X. L. Weng, W. L. Wang, Q. J. Meng and Z. B. Wu, *Catalysis Science & Technology*, 2018, **8**, 4364-4372.
144. J. Jung and M. Perrut, *Journal of Supercritical Fluids*, 2001, **20**, 179-219.
145. K. Byrappa, S. Ohara and T. Adschiri, *Advanced Drug Delivery Reviews*, 2008, **60**, 299-327.
146. R. P. Marin, S. A. Kondrat, T. E. Davies, D. J. Morgan, D. I. Enache, G. B. Combes, S. H. Taylor, J. K. Bartley and G. J. Hutchings, *Catalysis Science & Technology*, 2014, **4**, 1970-1978.
147. R. Adami, L. S. Osseo, R. Huopalahti and E. Reverchon, *Journal of Supercritical Fluids*, 2007, **42**, 288-298.
148. E. Reverchon, G. Della Porta, D. Sannino and P. Ciambelli, *Powder Technology*, 1999, **102**, 127-134.
149. G. J. Hutchings, J. A. Lopez-Sanchez, J. K. Bartley, J. M. Webster, A. Burrows, C. J. Kiely, A. F. Carley, C. Rhodes, M. Havecker, A. Knop-Gericke, R. W. Mayer, R. Schlogl, J. C. Volta and M. Poliakoff, *Journal of Catalysis*, 2002, **208**, 197-210.
150. E. Reverchon, I. De Marco and E. Torino, *Journal of Supercritical Fluids*, 2007, **43**, 126-138.

151. S. A. Kondrat, P. J. Smith, L. Lu, J. K. Bartley, S. H. Taylor, M. S. Spencer, G. J. Kelly, C. W. Park, C. J. Kiely and G. J. Hutchings, *Catalysis Today*, 2018, **317**, 12-20.
152. P. J. Smith, S. A. Kondrat, P. A. Chater, B. R. Yeo, G. M. Shaw, L. Lu, J. K. Bartley, S. H. Taylor, M. S. Spencer, C. J. Kiely, G. J. Kelly, C. W. Park and G. J. Hutchings, *Chemical Science*, 2017, **8**, 2436-2447.
153. A. Abebe, S. Admassie, I. J. Villar-Garcia and Y. Chebude, *Inorganic Chemistry Communications*, 2013, **29**, 210-212
154. Z. Q. He and P. Alexandridis, *Physical Chemistry Chemical Physics*, 2015, **17**, 18238-18261.
155. R. Sheldon, *Chemical Communications*, 2001, 2399-2407.
156. Z. H. Li, Z. Jia, Y. X. Luan and T. C. Mu, *Current Opinion in Solid State & Materials Science*, 2008, **12**, 1-8.
157. M. L. C. Passos, D. Costa, J. Lima and M. Saraiva, *Talanta*, 2015, **133**, 45-51.
158. B. R. Mellein and J. F. Brennecke, *Journal of Physical Chemistry B*, 2007, **111**, 4837-4843.
159. N. O. Nunez and M. Ocana, *Nanotechnology*, 2007, **18**, 7.
160. S. A. Ansari, L. S. Liu and L. F. Rao, *Dalton Transactions*, 2015, **44**, 2907-2914.
161. K. R. Seddon, *J. Journal of Chemical Technology and Biotechnology*, 1997, **68**, 351-356
162. S. Q. Cheng, J. L. Zhang, Z. F. Zhang and B. X. Han, *Chemical Communications*, 2007, 2497-2499.
163. K. Binnemans, *Chemical Reviews*, 2007, **107**, 2592-2614.
164. H. P. Steinruck and P. Wasserscheid, *Catalysis Letters*, 2015, **145**, 380-397.
165. C. L. Hussey, *Pure and Applied Chemistry*, 1988, **60**, 1763-1772.
166. Z. H. Li, A. Gessner, J. P. Richters, J. Kalden, T. Voss, C. Kubel and A. Taubert, *Advanced Materials*, 2008, **20**, 1279-1285.
167. A. Abo-Hamad, M. Hayyan, M. A. AlSaadi and M. A. Hashim, *Chemical Engineering Journal*, 2015, **273**, 551-567.
168. A. P. Abbott, G. Frisch, J. Hartley and K. S. Ryder, *Green Chemistry*, 2011, **13**, 471-481.
169. G. Chatel, J. F. B. Pereira, V. Debbeti, H. Wang and R. D. Rogers, *Green Chemistry*, 2014, **16**, 2051-2083.
170. N. V. Plechkova and K. R. Seddon, *Chemical Society Review*, 2008, **37**, 123-150.
171. R. Hayes, G. G. Warr and R. Atkin, *Chemical Reviews*, 2015, **115**, 6357-6426.
172. Z. Ma, J. H. Yu and S. Dai, *Advanced Materials*, 2010, **22**, 261-285.
173. R. P. Swatloski, J. D. Holbrey and R. D. Rogers, *Green Chemistry*, 2003, **5**, 361-363.
174. D. Depuydt, W. Dehaen and K. Binnemans, *Industrial & Engineering Chemistry Research*, 2015, **54**, 8988-8996.
175. N. Papaiconomou, J. M. Lee, J. Salminen, M. von Stosch and J. M. Prausnitz, *Industrial & Engineering Chemistry Research*, 2008, **47**, 5080-5086.
176. J. H. Davis, *Chemistry Letters*, 2004, **33**, 1072-1077.

177. P. Nockemann, B. Thijs, S. Pittois, J. Thoen, C. Glorieux, K. Van Hecke, L. Van Meervelt, B. Kirchner and K. Binnemans, *Journal of Physical Chemistry B*, 2006, **110**, 20978-20992.
178. A. P. Abbott, G. Capper, D. L. Davies, K. J. McKenzie and S. U. Obi, *Journal of Chemical and Engineering Data*, 2006, **51**, 1280-1282.
179. J. M. Hartley, C. M. Ip, G. C. H. Forrest, K. Singh, S. J. Gurman, K. S. Ryder, A. P. Abbott and G. Frisch, *Inorganic Chemistry*, 2014, **53**, 6280-6288.
180. A. P. Abbott, R. C. Harris, F. Holyoak, G. Frisch, J. Hartley and G. R. T. Jenkin, *Green Chemistry*, 2015, **17**, 2172-2179.
181. A. P. Abbott, G. Capper, D. L. Davies, R. K. Rasheed and V. Tambyrajah, *Chemical Communications*, 2003, 70-71.
182. E. L. Smith, A. P. Abbott and K. S. Ryder, *Chemical Reviews*, 2014, **114**, 11060-11082.
183. Y. T. Dai, J. van Spronsen, G. J. Witkamp, R. Verpoorte and Y. H. Choi, *Journal of Natural Products*, 2013, **76**, 2162-2173.
184. Q. H. Zhang, K. D. Vigier, S. Royer and F. Jerome, *Chemical Society Reviews*, 2012, **41**, 7108-7146.
185. H. Sun, Y. Li, X. Wu and G. H. Li, *Journal of Molecular Modeling*, 2013, **19**, 2433-2441.
186. F. Pena-Pereira and J. Namiesnik, *ChemSusChem*, 2014, **7**, 1784-1800.
187. A. P. Abbott, G. Capper, D. L. Davies, R. K. Rasheed and P. Shikotra, *Inorganic Chemistry*, 2005, **44**, 6497-6499.
188. Z. Liu, S. Z. El Abedin and F. Endres, *Electrochemistry Communications*, 2015, **58**, 46-50.
189. S. M. Shuwa, R. S. Al-Hajri, B. Y. Jibril and Y. M. Al-Waheibi, *Industrial & Engineering Chemistry Research*, 2015, **54**, 3589-3601.
190. P. Billik, P. Antal and R. Gyepes, *Inorganic Chemistry Communications*, 2015, **60**, 37-40.
191. J. Y. Dong, Y. J. Hsu, D. S. H. Wong and S. Y. Lu, *Journal of Physical Chemistry C*, 2010, **114**, 8867-8872.
192. J. Y. Dong, W. H. Lin, Y. J. Hsu, D. S. H. Wong and S. Y. Lu, *Crystengcomm*, 2011, **13**, 6218-6222.
193. Y. H. Lu, W. H. Lin, C. Y. Yang, Y. H. Chiu, Y. C. Pu, M. H. Lee, Y. C. Tseng and Y. J. Hsu, *Nanoscale*, 2014, **6**, 8796-8803.
194. S. Datta and L. Torrente-Murciano, *Current Opinion in Chemical Engineering*, 2018, **20**, 99-106.
195. T. Alammam, Slowing, II, J. Anderegg and A. V. Mudring, *Chemsuschem*, 2017, **10**, 3387-3401.
196. T. Alammam, Y. K. Chow and A. V. Mudring, *New Journal of Chemistry*, 2015, **39**, 1339-1347.
197. J. Luczak, M. Paszkiewicz, A. Krukowska, A. Malankowska and A. Zaleska-Medynska, *Advances in Colloid and Interface Science*, 2016, **227**, 1-52.
198. Y. Meng, J. L. Liu, Z. M. Zhang, W. Q. Lin, Z. J. Lin and M. L. Tong, *Dalton Transactions*, 2013, **42**, 12853-12856.
199. E. R. Parnham, E. A. Drylie, P. S. Wheatley, A. M. Z. Slawin and R. E. Morris, *Angewandte Chemie-International Edition*, 2006, **45**, 4962-4966.

200. O. S. Hammond, S. Eslava, A. J. Smith, J. F. Zhang and K. J. Edler, *Journal of Materials Chemistry A*, 2017, **5**, 16189-16199.
201. X. Ge, C. D. Gu, X. L. Wang and J. P. Tu, *Journal of Colloid and Interface Science*, 2015, **438**, 149-158.
202. X. Ge, C. D. Gu, X. L. Wang and J. P. Tu, *Journal of Colloid and Interface Science*, 2015, **454**, 134-143.
203. P. G. Jessop, D. J. Heldebrant, X. W. Li, J. Lu, J. P. Hallett, R. S. Jones, P. Pollet, C. A. Thomas, C. A. Eckert and C. L. Liotta, *Abstracts of Papers of the American Chemical Society*, 2005, **229**, U971.
204. P. G. Jessop, D. J. Heldebrant, X. W. Li, C. A. Eckert and C. L. Liotta, *Nature*, 2005, **436**, 1102.
205. I. Anugwom, L. Rujana, J. Warna, M. Hedenstrom and J. P. Mikkola, *Chemical Engineering Journal*, 2016, **297**, 256-264.
206. Z. Q. Yang, C. Q. He, H. Sui, L. He and X. G. Li, *Journal of CO2 Utilization*, 2019, **30**, 79-99.
207. D. J. Heldebrant, P. G. Jessop, C. A. Thomas, C. A. Eckert and C. L. Liotta, *Journal of Organic Chemistry*, 2005, **70**, 5335-5338.
208. T. Yamada, P. J. Lukac, M. George and R. G. Weiss, *Chemistry of Materials*, 2007, **19**, 967-969.
209. J. R. Vanderveen, J. Durelle and P. G. Jessop, *Green Chemistry*, 2014, **16**, 1187-1197.
210. P. G. Jessop, S. M. Mercer and D. J. Heldebrant, *Energy & Environmental Science*, 2012, **5**, 7240-7253.
211. L. Phan, J. R. Andreatta, L. K. Horvey, C. F. Edie, A. L. Luco, A. Mirchandani, D. J. Darensbourg and P. G. Jessop, *Journal of Organic Chemistry*, 2008, **73**, 127-132.
212. K. Bryant, G. Ibrahim and S. R. Saunders, *Langmuir*, 2017, **33**, 12982-12988.
213. P. G. Jessop, *Aldrichimica Acta*, 2015, **48**, 18-21.
214. P. G. Jessop, L. Kozycz, Z. G. Rahami, D. Schoenmakers, A. R. Boyd, D. Wechsler and A. M. Holland, *Green Chemistry*, 2011, **13**, 619-623.
215. P. G. Jessop, L. Phan, A. Carrier, S. Robinson, C. J. Durr and J. R. Harjani, *Green Chemistry*, 2010, **12**, 809-814.
216. P. Nanta, W. Skolpap, K. Kasemwong and Y. Shimoyama, *Journal of Supercritical Fluids*, 2017, **130**, 84-90.
217. P. Nanta, W. Skolpap, K. Kasemwong and Y. Shimoyama, *Chemical Engineering Science*, 2018, **179**, 214-220.
218. E. Reverchon, G. Della Porta, D. Sannino, L. Lisi and P. Ciambelli, in *Preparation of Catalysts VII*, eds. B. Delmon, P. A. Jacobs, R. Maggi, J. A. Martens, P. Grange and G. Poncelet, Elsevier Science, 1998, vol. 118, pp. 349-358.
219. E. Yilmaz and M. Soylak, *Analytica Chimica Acta*, 2015, **886**, 75-82
220. Z. M. Memon, E. Yilmaz and M. Soylak, *Journal of Molecular Liquids*, 2017, **229**, 459-464.
221. P. G. Jessop, *Faraday Discussions*, 2018, **206**, 587-601.
222. I. Juneidi, M. Hayyan and O. M. Ali, *Environmental Science and Pollution Research*, 2016, **23**, 7648-7659.

## Chapter 2 Experimental

### 2.1 Introduction

This chapter outlines the methods used to produce the catalysts, the characterisation techniques used to determine the physical properties of the catalyst and the catalyst testing procedure that are presented in this thesis. The chapter will also explore the theory of the characterisation techniques, while the theory and reasons behind the strategies of catalyst preparation are explained in Chapter 1 and the relevant results chapters.

#### 2.1.1 Chemicals list

**Table 2.1: DES components and switchable additives purchased**

Sample	Chemical formula	Grade/purity	Company	Chapters
Choline chloride	$((\text{CH}_3)_3\text{NCH}_2\text{CH}_2\text{OH})\text{Cl}$	Bio reagent 98%	Sigma Aldrich	3, 6
Urea (pellets)	$\text{CO}(\text{NH}_2)_2$	99.5%	Sigma Aldrich	6
Oxalic acid dihydrate	$\text{C}_2\text{H}_2\text{O}_4 \cdot 2\text{H}_2\text{O}$	ACS grade 99%	Sigma Aldrich	3
Oxalic acid (anhydrous)	$\text{C}_2\text{H}_2\text{O}_4$	Anhydrous Puriss $\geq 99\%$	Sigma Aldrich	3
Triethylamine	$(\text{CH}_3\text{CH}_2)_3\text{N}$	$\geq 99\%$	Sigma Aldrich	5, 6

**Table 2.2: The precursor metal salts used for this work**

Sample	Formula	Grade/purity	Company	Chapter
Manganese (II) acetate tetrahydrate	$\text{Mn}(\text{CH}_3\text{CO}_2)_2 \cdot 4\text{H}_2\text{O}$	99%	Sigma Aldrich	3, 5
Manganese (II) nitrate tetrahydrate	$\text{Mn}(\text{NO}_3)_2 \cdot 4\text{H}_2\text{O}$	97%	Sigma Aldrich	3, 4, 5
Manganese (II) chloride tetrahydrate	$\text{MnCl}_2 \cdot 4\text{H}_2\text{O}$	ACS reagent grade	Sigma Aldrich	3
Cobalt (II) acetate tetrahydrate	$\text{Co}(\text{CH}_3\text{CO}_2)_2 \cdot 4\text{H}_2\text{O}$	ACS reagent grade 98%	Sigma Aldrich	3
Iron (II) acetate	$\text{Fe}(\text{CH}_3\text{CO}_2)_2$	95 %	Sigma Aldrich	3
Iron (II) oxalate dihydrate	$\text{Fe}(\text{C}_2\text{O}_4) \cdot 2\text{H}_2\text{O}$	98%	Sigma Aldrich	3
Copper (II) acetate monohydrate	$\text{Cu}(\text{CH}_3\text{CO}_2)_2 \cdot \text{H}_2\text{O}$	98%	Sigma Aldrich	5, 6
Copper (II) nitrate hemipentahydrate	$\text{Cu}(\text{NO}_3)_2 \cdot 2.5\text{H}_2\text{O}$	Reagent grade 98%	Sigma Aldrich	4, 5, 6
Zinc (II) nitrate hexahydrate	$\text{Zn}(\text{NO}_3)_2 \cdot 6\text{H}_2\text{O}$	>99.0%	Sigma Aldrich	6
Zinc (II) oxide	ZnO	99 %	Sigma Aldrich	6

**Table 2.3: Acids, Bases and solvents**

Sample	Formula	Grade/purity	Company	Chapter
Sodium hydroxide (pellets)	NaOH	Reagent grade	VWR	4
Sodium carbonate (anhydrous)	$\text{Na}_2\text{CO}_3$	Reagent grade	Fischer	4
Ethanol	$\text{CH}_3\text{CH}_2\text{OH}$	Absolute 99.8%	VWR	3, 4, 5, 6
Methanol	$\text{CH}_3\text{OH}$	HPLC grade 99.8 %	VWR	3
Nitric acid	$\text{HNO}_3$	70% in water	VWR	3, 5, 6 (MP-AES)
Hydrochloric acid	HCl	35 % in water	VWR	3, 5, 6 (MP-AES)

## **2.2 Catalyst preparation**

### **2.2.1 Deep eutectic solvents**

In this work, choline chloride with either urea in a 1:2 molar ratio or oxalic acid in a 1:1 molar ratio was used to prepare some of the catalysts. The formation of deep eutectic solvents outlined here is well established in the literature<sup>1-4</sup>. This method used an anti-solvent approach using water or a water-alcohol mixture to precipitate a metal precursor from the DES.

#### **2.2.1.1 Choline chloride-oxalic acid for metal oxide preparation**

Choline chloride and oxalic acid (anhydrous or dihydrate) were mixed in a 1:1 molar ratio in a round bottom flask and the mixture was heated to 82 °C and left until a homogenous liquid had formed. The time taken depended on the oxalic acid used; 1 hour for oxalic acid dihydrate and 2 hours for anhydrous oxalic acid.

The metal salt; cobalt acetate tetrahydrate, iron acetate, manganese acetate, manganese nitrate or manganese chloride, was added to the choline chloride-oxalic acid deep eutectic solvent at a molar ratio of 0.1:1:1 of metal salt:oxalic acid:choline chloride. The mixture was heated to 120 °C for 1 hour and then 150 °C for 2 hours. The mixture was then cooled to 65 °C prior to the addition of the anti-solvent.

The anti-solvent mixtures were comprised of either deionised water, 50:50 volume ratio of water-ethanol, 50:50 (volume) of water-methanol, pure methanol or ethanol.

Fast precipitation: The deep eutectic mixture was poured into the anti-solvent mixture (600 ml) and left under vigorous stirring for 1 hour during which time a precipitate formed. The metal oxalates were then filtered under vacuum

and washed with deionized water and ethanol before being dried under vacuum at 60 °C for 15 hours.

Slow precipitation: 100 ml of the anti-solvent was injected using a syringe pump at a rate of 1 ml min<sup>-1</sup> followed by 100 ml injected at 4 ml min<sup>-1</sup>. The oxalates were then filtered and washed with deionized water and ethanol before being dried under vacuum at 60 °C for 15 hours.

The oxalate precursors (approximately 0.5-0.75 g) were calcined in a furnace opened/exposed to an air flow at 300 °C, 350 °C, 400 °C and 500 °C for 3 hours with a heating rate of 2 °C min<sup>-1</sup>.

#### **2.2.1.2 Choline chloride-urea for copper/zinc oxide preparation**

Choline chloride and urea were added in a 1:2 molar ratio in a round bottom flask. The mixture was heated to 82 °C, and after 2 hours a clear homogeneous liquid formed. Zinc oxide was dissolved in the DES with a zinc concentration of 28000 ppm at 82 °C and left for 2-3 days to dissolve to form a single phase solution.

Fast precipitation: The DES was poured into deionised water (1500 ml) containing of copper acetate or copper nitrate with the concentration depending on the target loading. A blue precipitate formed which was then filtered and washed with deionised water and ethanol and dried at 60 °C for 15 hours.

Slow precipitation: the copper salt (copper acetate or copper nitrate) was dissolved in 100 ml of deionised water and injected into the deep eutectic mixture at a rate of 1 ml min<sup>-1</sup> followed by 600 ml at a rate of 2 ml min<sup>-1</sup>. The precipitate was then filtered and washed with deionised water and ethanol and dried at 60 °C for 15 hours.

Approximately 0.5-1.0 g of the precursor (unless otherwise stated) were calcined in a furnace, exposed, to an airflow of approximately 10 ml min<sup>-1</sup> at 350 °C for 3 hours with a heating rate of 5 °C min<sup>-1</sup>.

## 2.2.2 Oxalate gel method for cobalt oxide preparation

Cobalt acetate (5.83 g, 23 mmol) was dissolved in 200 ml of ethanol and left to stir at room temperature for 1 hour. Oxalic acid dihydrate (3.03 g, 24 mmol) was added to the solution and a pink precipitate formed, which was left in the solution under stirring for 1 hour. The solid was then filtered, washed with ethanol and deionised water and dried at 60 °C under vacuum for 15 hours. The cobalt oxalate was calcined at 300 °C or 500 °C for 3 hours with a heating rate of 2 °C min<sup>-1</sup> to form the cobalt oxide catalyst.

## 2.2.3 Supercritical anti-solvent process

### 2.2.3.1 Reactor set up and design

All supercritical anti-solvent experiments were performed on the Separex built supercritical reactor set up in the supercritical anti-solvent (SAS) configuration (**Figure 2.1**). The reactor (**Figure 2.2**) was set up in SAS flow process although this reactor can be setup for other supercritical processes (such as GAS) these were not used for the work in this thesis. More detail on the theory and history of the supercritical anti-solvent precipitation process is discussed in Chapter 1 (Section 1.5).

The supercritical reactor was linked to a 55 bar cylinder of CO<sub>2</sub>. A pump was used to pressurise the reactor to supercritical conditions, above 78 bar, while the pressure of the supercritical rig was controlled by the back-pressure regulator, during the reaction and the depressurisation stage. The metal precursor solution was added to the precipitation vessel via a HPLC pump at a fixed flow rate during the process. Prior to the addition of the metal precursor solution, pure ethanol was injected for 10 minutes to allow the supercritical system to equilibrate before the anti-solvent precipitation.

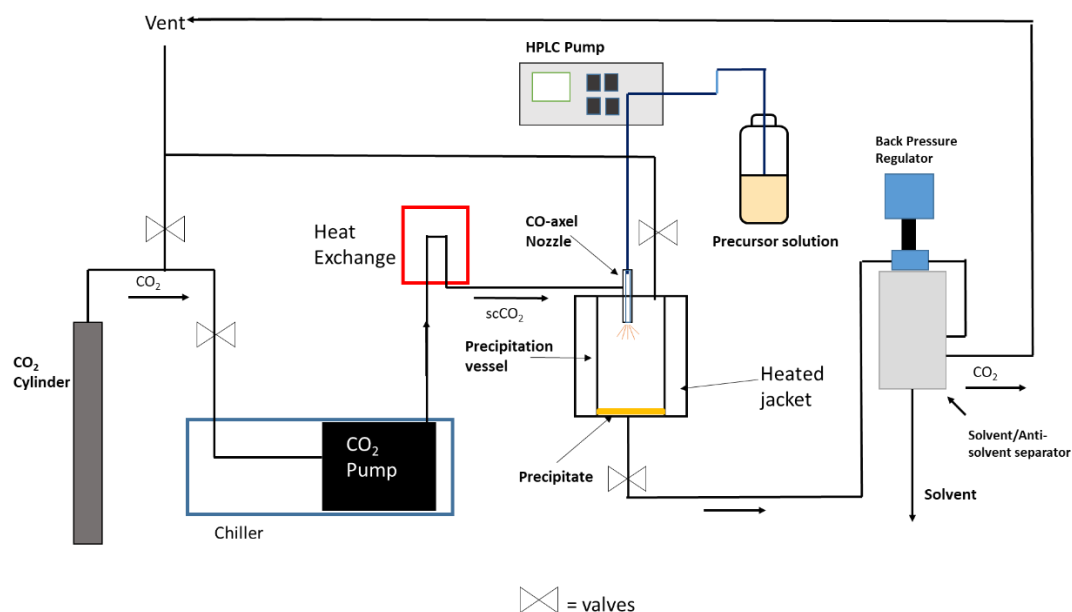


Figure 2.1: Diagram of the Separex supercritical rig setup for SAS

### 2.2.3.2 Supercritical anti-solvent precipitation of cobalt and manganese carbonate

Manganese acetate tetrahydrate or cobalt acetate tetrahydrate was dissolved in 600 ml of ethanol at a concentration of  $7 \text{ mg ml}^{-1}$ . The reactor was pressurised to 120 bar, with a  $\text{CO}_2$  flow rate of  $7 \text{ kg h}^{-1}$  and heated to  $38 \text{ }^\circ\text{C}$ . Ethanol was injected at a rate of  $3.75 \text{ ml min}^{-1}$  using a HPLC pump for 10 minutes prior to the addition of the metal acetate mixture to allow the system to equilibrate. The precursor solution was pumped into the system at a rate of  $3.75 \text{ ml min}^{-1}$ . Once the solution had been pumped the system was left under supercritical condition for 20 minutes to allow drying before being depressurised.

The precursors were calcined in a furnace exposed to an air flow at  $500 \text{ }^\circ\text{C}$  for 3 hours with at heating rate of  $2 \text{ }^\circ\text{C min}^{-1}$ .



**Figure 2.2: Photograph of the Separex build supercritical rig set up for the SAS method used to make the oxide in this thesis**

### **2.2.3.3 Supercritical anti-solvent precipitation of copper manganese carbonate**

Copper acetate monohydrate and manganese acetate tetrahydrate were dissolved, at 1:2 molar ratio of Cu:Mn, in 500 ml of 15% (vol) water in ethanol mixture with a total metal concentration of  $9.85 \text{ mg ml}^{-1}$ . The supercritical reactor was pressurised to 110 bar and heated to  $38 \text{ }^\circ\text{C}$ . Ethanol was injected for 10 minutes to allow the system to equilibrate before the addition of the copper-manganese acetate-ethanol mixture. The precursor mixture was pumped into the system at a rate of  $4.5 \text{ ml min}^{-1}$ . After 95% of the solution had been pumped, the system was left under supercritical conditions for 20 minutes to allow the precipitate to dry before the system was depressurised.

The precursors were calcined in a furnace exposed to an air flow at  $350^\circ\text{C}$  and  $400 \text{ }^\circ\text{C}$  for 3 hours with at heating rate of  $2 \text{ }^\circ\text{C min}^{-1}$ .

#### **2.2.4 Preparation of crednerite and spinel derivatives by hydrothermal synthesis**

The delafossite phase were made using previously a published method<sup>5</sup>.

Manganese nitrate tetrahydrate (3.76 g, 14.9 mmol) and copper nitrate hemipentahydrate (3.48 g, 14.9 mmol) were dissolved in 35 ml of water. Sodium hydroxide (4.4 g, 110 mmol in 35 ml of water) was added to the solution. The brown slurry was then transferred to polytetrafluoroethylene/PTFE liner which was then placed in a 125 ml stainless steel autoclave (Parr) and heated to 82 °C for 24 hours. The precipitate was poured into 1500 ml of water then filtered and washed with deionised water and ethanol. The product was then dried at 60 °C under vacuum for 16 hours.

CuMnO<sub>2</sub> was calcined in a furnace exposed to a flowing air system at either 300 °C, 350 °C, 400 °C or 500 °C for 3 hours with a heating rate of 5 °C min<sup>-1</sup> to form the spinel phase catalysts.

#### **2.2.5 Preparation of copper manganese oxides by co-precipitation**

The co-precipitation was carried out using a Metrohm Titrando auto-titrator based on previously published methods<sup>6</sup>.

Copper nitrate hemipentahydrate (2 M) and manganese nitrate tetrahydrate (2 M) were mixed at a volume ratio of 1:2 or 1:1 Cu:Mn. The solution was heat to 82 °C and sodium bicarbonate (2 M) was added with the rate of addition varied to maintain a solution pH of 8.3. After mixing the solution was aged at 80 °C for 1 hour. The precipitate was filtered and washed with hot water. The resultant copper manganese carbonate was calcined at 350 °C, 400 °C and 500 °C under flowing air with a heating rate of 2 °C min<sup>-1</sup> to form the hopcalite phase oxide/CuMn<sub>2</sub>O<sub>4</sub>.

### 2.2.6 Switchable solvent experiment for metal oxide preparation

The standard preparation (unless otherwise stated): Triethylamine (5.56 ml) and water (4 ml) were added (1:1 molar ratio or 1.4:1 volume ratio) to a round bottom Radley flask equipped with a gas adapter. The flask was then filled with N<sub>2</sub> (1 bar) for 30 minutes, while being degassed twice to remove trace amounts of CO<sub>2</sub>.

The solvent was switched by changing to a CO<sub>2</sub> atmosphere (1 bar) for 30 minutes to 1 hour, being degassed regularly until a single-phase solvent had formed.

A stock solution with total metal concentration of 7 M consisting of 2.33 M of copper nitrate or acetate and 4.67 M of manganese nitrate/acetate for copper manganese oxides or 3.5 M of copper nitrate and 3.5 M zinc nitrate for copper zinc oxide preparation was made up prior to the addition.

4 ml of the metal nitrate solution, with a total metal concentration of 7 M, unless otherwise stated, was injected into the solvent under either the carbon dioxide or nitrogen atmosphere. The sample was left under a carbon dioxide atmosphere for 1 hour (except for aging studies) after metal salt addition. The precipitated sample was then centrifuged and washed with 3x40 ml of deionised water then 30 ml of ethanol. The sample was dried under vacuum for 15 hours at 60 °C.

The carbonate samples were then calcined in a furnace opened/exposed to an to an airflow at either 250 °C (copper-zinc oxide only), 350 °C, 400 °C and 500 °C at a heating rate of 2 °C min<sup>-1</sup> for 3 hours.

## 2.3 Catalyst characterisation: theory and methods

### 2.3.1 Powder X-ray diffraction

X-ray diffraction (XRD) is a technique used to determine the bulk structure and phase of a prepared material. XRD is one of the most used characterisation techniques in the fields of material science and catalyst characterisation. As a bulk method however, it only gives an average determination of the structure and only can be used to identify crystalline samples. However, XRD has the advantage that it can be carried out under both atmospheric and reaction conditions and therefore *in situ* experiments can be performed<sup>7</sup>.

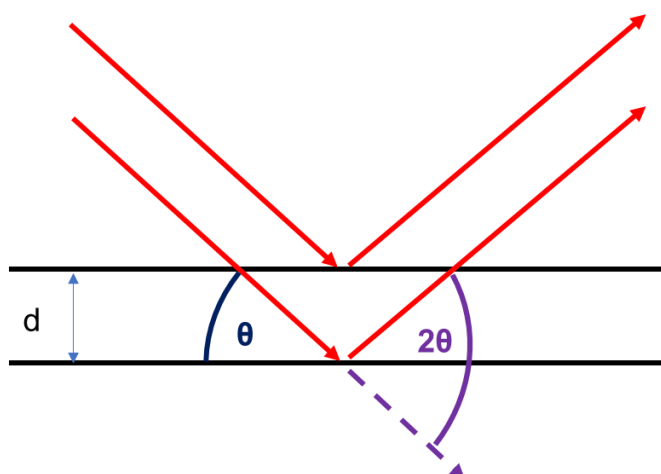


**Figure 2.3: Diffraction of X-rays by a crystalline lattice at angle  $\theta$**

XRD works on the elastic scattering of the X-rays by the crystal lattice. When the X-ray enters the lattice at an angle of  $\theta$  it is diffracted (**Figure 2.3**), however the waves that are diffracted must be in phase with each other to produce constructive interference, which enhance the amplitude of the diffracted beam so that it is detectable<sup>7, 8</sup>. It is the small wavelength of X-rays that allows them to be diffracted by the crystal lattice and hence be used to determine the crystal structure of a material<sup>7</sup>. The diffracted peaks that are detected are often referred to as reflections<sup>8</sup>.

The angle at which X-rays, of a monochromatic wavelength, are diffracted can give information of the distance between the lattice plane known as the

d-spacing. This relationship is summarised in the Bragg equation (Figure 2.4)<sup>7</sup>.

$$n\lambda = 2d\sin\theta$$

**Figure 2.4:**The Bragg equation where  $n$  is the order of refraction and  $\lambda$  is the wavelength of the X-rays,  $d$  is the lattice spacing and  $\theta$  is the diffracted angle.

The angle of diffraction, is characteristic of the lattice plane (with miller indices of (h k l)) which it is diffracted from and as a result of this each crystal phase will produce a set of diffractions from various planes different angles, which produces a pattern that can be used to identify the phase and structure of that material<sup>7-9</sup>.

The X-rays that are used for diffraction are generated through collision of high-speed electrons with a metal surface such as Cu or Mo. The collision of electrons with a target metal results in the ejection of an electron from a core orbital which creates an electron hole. This hole is filled by another electron moving down from a higher orbital, with the excess energy of that electron being emitted in the form of X-rays of a characteristic wavelength/energy<sup>7, 8</sup>. This method of generating X-rays is also used for the X-ray photoelectron spectroscopy (Section 2.3.2). The wavelength of the generated X-rays, varies with different targets and Cu  $K_{\alpha}$  (used to generate XRD in this thesis) has a wavelength ( $\lambda$ ) of 0.154 nm. The  $K_{\alpha}$  refers to the fact that electrons come from the k shell.

X-ray diffractometers are usually set up as shown in **Figure 2.5**. The sample is placed in a holder so that the top is as flat as possible. The X-ray source and detector rotate around the sample on the X-Y axis relative to the sample in order to measure X-ray counts at different values of  $\theta$ , while the sample itself is rotated horizontally to reduce errors that might be caused such as diffractions that could be caused by misaligned crystals, which are averaged out by the rotation.

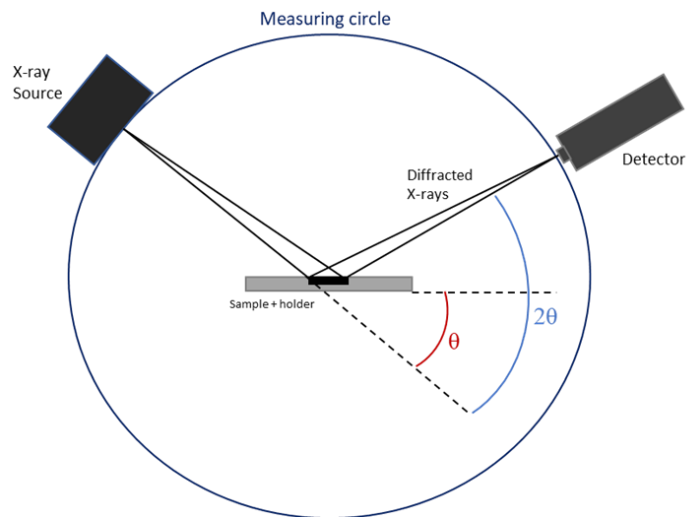


**Figure 2.5: The set up used to detected the diffracted X-rays at different angles<sup>8</sup>**

Both the peak shape and the peak's full width at half maximum give information on the material such as the extent of crystallinity but also the size of the particles, since a perfect crystal would have long range order and therefore would give an intense, sharp reflections. With smaller crystals these reflections reduce in size due to destructive interference and scattering caused by the large number of smaller crystallites<sup>9</sup>. The relationship between the crystallite size and the size/ intensity of the reflection peak is summarised in the Scherrer equation (**Figure 2.6**).

$$D = \frac{k\lambda}{\beta \cos\theta}$$

**Figure 2.6: The Scherrer equation**

Where  $D$  is the average (mean) crystallite size for that particular plane,  $k$  is a constant usually 0.9 to 1 (0.9 was used in this work),  $\theta$  is angle of diffraction and  $\beta$  is the broadening of the peak.

Both standard and *in situ* XRD were performed on a PANalytical X'pert Pro using a Cu  $K_{\alpha}$  source with a voltage setting of 40 kV and current setting of 40 mA.

The samples were either placed in an Al sample holder or loaded onto a non-reflective Si wafer depending on the sample volume available for analysis. The scans were taken from a  $2\theta$  angle of  $5^\circ$  to  $80^\circ$  at a scan rate of  $2^\circ \text{ min}^{-1}$ .

For the *in situ* experiment of crednerite, the sample (200 mg) was mounted on using an Anton Parr XRK 900 cell with air flowing through the sample at a rate of  $10 \text{ ml min}^{-1}$ . The first XRD was taken at  $50^\circ \text{C}$  and then the sample was heated to  $200^\circ \text{C}$ - $600^\circ \text{C}$  with an XRD scan being performed at each  $100^\circ \text{C}$  interval.

PANalytical Highscore was used to match the XRD data to the crystal group and identify the sample phase using the International centre for diffraction data (ICDD) database. The crystallite size using the Scherrer equation was also determined using PANalytical High score software.

### 2.3.2 X-ray photoelectron spectroscopy

X-ray photoelectron spectroscopy (XPS) is the analysis of electrons that are ejected from an atom using X-rays of sufficient energy to eject the electrons from a core orbital of an atom, which is known as the photoelectric effect. The energy required to eject the electron from the orbital is known as the binding energy (B.E. or  $E_b$ ) and is expressed in the equation below (Figure 2.7)

$$E_{B.E} = h\nu - E_{K.E} - \phi$$

**Figure 2.7:** The relationship between the binding energy and the energy required to eject the electron from an orbital<sup>9,10</sup>

$E_{K.E}$  is the kinetic energy of the ejected electron,  $h\nu$  is the energy of the photon used to eject the electron and  $\phi$  is the work function and is the energy required to eject the electron into a vacuum<sup>10</sup>.

The binding energy of the electron is determined by the energy of the atom in its initial (with full electrons) and final state (-1 electron) also referred as  $E_i$  and  $E_f$  in **Figure 2.8**. The energy of the final state is determined by how well electron cloud stabilised the positive hole left by the ejected electron<sup>9</sup>.

$$E_{K.E} = h\nu - (E_F - E_I) - \phi$$

**Figure 2.8: The relationship between kinetic energy of an ejected electron with the initial and final energy of the atom which it was ejected from**

The energy of the final state of an atom is determined not just by the element or oxidation state but also by its environment and its surrounding components (e.g. OH or O). This is one of the advantageous aspects of XPS since it aids identification of not only the oxidation state of a species but its environment and therefore could be used to determine possible active sites<sup>10</sup>. It can also give indication into the structure of the surrounding environment, for example a Cu<sup>+</sup> that is in an octahedral structure will have a different binding energy to one in a tetrahedral structure<sup>11</sup>.

Due to the high probability of electron collision in the bulk, the distance or mean free path, that the electrons can travel is very low and therefore only electrons close to the surface can be observed on XPS, which allows the use of the technique for surface analysis which is helpful in characterising heterogeneous catalysts<sup>7,9</sup>.

The X-rays in XPS are generated in a similar manner to how they are generated with XRD (as described in Section 2.2.1); high energy electrons are bombarded against a metal target that produces X-rays of a characteristic energy. For XPS used in this thesis an Al target is used which produce X-rays with an energy of 1486.6 eV<sup>12</sup>.

The pattern of binding energies that an element/oxidation state produces is dependent on both the orbital and the spin of the electrons that are ejected. Electrons of different spins in the same orbital will have different binding energies due to spin orbit coupling and momentum  $J=L+S$  where  $J$  is total momentum,  $S$  is the spin  $\pm\frac{1}{2}$  and  $L$  is the orbital momentum<sup>7,9,13</sup>.

This results in XPS producing two peaks with electrons ejected from either a p, d and f orbitals but not an s orbital since that only has two electrons<sup>9,14</sup>. For example Cu (0) will give two p-orbital peaks at for the p<sub>3/2</sub> at B.E.=932.6 eV and p<sub>1/2</sub> at 951.9 eV<sup>14</sup>.

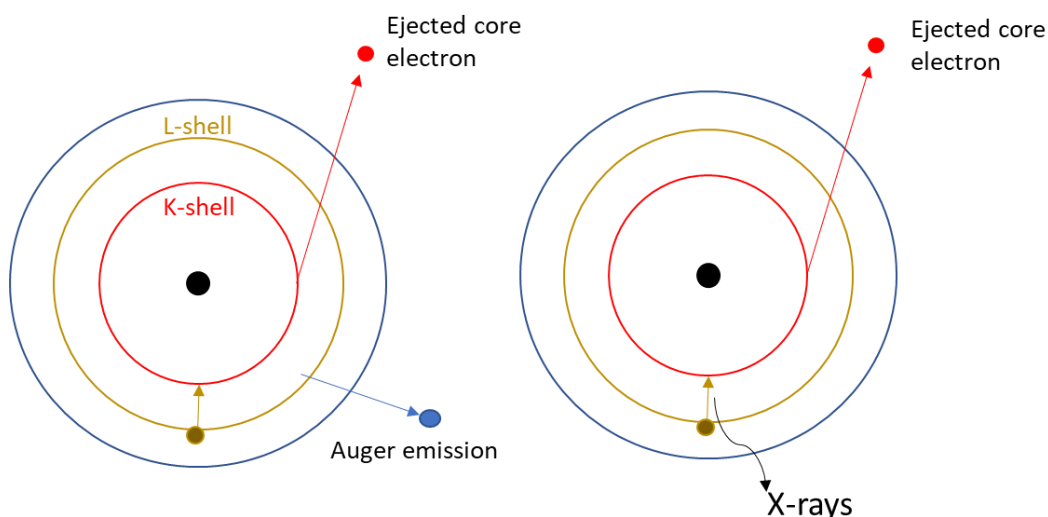


**Figure 2.9: The result of an electron hole being created a) Auger emission and b) X-ray fluorescence. A similar process can also occur in electron microscopy<sup>15</sup>**

When an electron is knocked out of a core orbital two other process can occur: 1) An electron from higher (valance) orbital moves down to a lower orbital and gives out electromagnetic radiation a process is known as X-ray fluorescence (**Figure 2.9 b**).

2) An electron from a higher orbital is moved down to fill the hole, and transfers its energy to another electron which is then also ejected, a process known as Auger spectroscopy (**Figure 2.9 a**)<sup>12</sup>. Although Auger electrons have a different energy range they can appear in the main XPS spectra. Using two X-ray sources can identify these peaks<sup>9</sup>

Another factor that can occur which would show up in final XPS spectra is shakeup which occurs due to the photoelectron giving energy to another electron resulting in an additional peak at a higher binding energy<sup>9, 12</sup>. These additional peaks can appear in the spectra of several elements, depending on the oxidation state such as  $\text{Cu}^{2+}$ ,  $\text{Mn}^{2+}$  and  $\text{Fe}^{3+}$ . This can be used as an aid in identifying element, oxidation and surrounding species<sup>14, 16</sup>.

The XPS experiments was performed by Dr David Morgan on a Thermo Fischer Scientific K-alpha<sup>+</sup> spectrometer. Samples were analysed using an Al X-ray source (72 W) over an elliptical area of 400x800  $\mu\text{m}$ . The samples were charged neutralised using argon ions and electrons. For survey scans

the data was recorded with energy passes of 150 eV with a 1 eV step and for high resolution scans a pass of 40 eV (1 eV step). Data analysis was carried out using the CasaXPS program.

Published material and online references were used as a guide for the assignment of the peaks to the appropriate elemental state<sup>14,16</sup> The peak were fitted to best represent the spectra that was produced. This was done using the Casa XPS program.

### 2.3.3 Electron microscopy

Electron microscopy is the use of electrons to visualise objects, usually in the  $\mu\text{m}$ -nm range and is a widely used technique in many fields of science<sup>7</sup>. Using electrons rather than light has several advantages. Firstly electrons can be diffracted, like electromagnetic radiation (De Broglie relationship) but have a wavelength of less than 0.1 nm which can produce images with greater resolution and higher quality than could be achieved with an optical microscope giving details about the surface of the object that may give important information<sup>7, 15</sup>.

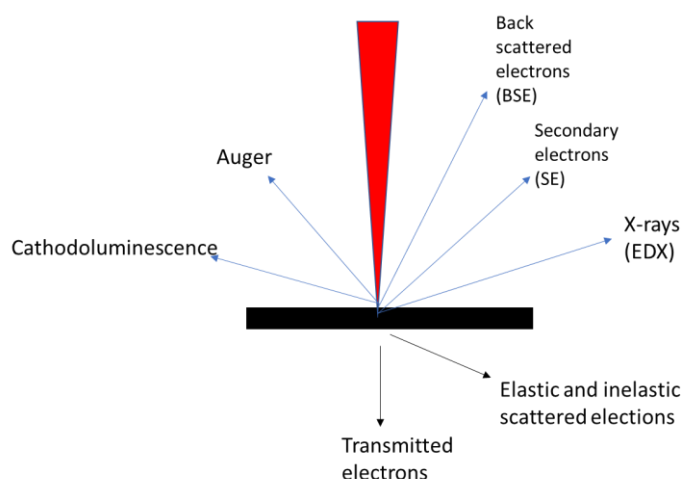


**Figure 2.10: The different processes that can occur when a focused electron beam is used to probe a surface<sup>17</sup>**

Secondly when an electron beam hits a sample, there are several processes that can occur such as transmission, Auger and energy dispersive X-rays, each giving different information and insight into the nature of the sample being analysed<sup>9</sup>. There are many types of electron microscopy techniques

the such as scanning electron microscopy (SEM)<sup>18</sup>, transmission electron microscopy (TEM) and scanning transmission electron microscopy (STEM).

### **2.3.3.1 Scanning electron microscopy**

Scanning electron microscopy is the use of an electron beam to probe the surface of the material and produce an image of the surface. The electrons can be generated through different methods such as using a heated tungsten filament, emitting electrons through thermionic emission or using a high electric field to remove electrons known as a field emission gun (FEG)<sup>15, 18</sup> which is used on the Tescam Mira3 SEM that produced the images in this thesis. The emitted electrons are then passed through a series of scan coils, objective lens and apertures to refine this to a small beam over a square area with a x and y direction known as a raster.<sup>7, 18</sup>

The depth at which the electrons penetrate the sample is dependent on the accelerating voltage used. Typically, this would be around 5 kV to 30 kV with higher voltages penetrating further into the sample. When the electron beam is focused on a small area there are several events that can occur; back scattered electrons, secondary electrons and X-ray fluorescence from the sample (see section 2.3.2<sup>7, 17</sup>).

Secondary electrons are due to the energy interaction from the electron beam to the atoms of the sample giving enough energy to eject an electron. In the bulk, the ejected electron rapidly loses energy and therefore does not travel far but if the electron is near the surface it can escape (into vacuum) and can be detected<sup>18</sup>. As a result, secondary electrons detection gives an image of the surface of the material.

Back scattered electrons originated from scattering of the electrons from the electron beam throughout the sample and subsequently escape into the vacuum<sup>15</sup>. The scattering of the electrons is affect by the size of the atom, with heavy atom scattering more electrons than lighter atoms one and giving a brighter image<sup>18</sup>. This therefore mean this technique could be used to differentiate between different element although this does not work well with element of similar mass (e.g. Cu/Zn or Mn/Fe).

### **2.3.3.2 Energy dispersive X-ray spectroscopy**

Energy dispersive X-ray spectroscopy (EDX) is a method of using the electron beam to gather information about the elements present in the sample. This technique can be used for mapping elements across an area that is being analysed and is useful in determining elemental mixing and assigning morphologies and features to a particular element.

The X-rays are created from the samples in a similar manner to what was seen with XRD and XPS. When the electron beam collides with an element it can give some of its energy to one of the electrons in the atom, which subsequently gets ejected and creates a hole. This hole is then filled by an electron from a higher orbital moving down and, in the process, emits X-rays. The energy of these X-rays is based on the orbitals that the electron moved from. Because different elements have electron configurations and orbital energies, the energy of the emitted X-rays is going to vary and therefore each element produces a “finger print” which can be used to identify and quantify elements present as well as map out the location and distribution of elements onto an SEM image of the sample<sup>9</sup>.

### **2.3.3.3 SEM and EDX method**

All SEM were performed on Tescam Mira3 (FEG-SEM) with the electrons being generated by a tungsten tip, field emission gun. Imaging was done using in-beam secondary electron detector and an electron beam with an accelerating voltage of 5-15 kV (depending on the sample). View fields, working distance, electron detection type and accelerating voltage are specified in the images.

The copper-manganese sample in Chapters 4 and 5 and the copper-zinc oxide samples in Chapter 6 were suspended on a carbon film and were

coated with a 10 nm AuPd coating to reduce charging effects that occur due to electrostatic build up from the beam which can interfere with the imaging<sup>18</sup>.

The oxalate needles in Chapter 3 were loaded onto a 3.05 mm 300 mesh Cu grids with a holey carbon film and placed on a STEM sample holder.

EDX analysis was performed with using an Oxford-instrument X-Max<sup>N</sup> 80 which was fitted to the Tescam Mira3 and was inserted during EDX analysis but retracted for SEM analysis. All EDX data were recorded, analysed and reported using the Oxford AZtec program.

SEM images that were performed by Dr Thomas Davies are specified in the caption below the figure.

#### **2.3.4 Thermal gravimetric analysis and differential scanning calorimetry**

Thermal gravimetric analysis (TGA) is simply a technique for measuring the change in weight of a sample over a temperature range at a selected heating rate and atmosphere. This can be used to determine the temperature range in which a precursor either breaks down, combusts or oxidises depending on the sample and atmosphere used. This is useful in seeing how the catalyst precursor degrades under different conditions. The degradation of a catalyst precursor can give important information on how the final catalyst forms. This includes how the thermal degradation affects the catalytic activity of the final oxide, insight into the precursor structure, when a metal oxide changes its oxidation state and indication of phase formation<sup>8,19</sup>.

Differential scanning calorimetry (DSC) is the measurement of the difference in heating between the sample and a reference sample and keeping the heating rate consistent by increasing or decreasing the power to the sample. This can be used to determine whether reaction is exothermic or endothermic and can give an indication as to whether a mass loss at a certain temperature range is a single or multiple decomposition as well as giving some indication into the nature of the precursor<sup>8</sup>.

Two pieces of equipment were used for TGA and TGA/DSC. The majority of the TGA analysis was performed on a Perkin Elmer TGA 4000 equipped with an auto sampler. The crucibles were weighed in the machine prior to the addition of the sample (5-10 mg). The standard TGA programme used during this work, unless otherwise stated, consisted of an initial 2 minutes hold at 30 °C to allow stabilisation before proceeding from 30 °C to 900 °C at a heating rate of 5 °C min<sup>-1</sup> under a flowing air system of 30 ml min<sup>-1</sup>.

DSC/TGA runs were performed on a Setaram TGA/DTA. The sample (5-10 mg) was placed in a pre-weighed crucible and heated from 30 to 800 °C at a heating rate of 1 °C min<sup>-1</sup>, under an air flow of 30 ml min<sup>-1</sup>.

### **2.3.5 Temperature programmed reduction**

Temperature programmed reduction (TPR) is a technique used to measure the temperature a catalyst would reduce to a metallic state or lower oxidation state under a reducing atmosphere such as 10% H<sub>2</sub>/Ar or CO/He<sup>9, 20</sup>. When the catalyst reaches a certain temperature, under the reducing atmosphere it will reduce to a lower oxidation state and oxidise the gas (H<sub>2</sub> to H<sub>2</sub>O or CO to CO<sub>2</sub>), which would produce a signal on a thermal conductivity detector (TCD) due to the change in atmosphere (see Section 2.4.1.4).

As well as determining temperature of reduction, TPR can also give information on other factors such as crystallite size or give information on mixed oxides systems. For example, with copper manganese oxides if the copper and manganese are well integrated into a spinel AB<sub>2</sub>O<sub>4</sub> structure, the manganese would facilitate the reduction of the copper and resulting in a change in the reduction temperature with the Cu<sup>2+</sup> to Cu<sup>0</sup> and Mn<sup>3+</sup> to Mn<sup>2+</sup> reduction peak partly merged. In comparison a phase separated material comprising of CuO and Mn<sub>2</sub>O<sub>3</sub> would produce two separate peaks at higher temperatures<sup>21</sup>. This would give an indication of the extent of interaction between the metals but other techniques such as XPS would be needed to reinforce this observation.

Temperature programmed reduction was performed on a Quantachrome ChemBET Pulsar instrument. 0.05 g of the sample was placed in a glass

tube held in place by quartz wool. The sample was pre-treated to 110 °C under helium and held at 110 °C for 30 minutes to remove any surface species. Temperature programmed reduction under a 10% H<sub>2</sub>/Ar atmosphere from 30 to 800 °C at a heating rate of 10 °C min<sup>-1</sup>.

### 2.3.6 Surface area analysis

The performance of a catalyst in many catalytic processes is related to the surface area of the catalyst and/or support. The surface area of a catalyst can be defined by two parameters; the first is total surface area of the whole material and the second is specific surface area of the active component. Total surface area can be determined through physisorption techniques while specific surface area can be worked out through chemisorption techniques using gases such as N<sub>2</sub>O or CO.

#### 2.3.6.1 Total surface area

Total surface area is measured using physical adsorption of an inert gas, such as N<sub>2</sub>, onto the surface of the material. By measuring the adsorbent gas volume and pressure as making the assumption that the adsorbent occurs mostly as a monolayer and cover the entire surface, then the surface area of the material can be calculated. Adsorption experiments were carried out at 77 K, to allow the nitrogen to condense on the surface. However multilayers, of adsorbent can form on the surface of the material.

The Brunauer-Emmett-Teller (BET) equation in, **Figure 2.11**, can be used to calculate the surface area from physisorption on a surface<sup>22, 23</sup>.

$$\frac{P}{v(P_0 - P)} = \frac{1}{v_m C} + \frac{C - 1}{v_m C} \cdot \frac{P}{P_0}$$

**Figure 2.11: The Brunauer Emmett Teller equation**

Where  $P_0$  is saturated pressure,  $P$  is the equilibrium pressure and  $v_m$  is the monolayer capacity.  $C$  is the measurement of how well defined the isotherm is and is derived from the equation in **Figure 2.12**.

$$C = e^{\frac{H_{ad}-H_l}{RT}}$$

**Figure 2.12: The relationship between the C constant in the BET equation and the enthalpy of adsorption of the monolayer**

Where  $H_{ad}$  is the enthalpy of the adsorbed monolayer on the surface of the material and  $H_l$  is the enthalpy given out by the formation of the additional layers of gas molecules on top of the surface adsorbents. When the enthalpy of forming the additional physisorbed layers  $H_l$  is high, the C value is low which means that it is more favourable to form multiple layers of adsorbent which means that the accuracy of the determined surface based on a monolayer is lower<sup>22</sup>. If  $H_{ad} > H_l$  and therefore C is high then the formation of a monolayer adsorbent is more likely to occur than a multilayer<sup>22</sup>.

The 5-point surface area analysis of the samples were performed on a Micromeritics Gemini 2360. 100 mg of the sample was put into a 9.6 mm x 155 mm tube and degassed under nitrogen on a Flow-Prep 060 at 110 °C for 1 hour for metal oxides and 60 °C for 16 hours for precursor materials. The lower temperature for the metal precursors was to ensure that these materials did not degrade prematurely during the degassing stage.

The samples and tubes were reweighed after degassing. The sample was then fitted to the instrument (Micromeritics Gemini 2360) that was fitted with a second, empty tube (9.6 mm x 155 mm) as a reference.

### 2.3.6.2 N<sub>2</sub>O Cu surface area analysis

One method of determining the specific surface area of metallic copper on a material surface is through chemisorption of N<sub>2</sub>O. The basic principle is relatively simple: N<sub>2</sub>O reacts with Cu(0) to form CuO and N<sub>2</sub><sup>24</sup> on the surface of the Cu(0) particle (**Figure 2.13**).

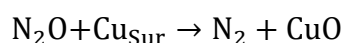


**Figure 2.13: N<sub>2</sub>O titration on a Cu(0) surface**

One advantage of using  $\text{N}_2\text{O}$  is that below  $100\text{ }^\circ\text{C}$   $\text{N}_2\text{O}$  only rapidly reacts with the surface copper and not the bulk<sup>25</sup>, therefore any  $\text{N}_2$  that formed would only be as a result of the reaction of  $\text{N}_2\text{O}$  with the surface copper. Another advantage is that the ratio should be 1:2  $\text{N}_2\text{O}$ :  $\text{Cu}_{\text{sur}}$ <sup>24</sup>. Using this, if the amount of  $\text{N}_2\text{O}$  converted to  $\text{N}_2$  is calculated based on the  $\text{N}_2$  detected against the theoretical value of  $\text{N}_2$  for total conversion and a fixed volume was injected over a known mass/Cu loaded catalysts then the surface area of Cu can be determined<sup>24, 25</sup>.

50-75 mg of the calcined CuO/ZnO was placed into a U-shaped glass tube and suspended by quartz wool. The sample was reduced at  $260\text{ }^\circ\text{C}$  under a 10%  $\text{H}_2/\text{Ar}$  mixture at a heating rate of  $10\text{ }^\circ\text{C min}^{-1}$  to  $140\text{ }^\circ\text{C}$  then  $2\text{ }^\circ\text{C min}^{-1}$  to  $250\text{ }^\circ\text{C}$  (to reduce any potential sintering) and left for 20 minutes. The gas flow was changed to helium and the sample was then cooled down to room temperature. The sample was then reweighed, to determine the mass loss during reduction.

The sample was then placed back into the instrument and heated to  $65\text{ }^\circ\text{C}$  under helium flow.  $\text{N}_2\text{O}$  (1 bar) was filled into a sample loop of  $113\text{ }\mu\text{L}$  which was injected at 5 minutes intervals onto the Cu/ZnO catalyst for a total of 12 times followed by 4 injections with nitrogen which were used as reference peaks. The gas was passed through a  $5\text{ \AA}$  molsieve to remove any unreacted  $\text{N}_2\text{O}$  and other impurities so that only  $\text{N}_2$  from the reduction of surface  $\text{Cu}^{2+}$  to Cu is detected.

### 2.3.7 Infra-red spectroscopy

Infra-red (IR) spectroscopy is the use of electromagnetic radiation with a wavelength between  $100000\text{ nm}$  and  $700\text{ nm}$ , which correlates to  $100\text{-}14000\text{ cm}^{-1}$  to induce a vibrational mode for a diatomic bond with a dipole moment.

When the bond is exposure to IR light, the molecule is excited to a higher vibrational state and act as a harmonic oscillator which become more anharmonic at higher vibrational energy levels. Because a harmonic oscillator is dependent on the mass and the force constant (**Figure 2.14**), the

frequency of the vibration is related to the force constant i.e. the strength of the bond<sup>13</sup>.

$$\nu = \frac{1}{2\pi} \sqrt{\frac{k}{\mu}}$$

**Figure 2.14: Relationship between the frequency of oscillation and force constant, where  $\nu$ =frequency of oscillation  $\mu$ = reduced mass and  $k$ = force constant<sup>13</sup>**

When the IR radiation is at the frequency of oscillation, it will be absorbed at that wavelength, with the rest of the spectrum being transmitted through the sample to the detector. The data can be plotted in frequency against either transmittance (the % of light passed through) or absorbance (the % of light that is absorbed by the molecule during vibration)<sup>26</sup>.

Most modern spectrometers instead of measuring the absorbance/transmittance of each wavelength individually, the machine uses an interferometer, a device that uses moving mirrors and beam slitters to create a series of interference patterns known as an interferogram<sup>13, 27</sup>. After the beam has passed through the sample, the resulting interferograms are translated from a time-based domain to a frequency domain using a mathematical function known as a Fourier transformation (FT) which produces an IR spectrum<sup>13, 27</sup>. This method has the advantage of fast measurements and production of spectra compared to measuring different wavelengths using a monochromator.

Attenuated total reflectance or ATR is a method of IR detection where the entire IR beam is totally internally reflected off a crystal due to the angle of the beam being less than the critical angle  $\theta_c$ <sup>13, 28</sup>. However, due to constructive interference between the incoming and outgoing waves, the amplitude of the wave appears above the crystal surface, which is referred to as an evanescent wave<sup>28</sup>. It is the evanescent wave that interacts with the sample on top of the ATR crystal, but this affects the IR beam and as such the vibrational change is detected<sup>28</sup>.

The Infra-red spectra were recorded on a Bruker Vertex 70 equipped with an ATR cell and two detectors: 1) mercury cadmium telluride (MCT) and 2) deuterated triglycine sulphate (DTGS). For the measurement of metal oxide

and metal oxide precursors the DTGS detector was used since this type of detector was better at reading in the lower wavenumber range  $1000\text{-}400\text{ cm}^{-1}$  than the MCT<sup>28</sup> where metal oxygen vibration for materials such as  $\text{Co}_3\text{O}_4$  and  $\text{Mn}_3\text{O}_4$  is more likely to occur<sup>29</sup>.

A background of 16 scans was recorded prior to the sample scan (which comprised of 32 scans). The sample was then placed on the ATR cell and pressed onto the crystal. The sample was then exposed to the IR beam for 32 scans on an aperture setting of  $6\text{ cm}^{-1}$ .

Most experiments (apart from some in Chapter 6) were performed in transmittance mode using the DTGS detector and an aperture size of  $6\text{ cm}^{-1}$ . The DES precipitated Cu/ZnO precursor in Chapter 6 used absorbance mode ( $6\text{ cm}^{-1}$  aperture) with the MCT detector.

### **2.3.8 Microwave plasma atomic emission spectroscopy**

Microwave plasma atomic emission spectroscopy (MP-AES) is a technique used to analysis the concentration of metals in a solution.

When an atom is exposed to energy such as heat, electromagnetic radiation or collision, an electron can be promoted from its ground state orbital to a higher, excited state orbital. However, this configuration is unstable and the electron returns to the ground state orbital by emitting the excess energy in the form of electromagnetic radiation. An atom can have electrons that are excited to different energy levels and therefore give different wavelengths as they relax to the ground state but each of these wavelengths is characteristic (and consistent) of the difference in energy between the excited state orbital and the ground state orbital<sup>27</sup>. Because each element has a different electron configuration, the wavelengths will also differ between elements, hence the technique can be used to identify an element, although there are many elements that may emit radiation at similar wavelengths.

In addition the probability of an electron to occupy a certain orbital and emit a characteristic wavelength is consistent therefore the proportion of atoms emitting a certain wavelength gives an intensity that correlates to the

concentration of those atoms<sup>30</sup>. This gives a method of working out the concentration of different elements in a sample if a calibration plot of the concentration against intensity of the wavelength for those elements had been performed. This is technique known as atomic emission spectroscopy (AES)<sup>30</sup>.

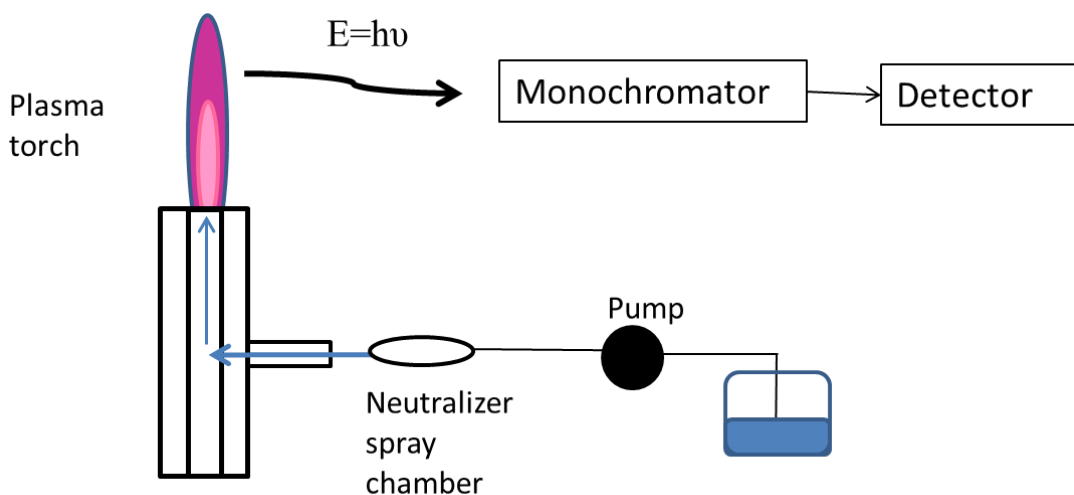


**Figure 2.15: An electron that has been excited returning to the ground state and emitting an electromagnetic wave which is the detected by a spectrometer**

In order to excite the elements to a higher energy and to atomise the molecule into single atoms, very high temperatures are required. This is achieved using a microwave induced plasma of nitrogen which can reach temperature of 6000-10000 °C, enough to atomise the molecules<sup>31</sup>.

The sample is pumped into a neutralizer spray chamber that converts the dissolved sample into an aerosol that is then injected into the plasma torch that atomises and excites the atoms to produce the wavelength (as shown in **Figure 2.15**)<sup>31</sup>. The light is then passed through a monochromator, to isolate the desired wavelength from the rest of the spectrum that would be produced from other elements or the plasma. The light (of the desired wavelength) is then passed through a series of lenses before being detected by a spectrometer<sup>30</sup>.

**Table 2.4: Wavelength used for MP-AES for each of the metals**

Metal	Wavelength 1/nm	Wavelength 2/nm
Cobalt	340.512	347.404
Manganese	279.482	403.076
Iron	302.064	371.993
Zinc	213.857	481.053
Copper	324.754	327.395

For MP-AES analysis 50-75 mg of the sample was dissolved in 10 % (volume) aqua regia(1:3 HCl: HNO<sub>3</sub>) (mixture was 1:6 of 36% HCl/water:70% HNO<sub>3</sub>/water) in water solution and left overnight to digest. The solution was then diluted so that the total concentration of metals in the mixture was approximately 10-30 ppm. Reference solutions of the metal from 1000 ppm stock solutions (dissolved in HNO<sub>3</sub>/water) were made to concentrations of 5 ppm, 10 ppm 20 ppm and 30 ppm in order to calibrate the MP-AES before analysing the solution. Each metal concentration was analysed using two wavelengths so that an average concentration could be determined. The wavelength chosen are shown in **Table 2.4**.

## **2.4 Catalysts testing**

### **2.4.1 Gas chromatography**

For all catalyst testing experiments, the products were measured by online gas chromatography (GC). Gas chromatography is the separation of gas or liquid mixtures using a column (stationary phase) with a gas (e.g. helium) as the mobile phase<sup>32</sup>. The Gas Chromatographs used in this work were an Agilent 7890b equipped with an FID and TCD for propane oxidation and methanol synthesis and an Agilent 490 Micro GC for CO oxidation.

### **2.4.1.1 Columns**

Columns are an essential part of any chromatograph technique. The column is the part that separates the gas mixture based on the retention time of the components (i.e. how well a molecule interacts or sticks to the column). This interaction comes in many forms depending on what is being separated, for example a molecular sieves column separates analytes based on their size (since molecular sieves have a well-defined pore structure)<sup>33</sup>. Columns are usually placed in an oven with either constant or varying temperature to help separate the components.

In GC columns are divided into two types, packed or capillary. The packed columns have a larger internal diameter of 2-4 mm and are typically shorter, usually 2-3 m<sup>33</sup> and are packed with the stationary phase supported in a porous material<sup>32</sup>. The second type are capillary columns, also known as open tubular, are thinner than pack columns and have an internal diameter of <1mm and have the stationary phase coated on the inside<sup>32</sup>.

### **2.4.1.2 Backflush**

The GC used for CO oxidation (Agilent 490) is equipped with a back flush. Back flushing is a process of removing unwanted products. The gas sample is initially separated on a pre-column, and the quickly eluting sample would then pass through a pressure point to the main column. After a selected time the system would reverse the flow before the pressure point, removing the unwanted products to vent. For the CO oxidation GC, backflush is used to prevent carbon dioxide and water from entering the molecular sieves column as these products can block this type of column, and the backflush also allows direct analysis of carbon monoxide concentration relative to oxygen and nitrogen peaks<sup>33</sup>.

### 2.4.1.3 Injection valves

For gas sampling using an online GC (not the Agilent 490 used in CO oxidation), the sample is injected using a sample loop. This is a relatively simple concept whereby the gas sample is flowed through a sample loop of a known, fixed volume as shown in **Figure 2.16 a**<sup>27</sup>. When the GC injects (**Figure 2.16 b**), the sample loop is switched so that the carrier gas flows through the loop and into the column<sup>32</sup>. This occurs for a few seconds before the valve is switched back for refilling. This is a very efficient method of injection of a sample to a column with <0.5% variation in the gas volume.

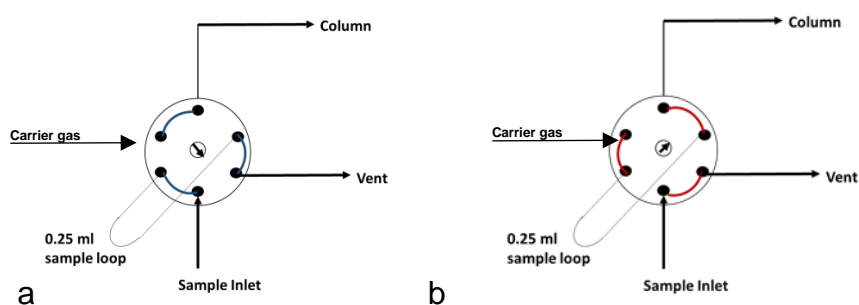


**Figure 2.16: GC sample loop in a) loading and b) inject**

### 2.4.1.4 GC detectors

There are a variety of detectors used to detect the end product, however the two most common used are flame ionisation detector (FID) and thermal conductivity detector (TCD)<sup>32</sup>. FID, commonly used for detecting organic compounds, essentially work by exposing the analyte to a hydrogen-air flame which pyrolyzes the molecule into ions and electrons. These ions/electrons then interact with an electrode which give a response. TCD consists of two heated coils, with one of the coils in exposed to the analyte gas and the other under the carrier gas as a reference.

The resistance of these coils is dependent on the atmosphere they are under. Hydrogen and helium have a higher thermal conductivity than other

gas so when the gas composition changes the thermal conductivity of the gas rapidly changes which changes resistance of the coil thereby creating a signal when an analyte comes off the column into the TCD<sup>32</sup>.

GC and the equipment (Chembet Pulsar) used for TPR and N<sub>2</sub>O decomposition utilise TCD for detection but these operate differently. The TPR measures the change in conductivity of a gas before and after it had passed over a catalyst bed while the TCD of a GC works by measuring the difference between the separated gas mixture and carrier gas reference<sup>9, 27, 32</sup>. The detectors do not explicitly tell what the analyte is, only that there is a gas component being separated at a specific time or temperature. The assignment of the peaks area based on calibrated runs with known sample compositions and concentrations.

#### 2.4.1.5 GC layout Diagrams

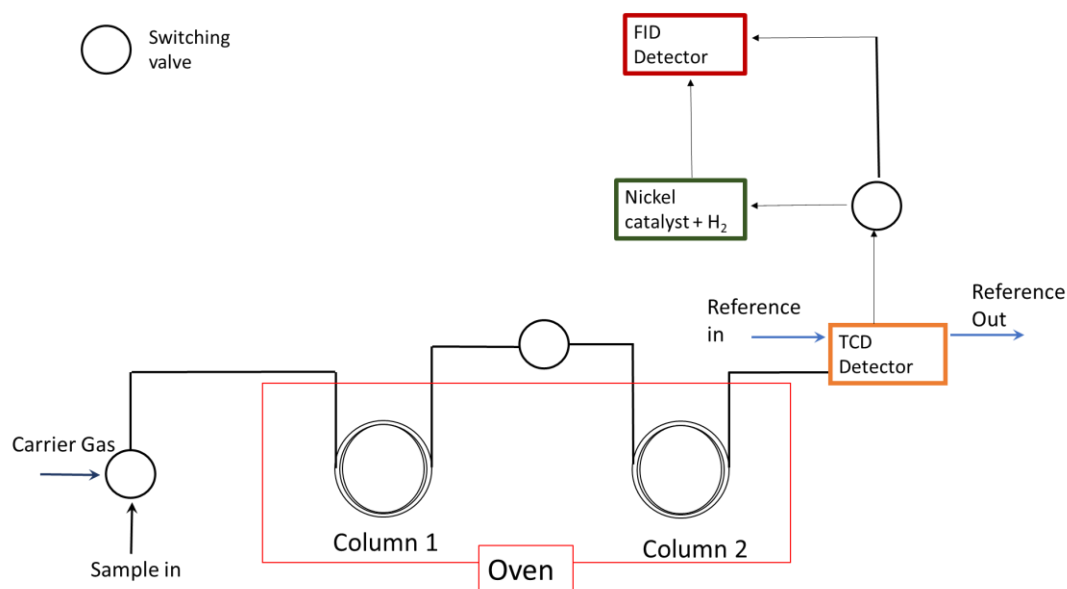


**Figure 2.17: Column and switching valve layout for the GC (Agilent 7890) used for propane oxidation**

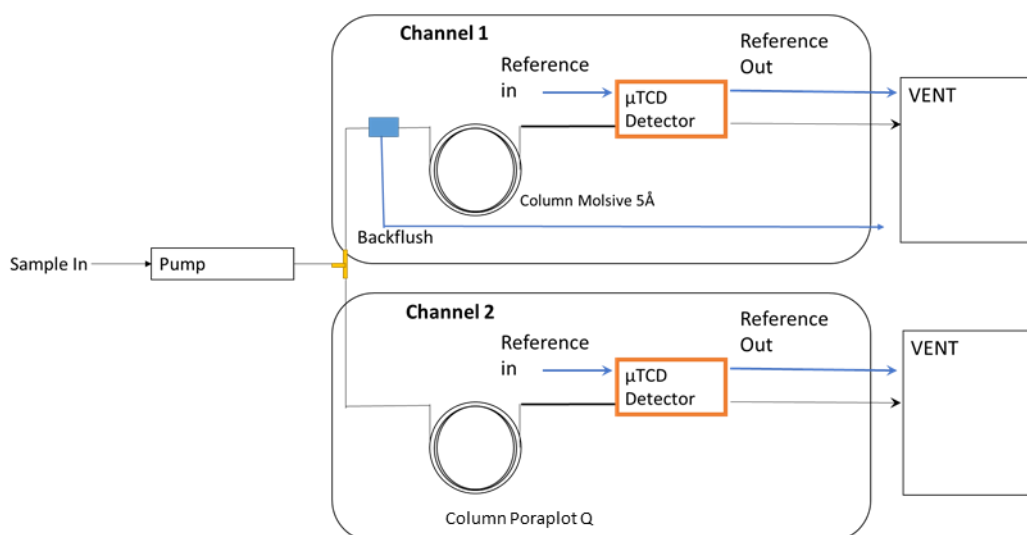


**Figure 2.18: Channel and column layout for the micro GC (Agilent 490) used for CO oxidation**

## 2.4.2 Carbon monoxide oxidation reaction

Carbon monoxide oxidation reaction was performed in a glass U-shape reactor (6 mm outer diameter, with a 4 mm inner diameter) placed in a programmable water bath (Thermo Versa cool) as shown in **Figure 2.19**.

50 mg of the catalyst was placed in the U-shaped glass reactor (6 mm overall diameter 4 mm inner diameter) and held in place by glass wool. The inlet of the glass reactor was connected the gas feed of 4850 ppm CO/air or N<sub>2</sub> which was controlled by mass flow controller set to a flow rate of 20 ml min<sup>-1</sup>, which gives a gas hourly space velocity (GHSV) of 19100 s<sup>-1</sup>. The outlet of the glass reactor was connected to a gas chromatogram that sampled and analysed the outgoing gas mixture.

Gas chromatography was performed on an Agilent Micro GC 490 fitted with two channels (**Figure 2.17**). Channel 1 is fitted with a 10 meter molsieve 5Å, heated to 120 °C with a heated injector (80 °C). Channel 2 is fitted with a 10 meter Poraplot Q heated to 80 °C. The pressure on both columns was maintained at 150kPa. The reaction gases on both columns were analysed by TCD.

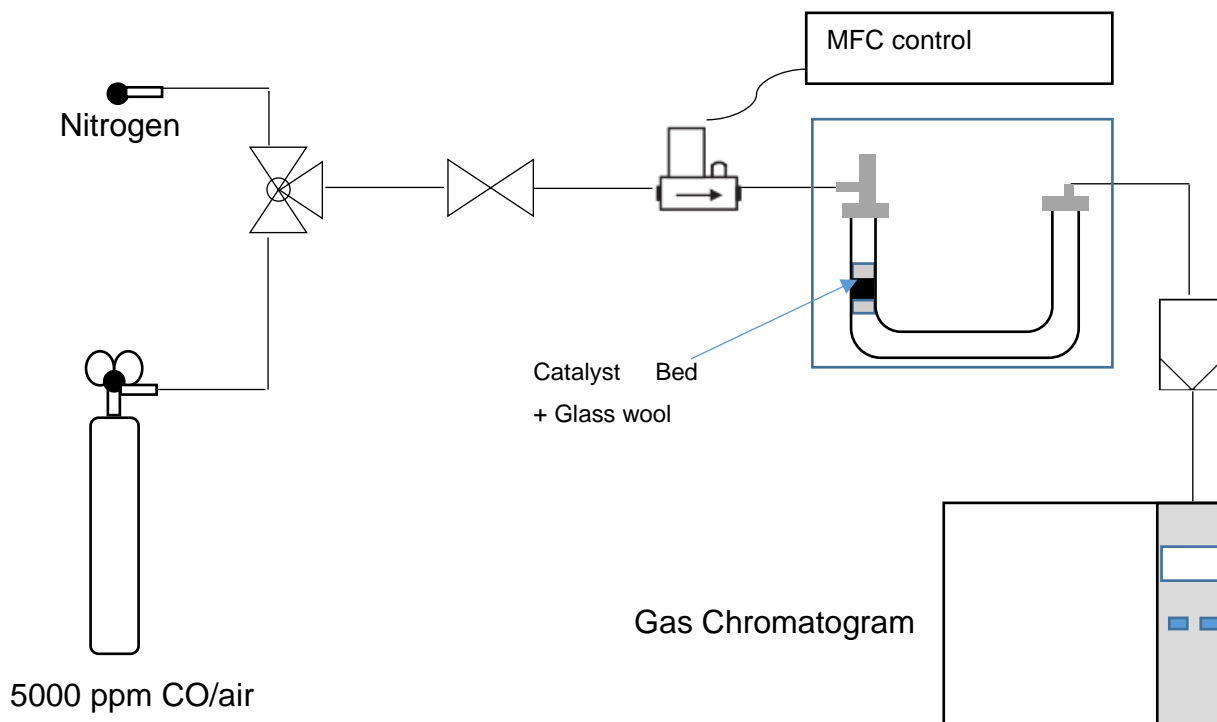


**Figure 2.19: Diagram of the reactor used for carbon monoxide oxidation symbols are defined in Table 2.6**

The GC reports both channels independently of each other to give two chromatograms. It should be noted here that this is different to how the propane oxidation GC (Agilent 7890 A) (Section 2.3.3) give its chromatogram in that the chromatogram gives two different separations whereas the propane oxidation gives two different methods of detection (FID and TCD) from the same product separation.

**Table 2.5: List of the retention time and peak heights for CO oxidation for no conversion (Channel 1) and maximum conversion (channel 2)**

Channel 1			Channel 2		
Retention time/ min	Gas	Peak maximum	Retention time/ min	Gas	Peak maximum
0.482	O <sub>2</sub>	19.757±0.05	0.373	N <sub>2</sub> /O <sub>2</sub>	98.856±0.05
0.546	N <sub>2</sub>	79.738±0.05	0.480	CO <sub>2</sub>	0.505±0.05
0.809	CO	0.465±0.05	0.935	CO/H <sub>2</sub> O	0.639±0.05

The CO maximum was worked out by performing a blank reaction with no catalyst. The CO peak at no conversion is  $0.465 \pm 0.02$  (based on variations observed during blank runs), which corresponds to the 4850 ppm of CO in the air mixture. On Channel 2 the CO<sub>2</sub> peak at maximum conversion was  $0.500 \pm 0.005$ .

$$\text{a) } CO \text{ conversion } \% = 100 - \frac{CO \text{ counts}}{CO \text{ counts for no conversion}} \times 100$$

$$\text{b) } CO \text{ conversion } \% = \frac{CO_2 \text{ Counts}}{CO_2 \text{ counts at total conversion}} \times 100$$

$$\text{c) } Conversion \text{ (mol m}^{-2}\text{s}^{-1}\text{)} = \frac{(\text{mols of CO per second}) \times (\% \text{ of CO Converted})}{(\text{surface area of catalyst}) \times (\text{catalyst mass})}$$

**Figure 2.20: The calculations used for work out CO conversion using a) CO peak in channel 1, b) CO<sub>2</sub> peak in channel 2 and c) the calculation used to determine surface area normalised conversion**

### 2.4.3 Propane oxidation

The propane oxidation was done under a 5000 ppm mixture of propane in synthetic air. The reaction was done on a reactor set up in **Figure 2.21** which was designed for both propane oxidation and oxidative dehydrogenation reactions.

The catalyst (50 mg-120 mg) was placed in a quartz tube (internal diameter 7 mm) and held in place with quartz wool to ensure a 10 mm long catalyst bed (unless otherwise stated) which gave a GHSV of  $6200 \text{ h}^{-1}$  at a flow rate of  $40 \text{ ml min}^{-1}$ . A thermocouple was inserted so that it was resting just above the catalyst bed. The reaction gas mixture was flowed through the bypass for the first hour before being flowed through the catalyst bed. The catalyst bed would then be heated from 200-400 °C (from 100 °C with cobalt based oxides) at 50 °C increment and held at each temperature increment for 1 hour (or for 45 minutes for iron oxide) to allow for stabilisation and averaging.

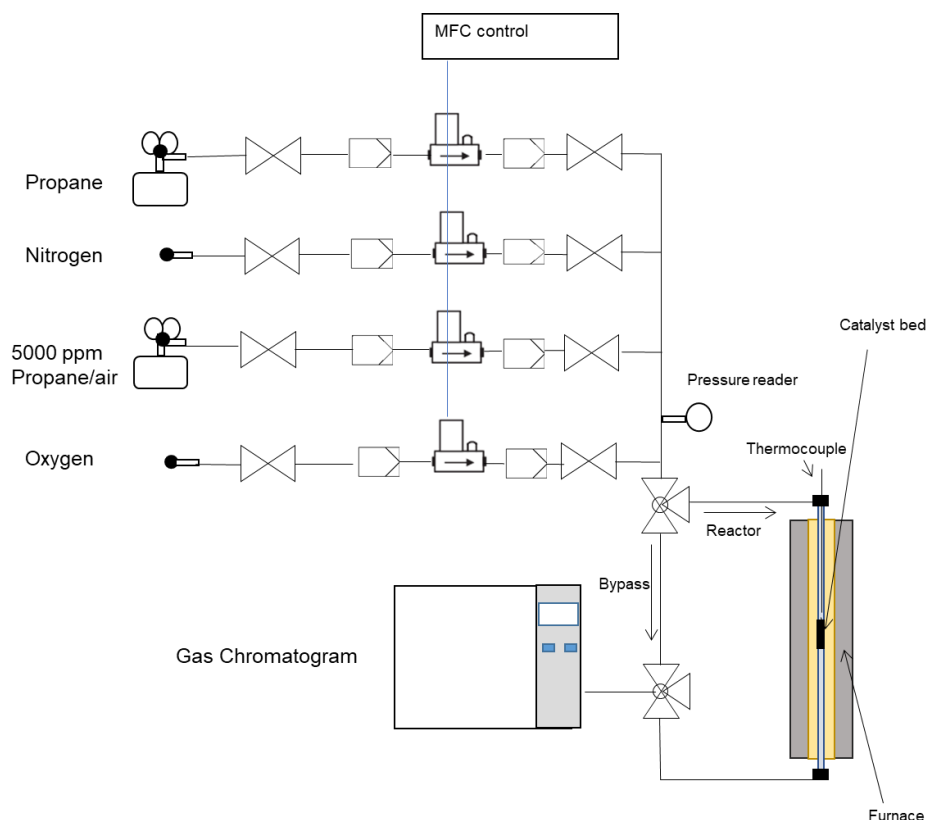


Figure 2.21: Schematic of the reactor used for propane oxidation

$$\begin{aligned}
 \text{a) } C_3H_8 \% &= \frac{C_3H_8 (ppm)}{C_3H_8 (ppm) \text{ for no conversion}} \times 100 \\
 \text{b) } CO_2 \text{ selectivity } \% &= \frac{CO_2 (ppm)}{C_3H_6 (ppm) + C_2H_4 (ppm) + CO_2 (ppm) + CO (ppm)} \\
 \text{c) } \text{Conversion } (mol g^{-1} s^{-1}) &= \frac{(\text{mols of propane per second}) \times (\% \text{ of propane converted})}{(\text{catalyst mass})}
 \end{aligned}$$

Figure 2.22: The calculation to work out a) propane conversion, b) CO<sub>2</sub> selectivity and c) mass normalised rate normalised activity

For deactivation studies on cobalt the reactor was heated to 250 °C and held for 16 hours with sampling every 15 minutes (GC run time). The products were analysed using an on line Agilent GC 7890A. The gases were separated with a Haysep Q and molsive 5Å columns and analysed with an FID and TCD. The GC was equipped with a methaniser, an nickle catalyst that converts CO and CO<sub>2</sub> to methane so that it can be detected by the the FID<sup>34, 35</sup>. Propane conversion, CO<sub>2</sub> selectivity (Figure 22 a and b) were worked out by converting the counts to concentration in ppm using the

response factor, a constant that is worked out from plotting known concentrations against GC counts.

Error in propane conversion was worked out by repeating a catalyst run with the same material and was found to be 9.8% of the value calculated (e.g. for 50 % conversion the error would be  $\pm 4.9$  %).

#### 2.4.4 Methanol synthesis testing

All methanol synthesis testing presented in this thesis was performed by Dr James Hayward. The reaction was performed on a 6 bed reactor (**Figure 2.23**). (0.1 g) of the CuO/ZnO was placed in a stainless-steel reactor tube, suspended by quartz wool, and reduced in situ under a 5% H<sub>2</sub>/He (25 ml min<sup>-1</sup>) at 225 °C prior to the testing, to form the active Cu/ZnO catalyst.

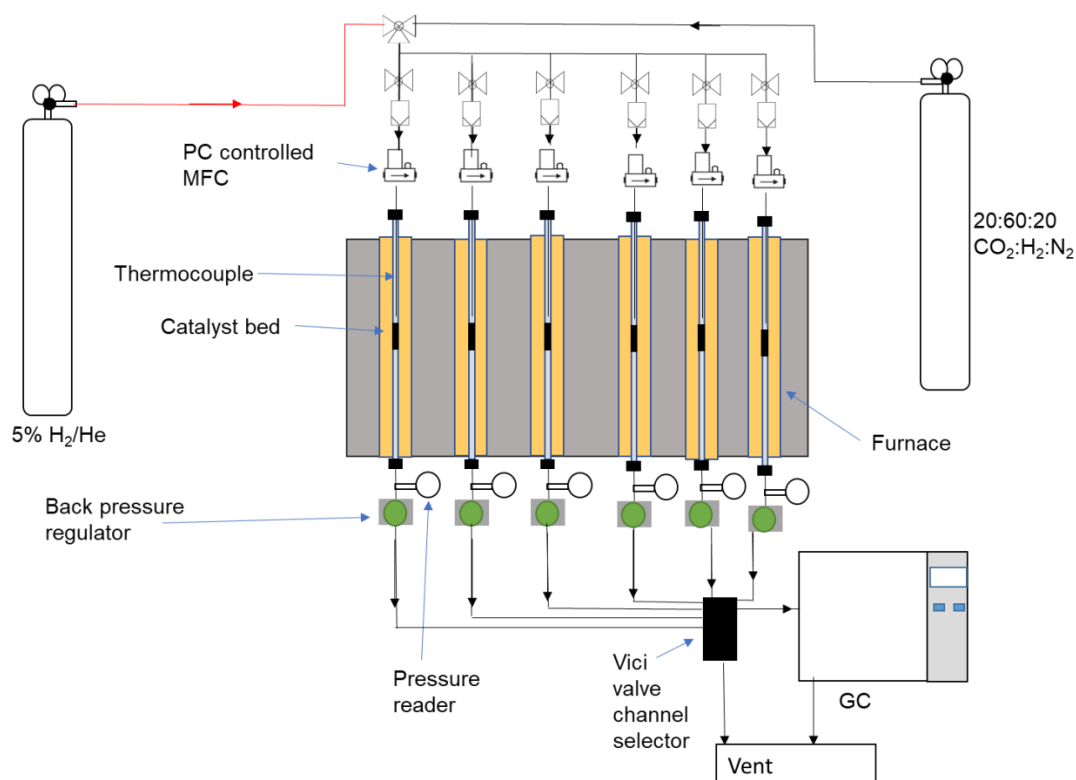


**Figure 2.23: Diagram for the reactor used for methanol synthesis testing**

After reduction the reactor was then cooled down to room temperature and the gas flow was switched to a (20:60:20) CO<sub>2</sub>:H<sub>2</sub>:N<sub>2</sub> gas mixture and the

pressure set to 20 bar using a back pressure regulator. The reactors were then heated to 200 °C, 225 °C and 250 °C. The reactor was held at each temperature interval for 200 minutes. Each catalyst bed had its own independent MFC and temperature controlled furnace. Product were analysed on an Agilent 7890b equipped with an FID and TCD with a gas sampling run time of 25 minutes. A Vici valve was used to select each individual catalyst reactor. The GC peaks were translated to concentrations using the response factor and the molar flow rate of the total gas and CO<sub>2</sub> at standard temperature and pressure. These values were then used to calculate carbon dioxide conversion, methanol selectivity and yield using the equations shown in **Figure 2.24**

$$\text{a) } CO_2 \text{ conversion } \% = \frac{\text{concentration of products (mol min}^{-1}\text{)}}{\text{concentration of feed } CO_2 \text{ (mol min}^{-1}\text{)}} \times 100$$

$$\text{b) } CH_3OH \text{ selectivity } \% = \frac{CH_3OH \text{ (mol min}^{-1}\text{)}}{CH_3OH + CH_4 + CO + CH_3OCH_3 \text{ (mol min}^{-1}\text{)}} \times 100$$

$$\text{c) } CH_3OH \text{ Yield } \% = \frac{CH_3OH \text{ (mol min}^{-1}\text{)}}{\text{theoretical maximum } CH_3OH \text{ from } CO_2 \text{ feed (mol min}^{-1}\text{)}} \times 100$$

**Figure 2.24: Methanol synthesis calculations a) CO<sub>2</sub> conversion b) CH<sub>3</sub>OH selectivity and c) CH<sub>3</sub>OH Yield**

**Table 2.6: Definition of symbols**

Symbol	Meaning
	Valve
	Three Way Valve
	Mass Flow Controller
	Gas Filter

## 2.5 Chapter 2 References

1. A. P. Abbott, G. Capper, D. L. Davies, R. K. Rasheed and V. Tambyrajah, *Chemical Communications*, 2003, 70-71.
2. J. Y. Dong, Y. J. Hsu, D. S. H. Wong and S. Y. Lu, *Journal of Physical Chemistry C*, 2010, **114**, 8867-8872.
3. A. P. Abbott, G. Capper, D. L. Davies, K. J. McKenzie and S. U. Obi, *Journal of Chemical Engineering Data*, 2006, **51**, 1280-1282.
4. A. P. Abbott, G. Capper, D. L. Davies, R. K. Rasheed and P. Shikotra, *Inorganic Chemistry*, 2005, **44**, 6497-6499.
5. D. H. Xiong, Q. Q. Zhang, Z. J. Du, S. K. Verma, H. Li and X. J. Zhao, *New Journal of Chemistry*, 2016, **40**, 6498-6504.
6. T. J. Clarke, S. A. Kondrat and S. H. Taylor, *Catalysis Today*, 2015, **258**, 610-615.
7. R. Prins, A. Wang and X. Li, *Introduction to Heterogeneous Catalysis*, Imperial College Press, London, 2016.
8. L. Smart and E. Moore, *Solid State Chemistry An Introduction*, Taylor & Francis, Boca Raton, 2005.
9. J. W. Niemantsverdriet, *Spectroscopy in Catalysis*, Wiley, Weinheim, Third edition, 2007.
10. E. M. Vass, R. Schlog and Detre Teschner, in *Metal Oxide Catalysis* Wiley, 2009, volume 1, chapter 6, pp. 243-298.
11. S. A. Kondrat, T. E. Davies, Z. L. Zu, P. Boldrin, J. K. Bartley, A. F. Carley, S. H. Taylor, M. J. Rosseinsky and G. J. Hutchings, *Journal of Catalysis*, 2011, **281**, 279-289.
12. J. M. Hollas, *Modern Spectroscopy*, Wiley, Chichester, 2004.
13. C. N. Bandwell and E. M. McCash, *Fundamentals of Molecular Spectroscopy*, McGraw-Hill, Fourth edition, 1994.
14. M. C. Biesinger, L. W. M. Lau, A. R. Gerson and R. S. C. Smart, *Applied Surface Science*, 2010, **257**, 887-898.
15. P. J. Goodhew, J. Humphreys and R. Beanland, *Electron Microscopy and Analysis*, CRC Press, 2001.
16. M. C. Biesinger, B. P. Payne, A. P. Grosvenor, L. W. M. Lau, A. R. Gerson and R. S. Smart, *Applied Surface Science*, 2011, **257**, 2717-2730.
17. W. Zhou, in *Metal oxide Catalysis*, eds. S. David Jackson and S. J. Hargreaves, 2009, volume 1, chapter 10, pp.443-485
18. R. F. Egerton, *Physical Principles of Electron Microscopy*, Springer, New York, 2005.
19. S. Bennici and A. Auroux, in *Metal Oxide Catalysis*, eds. S. David Jackson and J. S. J. Hargreaves, Wiley, Weinheim, 2009, volume 1, chapter 9, pp. 391-436.
20. H. Knozinger, in *Handbook of Heterogeneous Catalysis*, Wiley, Weinheim, 2008, volume 2, chapter 3.2, pp. 1080-1085.
21. F. C. Buciuman, F. Patcas and T. Hahn, *Chemical Engineering and Processing-Process Intensification*, 1999, **38**, 563-569.
22. G. C. Bond, *Heterogeneous Catalysis: Principles and Applications*, Clarendon, Oxford, Second edition, 1987.

23. M. Bowker, *The Basis and Applications of Heterogeneous Catalysis*, Oxford University Press, 1998.
24. O. Hinrichsen, T. Genger and M. Muhler, *Chemical Engineering & Technology*, 2000, **23**, 956-959.
25. J. J. Scholten and J. A. Konvalinks, *Transactions of the Faraday Society*, 1969, **65**, 2465-2473
26. G. Busca, in *Metal Oxide Catalysis*, eds. S. D. Jackson and S. J. Hargreaves, Wiley, Weinheim, 2009, volume 1, chapter 3, pp. 95-175
27. D. A. Skoog, D. M. West, F. J. Holler and S. R. Crouch, *Fundamental of Analytical Chemistry*, Ninth Edition, 2014.
28. B. C. Smith, *Fundamentals of Fourier Transform Infrared Spectroscopy, Second Edition*, CRC Press, 2011.
29. C. W. Tang, C. B. Wang and S. H. Chien, *Thermochimica Acta*, 2008, **473**, 68-73.
30. P. C. Uen, in *Atomic Spectroscopy in Elemental Analysis*, ed. M. Cullen, Blackwell Publishing, CRC Press, 2004, chapter 5
31. W. Li, P. Simmons, D. Shrader, T. J. Herrman and S. Y. Dai, *Talanta*, 2013, **112**, 43-48.
32. D. Kealey and P. J. Haines, *Analytical Chemsitry*, BIOS Scientific Pubishers, 2002.
33. L. Szesepy, *Gas Chromatography*, London Iliffe books, 1970.
34. J. Porter and D. H. Volman, *Analytical Chemistry*, 1962, **34**, 748-749
35. M. Filgueira, R. Chakrabarti, M. Devlin and F. Huby, *Journal of Chromatography A*, 2019, **1599**, 231-238

# Chapter 3 Choline Chloride-Oxalic Acid Based Deep Eutectic Solvents for the Preparation of Metal Oxalate Precursors for Metal Oxide Catalyst

## 3.1 Introduction

### 3.1.1 Background on deep eutectic solvents and metal oxalates

The use of deep eutectic solvents (DES) to make metal oxides as catalyst or for other applications has been rapidly expanding over the last few years due to a better understanding of DES systems<sup>1-3</sup>. The advantage of DES over ionic liquids has mostly been focused on the cheapness of their components and their less complex synthesis<sup>4</sup> as well as their components being less toxic although this is not always the case<sup>5</sup>.

A choline chloride-urea mixture has been established as a DES for the preparation of metal oxides or metal oxide precursors such as ceria for CO oxidation<sup>6</sup>. This method utilised ionothermal conditions which resulted in the breaking down of urea, to form a cerium oxycarbonate precursor or forming the oxide depending on the conditions used<sup>6</sup>. Ionothermal synthesis has also been used to make other oxide precursors such as manganese carbonate<sup>7</sup> or a cobalt-iron double layer hydroxide<sup>3</sup> which are then calcined to form the metal oxide. The use choline chloride-urea can also be used to prepare metal oxides via other technique such as precipitation using an anti-solvent<sup>8</sup>.

Another DES that could be utilised is choline chloride and oxalic acid. This was one of the DES that Abbott *et al.* had reported in 2004<sup>9</sup> and has been used for various applications but very little in the synthesis of metal oxalates as a metal oxide precursor. A few studies were done on making metal oxalate in DES such as the formation of gallium oxalate<sup>10</sup> or lanthanide oxalates (dysprosium and erbium)<sup>11</sup>, using ionothermal synthesis at a temperature of 120 °C, over a 3-day period. These metal oxalates were formed during the ionothermal synthesis followed by washing with water to remove the precursor choline chloride and excess oxalic acid. Another study looked into the use of choline chloride oxalic acid, alongside other choline

DES mixtures, as a template to make  $\text{MgFe}_2\text{O}_4$  by mixing the metal oxides in the DES, then calcining the mixture, although this resulted with some degree of phase separation<sup>12</sup>.

The use of metal oxalate as precursors for both single and mixed metal oxides has been widely established, including applications in the preparation of catalysts<sup>13,14</sup>. Using metal oxalates have an advantage in that the metal oxide can retain the initial morphology of the metal oxalate after calcination<sup>15</sup>, meaning that the formation of the initial oxalate can be used as a route to achieving metal oxides with controlled morphologies. Another advantage of oxalates is that different metal oxide phase can be achieved by using different calcination conditions and atmospheres<sup>16</sup>.

Previous methods of making metal oxalate with controlled morphologies such as nanorods or polyhedrons include surfactant assisted growth with bis(2-ethylhexyl)sodium sulfosuccinate<sup>15,17</sup>. Cobalt oxalate has also been synthesised with ionic liquids (such as [BMIM] [BF<sub>4</sub>]) under microwave power which favoured linear growth forming nanorods<sup>18</sup>. Another example included the controlled precipitation of cobalt oxalate from organic solvents (such as N,N-dimethylacetamide) with the addition of water<sup>19</sup>.

However, if the metal oxalate can be precipitated from a DES using a controlled anti-solvent process then a new route for making metal oxalates with a degree of controlled morphology and shape of the precipitated oxalate could be achieved.

### 3.1.2 Overview of the preparation method for cobalt, manganese and iron oxalate

The design of the methodology was based on the three steps required for controlled synthesis of the oxalate precursors. The first step involved dissolving the metal salt into the DES (formed at approximately 80 °C); secondly water was removed (by heating to 150 °C after allowing the system to stabilise at 120 °C for 1 hour); and thirdly the anti-solvent was added after cooling to precipitated the metal oxalate. This protocol was used for all metal oxalate preparations in this chapter.

Cobalt acetate was dissolved in the choline chloride-oxalic acid mixture at a ratio of 0.1:1:1 of cobalt acetate:choline chloride:oxalic acid. The cobalt oxalate mixture was precipitated in a range of anti-solvents; pure water, 50:50 (volume ratio) water-ethanol, 50:50 water-methanol, pure ethanol and pure methanol. For a long precipitation time, the anti-solvent (100 ml) was injected at a rate of 1 ml min<sup>-1</sup> followed by 100 ml at a rate of 4 ml min<sup>-1</sup> with the. For a fast precipitation the DES-metal oxalate mixture was poured into 600 ml of the anti-solvent.

During the precipitation of the cobalt oxalate with the 50:50 water-ethanol anti-solvent, the DES formed a highly viscous gel, which required stirring. At least 100-200 ml of water-ethanol anti-solvent to 40 g of DES was required to break the eutectic and precipitate the metal oxalate. In contrast pure water mixed into the DES-metal gel for the first 10 ml (to 40 g of the DES) before the cobalt oxalate precipitated.

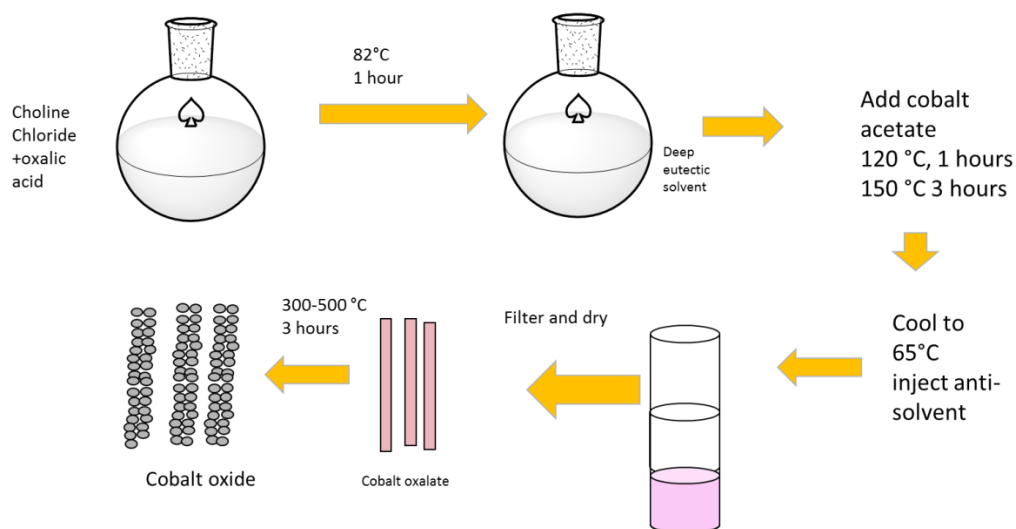


**Figure 3.1: The process of making cobalt oxalate and the cobalt oxide catalyst in this chapter using deep eutectic solvent through the anti-solvent process**

When water or water-ethanol/methanol anti-solvent mixtures were used the mixture would form a light pink precipitate. However, when pure ethanol was used the mixture formed a purple gel-like precipitate and if dried would revert back to the blue cobalt-choline chloride-oxalic acid gel rather than a pink solid that would be expected for cobalt oxalate.

This would suggest that the ethanol was mixed with the gel but did not precipitate the cobalt oxalate out of the DES mixture. When pure methanol was used a dark pink precipitate formed but characterisation data showed that this was not a pure cobalt oxalate hydrate as per when water was used (see Section 3.2.3)

The methodology was also applied to manganese and iron oxalate to see if this technique could be used to make other metal oxalates. The method was also applied to make mixed metal oxalates cobalt manganese and iron manganese.

### **3.1.3 Aims of the chapter**

The aim of this chapter was to investigate the potential of choline chloride-oxalic acid deep eutectic solvent for tailoring the shape and morphology of metal oxalates as precursors to metal oxides focussing on cobalt manganese and iron oxides as catalysts for the total oxidation of volatile organic compounds (VOCs).

The different conditions as anti-solvent mixture, rate of addition of the anti-solvent to the DES and precursor metal salt were varied to observe the effect on morphology and surface area of the materials. The materials were compared to conventionally synthesis metal oxalate and oxides derivatives to determine the advantages of using this methodology. The catalysts were also tested for propane oxidation as a model for assigning their catalytic activity relative to catalyst made from other methods such as supercritical anti-solvent (SAS) precipitation<sup>20</sup> and metal oxalate made using oxalic sol-gel procedure<sup>21</sup>.

## **3.2 Cobalt oxalate**

### **3.2.1 Synthesis of cobalt oxalate and cobalt oxide and comparison to standard**

Cobalt oxide was chosen as the initial material to assess the methodology.  $\text{Co}_3\text{O}_4$  is a known active catalyst for volatile organic compound oxidation (VOC) and some cobalt oxide catalysts that were studied for this reaction have been prepared from cobalt oxalate<sup>22</sup>. Cobalt oxide is also a good catalyst to test this method on since the method of preparation affects the particle shape and crystallite size of cobalt oxide which can impact on their catalytic activity<sup>23</sup>. The use of DES and controlled anti-solvent system could potentially be used to achieve highly active cobalt oxide catalysts.

The cobalt oxide derived from the DES prepared oxalate was compared with supercritical anti-solvent precipitated cobalt acetate and metal oxalate prepared by oxalate gel method<sup>14, 24</sup>.

The anti-solvent mixture that was initially chosen was a 50:50 (volume ratio) water: ethanol mixture. The materials prepared by this method were compared with materials synthesised by oxalate gel method where the metal oxalate was precipitated in an ethanol solution. One aim of this work was to demonstrate that the cobalt oxalate could be precipitated from the DES in a controlled manner achieving morphologies that could not be easily obtained using the oxalate gel method.

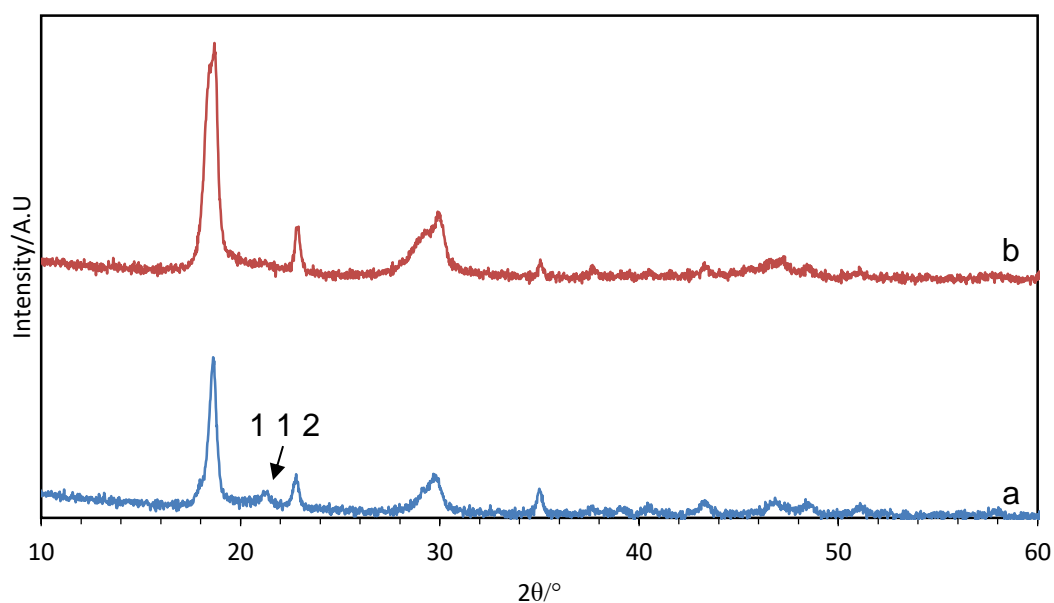


**Figure 3.2:** XRD of the cobalt oxalate precipitated using a) the oxalate gel method and b) DES anti-solvent method using 50:50 water: ethanol anti-solvent

The XRD pattern of the precipitate (**Figure 3.2**) confirmed that the cobalt oxalate had precipitated from the DES in the anti-solvent mixture by the reflections at  $18.6^\circ$  (2 0 2),  $22.7^\circ$  (1 1 2),  $29.5^\circ$  and  $34.9^\circ$ . However, the XRD pattern of the cobalt oxalate precipitated from DES and that precipitated by oxalate gel have some notable differences, such as the reflection at  $2\theta=21.3^\circ$  which corresponds to the (1 1 2) plane that is missing in the sample that was prepared by DES anti-solvent. In addition, there appears to be two reflections at  $2\theta=18.3^\circ$  and  $18.7^\circ$  in the DES precipitated sample but not in the oxalate gel. This would suggest that the cobalt oxalate from the precipitated oxalate gel method had an orthorhombic structure (based on the single peak at

$2\theta=18.6^\circ$  and  $21.3^\circ$ ), while the DES precipitated oxalate was a monoclinic phase.

FTIR analysis (**Figure 3.3**) showed vibrational peaks that corresponded with the cobalt oxalate hydrates with peaks at  $3350\text{ cm}^{-1}$  (O-H),  $1614\text{ cm}^{-1}$  (C-O) symmetrical stretching  $1357\text{ cm}^{-1}$  and  $1309\text{ cm}^{-1}$  (C-O asymmetric stretching) corresponding to the oxalate species. The peaks all belong to the cobalt oxalate<sup>25</sup>, with no additional vibrations that could come from residual species, such as choline chloride, visible in the spectra, suggesting that the choline and remaining DES (choline chloride and excess oxalic acid) was removed during the precipitation and washing process.

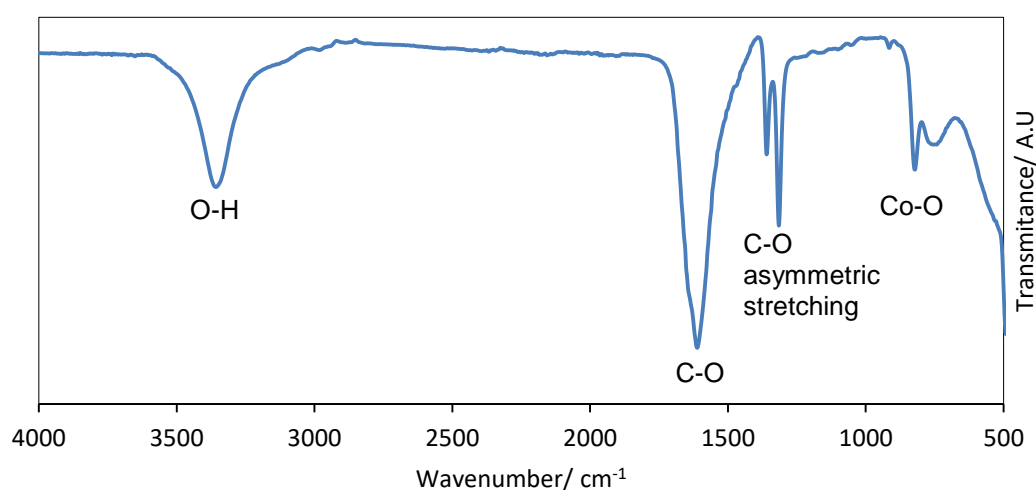


**Figure 3.3: FTIR of cobalt oxalate precipitated from choline chloride-oxalic acid in water-ethanol anti-solvent**

The TGA/DSC of the sample (**Figure 3.4**) showed two mass losses. The first (endothermic) loss at  $135\text{--}162^\circ\text{C}$  (with a 17.3% weight loss) corresponds to the loss of crystalline water. This is followed by a large exothermic peak at  $275^\circ\text{C}$  (38% weight loss) which would be the decomposition of the oxalate to carbon dioxide, carbon monoxide and the metal oxide. The overall profile shows a mass loss typical of cobalt oxalate decomposition in terms of both temperatures of mass loss and the % weight change. This would suggest, along with the FTIR, that there was very little choline chloride left in the sample although any remaining choline chloride might burn off during the large exotherm at  $275^\circ\text{C}$  (decomposition temperature of choline chloride is  $302^\circ\text{C}$ ).

The cobalt oxalates made with other precipitation methods and reference methods had the same TGA profile. The exception to this was when pure methanol was used to precipitate described later (see Section 3.2.3).

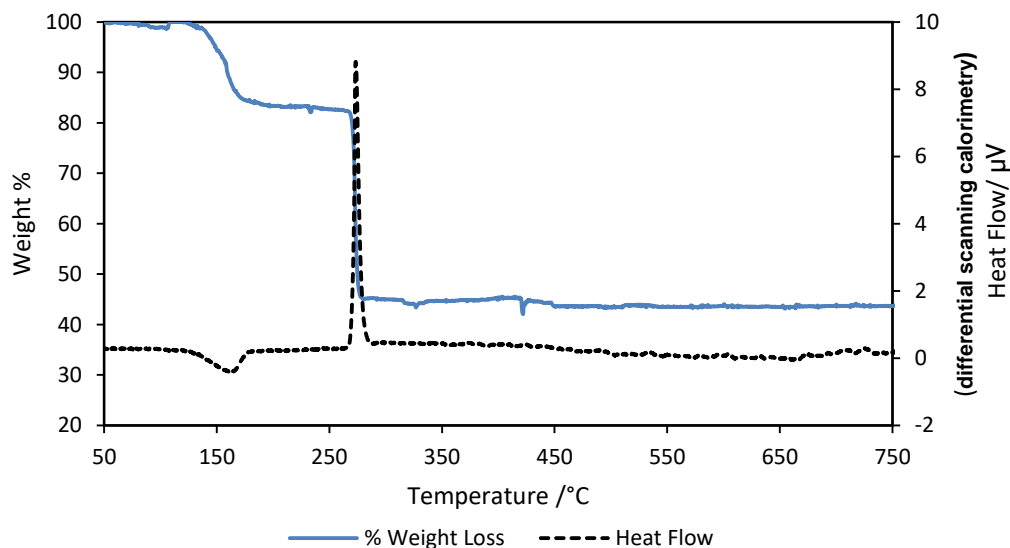


**Figure 3.4: Thermal gravimetric analysis and differential scanning calorimetry of cobalt oxalate precipitated from the choline chloride-oxalic acid DES in water-ethanol anti-solvent**

XRD analysis on the calcined samples (**Figure 3.5**) confirmed that the cobalt oxalate formed  $\text{Co}_3\text{O}_4$  after calcination at 500 °C. The DES precipitated sample had a much higher degree of crystallinity than the oxalate gel precipitated sample and this is reflected in their surface areas with the oxalate gel having  $22 \text{ m}^2 \text{ g}^{-1}$  ( $\pm 2 \text{ m}^2 \text{ g}^{-1}$ ) compared to the  $15 \text{ m}^2 \text{ g}^{-1}$  ( $\pm 2 \text{ m}^2 \text{ g}^{-1}$ ) of the DES and the supercritical anti-solvent precipitated materials.

The low surface area is probably a result of the sintering process that occurred during the calcination at 500 °C leading to larger crystallites and lower surface areas (**Table 3.1**), although this also occurred with the oxalate gel material.

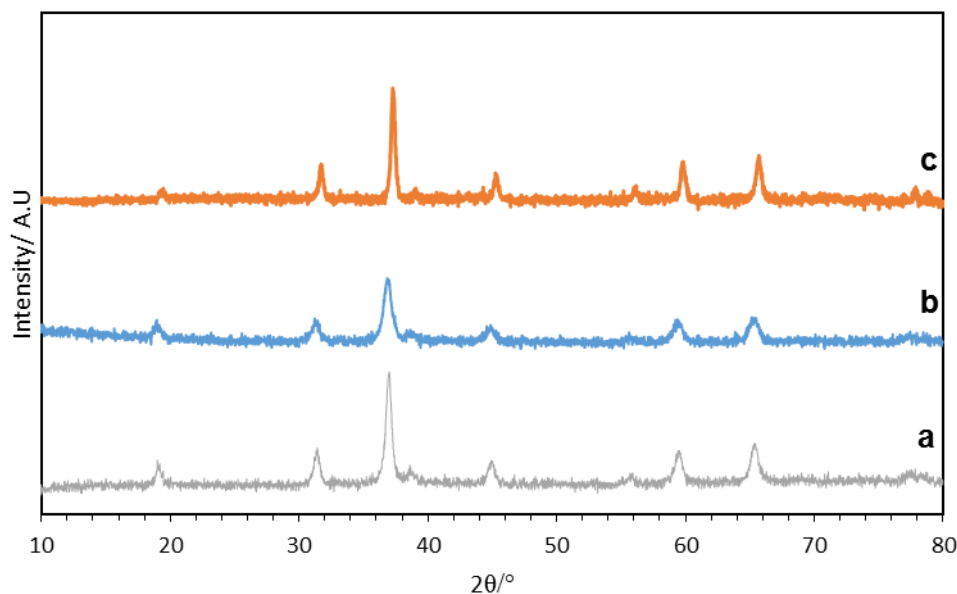


**Figure 3.5:** XRD of the cobalt oxide calcined at 500 °C from precursor prepared by a) DES, b) oxalate gel and c) supercritical anti-solvent precipitated cobalt acetate

**Table 3.1:** Surface area (5 point BET) and XRD crystallite size ( $\pm 2$  nm)(of the  $\text{Co}_3\text{O}_4$  catalysts prepared DES, oxalate gel and supercritical anti-solvent precipitation ( $\pm 2 \text{ m}^2 \text{ g}^{-1}$ ))

Preparation method	Surface area/ $\text{m}^2 \text{ g}^{-1}$	Crystallite size $2\theta=36.8^\circ$ /nm
DES-oxalate	15	37.9
SAS (cobalt acetate)	16	27.9
Oxalate gel	22	35.6

SEM imaging of the cobalt oxalate that was precipitated using the 50:50 water-ethanol anti-solvent (**Figure 3.6 a**), showed that the precipitate had primarily formed rod shaped cobalt oxalate. The cobalt oxalate rods formed here are similar to those that had previously been reported, that were synthesised under microwave power<sup>18,25</sup>. The formation of the rods in the ionic liquid solution however, was attributed to the polarisation of ions under microwave power but here the formation of the rods occurs during the anti-solvent precipitation.

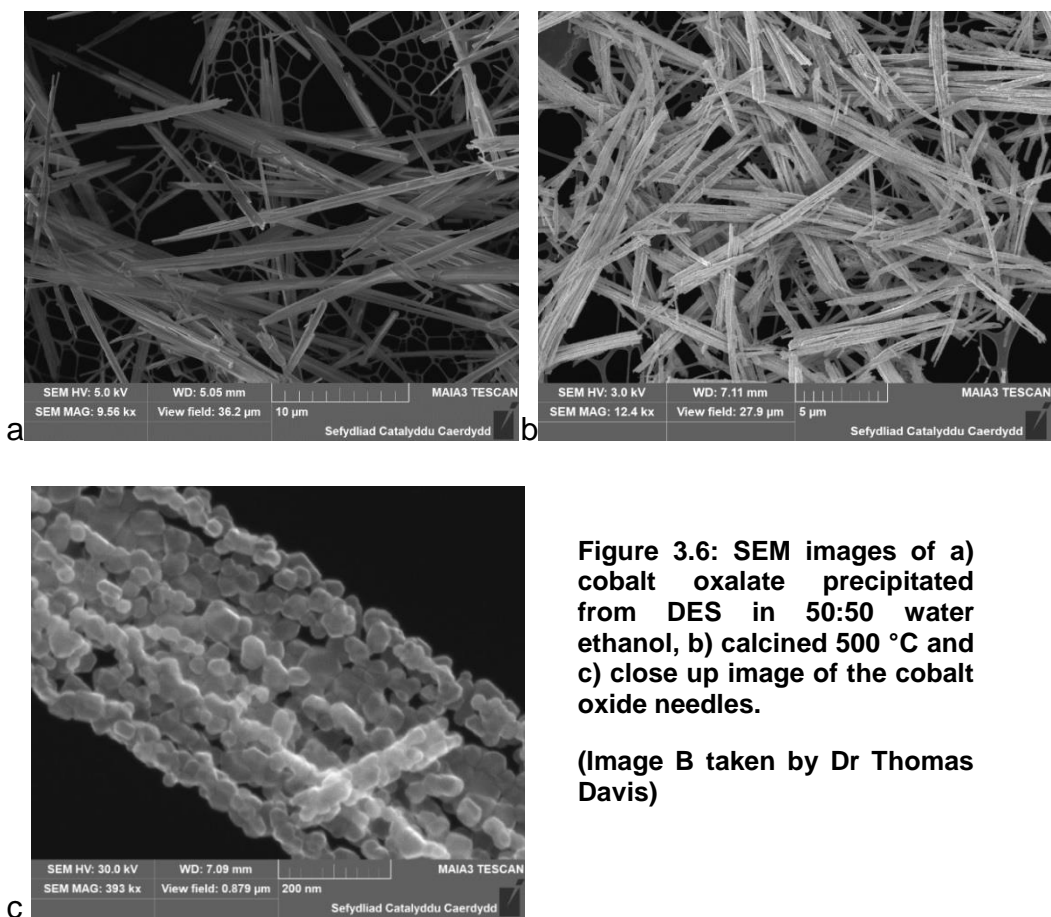


**Figure 3.6: SEM images of a) cobalt oxalate precipitated from DES in 50:50 water ethanol, b) calcined 500 °C and c) close up image of the cobalt oxide needles.**

**(Image B taken by Dr Thomas Davis)**

The calcined cobalt oxalate (**Figure 3.6 b and c**) retained the rod shaped morphology after calcination. However, the cobalt oxide had formed distinct crystallites that appeared to be joined together in the rods of the precursor. These crystallites were most likely formed during the high temperature calcination which resulted in the sintering observed by the XRD (**Figure 3.5**) and surface area analysis (**Table 3.1**).

Comparison of the SEM images of the cobalt oxide calcined at 500 °C from the cobalt oxalate prepared by DES (**Figures 3.6**) and oxalate gel (**Figure 3.7**) showed differences in morphology between the two preparation methods. While DES prepared cobalt oxalate formed needle like morphology, the oxalate gel formed clusters of oxides with no particularly ordered morphology. This would be a reflection on their preparation methods; oxalate from DES used a controlled addition of water-ethanol, which allowed the slow precipitation of the cobalt oxalate from the DES and favoured the liner growth. With the oxalate gel method however, the precipitation occurred in a less controlled manor, hence the more disparate morphology.

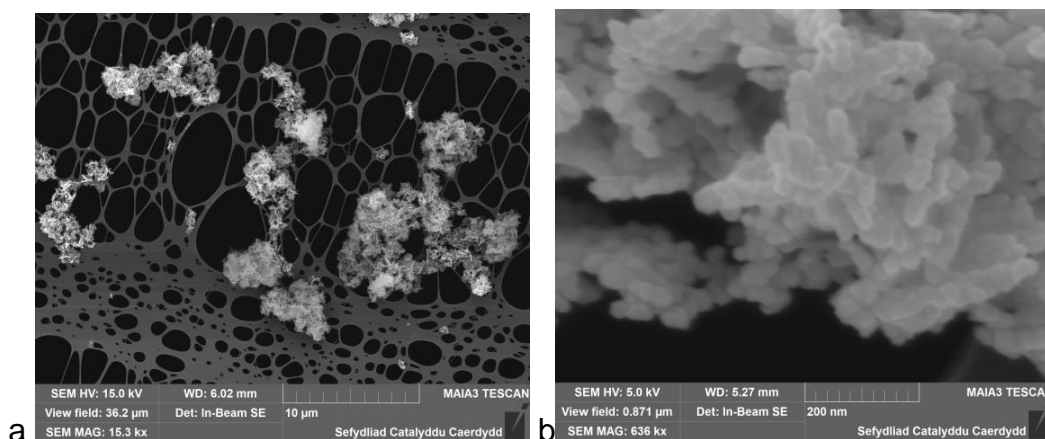


**Figure 3.7: a) and b) SEM images of  $\text{Co}_3\text{O}_4$  (calcined 500 °C) from cobalt oxalate prepared by oxalate gel**

The cobalt oxides made from the technique were tested as VOC catalyst for the total oxidation of propane, to see how they compare in terms of conversion / catalyst activity to cobalt oxide calcined 500 °C from precursors prepared by other techniques such as oxalate gel, supercritical anti-solvent or calcined cobalt acetate tetrahydrate.

**Table 3.2: The temperature of conversion at 10% and 90% for cobalt oxide catalyst with a 51-55 mg catalyst loading**

Catalyst	$T_{10}/\text{°C}$	$T_{50}/\text{°C}$	$T_{90}/\text{°C}$
DES	205	246	298
SAS	198	225	265
Acetate	216	271	321

The DES samples were using a catalyst loading of 50-55 mg and a GHSV of  $6200\text{ h}^{-1}$ . The low GHSV was due to the very low density of the DES cobalt oxide, which originating from the needles structure. Selectivity to  $\text{CO}_2$  (Figure 3.9) was usually within 95% after 250 °C for all catalyst although SAS

and DES lower selectivity at 150 °C due with higher amounts of CO that had formed during the reaction.

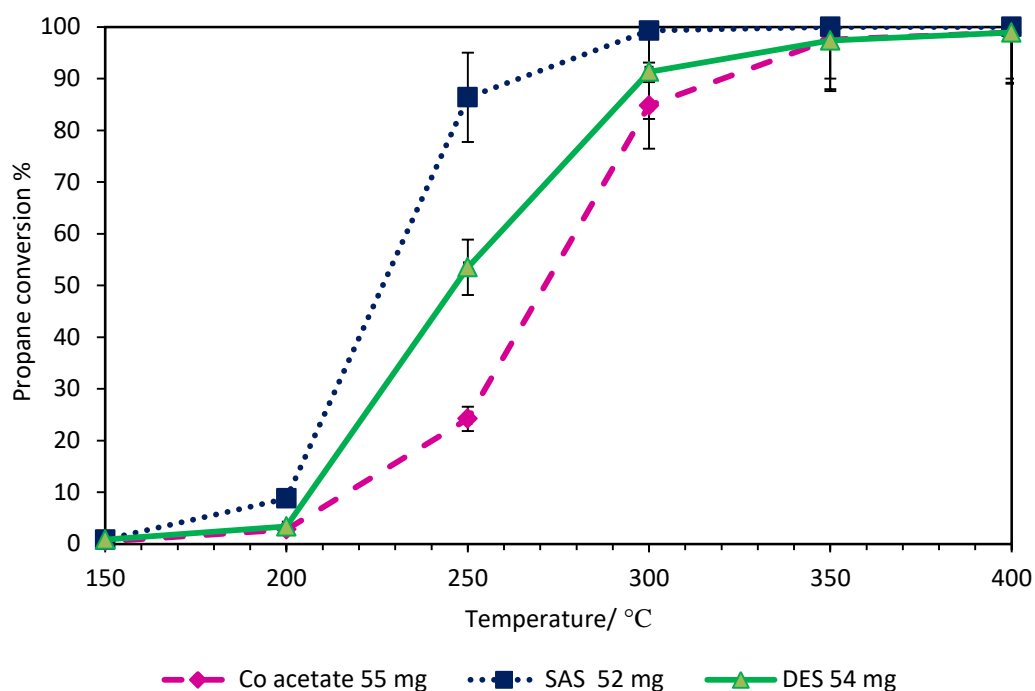


**Figure 3.8: Propane conversion for a range of cobalt catalyst calcined at 500 °C, loading at 52-55 mg**

The cobalt oxide catalysts derived from SAS precipitated acetate was shown to be the most active catalyst achieving total conversion at 300 °C. The DES anti-solvent catalyst was shown to be less active than the supercritical anti-solvent precipitated catalyst despite having similar surface areas. The higher activity of the supercritical anti-solvent catalyst over the DES oxalate however may be attributed to the smaller crystallite size which is linked to the catalytic activity of  $\text{Co}_3\text{O}_4$  for propane oxidation<sup>22</sup>. However the DES anti-solvent cobalt oxide catalyst was more active than the cobalt oxide formed from calcined acetate with a  $T_{50}$  of 246 °C for DES oxalate compared to  $T_{50}$  of 271 °C for the acetate.

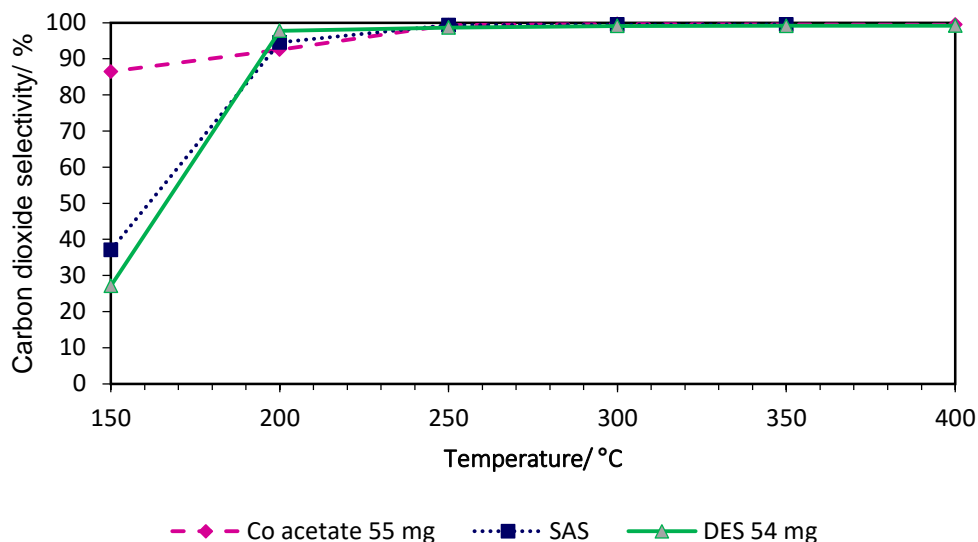


**Figure 3.9: Carbon dioxide selectivity of the different Cobalt oxide catalysts during the propane conversion shown in Figure 3.8**

Comparison of mass normalised activity of the DES anti-solvent derived cobalt oxide with oxalate gel at the same GHSV of  $6200 \text{ h}^{-1}$  (Figure 3.10) showed similar performance at  $200 \text{ }^\circ\text{C}$  with the oxalate gel being slightly better than the DES derived catalysts (which had archived 98% conversion at  $250 \text{ }^\circ\text{C}$  with 125 mg loading).

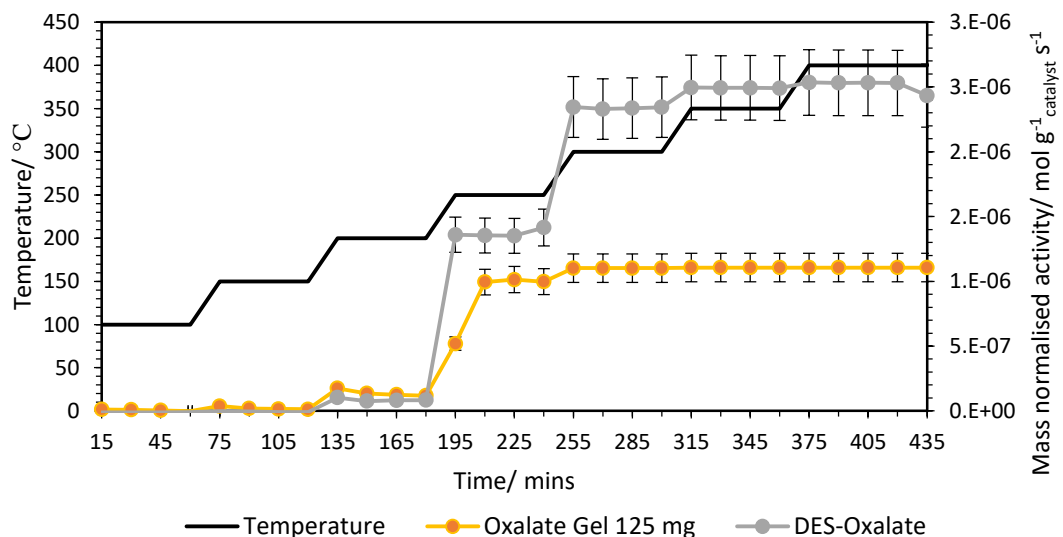


**Figure 3.10: Mass normalised activity of the cobalt oxide catalysts calcined from cobalt oxalate prepared by DES anti-solvent (54 mg) and oxalate gel (125 mg) GHSV =  $6200 \text{ h}^{-1}$  (error  $\pm 10 \%$  taking into account error of surface area and catalyst mass)**

### 3.2.2 Effect of heat treatment

The initial catalyst was calcined at 500 °C to form the oxide from the oxalate and also to ensure the removal of any residual oxalate or choline chloride. However as observed by XRD, BET and SEM analysis of the cobalt oxides, (notably the DES anti-solvent) showed reduced surface area and larger crystallites which reduced their catalytic activity. Therefore, the cobalt oxalate was also calcined at 300 °C, just above the main TGA mass loss to see if the surface area could be increased. In addition, the effect of different heat-treatment conditions such as calcination temperature, flow rate and heating rate was also investigated to see how the DES anti-solvent precipitated catalysts behaved under different calcination conditions and to see if the catalyst surface and activity can be optimised.

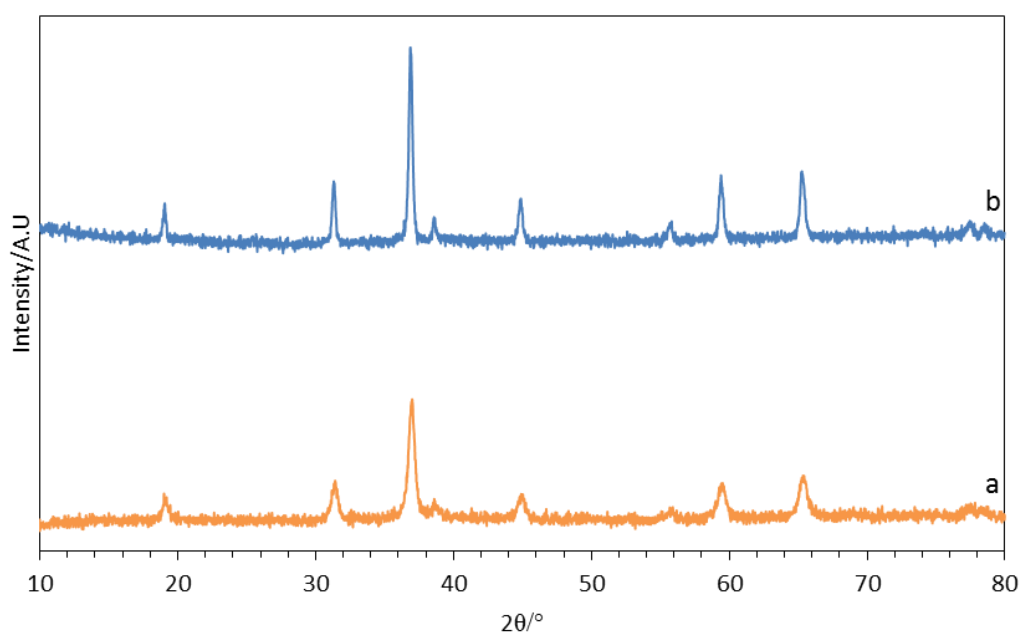


**Figure 3.11: XRD pattern of the cobalt oxide calcined from cobalt oxalate, precipitated in 50:50 water-ethanol at a) 300 °C and b) 500 °C**

The XRD pattern (**Figure 3.11**) of the calcined samples showed that after calcination at both 300 °C and 500 °C the oxalate decomposed to form a spinel  $\text{Co}_3\text{O}_4$  phase. As expected the sample calcined at 300 °C had a lower degree of crystallinity (**Table 3.3**) with a crystallite size of 19.6 nm (at

$2\theta=36.8^\circ$ ) as well as a higher surface area of  $55 \text{ m}^2 \text{ g}^{-1}$  compared to  $16 \text{ m}^2 \text{ g}^{-1}$  for the material calcined at  $500 \text{ }^\circ\text{C}$ .

**Table 3.3: Crystallite size ( $\pm 2 \text{ nm}$ ) for cobalt oxide synthesised by DES anti-solvent and oxalate gel calcined at  $300 \text{ }^\circ\text{C}$**

Sample preparation (airflow, heating rate)	Crystallite size ( $2\theta=36.8^\circ$ ) / nm
DES oxalate (Static $2 \text{ }^\circ\text{C min}^{-1}$ )	19.6
DES Oxalate (static, $1 \text{ }^\circ\text{C min}^{-1}$ )	19.5
DES Oxalate ( $75 \text{ ml min}^{-1}$ , $2 \text{ }^\circ\text{C min}^{-1}$ )	16.7
Oxalate gel (static, $2 \text{ }^\circ\text{C min}^{-1}$ )	15.2

The effect of heating rate and air flow rate during the calcination was also investigate for several reasons; firstly, the oxalate decomposition to cobalt oxide is an exothermic process so controlling the heating rate could decrease the likelihood of sintering. Secondly, the airflow can aid in removing residual carbon that may result from the rapid decomposition of the oxalate and residual DES (which could reduce or block surface sites).

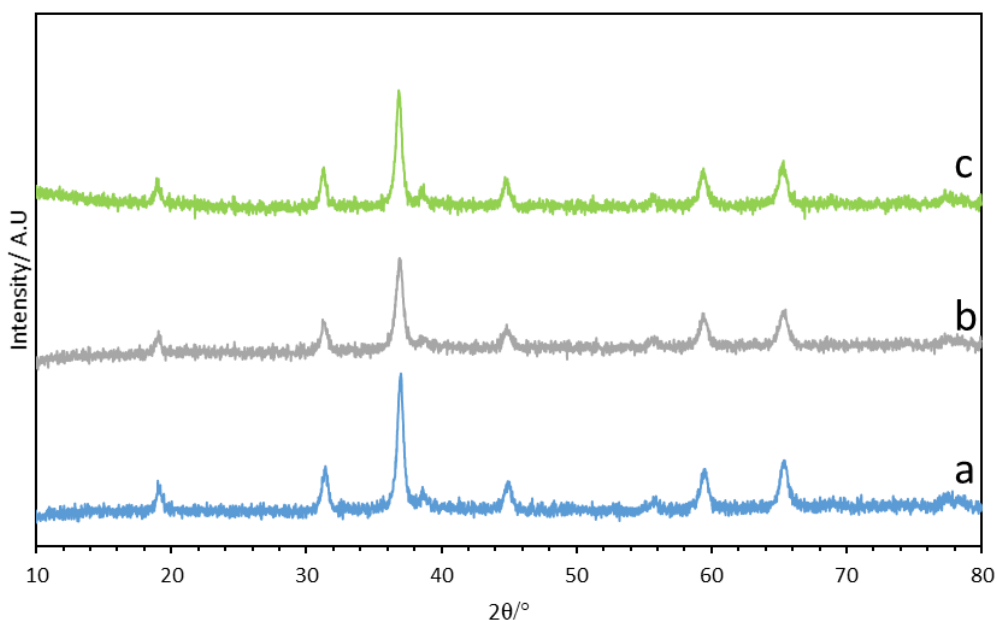


**Figure 3.12: The XRD patterns of the cobalt oxalate precipitated from DES in 50:50 water-ethanol anti-solvent with different heat treatments a) exposed air flow (approximately  $5 \text{ ml min}^{-1}$ )  $2 \text{ }^\circ\text{C min}^{-1}$  b) direct air flow ( $50 \text{ ml min}^{-1}$ )  $2 \text{ }^\circ\text{C min}^{-1}$  and c) open furnace (exposed to an air flow (approximately  $5 \text{ ml min}^{-1}$ )  $1 \text{ }^\circ\text{C min}^{-1}$ )**

The effect of the ramp rate and air flow was shown by XRD (**Figure 3.12**) to make some difference, with the sample calcined exposed to an air flow (open furnace) showed a higher degree of crystallinity (19.8 nm at  $2\theta=36.9^\circ$ ) compared to direct which airflow showed a smaller crystallite size (16.7 nm). The heating rate on the other hand did not show significant difference to the crystallinity of the sample.

Comparison of the SEM images (**Figure 3.13**) of the cobalt oxalate and the cobalt oxide materials calcined at different temperatures shows the change in crystallites over the calcination temperature range. The sample calcined at 500 °C (**Figure 3.13 a**) shows a series of larger crystallites while the sample calcined at 300 °C (**Figure 3.13 b**) did not show distinct crystallites in the needle structure. The 500 °C calcined materials showed that significant sintering had occurred resulting in the large crystallites seen in the SEM and observed by XRD.

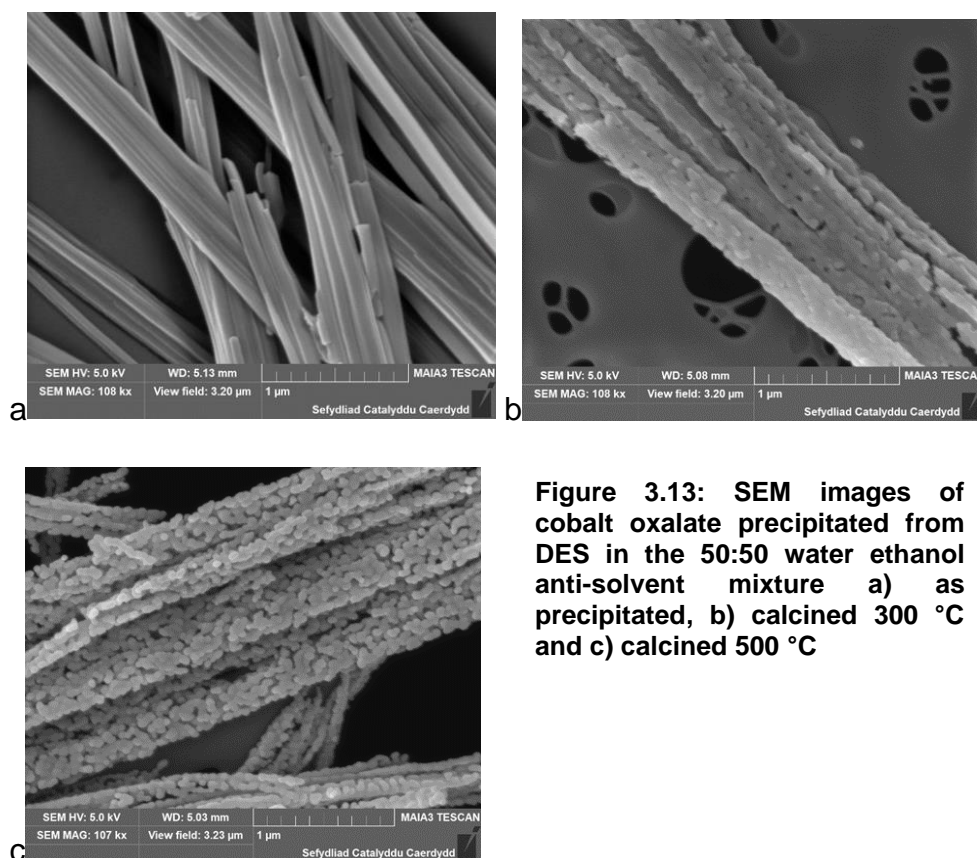


**Figure 3.13: SEM images of cobalt oxalate precipitated from DES in the 50:50 water ethanol anti-solvent mixture a) as precipitated, b) calcined 300 °C and c) calcined 500 °C**

The DES oxalate calcined at 300 °C showed significant improvement in catalytic activity over the catalyst calcined at 500 °C showing 100 % conversion by 250 °C (**Figure 3.14**). This increased in activity showed that the sintering that occurred after calcination at 500 °C had a significant effect on the catalytic performance of the cobalt oxide needles, which would be expected, by the rapid increase in crystallite size. The change in calcination conditions also appear to have had a rapid change in the catalytic activity of the DES-derived cobalt oxalates with the slow heating rate (1 °C min<sup>-1</sup>) catalyst showing the highest conversion (79% at 200 °C), despite the similar sized crystallite size to the sample calcined under airflow. The catalyst calcined under flowing air appeared to have the lowest conversion at 200 °C although like the others the conversion rapidly increased to 100 % by 250 °C with the light off occurring in the 150-250 °C range.

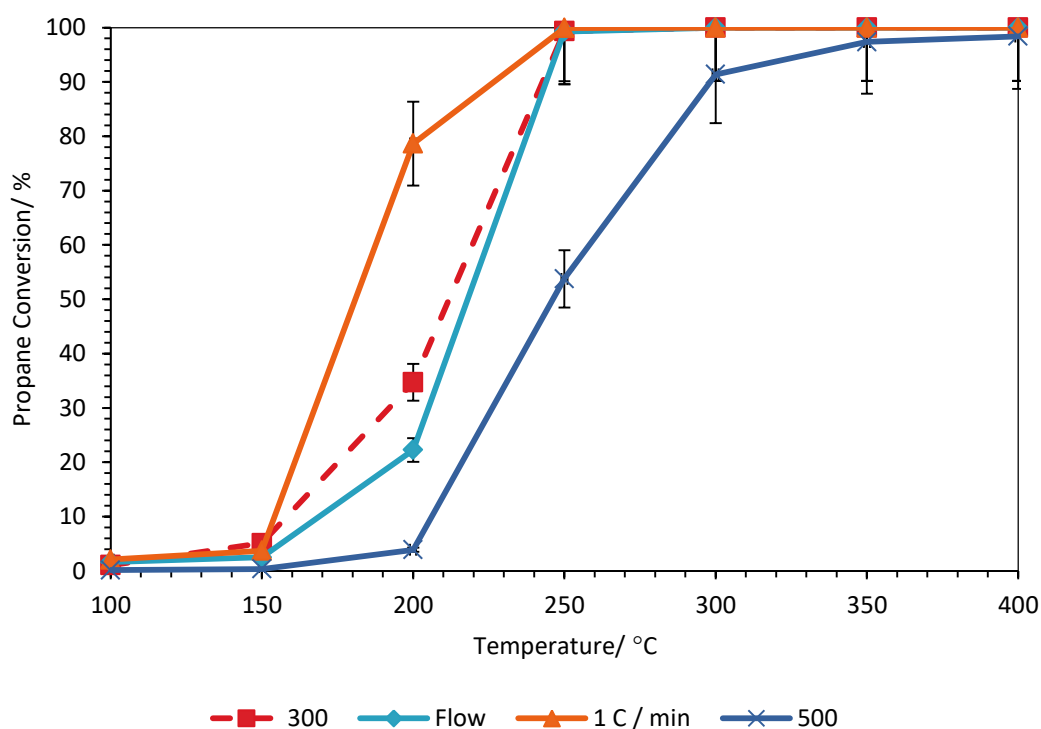


**Figure 3.14: Propane oxidation of the cobalt oxide calcined under different conditions (50-55 mg catalyst), GHSV 6200 h<sup>-1</sup>**

### 3.2.3 Effect of anti-solvent mixtures and rate of addition of anti-solvent

While the initial study into precipitating cobalt oxalate from DES was shown to make cobalt oxalate (and cobalt oxide) with rod-like morphology, the main objective of the method was to demonstrate the ability to change the morphology based on the anti-solvent process. As a result, different anti-solvent mixtures were used to see how these influence the morphology, surface area and catalytic activity. The anti-solvents chosen were: water, 50:50 water-methanol, pure methanol and pure ethanol. However, the pure ethanol anti-solvent resulted in the formation of a purple gel rather than a solid/powder precipitate.

In addition, with water and 50:50 water-ethanol, the rate of addition was also varied with the standard (slow) rate of anti-solvent addition of  $1 \text{ ml min}^{-1}$  being compared to material that formed from the rapid addition of the anti-solvent to the DES.

One of the factors considered when making the cobalt oxalate from the choline chloride-oxalic acid DES was the effect hydrated oxalic acid had on the metal oxalate and the corresponding oxide. Although the water should have been removed during the process at  $150 \text{ }^\circ\text{C}$ , the effect of using hydrated oxalic acid during the initial preparation stage should still be considered. A publication made by group of Gontrani *et al.* has shown through X-ray and ionic conductivity that there were both physical and structural differences between DES with the hydrated and anhydrous oxalic acid DES<sup>26</sup>. However DES based on choline chloride with an organic acid including oxalic acid, malonic acid and malic acid are known to undergo esterification to form an ester and water<sup>27</sup>. It should also be noted that the choline chloride- oxalic acid DES has a decomposition temperature of  $160\text{-}162 \text{ }^\circ\text{C}$ <sup>27</sup>.

When water, 50:50 water-ethanol and 50:50 water-methanol were used as anti-solvents were used a pink precipitate formed which was confirmed as cobalt oxalate by XRD and FTIR. The XRD pattern of the cobalt oxalate precipitated in 50:50 water methanol (**Figure 3.15 b**) had similar reflections as

the cobalt oxalate precipitated in 50:50 water: ethanol however, the precipitate had a single reflection at  $2\theta=18.4$ . The like the water-ethanol precipitated oxalate, the water methanol had no reflection at  $2\theta=21.3^\circ$  (1 1 2).

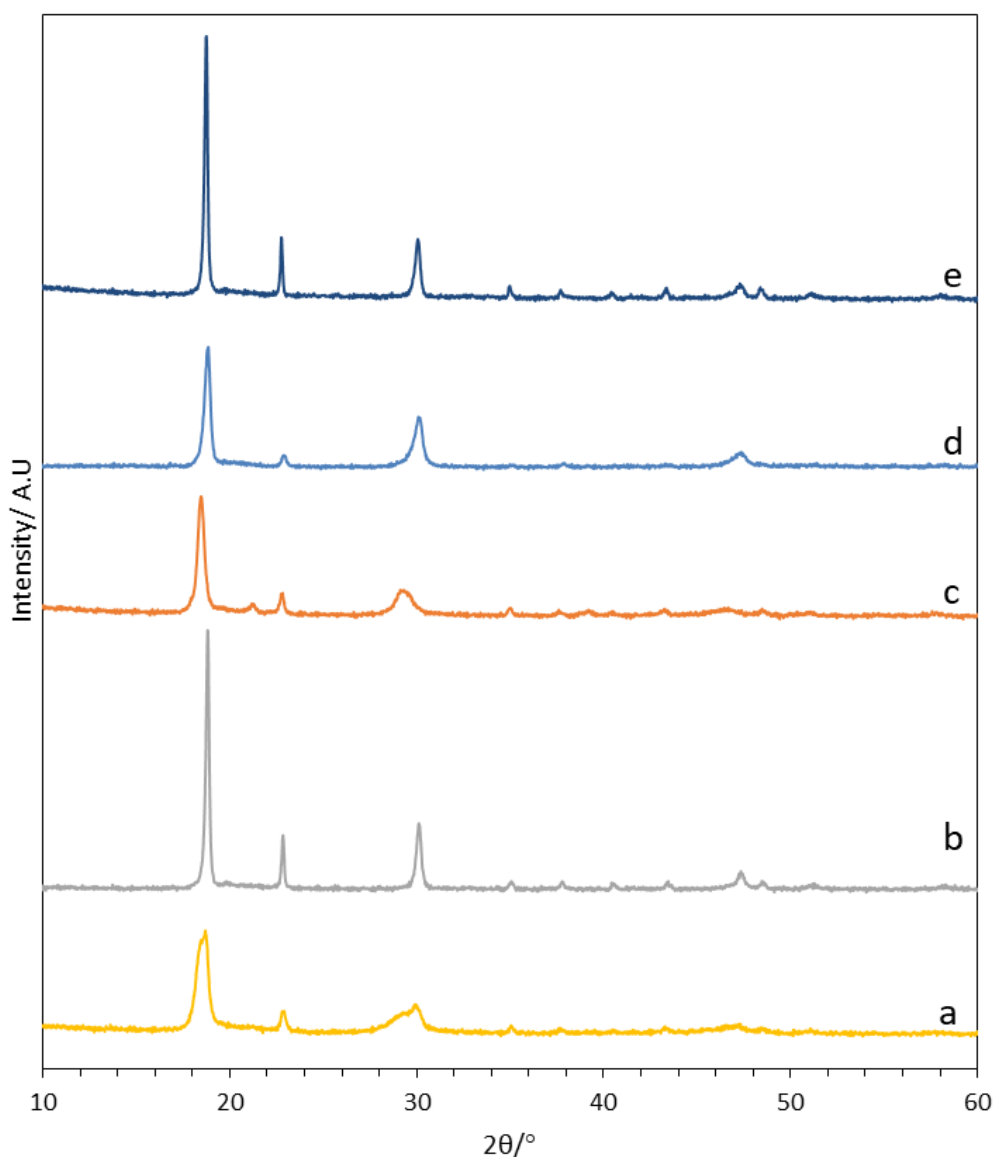


**Figure 3.15: XRD of the cobalt oxalate formed from DES with the anti-solvent of a) 50:50 water-ethanol (fast), b) 50:50 water-methanol, c) water fast precipitation, d) anhydrous oxalic acid 50 50 water ethanol and e) water slow**

The XRD pattern (**Figure 3.15 d**) of the sample formed using the anhydrous DES (precipitated in the water-ethanol anti-solvent mixture) showed the same reflections as the samples that form from the DES that used hydrated oxalic acid. Like the cobalt oxalate that used hydrated oxalic acid the

reflections at  $2\theta=21.3^\circ$  is not present. However, the reflection at  $2\theta= 30.1^\circ$  and  $48.3^\circ$  are notably larger in the anhydrous sample than they are in the hydrate sample.

The cobalt oxalate that was precipitated using water as the anti-solvent (**Figure 3.15 c**) showed the reflection at  $2\theta=21.3^\circ$  which was not present in the sample precipitated in the water-ethanol anti-solvents but was present in the XRD of the sample which was precipitated by the oxalate gel method, which had been identified as an orthorhombic structure. What is notable is that this reflection was also not present in the sample that was slowly precipitated with a water anti-solvent (**Figure 3.15 e**) which suggests that the reflection and the oxalate structure may depend on the rate of addition and precipitation of the cobalt oxalate.

The rate of precipitation appeared to have little effect on the 50:50 water-ethanol with the XRD patterns (**Figures 3.2 b and 3.15 a**) appearing very similar including the broader reflection at  $29-30^\circ$ , rather than the sharper reflection at  $30.2^\circ$  that appears with the water-methanol precipitated oxalate.

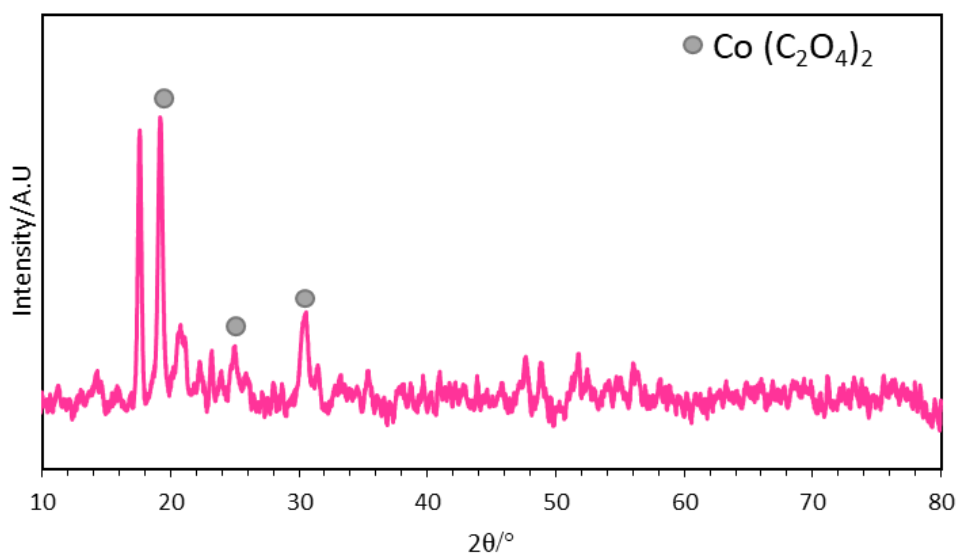


**Figure 3.16: XRD of the precipitate formed from DES using methanol anti-solvent**

The precipitate (**Figure 3.16**) formed using methanol as the anti-solvent showed a very different XRD pattern to those precipitated with water-alcohol anti-solvents but there were reflections notably at  $2\theta=19.2^\circ$  and  $30.3^\circ$  that can be assigned to the cobalt oxalate phase, however there are additional

reflections present in the XRD pattern such as  $17.4^\circ$  and  $21.0^\circ$  which do not originate from the cobalt oxalate. The intensities of the cobalt oxalate reflections were weaker than the other sample suggesting a more disordered sample showed that the cobalt oxalate had partially formed after the anti-solvent precipitation.

The FTIR of the cobalt species that was precipitated in pure methanol (**Figure 3.17 a**) shows vibrations associated with the cobalt oxalate. However, the FTIR of this sample also feature additional vibrations shifts at  $1750\text{ cm}^{-1}$ ,  $1474\text{ cm}^{-1}$ ,  $1190\text{ cm}^{-1}$  and  $956\text{ cm}^{-1}$  that are associated with choline chloride<sup>28-30</sup>. The FTIR of the cobalt, choline chloride-oxalic acid mixture prior to anti solvent process (**Figure 3.17 c**) showed both the choline chloride vibrations and the oxalic acid (although shifted) at  $1719\text{ cm}^{-1}$ ,  $1487\text{ cm}^{-1}$   $1176\text{ cm}^{-1}$  and  $951\text{ cm}^{-1}$ .

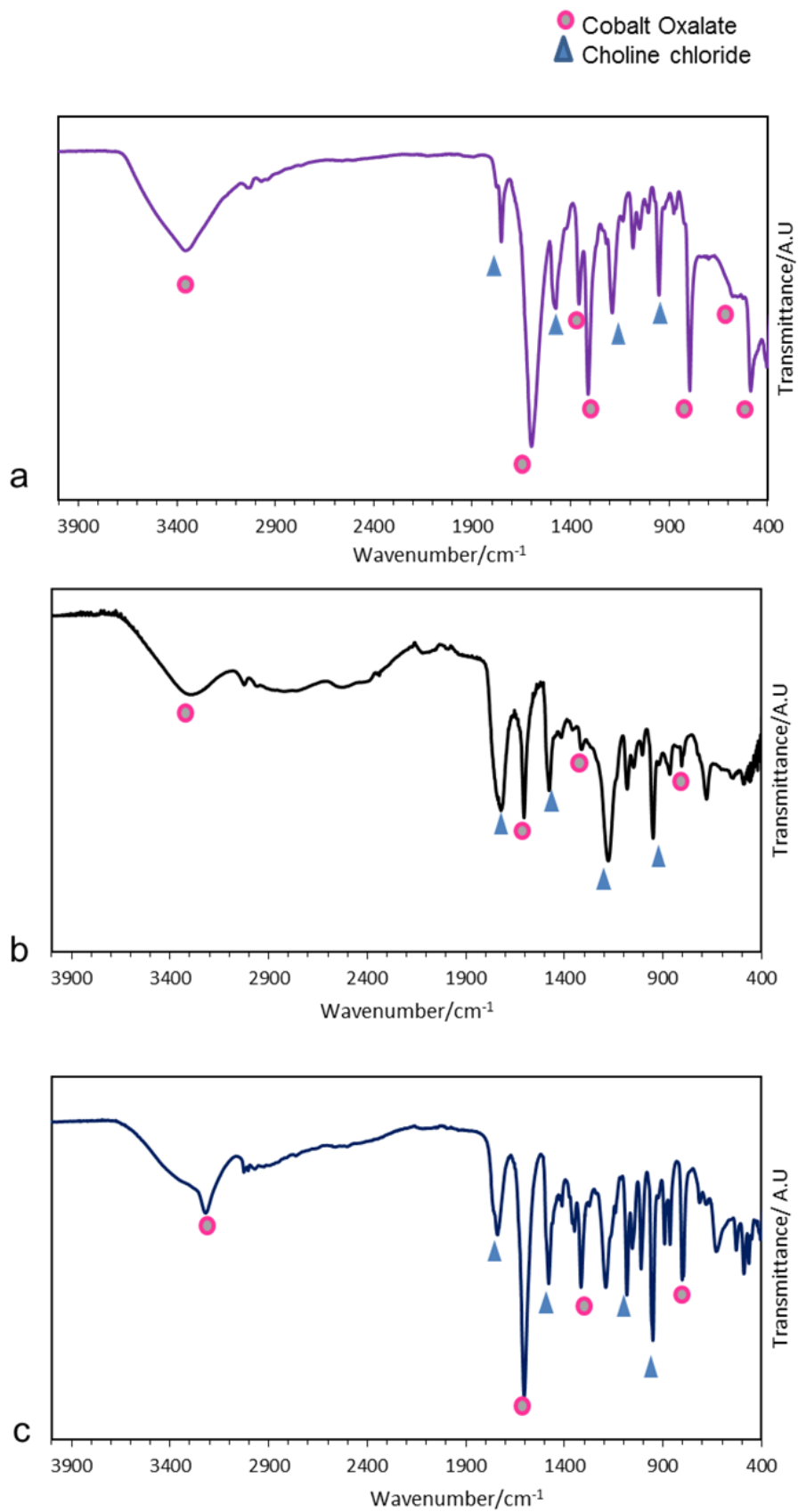


**Figure 3.17: FTIR of the cobalt sample that was precipitated in a) methanol and b) ethanol and c) FTIR of cobalt acetate dissolved in oxalic acid-choline chloride DES (after 3 hours 150 °C)**

When both methanol and ethanol was added, the band at  $1605\text{ cm}^{-1}$  (O-H bending) is notably stronger in these precipitate relative to the band at  $1716\text{--}1750\text{ cm}^{-1}$  than when the cobalt oxalate-DES mixture.

This showed that the methanol sample was not a pure oxalate but as a mixture of cobalt oxalate and choline chloride and that water is required to break down the DES and remove the excess choline and oxalic acid. By comparison there was little or no indication of residual choline chloride present in the material that was precipitated with a water containing anti-solvent. Since cobalt oxalate is mostly insoluble in water<sup>30</sup> the DES structure breaks down and cobalt oxalate precipitates out when a water or water-alcohol anti-solvent mixture is used.

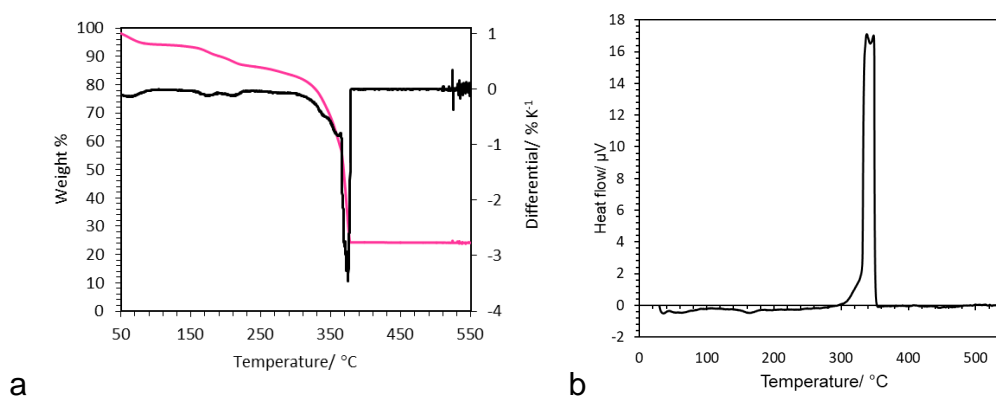


**Figure 3.18:** a) TGA profile of the cobalt precipitate using pure methanol (heating rate  $5\text{ °C min}^{-1}$ ) and b) DSC scan of the same precipitate heating rate  $1\text{ °C min}^{-1}$

The TGA profile of the sample precipitated in pure methanol (**Figure 3.18 a**) showed a completely different profile from cobalt oxalate hydrate. The main mass loss occurred at  $310\text{--}350\text{ °C}$  approximately  $50\text{ °C}$  higher than would be expected for a metal oxalate (as well as those precipitated by DES with water-based anti-solvent). The FTIR did show the presence of an oxalate species in the sample but the addition vibrational shifts (partially those associated with cobalt oxalate-DES mixture) would suggest that the sample is not a standard oxalate material.

A DSC scan (**Figure 3.18 b**) on the sample (at a heating rate of  $1\text{ °C min}^{-1}$ ) showed that the mass loss at  $350\text{--}370\text{ °C}$  (appearing at a lower temperature

in the DSC due to the lower heating rate) contributed to two large exothermic peaks, which would indicate that there was a two-part decomposition occurring (as was partially seen in the differential of the TGA). This two-part decomposition could possibly be the two components (choline chloride and oxalic acid/ cobalt oxalate) although this is above their expected decomposition temperatures.

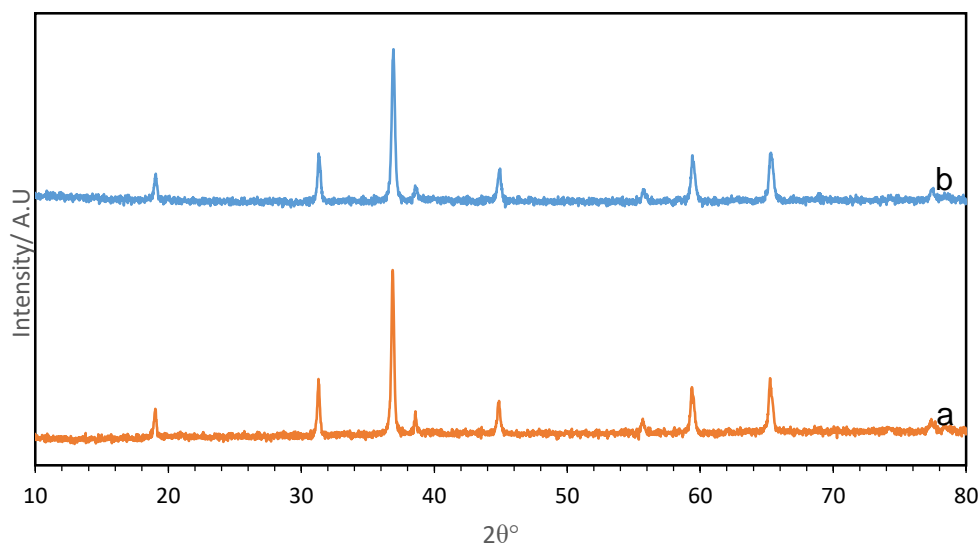


**Figure 3.19: XRD of the DES anti-solvent prepared cobalt oxide (calcined 500 °C) with anti-solvent mixture of a) water and b) made using anhydrous oxalic acid**

The XRD patterns (**Figures 3.19 and 3.20**) of the cobalt oxalates prepared with the different anti-solvents calcined at 300 °C showed the reflections of  $\text{Co}_3\text{O}_4$  with no other crystalline substance being present. Although the catalyst precipitated with methanol as the anti-solvent formed at a lower temperature the TGA determined although the mass loss did start to occur at 300 °C (from differential and DSC).

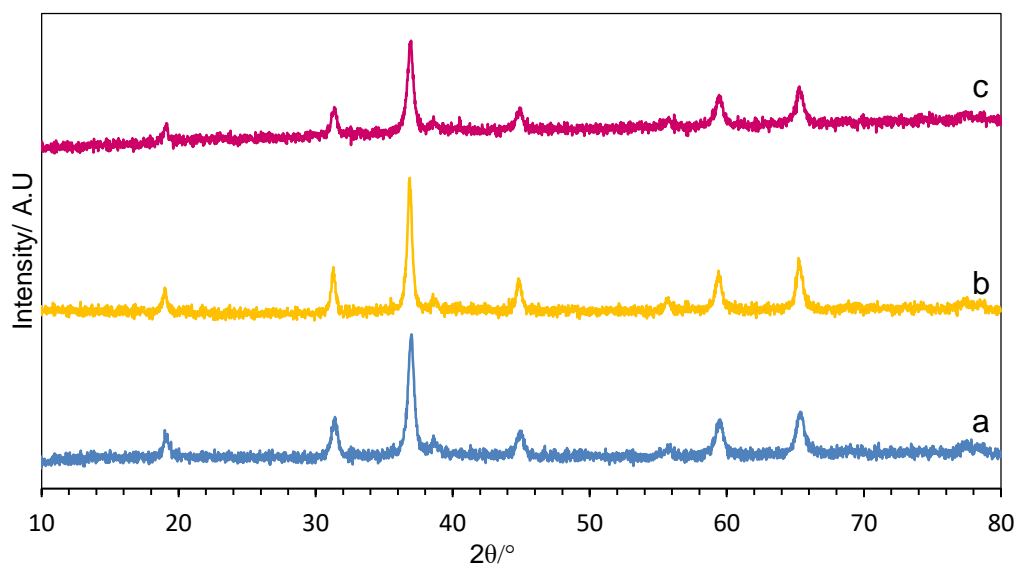


**Figure 3.20: XRD patterns of the DES-anti-solvent prepared cobalt oxides (calcined 300 °C) using anti-solvent of a) 50:50 water ethanol, b) water fast and c) methanol**

The different anti-solvents caused some variations in both crystallite size and surface areas (**Table 3.4**). The water precipitated oxalate calcined at 300 °C shows lower surface area ( $38 \text{ m}^2 \text{ g}^{-1}$ ) than the precipitate calcined at 300 °C with the water-ethanol or pure methanol precipitated oxalate showing surface area of  $52\text{-}54 \text{ m}^2 \text{ g}^{-1}$ . The samples calcined at 500 °C all show similar surface area of  $11\text{-}17 \text{ m}^2 \text{ g}^{-1}$  and larger crystallite sizes resulting from the sintering that occurred.

**Table 3.4: Surface area ( $\pm 2 \text{ m}^2 \text{ g}^{-1}$ ) and crystallite size of the calcined cobalt oxalates prepared by DES with various anti-solvents. n/a is used for values not taken.**

Sample	300 °C		500 °C	
	Surface area/ $\text{m}^2 \text{ g}^{-1}$	Crystalline size at $2\theta=36.9^\circ$ /nm	Surface area/ $\text{m}^2 \text{ g}^{-1}$	Crystalline size at $2\theta=36.9^\circ$ /nm
Anhydrous Water-ethanol	n/a	n/a	16	40.5
Water-ethanol	54	19.8	15	39.6
Water-slow injection	38	26.1	17	47.9
Water fast injection	n/a	n/a	11	45.3
Methanol	52	22	n/a	n/a

The effect of the anti-solvent mixture on the morphology of the oxalate was observed in the SEM images of the samples (**Figure 3.21**). The morphology did not change with the different rate of addition of the water-ethanol anti-solvent to the DES. Changing the anti-solvent to water-methanol showed the same needle shaped cobalt oxalates that had occurred when water-ethanol was used.

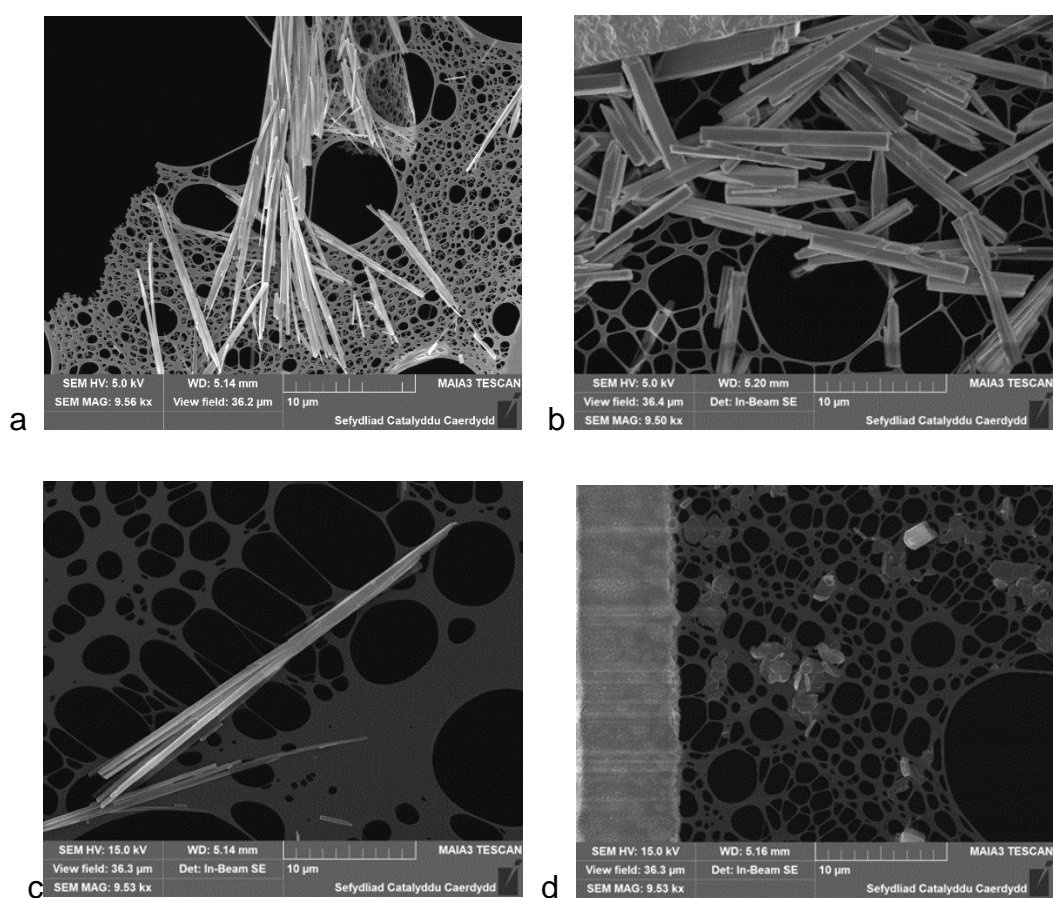


**Figure 3.21 SEM images of the cobalt oxalate prepared with different anti-solvents a) 50:50 water ethanol (fast), b) water slow, c) 50:50 water methanol and d) methanol**

The sample precipitated in water, with slow addition, showed some difference in morphology to the water-ethanol and water-methanol precipitated cobalt oxalates. The slow water precipitated cobalt oxalates still formed liner/rod like but these rods were both wider and shorter than the water-ethanol precipitated oxalate. This is in contrast to previous publications on the precipitation of zinc oxide from choline chloride urea which favours a more linear growth with pure water than water-ethanol mixture<sup>8</sup>.

The methanol precipitated sample (**Figure 3.21 d**) showed a very different morphology with plate shaped particles rather than the rods that were observed with the water and water alcohol precipitated oxalate. However, this precipitate was not a pure oxalate with some trace of DES/choline chloride remaining in the samples. The sample was only washed with methanol and had no water wash which would have removed the remaining DES but might not have formed the needles seen with water-methanol anti-solvent.

The SEM of the methanol precipitated sample after calcination at 300 °C (**Figure 3.22 a**) showed clusters of cobalt oxides that resembles the oxalate gel  $\text{Co}_3\text{O}_4$  rather than the rod or needle structures that formed after precipitation from the DES in the water and water-alcohol anti-solvents. This is due to the precursor still being a partial mixed in the DES with no defined morphology resulting in the calcined oxide forming clusters of oxide crystallites rather than the rod-shaped clusters that the water-ethanol and water precipitated cobalt oxide had formed.

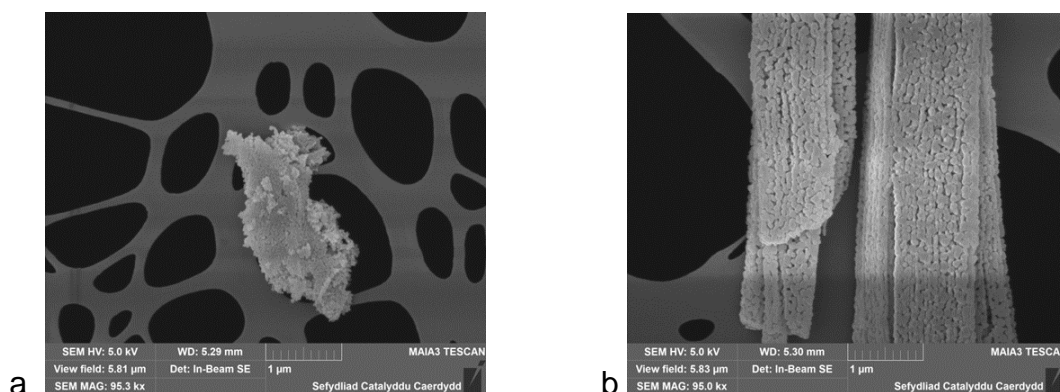


**Figure 3.22: SEM of the  $\text{Co}_3\text{O}_4$  catalysts formed from the DES a) methanol anti-solvent calcined 300 °C and b) water anti-solvent calcined 500 °C**

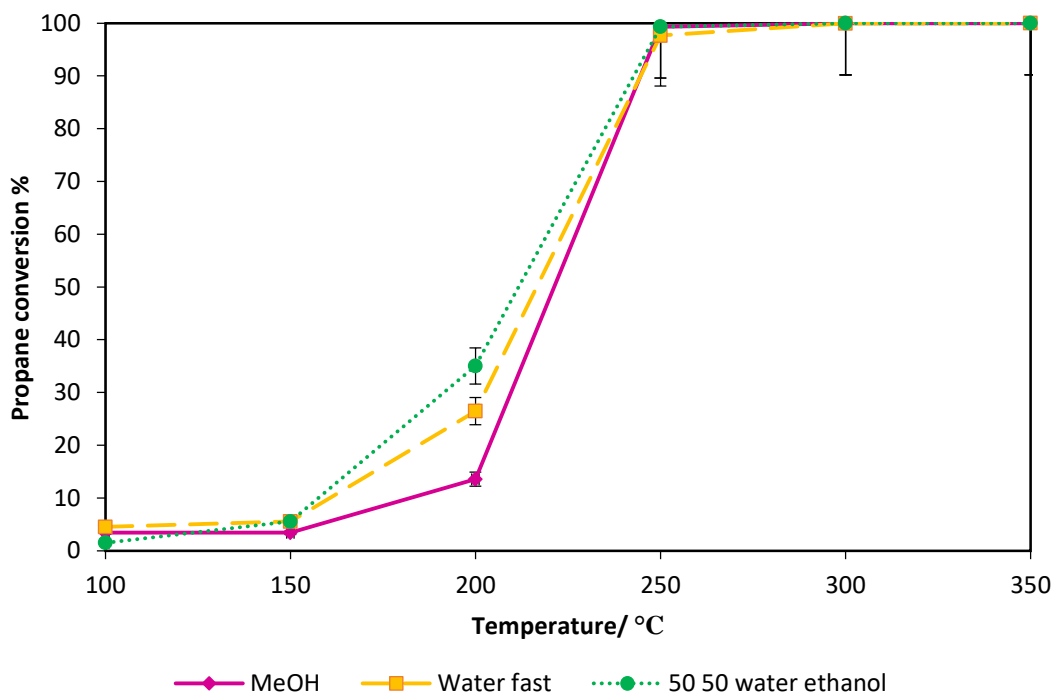


**Figure 3.23: Propane conversion using cobalt oxide catalysts prepared by DES anti-solvent calcined at 300 °C, 50-55 mg of catalyst, GHSV= 6200h<sup>-1</sup>**

The cobalt oxide (calcined at 300 °C) from the cobalt oxalate precipitated in the water-ethanol anti-solvent mixture was shown to be the most active propane oxidation catalysts out of the DES anti-solvent cobalt oxides. This is likely due to the higher surface area and smaller crystallite size than the water precipitated cobalt oxide. The methanol precipitated catalyst was shown to be the least active catalyst despite similar crystallite size and surface area. This is most likely due to the presences of residual choline chloride in the precursor sample which resulted in residual chloride species present in the calcined oxide which would have poisoned the catalyst and reduced its catalytic activity. However, all of these catalysts showed close to 100% propane conversion by 250 °C. Comparison of these catalysts to previous studies, from the literature<sup>20</sup>, on Co<sub>3</sub>O<sub>4</sub> catalysts synthesised by supercritical anti-solvent) showed that the DES precipitated catalysts showed similar conversion at 200 °C and 250 °C to the less optimised SAS Co<sub>3</sub>O<sub>4</sub> catalysts (calcined at 400 °C). However the more optimised SAS catalysts (that had 5-10% water/ethanol solvent) showed greater propane conversion

at lower temperatures compared to the DES-oxalate catalysts, especially those that were calcined at lower temperatures, showing 100% propane conversion at 200 °C<sup>20</sup>, compared to the 13-35 % propane (at 200 °C) conversion seen with the DES-oxalate prepared cobalt oxides (calcined at 300 °C)

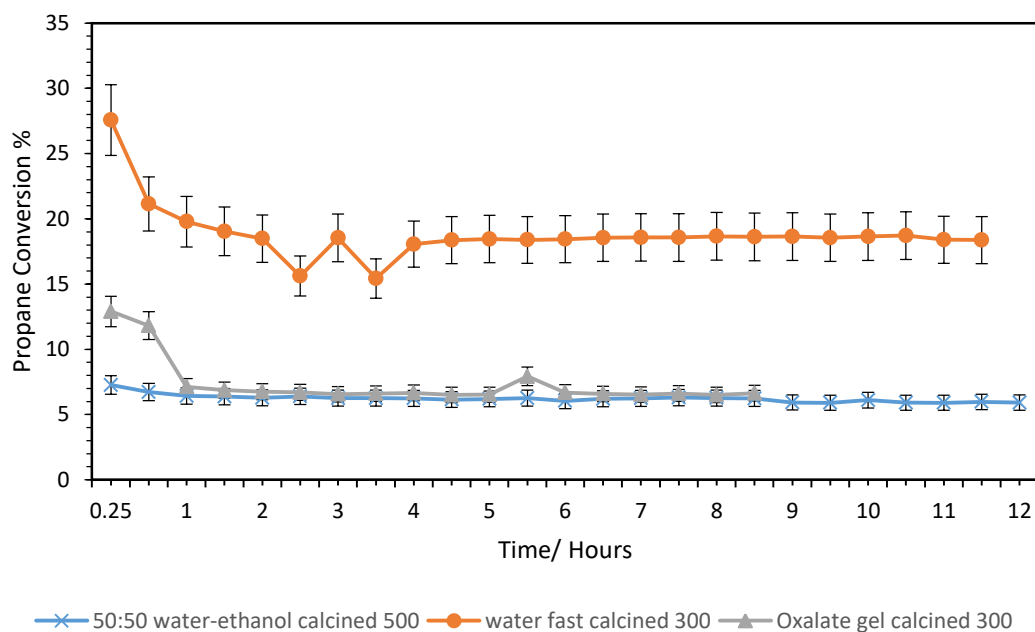


**Figure 3.24: Long term propane oxidation at 200 °C using cobalt oxide catalysts (75 mg) precipitated from DES and the oxalate gel-methods (error 9.8 %)**

The stability of the DES anti-solvent derived catalysts and one prepared by oxalate gel was investigated by performing propane oxidation at 200 °C for up to 12 hours (**Figure 3.24**). All three cobalt oxide catalysts showed an initial decrease but all stabilised within the first two hours. What is notable is that 50:50 water-ethanol precipitated catalysts showed the lowest deactivation while the catalyst precipitated in water with a fast anti-solvent (calcined 300 °C) showed a more rapid deactivation with a drop in propane conversion (from 28% to 19%) within the first hour and took longer to stabilise. The oxalate gel catalyst calcined at 300 °C appeared to be less active than the DES-water precipitated catalysts and also had a drop in propane conversion within the first hour.

### 3.3 Iron oxalate

The DES anti-solvent methodology was also applied for the precipitation of iron oxalate as iron oxide precursors. The salt that was chosen to dissolved in the DES mixture was iron (II) acetate to form iron (II) oxalate since iron (III) oxalates are soluble in water<sup>31</sup>. The iron oxalate was precipitated in two anti-solvent mixtures; 50:50 water-ethanol and pure water with slow addition of anti-solvent to solvent. Although the anti-solvent dissolved in the DES-iron oxalate better than the cobalt-DES vigorous stirring was still required to break up the gel that had formed.

The XRD patterns (**Figure 3.25**) of both iron precipitates confirmed that iron (II) oxalate had formed. The anti-solvent seemed to change the precipitated material with the water-ethanol only showing one reflection at  $18.4^\circ$  (2 0 0) whereas the water precipitated oxalate showing two reflections at  $18.4^\circ$  (2 0 0) and  $18.2^\circ$  (possibly from the (1 1 0)) as well as a larger reflection at  $2\theta=28.3^\circ$  (-3 1 2). This showed that the two anti-solvents precipitated different forms of iron oxalate similar to what was seen with the cobalt oxalate (Section 3.2.3).

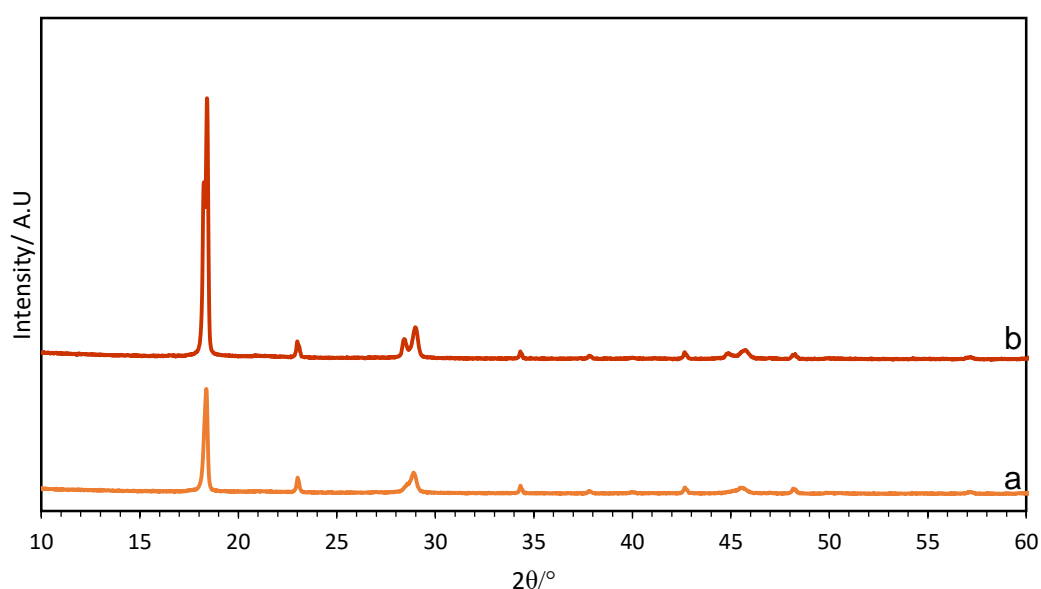


**Figure 3.25:** XRD of the iron oxalates precipitated from the DES in a) 50:50 water-ethanol and b) water

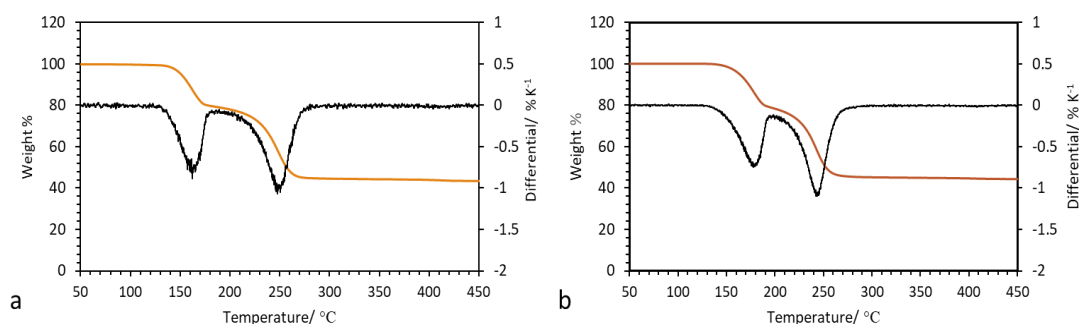


**Figure 3.26: TGA profile of the iron oxalate precipitated from DES in a) 50:50 water ethanol and b) water**

TGA profile for the two DES precipitated iron oxalates (**Figure 3.26**) show a loss of crystalline water occurring at 150 °C, followed by the main oxalate decomposition at 250 °C. There was no indication of any other decomposition product which showed that these samples were mostly iron oxalate and in addition the weight loss of 56% corresponding to the transition of iron oxalate to  $\text{Fe}_2\text{O}_3$ .

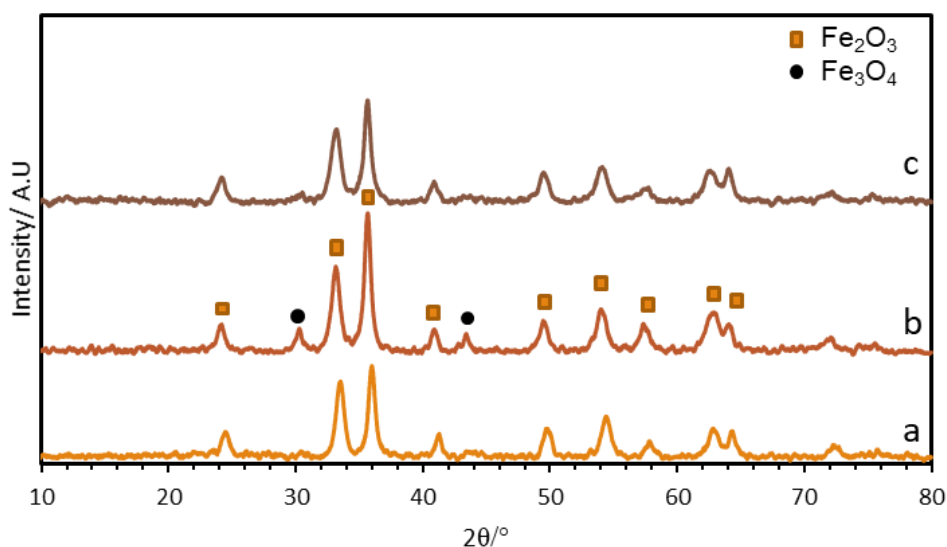


**Figure 3.27: XRD of the iron oxides calcined (300 °C) from the iron oxalates precipitated from DES in a) water, b) water-ethanol and c) calcined iron oxalate purchased from Sigma Aldrich**

The XRD of the calcined iron oxide at 300 °C (**Figure 3.27**) had confirmed the degradation of the oxalate and the formation of primary  $\alpha\text{-Fe}_2\text{O}_3$  which was shown as the only phase present in the reference oxalate (**Figure 3.27 c**) and the DES oxalate precipitated in water. The iron oxide derived from the

50:50 water:ethanol precipitated oxalate showed additional reflections at  $2\theta=30.5^\circ$  and  $43.6^\circ$  which could indicate the possible presence of  $\text{Fe}_3\text{O}_4$  or originating from  $\gamma\text{-Fe}_2\text{O}_3$  which has its reflections in the same region. Although given that iron oxalate degrades to  $\gamma\text{-Fe}_2\text{O}_3$  under inert atmosphere and  $\text{Fe}_3\text{O}_4$  under a static air<sup>15</sup> atmosphere the latter is more likely the phase. The iron oxide formed from the oxalate that was precipitated in water-ethanol mixture had an overall lower surface area (**Table 3.5**) than the iron oxide precipitated in water ( $221 \text{ m}^2 \text{ g}^{-1}$ ), with the samples generally having increased surface area with decreasing crystallite size at  $2\theta=35.7^\circ$  (1 1 0).

**Table 3.5: Surface area (BET 5 point) and crystallite size for the iron oxides after calcination of the iron oxalates at 300 °C, 3 hours, 2 °C min<sup>-1</sup>**

Iron oxide/oxalate sample	Surface area/ $\text{m}^2 \text{ g}^{-1}$	Crystallite size $2\theta=35.7^\circ$
Water	221 ( $\pm 10$ )	15.6
50:50 water-ethanol	55 ( $\pm 2$ )	19.2
Sigma Aldrich iron oxalate dihydrate	108 ( $\pm 10$ )	16.4

SEM images (**Figure 3.28**) of the iron oxalate showed that like the cobalt oxalate precipitated from the DES iron oxalate formed liner-rod like structures. However, the behaviour of iron oxalate in two anti-solvent mixtures differs to cobalt oxalate in that the iron oxalate precipitated in water showed longer and thinner rods whereas the iron oxalate precipitated in the water-ethanol mixture shows mostly shorter wider rods although some longer rods were present but less abundant.

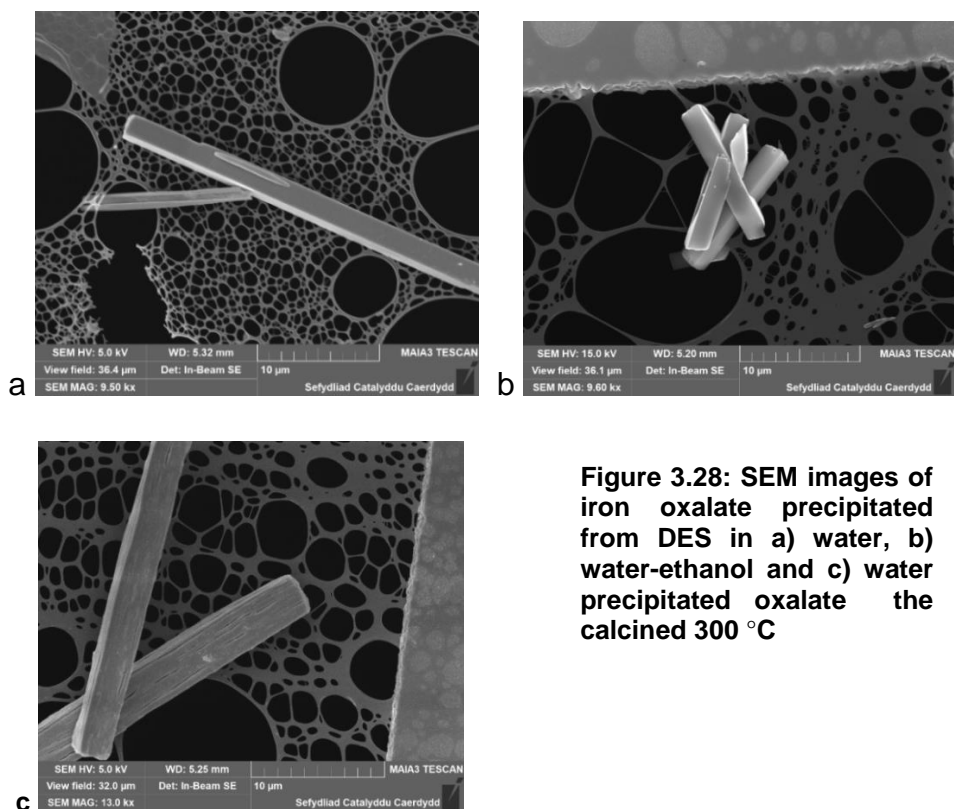


**Figure 3.28: SEM images of iron oxalate precipitated from DES in a) water, b) water-ethanol and c) water precipitated oxalate the calcined 300 °C**

This seems to correspond to the surface areas of the oxides as the iron oxide calcined from the iron oxalate precipitated in water had a higher surface area and longer rods whereas the iron oxide from the iron oxalate precipitated in the water-ethanol mixture that had shorter, wider rods with a lower surface area. The iron oxides retained the rod-like structure is after calcination at 300 °C. The high surface area could also be contributed to porosity of the water precipitated iron oxalate but without a more in depth surface area analysis it cannot be certain that this is the case.

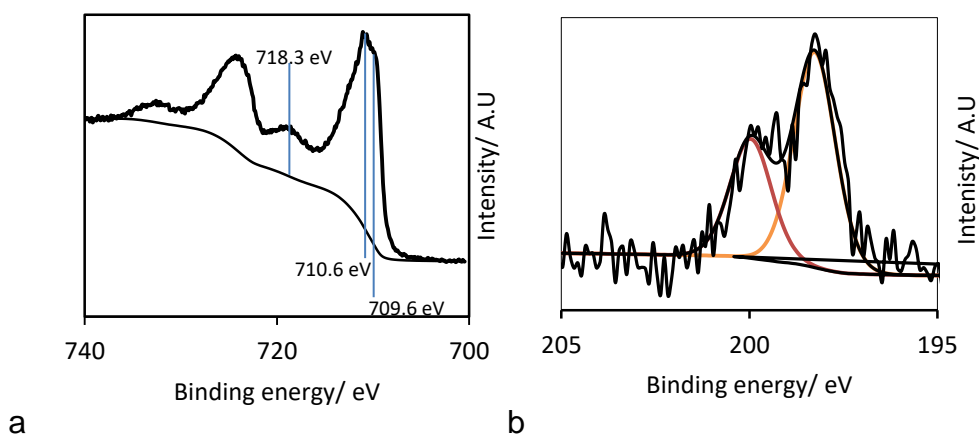


**Figure 3.29: XPS of the Iron oxide calcined from iron oxalate precipitated in water a) Fe 2p and b) Cl 2p regions**

XPS of the Cl 2p region (**Figure 3.29 b**) shows the presence of the chloride species in the final oxide even after washing and calcination at 300 °C. The binding energy of the Cl peak at 198.1 eV and 199.5 eV is within the region associated with metal chloride, which indicated that chlorine is binding to the iron rather than originating from residual organic chlorides that may have still been present. In comparison, there was no indication from XPS of chlorine present in the cobalt samples. The anti-solvent addition on the cobalt oxalate was greater than the iron and therefore more washing may be required to remove the chloride species. The Fe region (**Figure 3.29 a**) shows that the material precipitated in water was  $\alpha$ -Fe<sub>2</sub>O<sub>3</sub> based on the position of the satellite binding energy of 718.3 eV and the asymmetrical peak at 709.6 eV and 710.6 eV<sup>32</sup>.

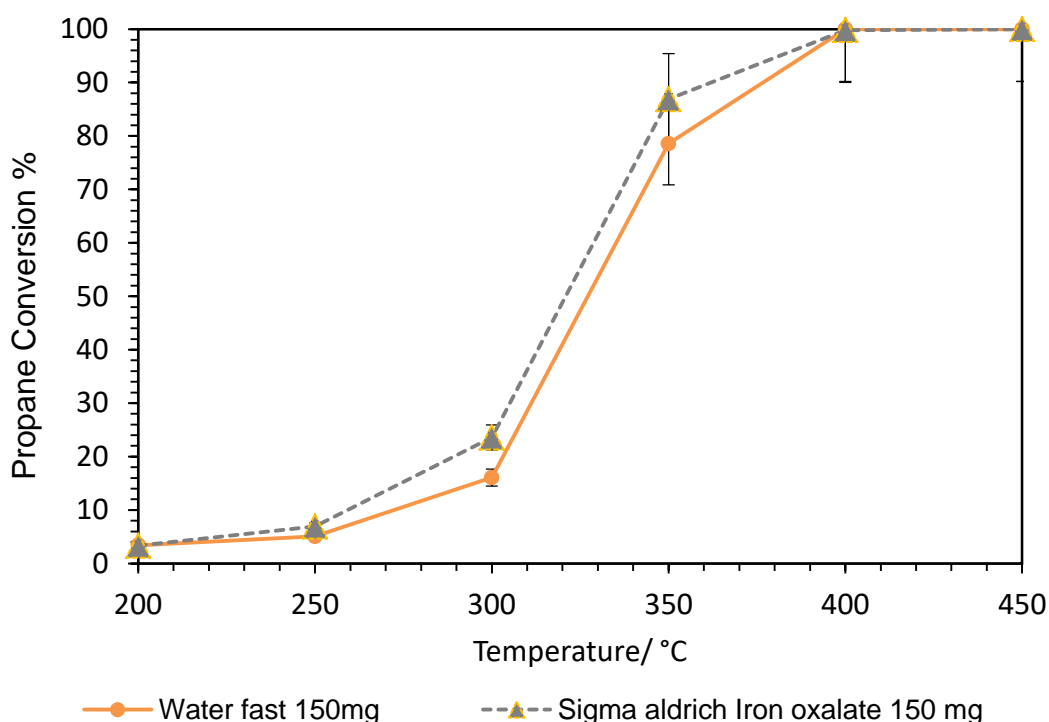


**Figure 3.30: Propane conversion of the iron oxides made from iron oxalate calcined at 300 °C at a GHSV of 6200 h<sup>-1</sup>.**

The propane conversion (**Figure 3.30**) between the water-fast anti-solvent precipitated catalyst and the iron oxide the was calcined from stock iron oxalate did not show significant difference in terms of propane conversion and light-off temperature despite having lower surface, with the stock showing a slightly better performance.

Like the cobalt oxalate, the 50:50 precipitated iron oxide had a much lower density and therefore the catalyst mass used to maintain the same volume (and GHSV). However, when the activity is normalised to surface area (**Figure 3.31**) the iron oxide precipitated from DES both showed similar activity at 300 °C, although at 350 °C the water precipitated catalyst was shown to be more active (due to the lower light off). The calcined oxalate catalyst however was more active in this respect than the DES precipitated catalysts.

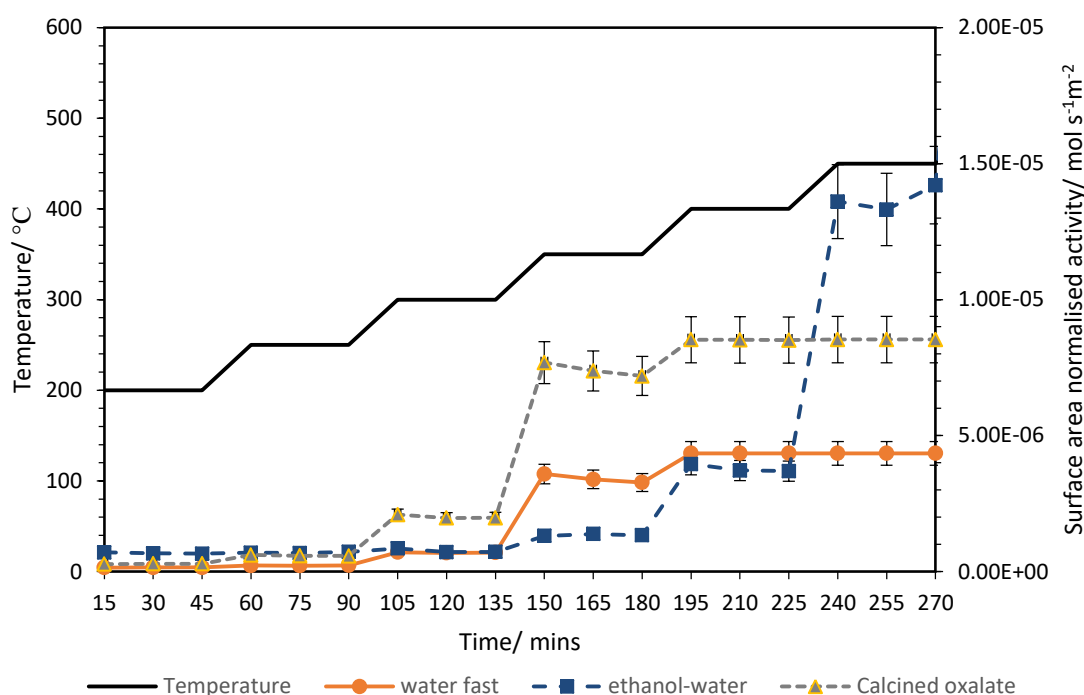


**Figure 3.31: Surface area normalised activity of the iron oxide catalysts prepared by DES and reference catalysts (error  $\pm 10\%$  taking into account error of surface area and catalyst mass)**

### 3.4 Manganese oxalate

Three manganese precursors were dissolved into the choline chloride-oxalic acid mixture: manganese chloride tetrahydrate, manganese acetate tetrahydrate and manganese nitrate tetrahydrate, to observe the effect of the salt on the morphology of the manganese oxalates precipitated from the DES using as the water anti-solvent.

The XRD patterns of the precipitates (**Figure 3.32**) confirmed the formation of manganese oxalate with all of the manganese precursors. However, the relative intensities of the reflections showed some variations between the three samples, notably the chloride sample where the reflection at  $2\theta=18.4^\circ$  and  $18.8^\circ$ , which correspond to the  $(-2\ 0\ 2)$  and  $(2\ 0\ 0)$ , are partially merged compared to those of the acetate and nitrate sample which had these reflections more as distinctively separate.

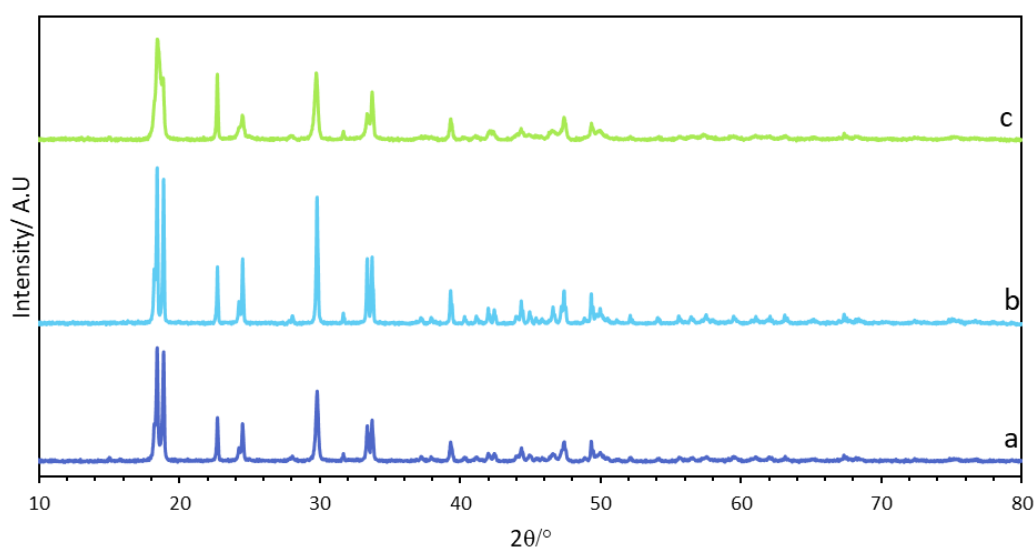


**Figure 3.32:** XRD of manganese oxalate precipitated from the DES (water anti-solvent) with the original manganese salt as a)  $\text{Mn}(\text{CH}_3\text{CO}_2)_2 \cdot 4\text{H}_2\text{O}$ , b)  $\text{Mn}(\text{NO}_3)_2 \cdot 4\text{H}_2\text{O}$  and c)  $\text{MnCl}_2 \cdot 4\text{H}_2\text{O}$

The TGA profile (**Figure 3.33**) of the precipitated manganese oxalates shows the expected profile<sup>16</sup> with the loss of crystalline water at  $115\text{--}145^\circ\text{C}$  followed by the main oxalate decomposition to  $\text{Mn}_5\text{O}_8$  (with some  $\text{Mn}_2\text{O}_3$ ) and  $\text{CO}_2/\text{CO}$ . The minor mass loss at  $450^\circ\text{C}$  occurred in the region where  $\text{Mn}_5\text{O}_8$  transforms into  $\text{Mn}_2\text{O}_3$ . The TGA profiles and the weight loss for these two

oxalates are almost identical showing that the initial manganese salt does not affect the degradation of the oxalate or the extent of residual choline chloride present.

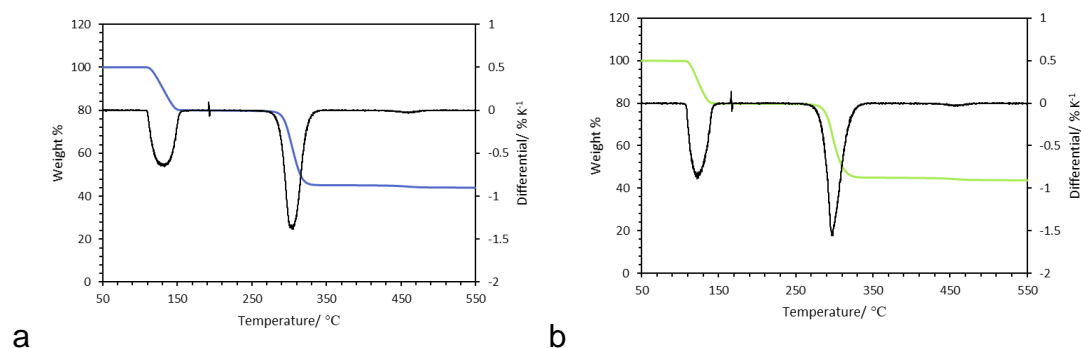


**Figure 3.33: TGA profile of manganese oxalate precipitated from DES with the original manganese salt as a)  $\text{Mn}(\text{CH}_3\text{CO}_2)_2 \cdot 4\text{H}_2\text{O}$  and b)  $\text{MnCl}_2 \cdot 4\text{H}_2\text{O}$**

The XRD pattern of the manganese oxalate (from manganese acetate) that was calcined at 350 °C (**Figure 3.34 a**) showed that the precursor had initially transformed into  $\text{Mn}_5\text{O}_8$  but would further oxidise to form  $\text{Mn}_2\text{O}_3$  at 500 °C. While the acetate sample was calcined at 350 °C and 500 °C, the TGA of the chloride sample showed a minor mass loss at 450 °C that is usually associated with the formation of  $\text{Mn}_2\text{O}_3$  from  $\text{Mn}_5\text{O}_8$ <sup>16</sup>.

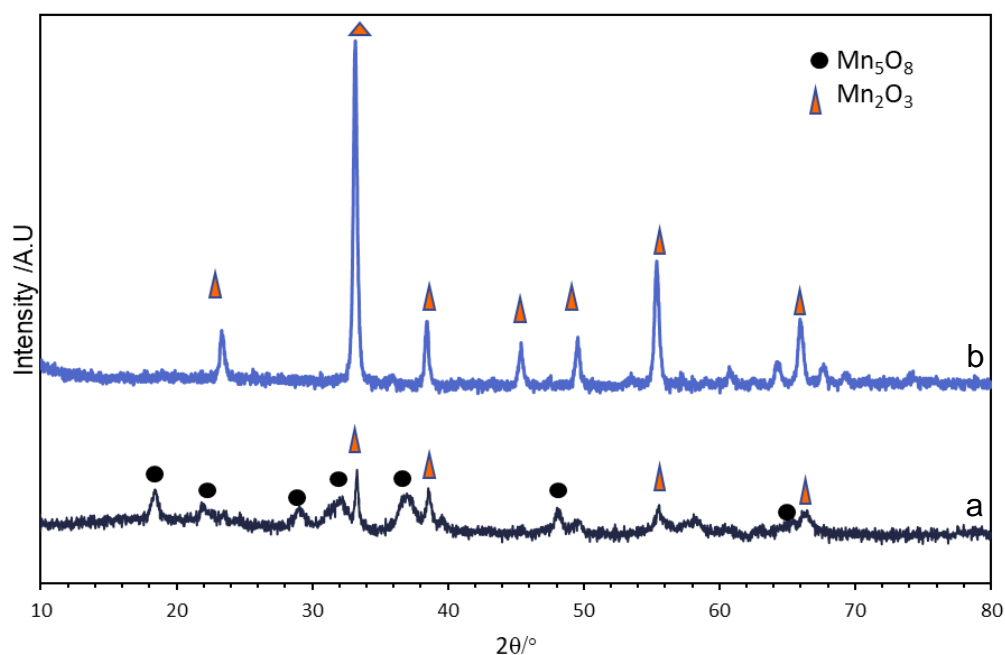


**Figure 3.34: XRD of manganese oxides from oxalate (acetate) formed at a) 350 °C and b) 500 °C**

The XRD patterns of all three samples (**Figure 3.35**) showed the formation of  $\text{Mn}_2\text{O}_3$  after calcination at 500 °C for 3 hours. The crystallite size at  $2\theta=33.1^\circ$  appear to vary when different precursors are used, although the surface areas of the three samples were within  $5 \text{ m}^2 \text{ g}^{-1}$  of each other and did not significantly vary for the different manganese salt used (**Table 3.6**).

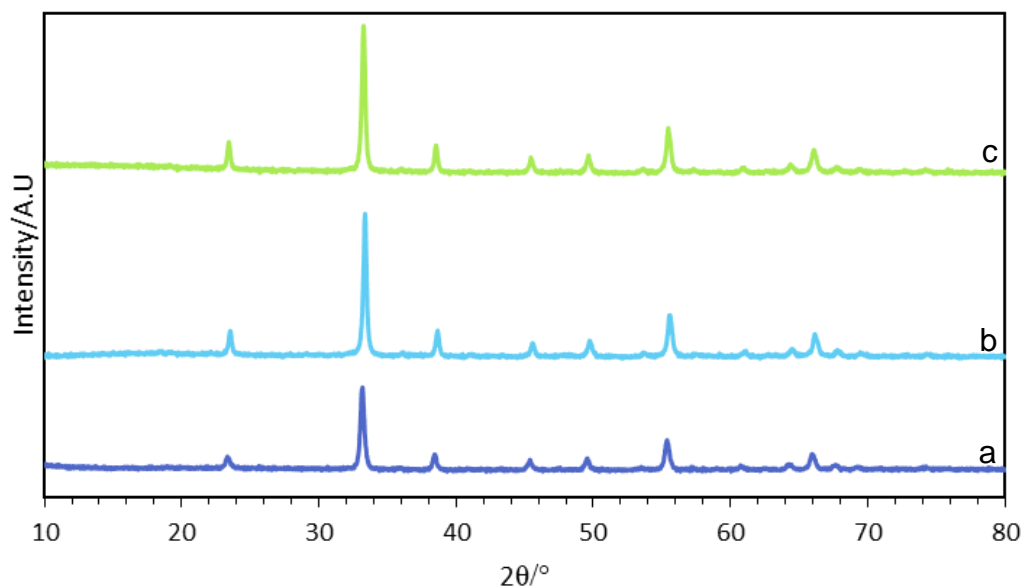


**Figure 3.35:** XRD patterns of the manganese oxides calcined at 500 °C from the oxalates precipitated from DES with the precursor manganese salt as a)  $\text{Mn}(\text{CH}_3\text{CO}_2)_2 \cdot 4\text{H}_2\text{O}$ , b)  $\text{Mn}(\text{NO}_3)_2 \cdot 4\text{H}_2\text{O}$  and c)  $\text{MnCl}_2 \cdot 4\text{H}_2\text{O}$

**Table 3.6:** Surface areas (error  $\pm 2 \text{ m}^2 \text{ g}^{-1}$ ) and crystallite size ( $\pm 2 \text{ nm}$ ) of the manganese oxalate and calcined derivatives

Manganese salt dissolved in DES	Manganese oxalate		$\text{Mn}_2\text{O}_3$ , 500°C	
	Surface area/ $\text{m}^2 \text{ g}^{-1}$	Crystal size $2\theta = 29.8^\circ$	Surface area/ $\text{m}^2 \text{ g}^{-1}$	Crystal size $2\theta = 33.1^\circ$
$\text{Mn}(\text{NO}_3)_2 \cdot 4\text{H}_2\text{O}$	2	64.1	26	30.8
$\text{Mn}(\text{CH}_3\text{CO}_2)_2 \cdot 4\text{H}_2\text{O}$	1	44.7	21	26.4
$\text{MnCl}_2 \cdot 4\text{H}_2\text{O}$	2	32.9	24	29.3

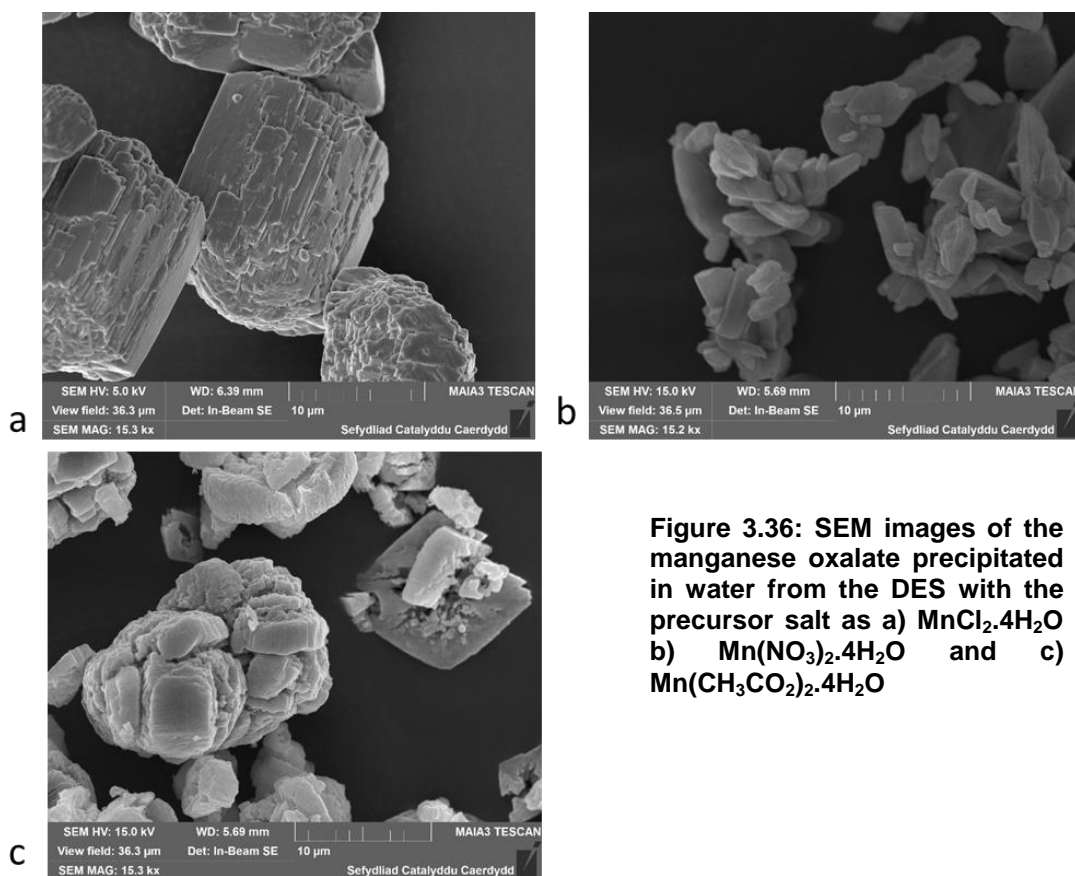


**Figure 3.36: SEM images of the manganese oxalate precipitated in water from the DES with the precursor salt as a)  $\text{MnCl}_2 \cdot 4\text{H}_2\text{O}$  b)  $\text{Mn}(\text{NO}_3)_2 \cdot 4\text{H}_2\text{O}$  and c)  $\text{Mn}(\text{CH}_3\text{CO}_2)_2 \cdot 4\text{H}_2\text{O}$**

The SEM images (**Figure 3.36**) of the manganese oxalates showed two interesting features. Firstly, the shape of the agglomerated particles differed between the three salts used with manganese chloride forming short and wide cylindrical shaped particles, nitrates forming smaller elliptical particles and acetates forming clusters of squared shaped particles.

The second interesting feature is that the shape of the manganese oxalates precipitated by DES is completely different from the rod-shaped cobalt oxalate and iron oxalate precipitated from DES. This shows that the metal oxalate precipitation during anti-solvent process varies with different metal/elements that are being precipitated. This suggests, the effect of the dissolved salt on the final shape of the oxalate might differ for each metal.

However, it should be noted that there was a delay from adding the anti-solvent to the DES in the precipitation of the manganese oxalate. It may be the case that the oxalate is not precipitating from the DES via the anti-solvent

procedure but dissolving in the water and precipitating from the oxalic acid present.

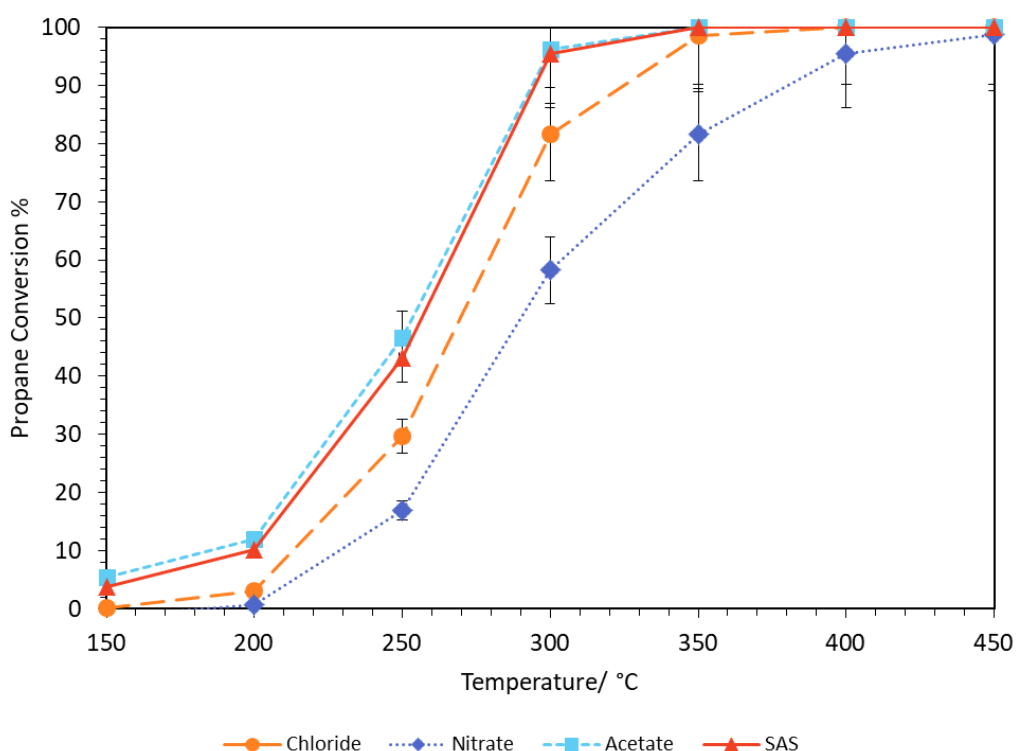


**Figure 3.37: Propane conversion using the manganese oxide catalyst calcined at 500 °C GHSV of 6200 h<sup>-1</sup>**

The propane total oxidation activity (**Figure 3.37**) for the three DES precipitated catalysts were compared to one made by supercritical anti-solvent precipitation which gives manganese carbonate that is then calcined at 400 °C. What is notable was that the acetate derived Mn<sub>2</sub>O<sub>3</sub> from the DES methodology showed similar activity to the Mn<sub>2</sub>O<sub>3</sub> oxide prepared by supercritical anti-solvent precipitated catalysts with a lower T<sub>50</sub> and similar T<sub>10</sub> (**Table 3.7**). The nitrate derived catalyst performed the worse despite having a slightly higher surface area than the other manganese oxides with T<sub>90</sub> at 368 °C compared to 294 °C for the acetate derived catalyst.

**Table 3.7:  $T_{10}$ ,  $T_{50}$  and  $T_{90}$  for the DES oxalate prepared  $Mn_2O_3$  catalyst and SAS precipitated  $Mn_2O_3$**

$Mn_2O_3$	$T_{10}$	$T_{50}$	$T_{90}$
SAS	199	260	295
DES nitrate	229	290	368
DES chloride	213	270	324
DES acetate	197	253	294

### **3.5 The preparation of mixed metal oxides using DES-oxalate method**

The previous sections have demonstrated that choline chloride-oxalic acid based DES can be used to precipitate single metal oxalate of cobalt, iron and manganese with anti-solvents with the ability to control morphology (at least for cobalt and iron oxalates). However the ability of the technique to make mixed metal oxalate and mixed metal oxides is just as important since mixed cobalt manganese and iron manganese catalysts are potentially useful catalysts<sup>33</sup>. Previous publications have shown that mixed cobalt-manganese oxalate prepared by oxalate gel and co-precipitation are a good precursor for the mixed oxides<sup>34</sup>.

Therefore, three mixed metal oxalates were made using the DES-oxalate method with the 50:50 water-ethanol anti-solvent; mixed  $CoMnO_x$  with fast and slow anti-solvent addition and a mixed  $FeMnO_x$  all having 1:1 metal ratio.

### 3.5.1 Cobalt manganese oxalate

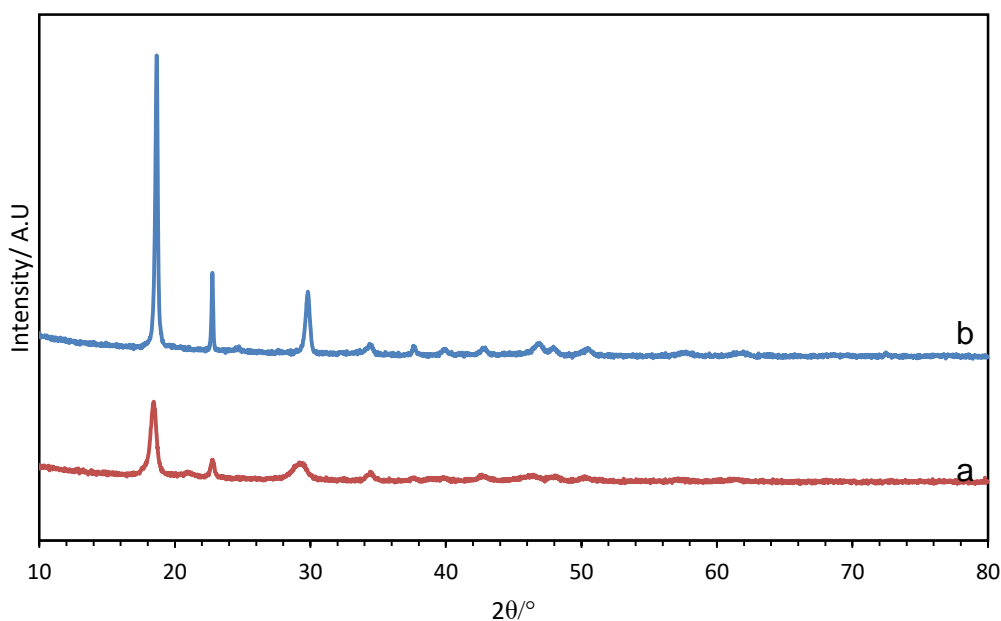


**Figure 3.38: XRD patterns of mixed Cobalt-manganese oxalate: a) oxalate gel method and d) DES method using 50:50 water-ethanol anti-solvent (fast).**

The XRD patterns of the cobalt manganese precipitate (**Figure 3.38**) shows reflections of a metal oxalate, with both cobalt oxalate and mixed cobalt manganese oxalate producing the same XRD patterns  $2\theta=18.6^\circ$ ,  $22.7^\circ$  and  $29.7^\circ$ . However, there is no indication of reflections that might originate from phase separated manganese oxalate which suggest that the metals are well integrated in one phase. The DES anti-solvent precipitated oxalate also appeared to have a higher degree of crystallinity than the oxalate gel prepared sample.

The XRD patterns of the calcined cobalt manganese oxides (**Figure 3.39**) only shows the reflections that could be assigned to either  $\text{Co}_3\text{O}_4$  or a mixed  $\text{Mn}_x\text{Co}_{3-x}\text{O}_4$ . A  $\text{Co}_{1.5}\text{Mn}_{1.5}\text{O}_4$  (1:1 Mn:Co) would produce this XRD pattern while cobalt-manganese oxide spinel with higher manganese content (2:1 Mn:Co) would give a different structure and produce a different XRD pattern<sup>35</sup>.

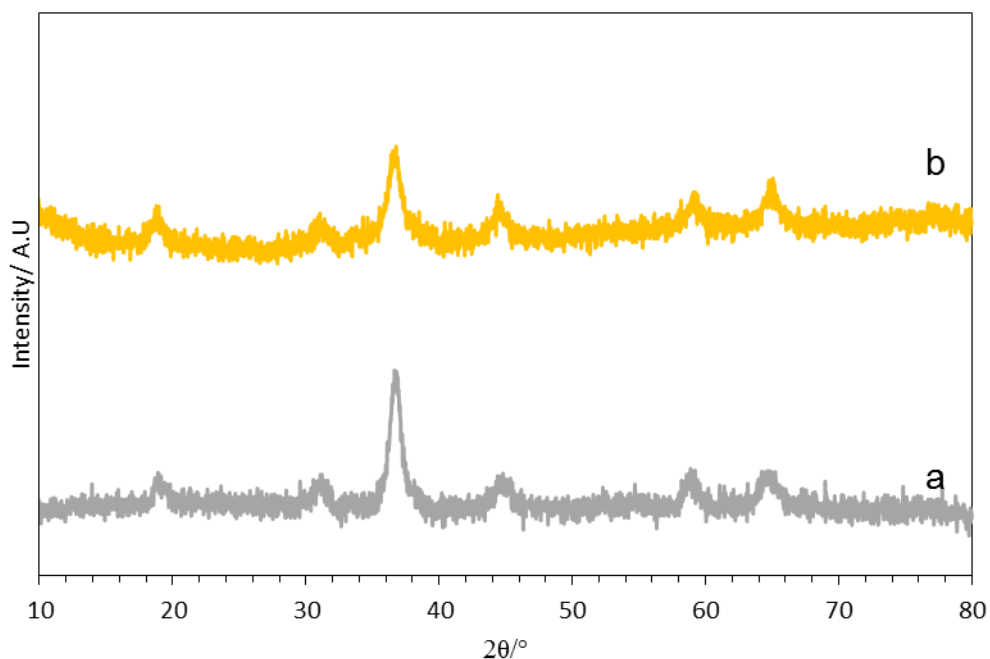


**Figure 3.39: XRD of the mixed cobalt-manganese oxide calcined at 300 °C precipitated in 50:50 water ethanol a) fast and b) slow injection**

There were no reflections visible that would indicate the presence of isolated manganese oxide (at least after calcination at 300 °C) suggesting that the manganese was either well integrated in a mixed cobalt-manganese oxide spinel or was not crystalline enough to be detected by XRD. The decrease in crystallinity might also be due to the substitution of manganese into the cobalt oxide structure. MP-AES (**Table 3.8**) analysis showed that there was a ratio close to 1:1 cobalt: manganese for both fast and slow precipitation showing that the cobalt and manganese precipitated close to the expect ratio. This would confirm that the calcined catalyst was a mixed cobalt manganese spinel oxide  $\text{Co}_{1.5}\text{Mn}_{1.5}\text{O}_4$  and the lack of manganese oxide reflections was not due to the lack of manganese in the material.

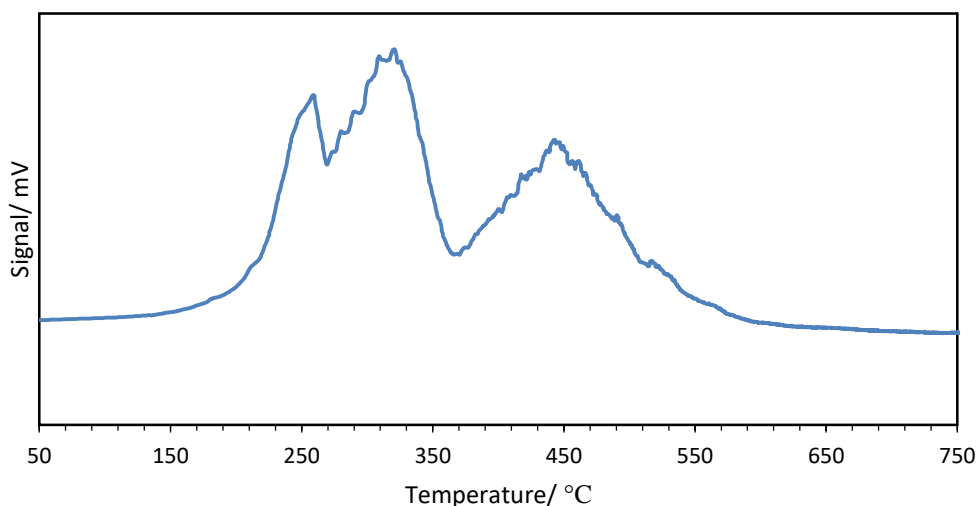


**Figure 3.40: TPR of cobalt-manganese oxide (calcined 300 °C) from the mixed oxalate that was precipitated in 50:50 water-ethanol anti-solvent (fast)**

TPR on the cobalt manganese oxide from 50:50 water-ethanol, calcined 300 °C (**Figure 3.40**) showed three main reductions at 260 °C, 325 °C and 450 °C. The first two reductions can be assigned to the cobalt reduction of Co(III) to Co(II) followed by the reduction of Co(II) to metallic Co<sup>34</sup>. The final reduction peak observed at 450 °C can be assigned to the reduction of the manganese phase, which is lower than the usual manganese reduction due to the presence of cobalt<sup>34</sup>. The TPR profile confirmed that the manganese and cobalt were both present which confirms, along with the MP-AES, that both cobalt and manganese precipitated during the anti-solvent process.

XPS on the Co 2p region of the mixed cobalt manganese (**Figure 3.41 a**) shows the main Co 2p<sub>3/2</sub> peak at 780.4 eV and 2p<sub>1/2</sub> at 795.6 eV. What is notable is the satellite at 786.5 eV is stronger in the mixed sample than it is in the pure Co<sub>3</sub>O<sub>4</sub> precipitated in the water-ethanol (calcined at 500 °C).

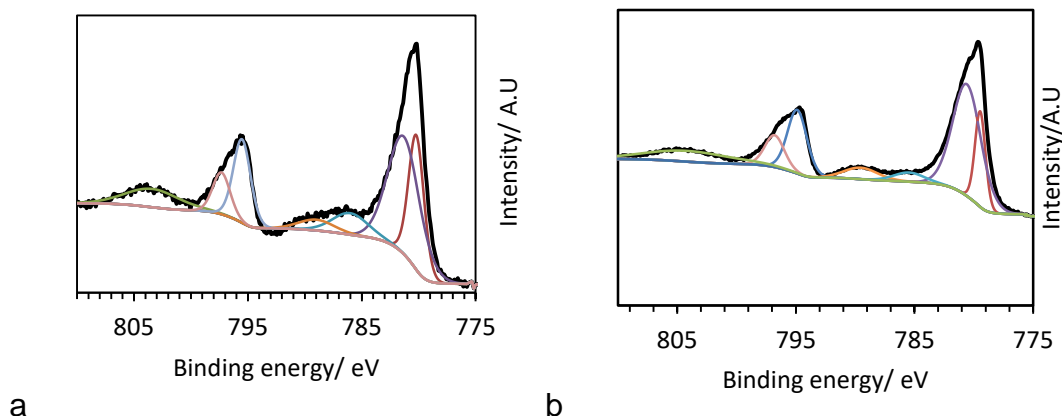


**Figure 3.41: XPS Co 2p region of a)  $\text{CoMnO}_x$  and b)  $\text{Co}_3\text{O}_4$  prepared by DES-oxalate**

In comparison, the Co 2p region of the cobalt oxide (**Figure 3.41 b**) precipitated from the DES shows a more typical  $\text{Co}_3\text{O}_4$  spectra featuring the satellite at 789.6 eV but no (or very weak) peak at 786.5 eV. This change in the Co XPS in the mixed cobalt manganese oxide compared to the  $\text{Co}_3\text{O}_4$  is similar to what has previously been shown for mixed cobalt manganese oxides<sup>36</sup>, providing further evidence that the cobalt manganese precipitated as a mixed system has some extent of the mixed oxide phase rather than phase separated cobalt oxide and manganese oxide.

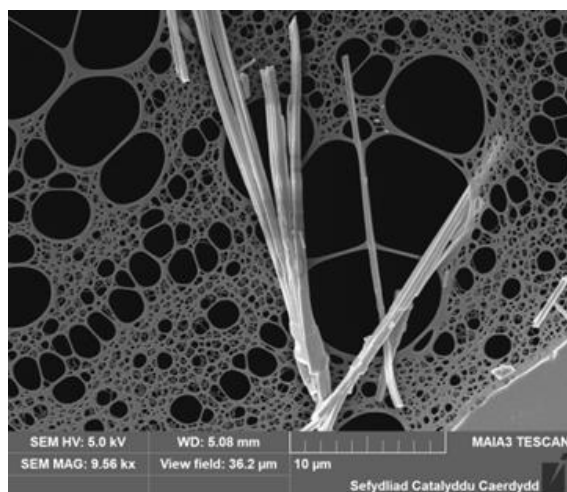


**Figure 3.42: SEM image of the cobalt manganese oxalate precipitated (slow inject) from DES into 50:50 water:ethanol anti-solvent**

SEM of the cobalt manganese oxalate (**Figure 3.42**) showed the formation of the linear-rod shaped particles that the single cobalt oxalate precipitated in the water-ethanol anti-solvent mixtures. This would suggest that the influence of the cobalt during the precipitation stage is higher than the manganese.

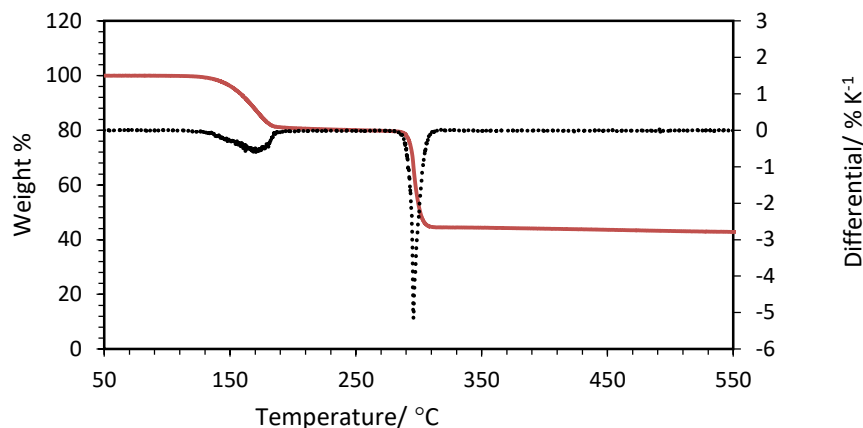


**Figure 3.43: TGA profile of the cobalt manganese oxalate precipitated from DES in 50:50 water:ethanol anti-solvent**

The TGA profile of both cobalt-manganese oxalate (**Figure 3.43**) showed the typical metal oxalate profile with only two mass losses at 140-185 °C (loss of crystalline water) and a sharper mass loss at 290 °C, associated with degradation of the oxalate to CO, CO<sub>2</sub> and the mixed metal oxide.

**Table 3.8: BET surface area ( $\pm 2 \text{ m}^2 \text{ g}^{-1}$ ), crystallite size and Co:Mn (determined by MP-AES) for the cobalt manganese oxides (calcined 300 °C) from DES in 50:50 water ethanol anti-solvent**

Sample	Surface area calcined 300 °C/ $\text{m}^2 \text{ g}^{-1}$	Crystallite size $2\theta=36.8^\circ$	Co: Mn (molar ratio) from MP-AES
Co Mn fast	58	10.8	1:1
Co Mn slow	60	8.0	1:1

### 3.5.2 Iron manganese oxalate

The XRD pattern of the mixed iron-manganese oxalate (**Figure 3.44**) was predominately that of manganese oxalate indicated that although manganese and iron oxalate have similar patterns and the iron reflections may be masked by the manganese oxalate. The MP-AES of the iron manganese gave a Fe: Mn ratio of 1:1.5 showing that there was an excess of manganese present in this sample indicating that manganese oxalate may have been the predominant phase that precipitated.

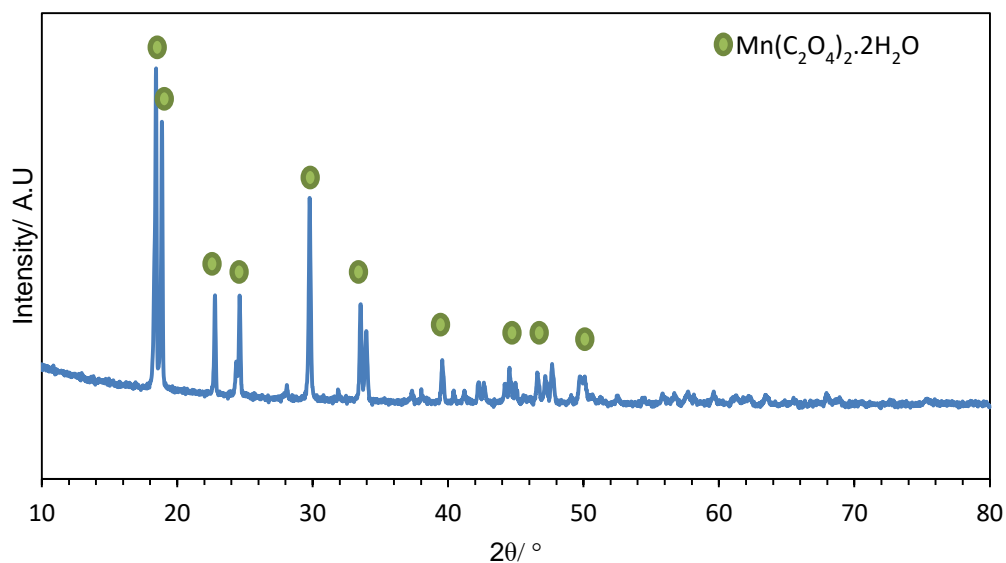


**Figure 3.44:** XRD of the iron manganese oxalate precipitated from the DES in 50:50 water ethanol

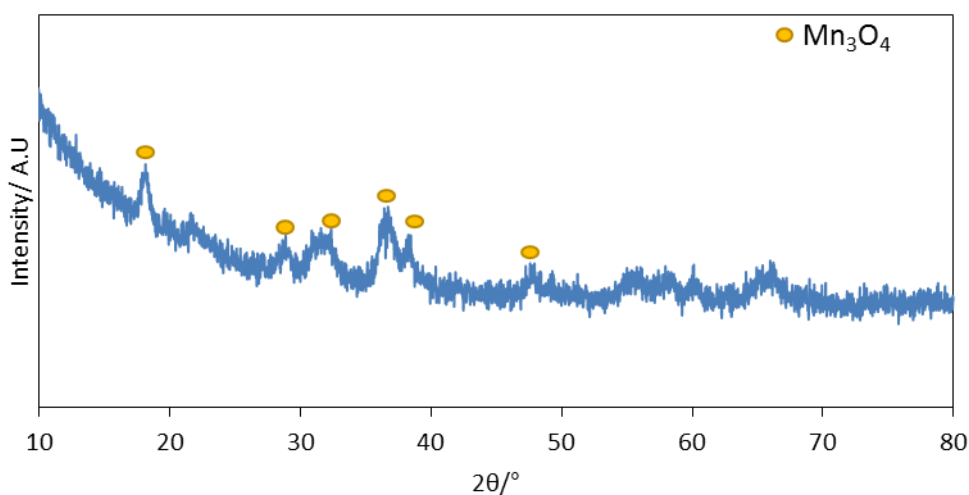


**Figure 3.45:** XRD of the mixed iron manganese oxide catalyst calcined from the iron manganese oxalate at 300 °C

The XRD pattern of the calcined iron-manganese material (**Figure 3.45**) showed reflections at  $2\theta=18.5^\circ$ ,  $29.0^\circ$ ,  $31.8^\circ$  and  $36.8^\circ$  that are assigned to  $\text{Mn}_3\text{O}_4$  phase. This would suggest that there was some degree of phase separation that had occurred with this material. Although the MP-AES

showed iron present in this sample there were no XRD reflection associated any iron oxide phase.

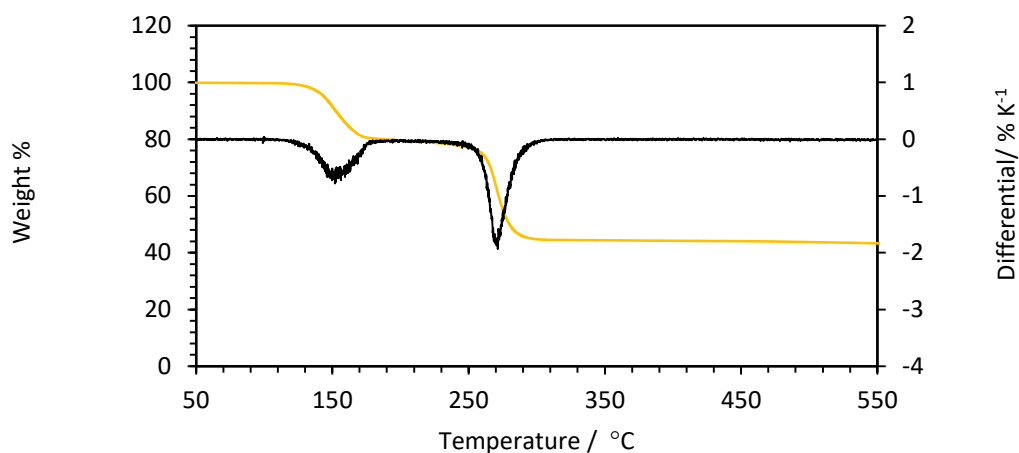


**Figure 3.46: TGA profile of the iron manganese oxalate**

The TGA of the iron-manganese oxalate (**Figure 3.46**) showed a typical metal oxalate decomposition with the water mass loss at 120-160 °C followed by the main decomposition at 240-260 °C. There was no further mass loss that would be associated with the formation of  $Mn_2O_3$  from  $Mn_5O_8$  or  $Mn_3O_4$  although the XRD had shown the formation of phase separated  $Mn_3O_4$  in the iron manganese oxide after calcination at 300 °C.

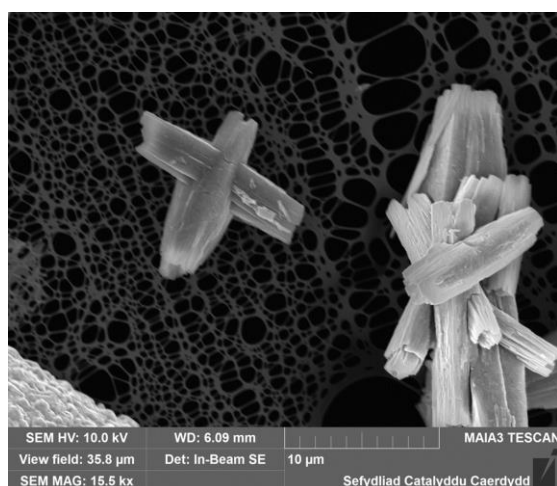


**Figure 3.47: SEM image of the iron manganese oxide oxalate precipitated calcined 300 °C from the iron manganese oxalate prepared by DES**

The SEM of the mixed iron-manganese oxide calcined at 300 °C (**Figure 3.45 b**) showed that the sample had formed shorter cuboid shaped rods, similar to the  $Fe_2O_3$  morphology from the iron oxalate precipitated in the water-ethanol anti-solvent. This shows that like the cobalt manganese (**Figure 3.4.2**) that the iron manganese oxalate and oxide formed

the morphology closer to that of the pure oxalate rather than that of the manganese oxalate. However, the size of the iron manganese rods is not consistent throughout the sample.

### 3.5.3 Mixed oxide catalyst testing

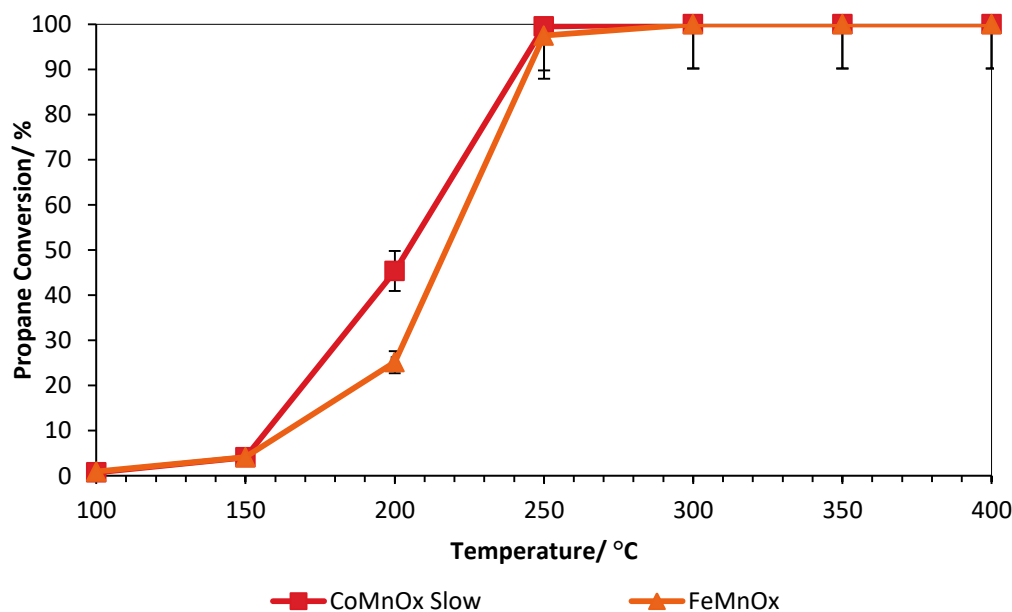


**Figure 3.48: Propane oxidation of the mixed metal oxides (75 mg) precipitated by DES-anti-solvent in 50:50 water-ethanol and calcined at 300 °C**

The propane conversion when using the mixed metal oxide catalyst (**Figure 3.48**) showed greater activity than the single oxides. This was more notable with the iron manganese catalysts showed an increased in activity over the single iron oxide with 100 % conversion by 300 °C and a  $T_{10}$  of 163 °C with a light off between 150-250 °C. The activity of the mixed iron manganese oxide catalysts was close to that of both cobalt and mixed cobalt manganese oxide catalysts of similar loading.

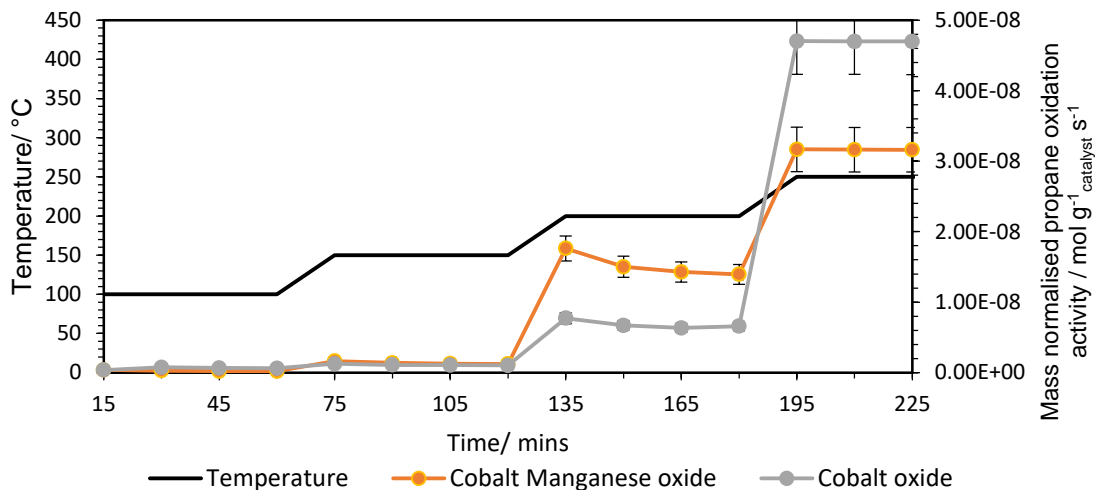


**Figure 3.49: Mass normalised propane oxidation activity with cobalt oxide (55 mg) and mixed cobalt manganese oxide (75 mg) prepared by DES anti-solvent with 50:50 water-ethanol calcined 300 °C (Error of  $\pm 10\%$  taking into account error of surface area, propane counts and mass of catalysts)**

The comparison of mass normalised activity (**Figure 3.49**) of the mixed cobalt-manganese oxide with the standard cobalt oxide prepared by DES anti-solvent showed that both had similar propane activity at 100 and 150 °C, with the mixed cobalt manganese showing a slightly better activity at 200 °C compared to the single cobalt oxide (at 250 °C both reached 100 % conversion). This increase in activity could originate from an interaction between cobalt and manganese in the mixed sample. This would support the XRD, TPR and XPS observations that the cobalt manganese oxide precipitated as a single phase  $\text{Co}_{1.5}\text{Mn}_{1.5}\text{O}_4$  rather than phase separate cobalt and manganese oxides.

### 3.6 Chapter 3 Conclusions

The method of using deep eutectic solvents as a way to make metal oxalate as precursor for metal oxide catalysts has been demonstrated to work for cobalt, manganese and iron oxide as well as mixed metal oxide. The use of a controlled anti-solvent technique to control the morphology has been shown to work for cobalt and iron oxalate precursors to make oxides with needle like structures which could be altered depending on the anti-solvent mixture. For cobalt oxalate the addition of ethanol or methanol to the anti-solvent formed longer needles. Manganese on the other hand did not form needles but it was demonstrated that the precursor salt used had an effect on the shape of the precipitate.

The cobalt oxide catalysts calcined from the cobalt oxalate precipitated using DES anti-solvent method were shown to be active for total oxidation of propane to CO<sub>2</sub> showing to be more active than cobalt oxide calcined from cobalt acetate but were not as active as cobalt oxide precipitated using supercritical anti-solvent process, due to the larger crystallite size of the DES-oxalate catalysts.

Changing the calcination conditions of cobalt oxalate prepared by DES anti-solvent however improved the catalytic activity, with the light off and T<sub>10</sub> and T<sub>100</sub> shifting to lower temperatures when the cobalt oxide was calcined at 300 °C and with a lower heating rate (1 °C min<sup>-1</sup>). Changing the anti-solvent also had a small effect on the catalytic activity but most of the cobalt oxide catalyst precipitated by DES had similar surface areas and crystallite size which resulted in a small difference in catalytic activity.

The methodology can be utilised to control the morphology of iron oxide although the effect different anti-solvents was opposite to cobalt with the iron oxalate forming longer rods in pure water as the anti-solvent and shorter when precipitated with water-ethanol anti-solvent. The iron oxalate was shown to produce iron oxide with very high surface areas of up to 221 m<sup>2</sup> g<sup>-1</sup>. The use of the method to make mixed metal oxalate and oxides was also shown to work for cobalt manganese oxide forming a mixed metal oxide

material while iron-manganese oxalate appeared to form some degree of phase separation with ( $\text{Mn}_3\text{O}_4$  being detected by XRD). Both catalysts showed improvements in mass normalised propane activity compared to the single oxides indicating that there was some degree of phase integration. Overall, this chapter has shown that metal oxalates preparation from choline chloride-oxalic acid based DES was a viable way to make catalyst with different morphologies. However, this was dependent on the metal under the parameters used and that in some cases such as iron, high surface area metal oxide could be formed.

### **3.7 Chapter 3 Future work**

The DES anti-solvent was shown to be a viable method for the preparation of cobalt, iron and manganese oxalate. However, this was the starting point for this methodology and there are various avenues to pursue and investigate in order to improve both the method and oxalate/oxide catalysts. For consistency during this chapter, all metal oxalates were prepared under the same conditions; 120 °C for 1 hour then 150 °C for 2 hours and cooling to 50 °C before anti-solvent additions. Modification of these parameters is another avenue of investigation to see the effect on the precipitation of the metal oxalate. Parameters that could affect the morphology could include temperature used, time the metal salt was left to dissolve into the DES and the concentration of metal salt used in the DES. The concentration may have a significant effect as the high concentration of metal salt in the DES could change the nucleation versus the growth rate of precipitation.

Other anti-solvent mixtures that had not been explored in this work such as ethylene glycol may also provide interesting change to the morphology of the cobalt oxalate and cobalt oxide. This method was only demonstrated with a few select examples (iron, manganese and cobalt) of metal oxalates, and as shown in this chapter, the method of precipitation is dependent on the metal that is being precipitated. Use of the method for other metal oxalate such as mixed copper-zinc oxalate or nickel oxalate could also be investigate to see if this method works for these systems.

### 3.8 Chapter 3 References

1. A. Abo-Hamad, M. Hayyan, M. A. AlSaadi and M. A. Hashim, *Chemical Engineering Journal*, 2015, **273**, 551-567.
2. F. X. Chen, S. L. Xie, J. H. Zhang and R. Liu, *Materials Letters*, 2013, **112**, 177-179.
3. X. Ge, C. D. Gu, X. L. Wang and J. P. Tu, *Journal of Colloid and Interface Science*, 2015, **454**, 134-143.
4. F. Pena-Pereira and J. Namiesnik, *ChemSusChem*, 2014, **7**, 1784-1800.
5. I. Juneidi, M. Hayyan and O. M. Ali, *Environmental Science and Pollution Research*, 2016, **23**, 7648-7659.
6. O. S. Hammond, K. J. Edler, D. T. Bowron and L. Torrente-Murciano, *Nature Communications.*, 2017, **8**, 7.
7. X. Ge, C. D. Gu, X. L. Wang and J. P. Tu, *Journal of Colloid and Interface Science*, 2015, **438**, 149-158.
8. J. Y. Dong, Y. J. Hsu, D. S. H. Wong and S. Y. Lu, *Journal of Physical Chemistry C*, 2010, **114**, 8867-8872.
9. A. P. Abbott, D. Boothby, G. Capper, D. L. Davies and R. K. Rasheed, *Journal of American Chemical Society*, 2004, **126**, 9142-9147.
10. Y. Meng, Y. C. Chen, Z. M. Zhang, Z. J. Lin and M. L. Tong, *Inorganic Chemistry*, 2014, **53**, 9052-9057.
11. Y. Meng, J. L. Liu, Z. M. Zhang, W. Q. Lin, Z. J. Lin and M. L. Tong, *Dalton Transactions*, 2013, **42**, 12853-12856.
12. A. Soldner, J. Zach, M. Iwanow, T. Gartner, M. Schlosser, A. Pfitzner and B. Konig, *Chemistry-a European Journal*, 2016, **22**, 13108-13113.
13. S. Ishikawa, D. R. Jones, S. Iqbal, C. Reece, D. J. Morgan, D. J. Willock, P. J. Miedziak, J. K. Bartley, J. K. Edwards, T. Murayama, W. Ueda and G. J. Hutchings, *Green Chemistry*, 2017, **19**, 225-236.
14. J. Hirayama, I. Orlowski, S. Iqbal, M. Douthwaite, S. Ishikawa, P. J. Miedziak, J. K. Bartley, J. Edwards, Q. He, R. L. Jenkins, T. Murayama, C. Reece, W. Ueda, D. J. Willock and G. J. Hutchings, *Journal of Physical Chemistry C*, 2019, **123**, 7879-7888.
15. W. W. Zhou, K. B. Tang, S. A. Zeng and Y. X. Qi, *Nanotechnology*, 2008, **19**, 9.
16. T. Ahmad, K. V. Ramanujachary, S. E. Lofland and A. K. Ganguli, *Journal of Materials Chemistry*, 2004, **14**, 3406-3410.
17. C. C. Yu, L. X. Zhang, J. L. Shi, J. J. Zhao, J. H. Gao and D. S. Yan, *Advanced Functional Materials*, 2008, **18**, 1544-1554.
18. W. W. Wang and Y. J. Zhu, *Materials Research Bulletin*, 2005, **40**, 1929-1935.
19. D. W. Wang, Q. H. Wang and T. M. Wang, *Inorganic Chemistry*, 2011, **50**, 6482-6492.
20. R. P. Marin, S. A. Kondrat, R. K. Pinnell, T. E. Davies, S. Golunski, J. K. Bartley, G. J. Hutchings and S. H. Taylor, *Applied Catalysis B-Environmental*, 2013, **140**, 671-679.

21. D. R. Jones, S. Iqbal, L. Thomas, S. Ishikawa, C. Reece, P. J. Miedziank, D. J. Morgan, J. K. Bartley, D. J. Willock, W. Ueda and G. J. Hutchings, *Catalysis Structure & Reactivity*, 2018, **4**, 12-23.
22. B. Solsona, I. Vazquez, T. Garcia, T. E. Davies and S. H. Taylor, *Catalysis Letters*, 2007, **116**, 116-121.
23. L. F. Liotta, H. J. Wu, G. Pantaleo and A. M. Venezia, *Catalysis Science & Technology*, 2013, **3**, 3085-3102.
24. I. Luisetto, F. Pepe and E. Bemporad, *Journal of Nanoparticle Research*, 2008, **10**, 59-67.
25. B. M. Abu-Zied, S. M. Bawaked, S. A. Kosa and W. Schwieger, *Applied Surface Science*, 2015, **351**, 600-609.
26. L. Gontrani, M. Bonomo, N. V. Plechkova, D. Dini and R. Caminiti, *Physical Chemistry Chemical Physics*, 2018, **20**, 30120-30124.
27. N. R. Rodriguez, A. van den Bruinhorst, L. J. B. Kollau, M. C. Kroon and K. Binnemans, *ACS Sustainable Chemistry & Engineering*, 2019, **7**, 11521-11528
28. D. Y. Yue, Y. Z. Jia, Y. Yao, J. H. Sun and Y. Jing, *Electrochimica Acta*, 2012, **65**, 30-36.
29. Y. Chen, D. K. Yu, Y. H. Lu, G. H. Li, L. Fu and T. C. Mu, *Industrial & Engineering Chemistry Research*, 2019, **58**, 7308-7317.
30. S. K. Saha, S. Dey and R. Chakraborty, *Journal of Molecular Liquids*, 2019, **287**, 11.
31. D. R. Lide, *CRC Handbook of Chemistry and Physics*, CRC press, 2001.
32. N. S. McIntyre and D. G. Zetaruk, *Analytical Chemistry*, 1977, **49**, 1521-1529.
33. B. Faure and P. Alphonse, *Applied Catalysis B-Environmental*, 2016, **180**, 715-725.
34. X. L. Zhang, J. H. Ye, J. Yuan, T. Cai, B. Xiao, Z. Liu, K. F. Zhao, L. Yang and D. N. He, *Applied Catalysis A-General*, 2018, **566**, 104-112.
35. K. Li, R. R. Zhang, R. J. Gao, G. Q. Shen, L. Pan, Y. D. Yao, K. H. Yu, X. W. Zhang and J. J. Zou, *Applied Catalysis. B-Environmental*, 2019, **244**, 536-545.
36. Q. Li, T. Odoom-Wubah, Y. P. Zhou, R. Mulka, Y. M. Zheng, J. L. Huang, D. H. Sun and Q. B. Li, *Industrial Engineering Chemistry Research*, 2019, **58**, 2882-2890.

# Chapter 4 Evaluation of Delafossite Phase Copper-Manganese Oxides and Spinel Derivatives for CO Oxidation.

## 4.1 Introduction

### 4.1.1 Background on delafossite materials

Delafossite materials are mixed metal oxides that consist of a  $ABO_2$ <sup>1-3</sup> with the A site as a monovalent metal such as  $Cu^+$ ,  $Ag^+$  or  $Pd^+$  and the B site as a trivalent metal such as  $Mn^{3+}$ ,  $Fe^{3+}$ ,  $Y^{3+}$  and  $Cr^{3+}$ <sup>2-5</sup>. Copper based delafossite materials have been of interest to many material scientists due to their P-type semiconductor properties and have been used in applications such as hydrogen production from photoelectrochemical splitting of water<sup>6</sup>.

Until recently delafossite based materials have rarely been used in gas phase heterogeneous catalysis, partially due to the high temperature heat treatments of up to 1100 °C under inert atmospheres required to achieve the delafossite phase<sup>1, 7</sup>. Such high temperature conditions result in surface areas of less than 1-2  $m^2 g^{-1}$ , which would limit their potential use as heterogeneous catalysts, or catalyst supports for oxidation reactions. Despite this, some groups have investigated the potential for copper-based delafossite in heterogeneous catalyst including the use as an alternative to  $CeO_2$  for oxygen storage in the three way catalyst<sup>1</sup>.

However, in recent years it has been demonstrated that under hydrothermal conditions of less than 200 °C (under both conventional heating or microwave heating), delafossite phase materials can be formed, reducing the excessive heat treatments require to form a pure delafossite phase material<sup>8</sup>.<sup>9</sup>. This technique has the potential for increased surface areas of delafossite materials since it avoids high temperature conditions and therefore potentially could produce delafossite materials higher surface areas than previously been achieved, therefore making them comparable to other mixed metal

oxide phases. This has already led to publication into the use of  $\text{CuCrO}_2$  for CO oxidation<sup>10</sup> and  $\text{CuFeO}_2$  and its spinel derivatives as a Fischer-Tropsch catalyst<sup>11</sup>.

Copper-manganese based delafossite, known as crednerite, could act as an interesting alternative CO oxidation catalyst to the more conventional spinel phase hopcalite. In addition, it is known that delafossite can oxidise to form the spinel phase in air at high temperature<sup>1, 12</sup> and could act as a potential precursor to hopcalite. Copper-manganese crednerite differs from regular delafossite in that it forms a monoclinic phase that results from the Jahn-Teller distortion caused by the  $\text{Mn}^{3+}$ <sup>13</sup>. The distortion creates an oxygen layer between the copper layer (in a linear form) and manganese layer (forming an octahedral  $\text{MnO}_6$ )<sup>13, 14</sup> resulting in a different layer of the  $\text{ABO}_2$  structure compared to other delafossite materials such as  $\text{CuCrO}_2$  or  $\text{CuFeO}_2$  which form a rhombohedral structure<sup>15</sup>.

Hopcalite, as discussed in Chapter 1, are mixed copper-manganese oxides in the spinel phase with the most common and active (for CO oxidation) having a 1:2 of copper: manganese in the form  $\text{CuMn}_2\text{O}_4$ <sup>16 17</sup>, although other ratios have been used as catalysts<sup>18, 19</sup>. Hopcalite have been applied as catalysts for a range of reactions but most notably in gas phase oxidation reactions such as CO, toluene and naphthalene oxidation<sup>20-22</sup> and have been noted to have CO oxidation activity close or equivalent to support precious metal catalysts<sup>23</sup>. Although hopcalite has been used as a catalyst for over 90 years<sup>24</sup>, it is still widely studied with the most common and refined method of preparation being co-precipitation<sup>16, 22, 25</sup>, although more recent alternative methods have been reported including supercritical anti-solvent precipitation and flame pyrolysis<sup>17, 18, 26, 27</sup>. Although these techniques have produced very active hopcalite, most require complex synthesis or in the cases of co-precipitation calcination conditions of 300-400 °C forming amorphous hopcalite<sup>20</sup>, which is the more active than the crystalline hopcalite<sup>28</sup>.

The hopcalite derived from crednerite is interesting in comparison because the hopcalite phase forms from another crystalline oxide i.e. crednerite whereas the co-precipitated hopcalite forms carbonate that breaks down into

an amorphous phase. In addition, the formation of both the spinel phase and isolated copper oxide may provide a copper-manganese catalyst with interesting properties compared with conventional co-precipitated hopcalite.

#### 4.1.2 Aims of Chapter 4

The aim of the work presented in this chapter is to use crednerite as prepared by hydrothermal synthesis and the spinel derivatives formed after heat treatment at 300-500 °C as catalysts for CO oxidation as a model of testing their potential as gas phase oxidation catalysis. The work is to compare both the physical properties and catalytic properties of crednerite and its spinel derivatives with copper-manganese oxide made from the more established co-precipitation method and to see if it can be used as an alternative to conventional hopcalite.

### 4.2 Crednerite synthesis

#### 4.2.1 Hydrothermal synthesis of crednerite

The crednerite sample was synthesised in a high-pressure static autoclave at 80 °C. The formation of the delafossite phase during the hydrothermal process is a result of an electron transfer from the manganese to the copper as shown in the equation below<sup>12</sup>.

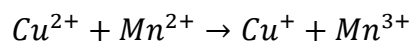


**Figure 4.1: The electron transfer process during the hydrothermal process**

The group of Zhao *et al.* found that the optimum conditions for making crednerite at lower temperatures was dependent on the quantity of NaOH used, with a molar ratio of 2.8:1:1 NaOH:Cu:Mn resulting in phase pure CuMnO<sub>2</sub>, whereas a lower amount of NaOH would result in phase separated CuO/Mn<sub>3</sub>O<sub>4</sub><sup>29</sup>. They noted that the concentration of sodium hydroxide also

played an important role in the mechanism for the formation of crednerite, also affecting the particle morphology and crystal size.

The large amount of sodium hydroxide used to form the crednerite can be useful to modify the crystallinity but it also poses a problem since sodium causes deactivation of copper manganese oxides during CO oxidation reactions<sup>30</sup>. As a result, the crednerite water mixture was poured into a minimum of 1500 ml of water (this also reduced the base concentration) and washed with a further 1000 ml of water and 200 ml of ethanol to remove the majority of the sodium and nitrate species.

The crednerite sample was prepared using a Cu:Mn ratio of 1:1 and 1:2, the latter as a way of comparing with more conventional hopcalite made from co-precipitation in the 1:2 Cu:Mn ratio.

#### 4.2.2 Spinel oxides derived from crednerite

It is known from literature that crednerite oxidises to the spinel phase and copper oxide when heated in air above 200 °C due to the oxidation of Cu<sup>+</sup> to Cu<sup>2+</sup> in air as shown by the equation in **Figure 4.2**<sup>29, 31</sup>. The formation of the spinel phase was later confirmed by X-ray diffraction (XRD) (**Figures 4.4 and 4.5**) and thermal gravimetric analysis (TGA) (**Figure 4.6**).

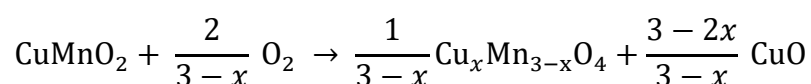


**Figure 4.2: The oxidation of crednerite to form the spinel phase x= amount of oxygen: copper-manganese**

Spinel phase copper-manganese is widely known for being a good CO oxidation catalyst, with the most established method being co-precipitation<sup>16, 22</sup>. This opens up a possible alternative route to make hopcalite catalysts from the crednerite and samples were heat treated at 200 °C, 300 °C, 350 °C, 400 °C and 500 °C to form the spinel phase. These spinel phase oxides could also be directly compared to hopcalite made from conventional or more established methods such as co-precipitation.

### 4.2.3 Hopcalite prepared by co-precipitation

Hopcalite made from co-precipitation was used as a standard for comparison of both the physical and catalytic properties with crednerite derived spinel oxides. Co-precipitation was chosen since it was one of the most common techniques for making hopcalite reported<sup>16, 22, 32</sup> and therefore a good example for comparison with crednerite derived hopcalite. The co-precipitated hopcalite prepared using published methods<sup>20</sup>, was synthesised with a Cu: Mn ratio of both at 1:2 and 1:1 to directly compare with both the more established and active hopcalite ratio (1:2)<sup>16</sup> and with the crednerite and its oxidised form (1:1).

### 4.3 Characterisation of crednerite and its spinel derivatives and comparison with co-precipitated hopcalite

The X-ray diffraction pattern of crednerite prepared with 1:1 Cu:Mn (**Figure 4.3 a**) confirmed that the  $\text{CuMnO}_2$  phase had formed, as shown with the reflections at  $31.28^\circ$  (0 0 2),  $33.01^\circ$  (2 0 0),  $36.99^\circ$  (-1 1 1) and  $40.48^\circ$  (1 1 1), with no other crystalline phase being detected. The XRD pattern confirmed that this was the monoclinic crednerite<sup>13</sup>. MP-AES analysis on the sample had confirmed that the crednerite had a ratio of 1:1 Cu:Mn, which would confirm the XRD analysis that  $\text{CuMnO}_2$  was primarily formed with no detectable phase separated species present.

The XRD pattern (**Figure 4.3 b**) of crednerite that was synthesised in a 1:2 Cu:Mn ratio however showed that the crenerite phase had mostly formed but there was also additional reflections that indicated high degree of phase separation, with the majority of these reflections being associated with  $\text{Mn}_3\text{O}_4$ . This would suggest the mechansim of an electron transfer from copper to manganese (**Figure 4.1**) to form the crednerite phase was still occuring under this hydrothermal conditions and that the crednerite was

formed primarily over the spinel phase with the excess manganese forming the spinel phase  $Mn_3O_4$ .

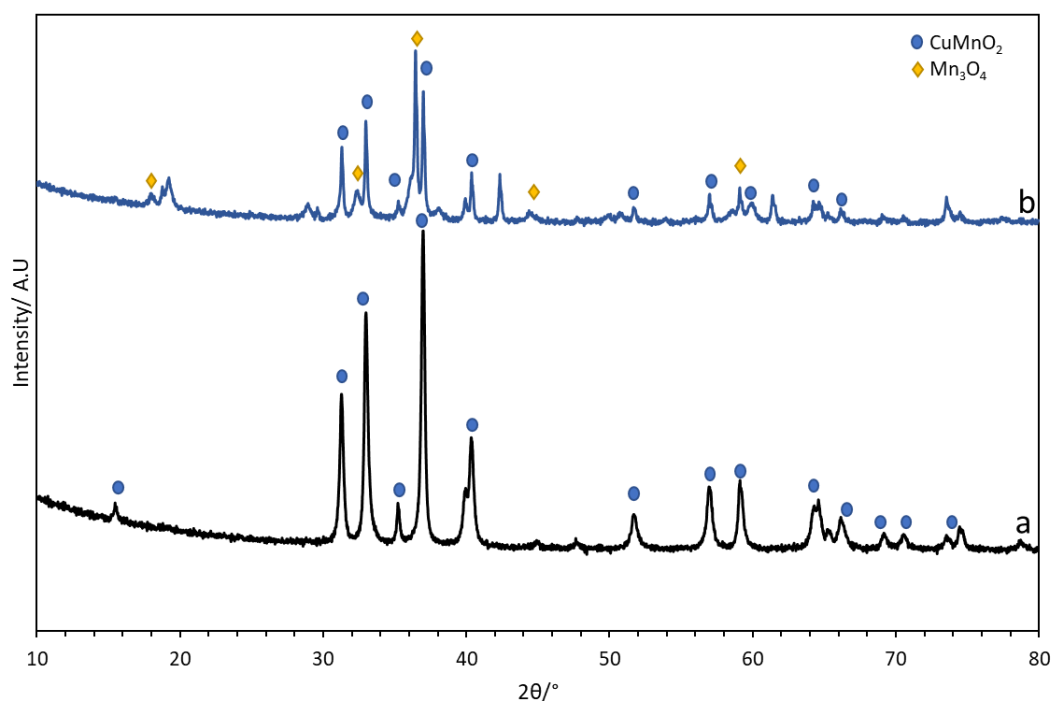


**Figure 4.3:** X-ray diffraction of crednerite prepared by hydrothermal synthesis with a Cu:Mn ratio of a) 1:1 and b) 1:2

It has been noted by other groups that with Cu and Cr, different ratios of Cu:Cr would form the spinel phase instead of the delafossite but these experiments were performed under slightly different conditions at a temperature of 180 °C<sup>10</sup>. Here it appears that the formation of the crednerite phase was more favourable due to the electron transfer over the mixed  $Cu_xMn_{3-x}O_4$ /spinel phase.

An *in situ* XRD study performed on the 1:1 Cu:Mn crednerite sample (**Figure 4.4**) from 50 to 600 °C showed that the crednerite phase was still stable under air to at least 200 °C but the sample subsequently, fully oxidised to the spinel phase by 300 °C with no trace of the reflection associated crednerite phase at 300 °C or above. This shows that the formation of the spinel occurred between 200 °C and 300 °C and that the  $Cu^+$  oxidises to  $Cu^{2+}$  resulting in the rearrangement of the structure of the oxide from a  $CuMnO_2$  phase to a spinel phase in this temperature region which was also observed by a mass increase in the TGA of crednerite (**Figure 4.6**).

The reflection for isolated CuO at  $2\theta=38.2^\circ$ , that forms during the oxidation of crednerite starts to become more intense and visible at around 400 °C. The reflection at  $2\theta=18.4^\circ$  that appears after 300 °C indicates possible formation of phase separated  $Mn_2O_3$  in this sample.

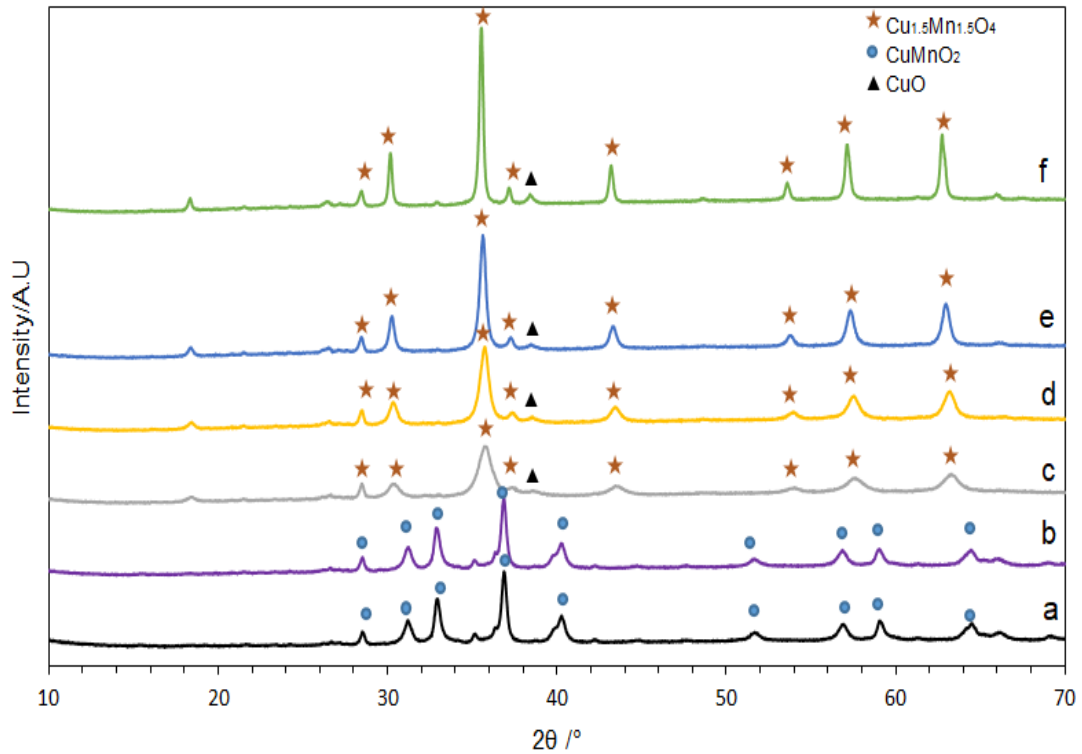


**Figure 4.4:** *In situ* X-ray diffraction performed on crednerite at a) 50 °C, b) 200 °C, c) 300 °C, d) 400 °C, e) 500 °C, f) 600 °C

The Scherrer equation (**Table 4.1**) shows that the crystallite size initially increases for crednerite from 50 to 200 °C at  $2\theta=37.4^\circ$  caused by the sintering of the crednerite at higher temperatures. The reflections of the spinel phase that forms after are less intense than those of the preceding crednerite phase, with the crystalline size (at  $2\theta=35.9^\circ$ ) being 14.6 nm. The rapid decrease in crystallinity is probably due to a structural rearrangement of the sample when it is oxidised from the crednerite phase into the spinel phase and copper oxide. However it should be noted that the spinel phase is still a crystalline phase at 300 °C, with the reflections of the spinel phase large enough to be observed which is important when comparing to the co-precipitated hopcalite later on (**Figure 4.11**).

X-ray diffraction (**Figure 4.5**) performed of the 1:1 Cu:Mn crednerite, calcined under a slight air flow (approximately  $5 \text{ ml min}^{-1}$ ) for 3 hours, confirmed the observations of the *in situ* XRD, with the crednerite phase still being stable up to 200 °C (even after 3 hours) but oxidises to the spinel phase at 300 °C and above. The presence of the spinel phase was confirmed by the reflections at  $18.66^\circ$  (1 1 1),  $20.56^\circ$  (2 2 0),  $35.97^\circ$  (3 1 1),  $43.51^\circ$  (4 0 0) and  $58.17^\circ$  (5 1 1).

**Table 4.1: Crystallite size of crednerite and spinel derivatives from the *in situ* XRD at  $2\theta=37.4^\circ$  for crednerite and  $2\theta=35.9^\circ$  for spinel**

Temperature	Crystallite size
50 (CuMnO <sub>2</sub> )	38.6
200 (CuMnO <sub>2</sub> )	41.7
CuMn-300	14.7
CuMn-350	19.2
CuMn-400	29.4
CuMn-500	45.3
CuMn-600	38.6

However, it should be noted that the reflections present in the XRD of the calcined samples shows that heat treatment of crednerite formed Cu<sub>1.5</sub>Mn<sub>1.5</sub>O<sub>4</sub> with no reflection at  $2\theta=38.8^\circ$  that would indicate the presence of phase separated copper oxide.

This would indicate that the conditions that these catalysts were formed favour the greater oxygen uptake (equation in **Figure 4.2**) and therefore formed the single phase Cu<sub>1.5</sub>Mn<sub>1.5</sub>O<sub>4</sub> over CuMn<sub>2</sub>O<sub>4</sub> and phase separate CuO.

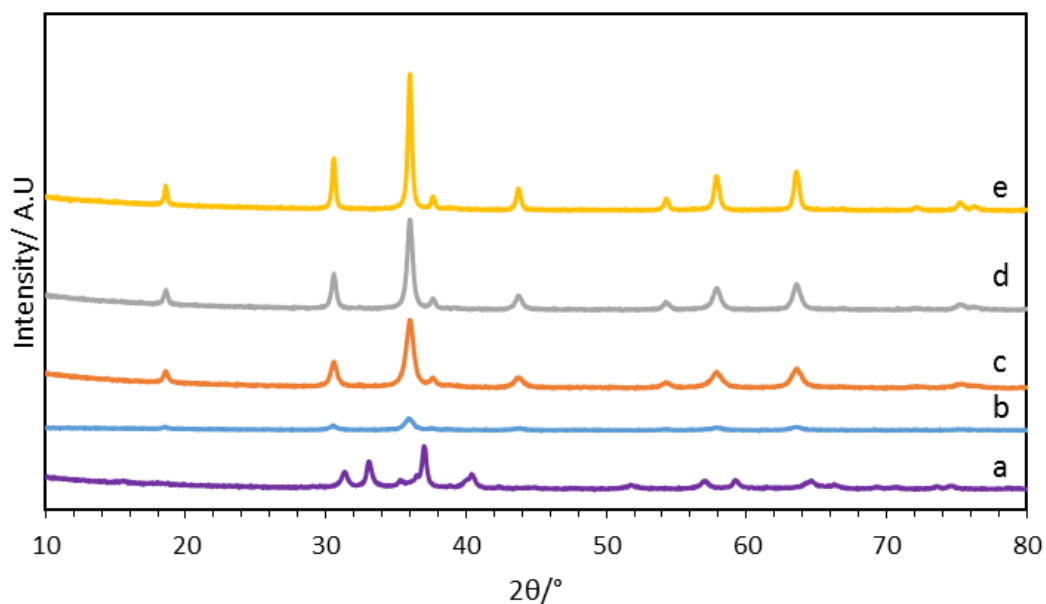


**Figure 4.5:** X-ray diffraction pattern of heat treated crednerite at a) 200 °C and spinel derivative formed at b) 300 °C, c) 350 °C d) 400 °C and e) 500 °C

As observed in the *in situ* XRD (**Figure 4.4**) the crednerite phase increases in crystallinity when heated to 200 °C but the subsequent spinel phase formed after 300 °C is a less crystalline phase due to the change of phase and rearrangement of the crednerite phase to the spinel phase. The crystalline size is slightly different to those seen in the *in situ* study but this could be due to error between the two experiments and these values are within the same range of each other. Thermal gravimetric analysis of the crednerite (**Figure 4.6**), performed under flowing air at a heating rate of 5 °C min<sup>-1</sup>, showed the mass of the catalyst increasing by 6% between at 250 °C and 350 °C. The initial water loss occurring between 100-200 °C and the mass gain at 250-350 °C corresponds to the oxidation of crednerite phase to the spinel phase, as observed in both XRD studies (**Figures 4.4 and 4.5**). The mass loss that occurs again above 600 °C has been attributed to the partial decomposition of the spinel phase back to CuMnO<sub>2</sub> which would only fully occur at higher temperatures<sup>31</sup>.

**Table 4.2: Crystalline size from X-ray diffraction and surface area of the crednerite derived spinel catalysts**

Sample/ calcination temperature /°C	Main phase	Crystalline size /nm		Surface area m <sup>2</sup> g <sup>-1</sup> (±2)
		2θ=35.9° (spinel) (±5 nm)	2θ=36.8° (crednerite) (±5 nm)	
Crednerite	CuMnO <sub>2</sub>	-	36.4	31
200	CuMnO <sub>2</sub>	-	45.5	39
300	Cu <sub>1.5</sub> Mn <sub>1.5</sub> O <sub>4</sub>	10.4	-	26
350	Cu <sub>1.5</sub> Mn <sub>1.5</sub> O <sub>4</sub>	14.0	-	22
400	Cu <sub>1.5</sub> Mn <sub>1.5</sub> O <sub>4</sub>	19.4	-	18
500	Cu <sub>1.5</sub> Mn <sub>1.5</sub> O <sub>4</sub>	31.4	-	19

Both XRD and TGA studies on crednerite shows that this material would be limited as catalyst for oxidation reactions below 200 °C as the phase would oxidise to the spinel phase. However, the phase is stable at higher temperatures under a non oxidising atmosphere such as nitrogen<sup>29</sup>.

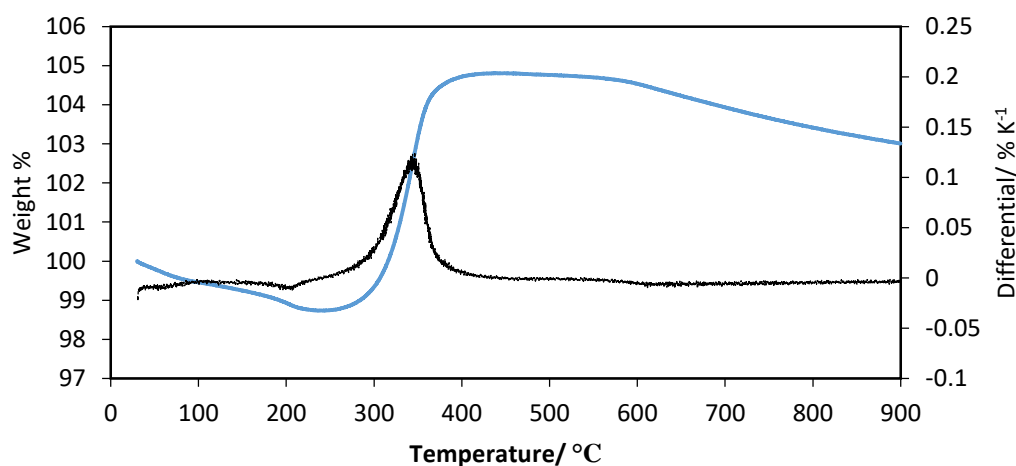


**Figure 4.6: Thermal Gravimetric analysis of the crednerite in air, 30 ml min<sup>-1</sup>, 5 °C min<sup>-1</sup>**

A parameter that could affect the formation of the spinel catalysts derived from crednerite is the conditions that the materials were calcined under, specifically the airflow rate over the catalysts during the heat treatment process. The crednerite sample however can also be used as a precursor to

the spinel phase, which as mentioned earlier is active for CO oxidation<sup>33</sup>, forming spinel phase as low as 250-300 °C.

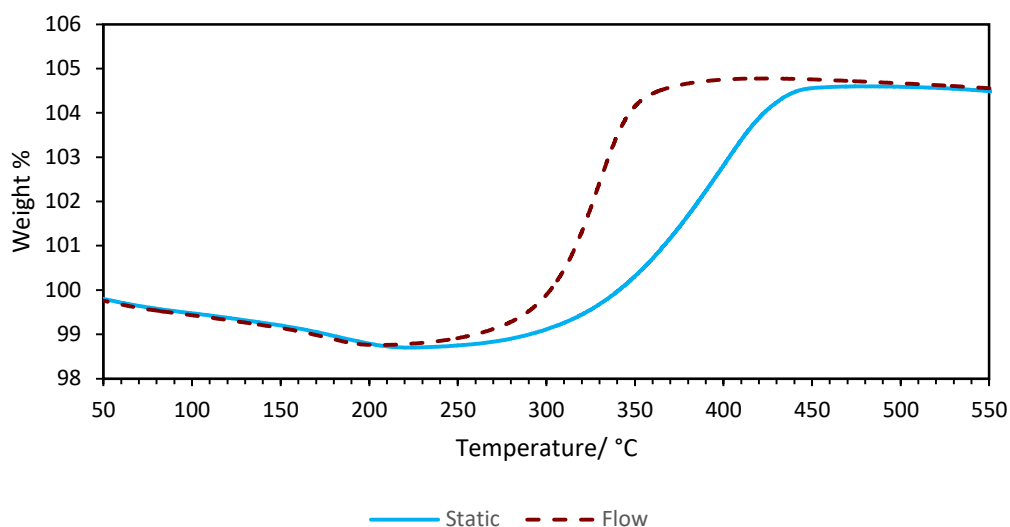


**Figure 4.7:** Thermal gravimetric analysis of crednerite under air static and flow of 75 ml min<sup>-1</sup> conditions, 5 °C min<sup>-1</sup>

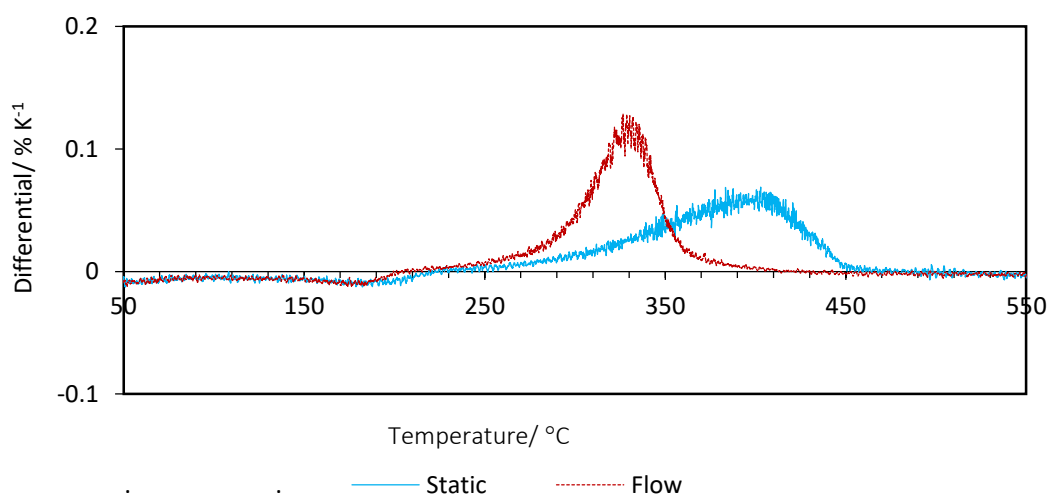


**Figure 4.8:** The differential of the TGA (from Figure 4.7)

Thermal gravimetric analysis of crednerite under static air and a flow of 75 ml min<sup>-1</sup> (**Figure 4.7**) showed that the uptake of oxygen to form the spinel phase occurred at a narrow temperature range (250-350 °C) for a higher flow rate (75 ml min<sup>-1</sup>) than it does for static conditions. The TGA profile under static conditions show that the increase in mass starts to occur at the same point (250 °C) but the whole mass increase occurs across a wider temperature range (250-450 °C) (**Figure 4.8**). This would suggest that the

crednerite would still oxidise to the spinel phase under a static system at 300-400 °C.

Comparison of the XRD of both spinel phase copper-manganese oxide that formed from heat treatment of crednerite under static and flow (100 ml min<sup>-1</sup>) (**Figure 4.9**) shows that the sample that was heat treated under flow had a notable reflection at  $2\theta=39.0^\circ$  which closely matches the (1 1 1) of CuO. Under static conditions of the same sample the reflection at  $2\theta=39.0^\circ$  is much weaker (it appears in this sample but the crednerite samples that were calcined while exposed to flowing air do not even have a reflection in this area). This would therefore suggest that the flow conditions during the heat treatment had an impact on the formation of a pure spinel phase or a mixed spinel and phase separate copper oxide. Based on the equation shown in **Figure 4.2**, the slower flow rates have greater oxygen up take that allows the formation of pure phase spinel. This might be due to the higher static/slow flow rate conditions allowing the oxygen to stay on the surface longer and thereby favouring the phase pure spinel over the phase separate spinel and CuO. It is also possible however that the other material had formed isolated CuO but these crystallites were too small to be detected by XRD.

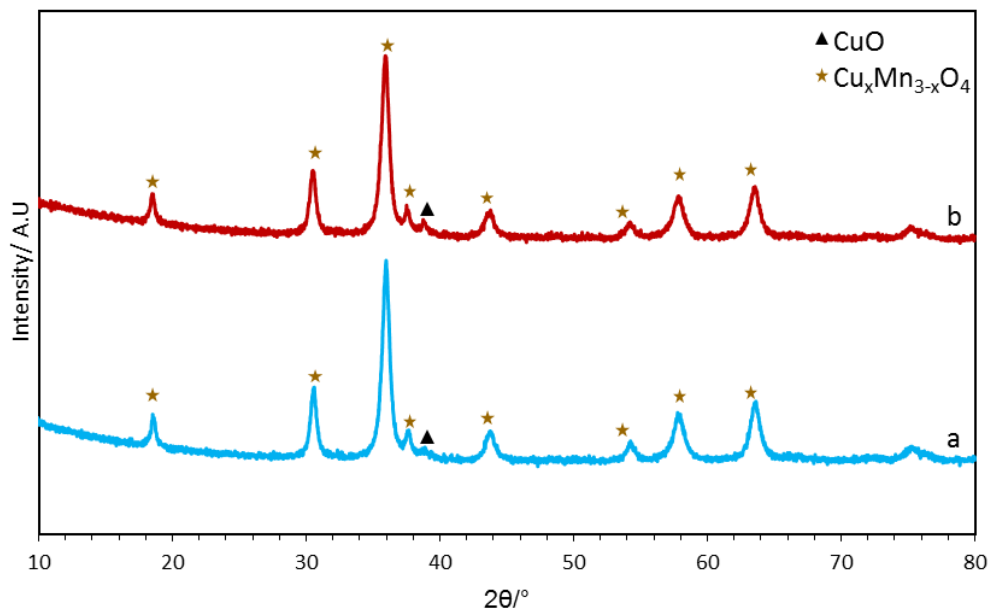


**Figure 4.9:** X-ray diffraction of crednerite calcined to 350 °C under a) static air and b) flowing air 100 ml min<sup>-1</sup>

**Table 4.3: Surface area of spinel derived by heat treatment of crednerite under different airflows ( $\pm 2 \text{ m}^2 \text{ g}^{-1}$ ) and crystallite size ( $\pm 5 \text{ nm}$ )**

Air flow conditions	Surface area/ $\text{m}^2 \text{ g}^{-1}$	Crystallite size at $2\theta=35.9^\circ$ /nm
Static	20	13.4
Exposed to air flow	22	14.0
Direct air flow ( $100 \text{ ml min}^{-1}$ )	22	13.6

Surface area analysis of the sample under both static and flow (**Table 4.3**) shows that the surface area of the sample under total static conditions had a surface area of  $20 \text{ m}^2 \text{ g}^{-1}$ , which, especially when taking the uncertainties of BET technique into account is not different to the surface area of the samples calcined in furnace exposed to an airflow and directly under airflow ( $100 \text{ ml min}^{-1}$ ). It should be noted here however that the surface area of the precursor (crednerite) was already relatively low at  $31 \text{ m}^2 \text{ g}^{-1}$  and the small differences in surface area observed may be a result of the crednerite already having a low surface area. The crystallite size at  $2\theta=35.9^\circ$  did not vary much between the static and flow conditions.

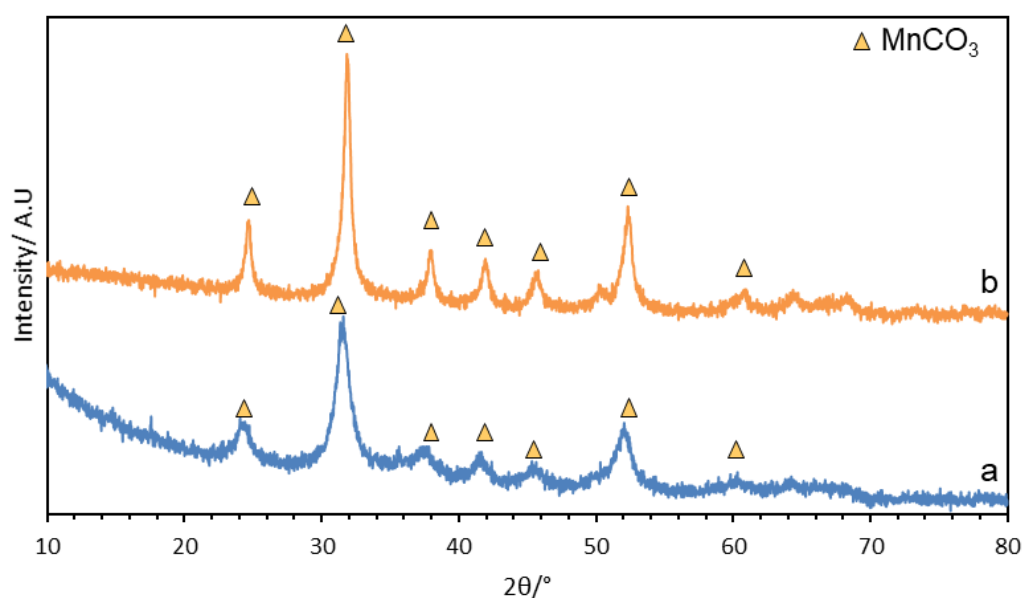


**Figure 4.10: The X-ray diffraction pattern of copper-manganese carbonate made from co-precipitation (pH 8.3) with a Cu:Mn ratio of a) 1:1 and b) 1:2**

The diffraction pattern of the copper-manganese precursor prepared by co-precipitation (**Figure 4.10**) showed that, for both ratios, the most predominant phase detected was the manganese carbonate phase rhodochrosite as confirmed by the reflections at  $24.2^\circ$  (0 1 2),  $31.6^\circ$  (1 0 4),  $37.6^\circ$ ,  $41.4^\circ$ ,  $45.1^\circ$  and  $51.9^\circ$ .

The X-ray diffraction pattern of the copper-manganese oxides calcined at  $400^\circ\text{C}$  (**Figure 4.11**) showed that the material was amorphous for the 1:2 Cu:Mn, while the 1:1 Cu:Mn showed a single broad reflection with a peak at  $2\theta=35.6^\circ$  but otherwise was also mostly amorphous. The amorphousness of the co-precipitated copper-manganese oxides at  $400^\circ\text{C}$  is interesting to note as all of the spinel oxides formed from crednerite are crystalline, with the  $\text{Cu}_{1.5}\text{Mn}_{1.5}\text{O}_4$  reflection being easily identifiable as a crystalline spinel phase formed at  $300^\circ\text{C}$  while the co-precipitated hopcalite is still amorphous at  $400^\circ\text{C}$ . This is most likely due to crednerite already being a crystalline oxide that is subsequently oxidised to the spinel phase while the co-precipitated hopcalite forms from the decomposition of the carbonate species which results in the formation of an amorphous phase at  $400^\circ\text{C}$ .

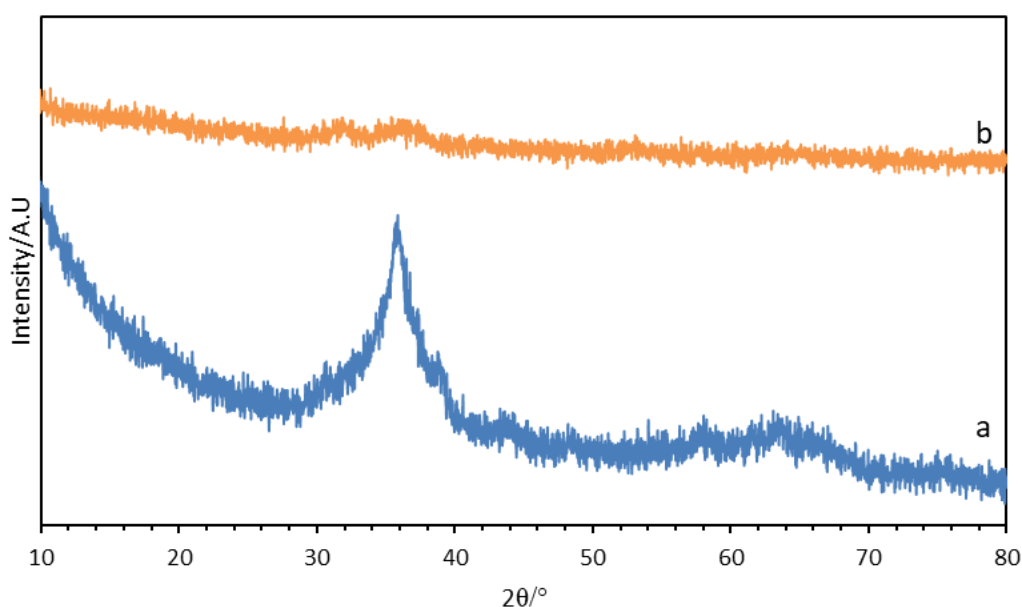


**Figure 4.11: XRD for Co-precipitated copper-manganese calcined at  $400^\circ\text{C}$  with a Cu:Mn ratio of a) 1:1 and b) 1:2**

The co-precipitated catalysts were shown to form crystalline material by 500 °C with the spinel phase reflections being identified by XRD (**Figure 4.12**). The 1:2 Cu:Mn contains additional reflections at  $2\theta=33.1^\circ$  and  $2\theta=23.0^\circ$ , suggesting possible phase separated  $\text{Mn}_2\text{O}_3$  present in the 1:2 co-precipitated sample after calcination at 500 °C. It is known that when hopcalite is calcined at temperatures of 500 °C and above, phase separation occurs and results in a less active catalyst<sup>17</sup>. The 1:1 co-precipitated hopcalite however appears to be phase pure, with no indication of the formation of phase separated  $\text{Mn}_2\text{O}_3$  formation.

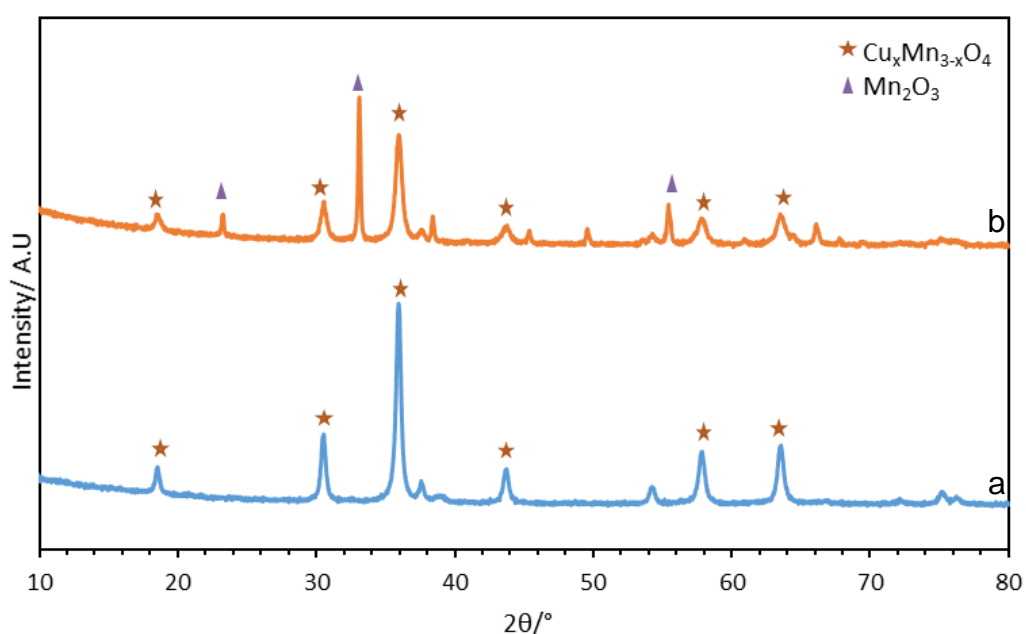


**Figure 4.12:** XRD for the co-precipitated catalyst calcined at 500 °C with a Cu:Mn ratio of a) 1:1 and b) 1:2)

The thermal gravimetric analysis on the both 1:2 and 1:1 co-precipitated copper-manganese carbonates (**Figure 4.13**) shows that they are stable until around 400 °C where the carbonates break down into  $\text{CO}$ ,  $\text{CO}_2$  and the spinel phase copper-manganese oxide. However, as seen in the XRD (**Figure 4.12**) crystalline hopcalite does not start to form until after 400 °C, being amorphous at 400 °C but crystalline by 500 °C. It should be noted that the decomposition of the carbonates occurs at a significantly higher temperature range (400-500 °C) than the oxidation of crednerite to the spinel phase, which occurs at a temperature range of 250-300 °C. However, the

crednerite derived spinel catalysts formed 300-400 °C had a lower surface area (Table 4.4) of 26 m<sup>2</sup> g<sup>-1</sup> at 300 °C and 18 m<sup>2</sup> g<sup>-1</sup> at 400 °C than the co-precipitated catalyst calcined at 400 °C which had 73 m<sup>2</sup> g<sup>-1</sup>.

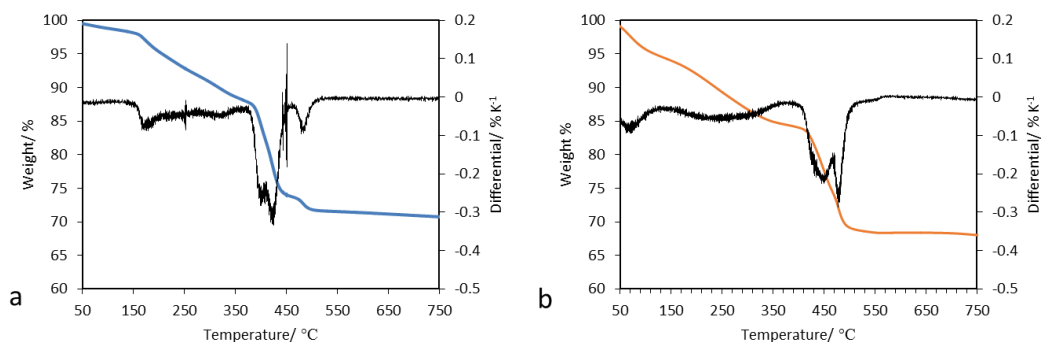


**Figure 4.13: Thermal gravimetric analysis of co-precipitated copper-manganese carbonate at a) 1:2 and b) 1:1 copper:manganese ratio**

**Table 4.4: A comparison of the surface area of the copper-manganese oxides from heat treated crednerite and co-precipitated**

Sample	Surface area m <sup>2</sup> g <sup>-1</sup>	
	Calcined 400 °C	Calcined 500 °C
Spinel from crednerite	18	19
Co-precipitation 1:1	47	24
Co-precipitation 1:2	73	21

X-ray photoelectron spectra of the crednerite in the Cu 2p (Figure 4.14 a) confirmed that the copper was in the +1 oxidation with the two peaks at 932.28 eV and 951.93 eV along with the satellite peak at 945 eV. The XPS did show peaks such as 933.8 eV that would indicate small amounts of Cu<sup>2+</sup> present on the surface, possibly due to surface oxidation. The manganese 2p region (Figure 4.14 b) showed two peaks at 652.9 eV with a shoulder peak at 649.0 eV, and a second peak at 641.8 eV. The lacked of a satellite peak in the region of 647 eV suggests that there is only Mn<sup>3+</sup> or Mn<sup>4+</sup> with Mn<sup>3+</sup> being more likely due to the phase being confirmed by XRD as CuMnO<sub>2</sub>, in which Mn is in the +3 state. However the shoulder peak at 649.2 eV is unusual but

does appear in all crednerite samples and those published previously<sup>29, 34</sup>. The O 1s region shows two peaks at 529.8 eV (which is associated with lattice oxygen) and 531.3 eV associated with adsorbed oxygen<sup>35</sup>.

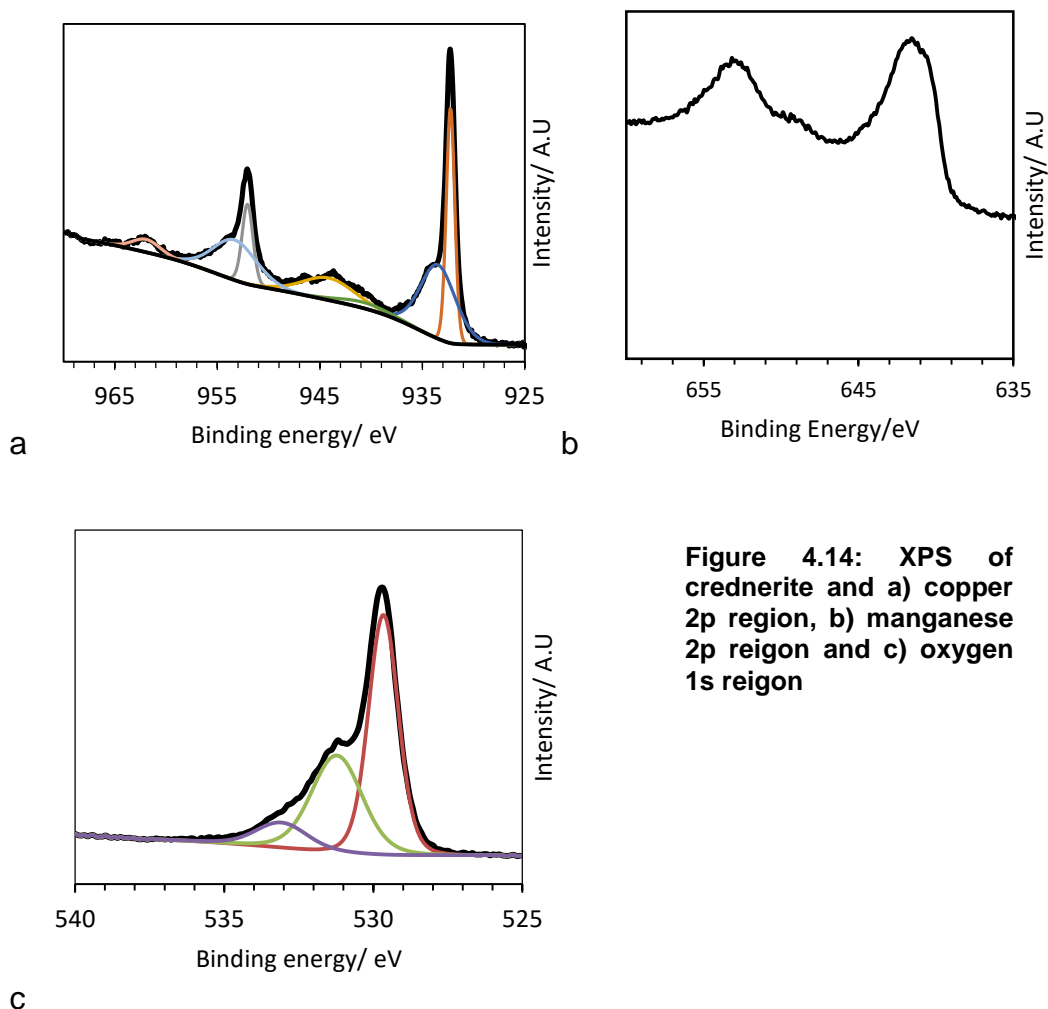
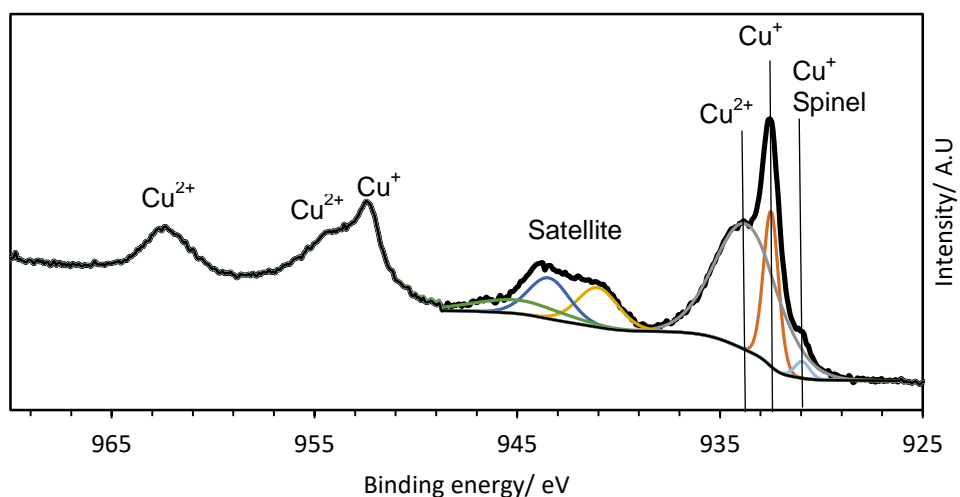
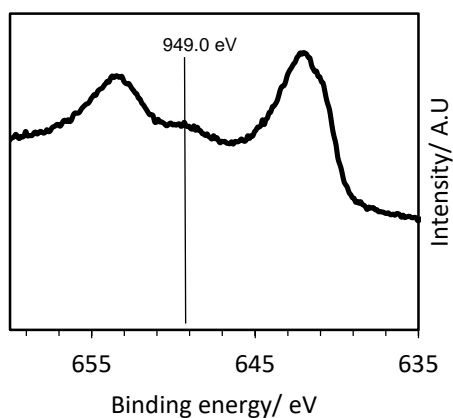


**Figure 4.14: XPS of crednerite and a) copper 2p region, b) manganese 2p region and c) oxygen 1s region**

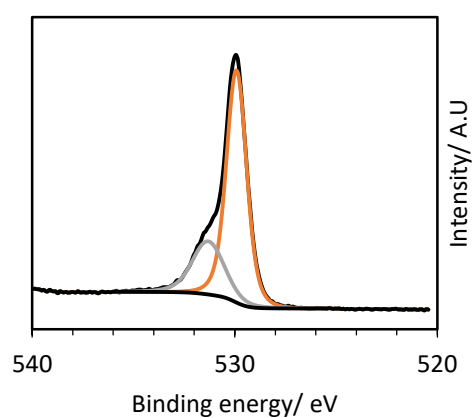
The XPS of the Cu 2p region of  $\text{CuMnO}_2$  that was heat treated at 200 °C (**Figure 4.15 a**) shows the existence of  $\text{Cu}^{2+}$  in the sample as evidenced by the strong satellites and difference in binding energies. The Cu 2p region however showed what appeared to be two additional copper-states one at 932.5 eV which would originate from  $\text{Cu}^+$  in the crednerite structure and the other weak at 931.0 eV due to  $\text{Cu}^+$  in the in a spinel phase octahedral site<sup>36, 37</sup> which suggests the formation of a spinel phase with a possible Cu-Mn redox coupling<sup>38</sup>. Since the XRD pattern (**Figure 4.5 a**) of the material calcined at 200 °C only showed  $\text{CuMnO}_2$ , which would suggest that the spinel phase had formed on the surface though partial oxidation during heat treatment at 200 °C but the bulk remained in the crednerite phase.



a



b



c

**Figure 4.15: XPS of crednerite after heat treated at 200 °C, 3 hours a) Cu 2p region, b) Mn 2p region and c) O 1s region**

X-ray photoelectron spectroscopy of the Cu 2p region of the spinel sample calcined at 300 °C (**Figure 4.16 a**) indicates that there is a mixture of both  $\text{Cu}^+$  and  $\text{Cu}^{2+}$  present in the sample, the broader peaks at 933.18 eV and 953.18 eV along with the strong satellites at 961.88 eV and 940.33-943.73 eV from  $\text{Cu}^{2+}$ . The sharp peaks at 930.68 eV originates from the  $\text{Cu}^+$ , the shift from 932 eV in crednerite to 930.7 eV in the spinel originate from the octahedral  $\text{Cu}^+$  of the spinel phase redox coupling with manganese<sup>36</sup>. The  $\text{Cu}^+$  930.7 eV

proves that the entire sample has formed the spinel phase and the  $\text{Cu}^+$  is originating from the redox properties of the spinel and not residual crednerite and the crednerite phase had oxidised to spinel after 300 °C. The Mn 2p spectra remained the same as the untreated crednerite with the two peaks at 641.58 eV and 653.06 eV. The feature at 649.0 eV which appears in the fresh crednerite samples does not occur in any of the spinel phase materials.

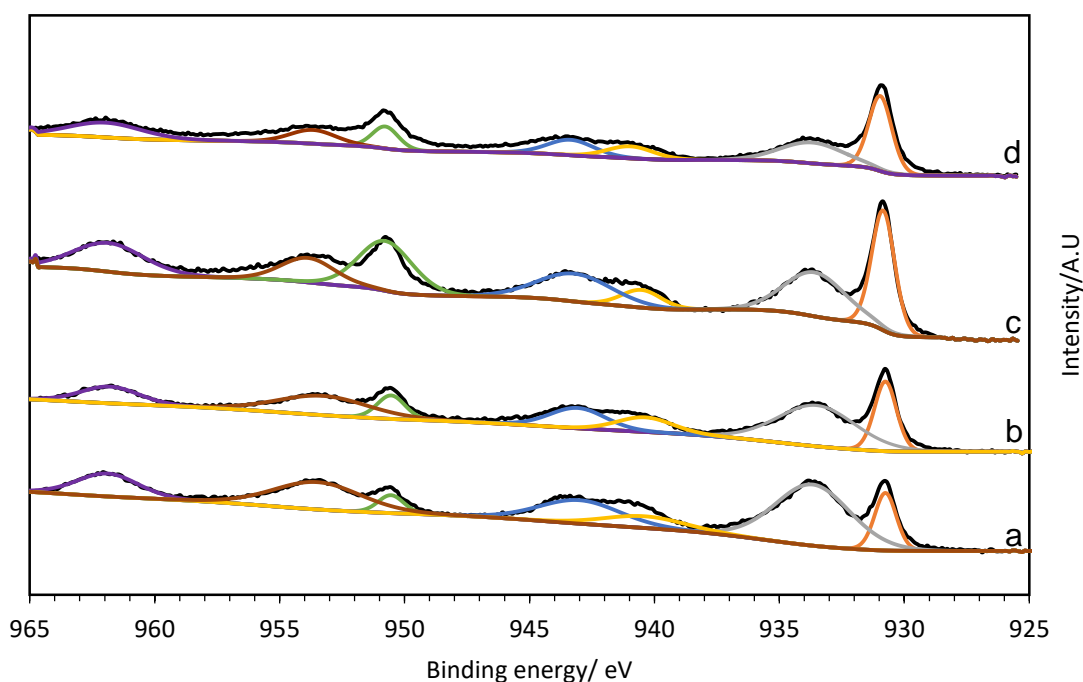


**Figure 4.16: XPS of the copper 2p region of the spinel phase oxides calcined at a) 300 °C, b) 350 °C, c) 400 °C and d) 500 °C**

The Cu 2p spectrum for the spinel formed at 350 °C (**Figure 4.16 b**) showed the same peaks at similar binding energies to the 300 °C spinel oxide ( $\text{Cu}^+$  at 930.68 eV and 950.88 eV). However, the intensities of the  $\text{Cu}^+$  peak relative to the  $\text{Cu}^{2+}$  peaks increases in the 350 °C compared to the 300 °C sample. Copper-manganese spinel oxides are known to undergo a redox coupling ( $\text{Cu}^{2+}$  and  $\text{Cu}^+$  with  $\text{Mn}^{3+}$  to  $\text{Mn}^{4+}$ )<sup>28, 38</sup>. The XPS would suggest that the redox coupling is greater in the 350 °C sample than the 300 °C and therefore would suggest a higher phase integration in the 350 °C and the formation of a more crystalline material<sup>28</sup> which is supported by XRD. The increase in  $\text{Cu}^+$  is associated with deactivation of the catalyst<sup>28, 37</sup>.

The Cu 2p spectra of the crednerite spinel heated to 400 °C and 500 °C (**Figure 4.16 c and d**) shows the presence of both  $\text{Cu}^+$  and  $\text{Cu}^{2+}$ , with the

intensity of the  $\text{Cu}^+:\text{Cu}^{2+}$  increasing again with increase in calcination temperature as the spinel phase becomes more crystalline and improved mixing of the copper and manganese resulting in a higher redox coupling.

The manganese 2p region (**Figure 4.17 left**) showed two broad peaks at 641.8 eV and 653.5 eV. However manganese (II-IV) oxides all have similar binding energies and it is known for these peaks to merge and the broadness of the peaks would suggest more than one oxidation state, which would occur in a redox coupled hopcalite<sup>37, 38</sup>. The satellite at 687.8 eV indicates the presence of  $\text{Mn}^{2+}$  in this sample<sup>39, 40</sup>.

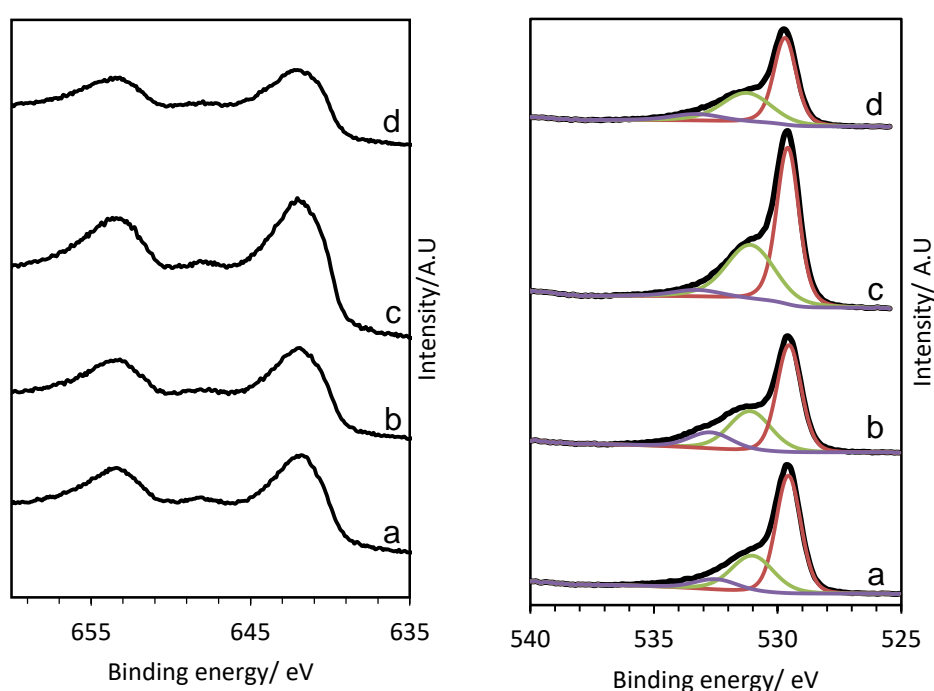


**Figure 4.17: (left) XPS of the manganese 2p region and (right) O 1s region for spinel catalysts calcined at a) 300 °C, b) 350 °C, c) 400 °C and d) 500 °C**

The XPS spectra of the Cu 2p region for the co-precipitated sample in a 1:2 ratio calcined at 400 °C showed that  $\text{Cu}^+$  (peaks at binding energies of 930.9 eV and 950.6 eV) was present in this sample. However the  $\text{Cu}^{2+}:\text{Cu}^+$  peak height was low, especially in comparison to the crednerite derived spinel catalysts formed at the same or lower temperatures.

The XPS of the co-precipitated catalyst calcined at 500 °C showed a large increase in  $\text{Cu}^+:\text{Cu}^{2+}$  in comparison to the co-precipitated sample calcined at

400 °C, comparable to the crednerite calcined at 500 °C, which would indicate an increase in crystallinity of the spinel phase, as seen with the XRD.

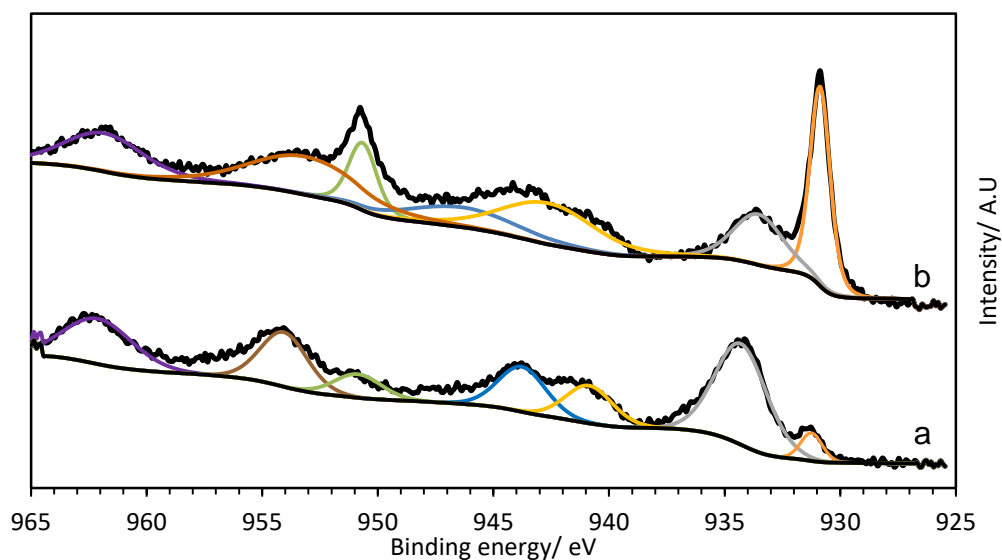


**Figure 4.18: XPS of the Cu 2 p region for the co precipitated copper-manganese oxides (1:2 ratio) calcined at a) 400 °C and b) 500 °C**

The Mn 2p region for the co-precipitated sample calcined at 400 °C (**Figure 4.19 left**) did not show a satellite peak at 647 eV which would possibly indicate that there is no or very little  $\text{Mn}^{2+}$  present in the system, while the 1:2 Cu:Mn, co-precipitated material calcined at 500 °C shows a possible satellite, it is not as prevalent as crednerite calcined at 300-500 °C.

Comparing the XPS spectra of the copper and manganese regions of the co-precipitated samples with that of crednerite derived spinel catalysts shows that there is more copper-manganese redox interaction present in the crednerite-derived samples based on the ratio of  $\text{Cu}^+:\text{Cu}^{2+}$  peaks present. This is notable in samples calcined at lower temperature 300-400 °C which showed a larger presence of  $\text{Cu}^+:\text{Cu}^{2+}$  than the co-precipitated sample calcined at 400 °C. The increase in interaction that causes the increase in  $\text{Cu}^+:\text{Cu}^{2+}$  ratio is related to the crystallinity of the sample. The samples that have the high  $\text{Cu}^+:\text{Cu}^{2+}$ , are fairly crystalline whereas the samples with very low  $\text{Cu}^+$  are less crystalline or amorphous (such as the co-precipitated sample calcined at 400 °C).

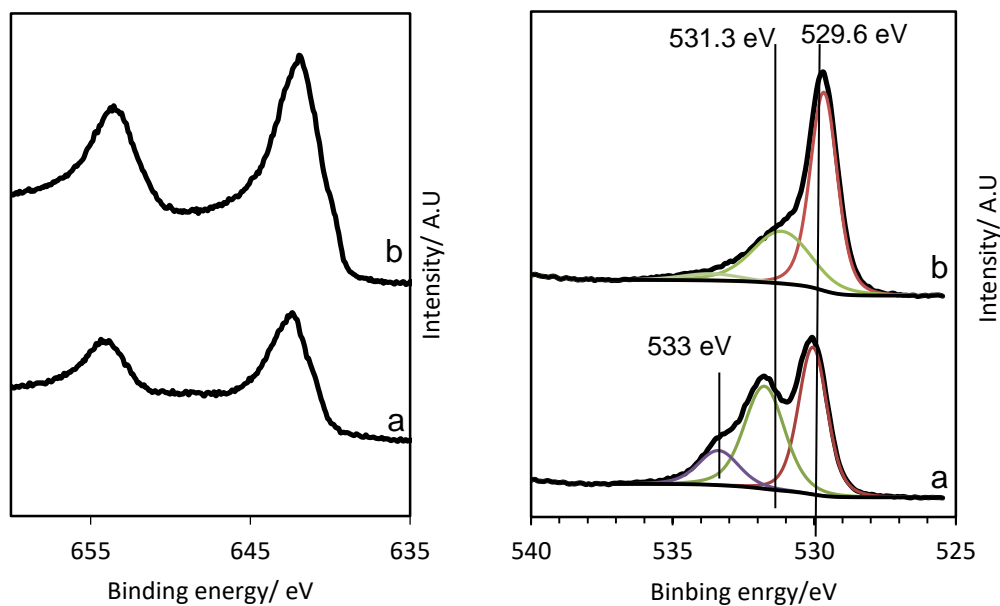


**Figure 4.19: XPS spectra of (left) manganese 2p region and (right) O 1s region for the co-precipitated copper-manganese oxides calcined at a) 400 °C and b) 500 °C**

The O 1s region for the calcined samples shows three peaks with binding energies of 529.6 eV (lattice oxygen), 531.3 eV (adsorbed oxygen) and 532.9-533.3 eV, which is associated with small amounts of hydroxyl species on the surface. The sample calcined at higher temperatures did not show significant changes in the oxygen XPS with the ratio of lattice:surface oxygen mildly decreasing with increased calcination temperature.

However, when compared with the O 1s XPS of the co-precipitated oxide calcined at 400 °C, it showed a larger ratio of adsorbed oxygen at 531.8 eV and surface OH groups (533.3 eV) compared with the more crystalline crednerite derived spinel phase.

**Table 4.5: Surface oxygen composition ( $\pm 5\%$ ) of the heat treated crednerite and co-precipitated catalysts**

Sample/ Calcination temperature	Lattice %	O 1s surface %	OH %
Crednerite 200 °C	73	27	-
Crednerite 300 °C	58	30	12
Crednerite 350 °C	50	33	17
Crednerite 400 °C	55	40	5
Crednerite 500 °C	53	39	8
Co-precipitation 1:2 Cu:Mn 400 °C	43	42	14
Co-precipitation 1:2 Cu:Mn 500 °C	61	35	4

Temperature programmed reduction (TPR) of the crednerite sample (**Figure 4.20**) performed under 10% H<sub>2</sub>/Ar, showed a large reduction peak at 200-220 °C (centred at 209 °C) caused by the reduction of Cu<sup>+</sup> to Cu<sup>0</sup> which results in the decomposition/collapse of the crednerite phase and possible Mn<sup>3+</sup> reduction to Mn<sup>2+</sup>. The TPR profile of the sample that was calcined at 200 °C shows an initial reduction peak appearing at 210 °C followed by a much broader reduction from 220 °C to 260 °C. This broader reduction could originate from manganese reduction (Mn<sup>3+</sup> to Mn<sup>2+</sup>) and isolated Cu<sup>2+</sup>/CuMn<sub>2</sub>O<sub>4</sub> that was shown by XPS to have existed in the sample after calcination at 200 °C.

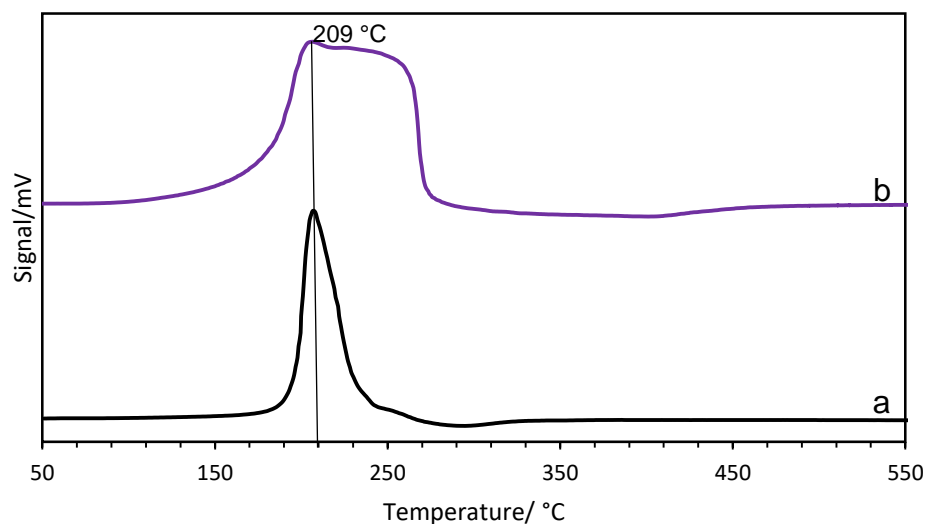


**Figure 4.20: Temperature programmed reduction of crednerite a) as synthesised and b) heat treated at 200 °C in air**

The temperature programmed reduction profile of the spinel phase catalysts formed at 300-500 °C (**Figure 4.21**) showed a general change with increasing calcination temperature. The 300 °C sample showed two reductions that had merged at 243 °C and 255 °C. The first reduction at 243 °C can be assigned to the reduction of  $\text{Cu}^{2+}$  to  $\text{Cu}^0$  while the second reduction is that of  $\text{Mn}^{3+}$  to  $\text{Mn}^{2+}$ .<sup>41</sup>

The spinel phased formed at 350 °C had a different reduction profile with an initial reduction peak at 200 °C which could be assigned to the reduction of dispersed  $\text{CuO}$  to  $\text{Cu}$ , while the bulk  $\text{Cu}^{2+}$  is assigned to the second peak at 260 °C. The manganese reduction ( $\text{Mn}^{3+}$  to  $\text{Mn}^{2+}$ ) occurred at around 305-325 °C. The sample calcined at 400 °C had a similar reduction to the one calcined at 350 °C with the dispersed  $\text{CuO}$  reduction at 190 °C followed by the bulk  $\text{Cu}^{2+}$  at 240 °C and the manganese reduction (which was broader than the 350 °C sample) at 270-330 °C. The 500 °C spinel showed an initial reduction at 190 °C while the  $\text{CuO}$  reduction and the manganese reduction occurred over a broader temperature range of 250-330 °C.<sup>41</sup>

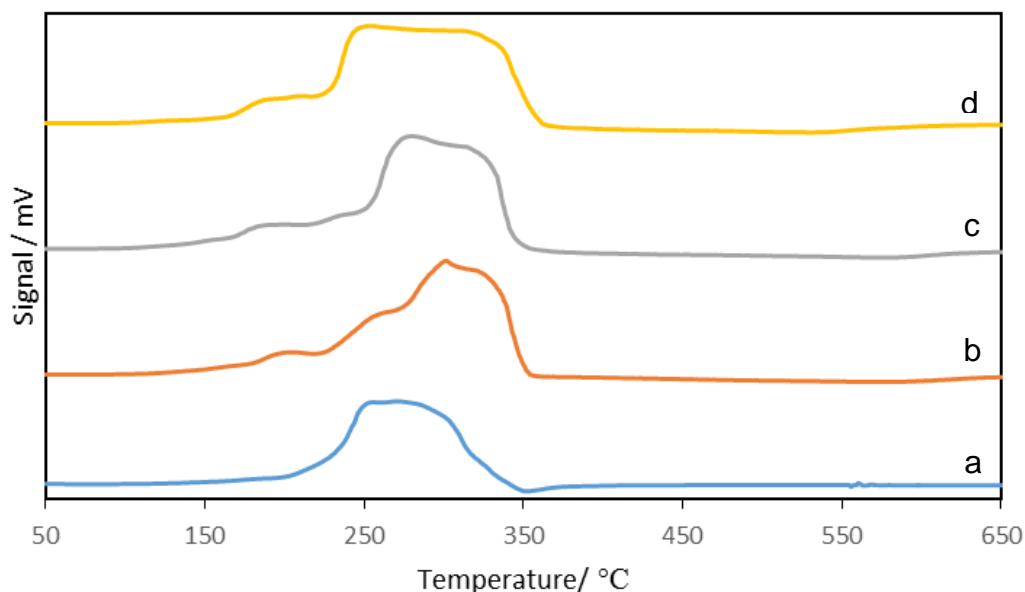


**Figure 4.21: Temperature programmed reduction of the spinel copper-manganese oxides formed at a) 300 °C, b) 350 °C, c) 400 °C and d) 500 °C**

The change in the TPR profiles between the spinel oxides calcined from 300 °C to 500 °C seem to suggest an increase in dispersed CuO, practically from 300 °C to 350 °C where the peak associated with more dispersed CuO starts to appear as well as shifting to lower temperatures (205 °C to 190 °C) with increasing calcination temperatures. This could indicate possible phase separation occurring although this was not observed by XRD.

The temperature programmed reduction profile of the both 1:1 and 1:2 co-precipitated spinel oxides calcined at 400 °C (**Figure 4.22**) showed a broad reduction starting from 150 °C-260 °C comprising of an initial peak at 203 °C ( $\text{Cu}^{2+}$  to  $\text{Cu}^0$ ) and a broad peak 232-260 °C being  $\text{Mn}^{3+}$  to  $\text{Mn}^{2+}$ . The co-precipitated samples calcined at 500 °C showed a reduction occurring at higher temperature with the 1:2 sample showing two reduction peaks at 285 °C and 306 °C, with the  $\text{Cu}^{2+}$  to  $\text{Cu}^0$  and followed by the  $\text{Mn}^{3+}$  to  $\text{Mn}^{2+}$ . The 1:1 Cu:Mn calcined at 500 °C had multiple reductions which might suggest some degree of phase separated or dispersed CuO (reduction at 211 °C) and manganese oxide (reduction at 358 °C).

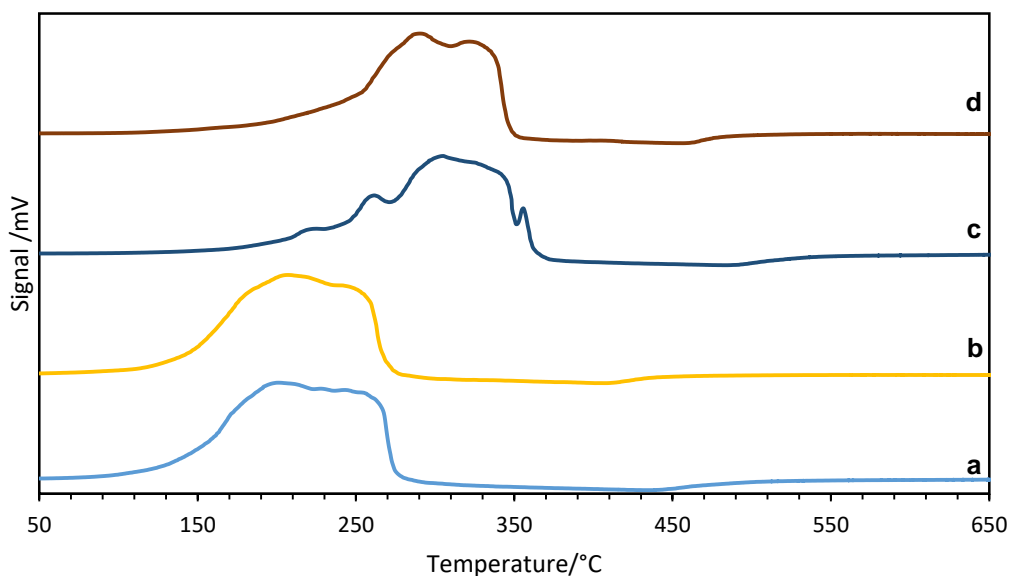


**Figure 4.22: TPR profile of co-precipitated copper manganese oxide a) 1:1 calcined 400 °C, b) 1:2 calcined 400 °C, c) 1:1 calcined 500 °C and d) 1:2 calcined 500 °C**

The difference in TPR profile between the co-precipitated samples calcined at 400 °C and 500 °C with the crednerite showed that the co-precipitated (calcined 400 °C) did not contain copper oxide that was present in the crednerite based spinel catalysts. This would confirm that CuO had formed during the calcination process, although this was not detected by XRD probably due to the spinel being the dominant crystalline phase, and the CuO being too small to be detected. However, it should be noted that the co-precipitated samples were mostly amorphous which may affect their TPR profile. In addition, the possible presence of residual carbonates (left over from calcination) and may contribute to the reduction profile<sup>20</sup>.

Comparison of the SEM images of the co-precipitated spinel calcined at 400 °C (**Figure 4.23 f**) compared with the crednerite derived spinel oxides (**Figure 4.23 a-e**) showed vary different morphologies. The crednerite particles formed a plate like morphology, which was retained in spinel oxides even after heat treatment as high as 400 °C, although the particles at 500 °C appeared to be slightly larger possibly due to the crystallization of the spinel phase. In comparison, the co-precipitated copper-manganese oxide had a much different structure, forming a flower like structures made up from smaller oval particles.

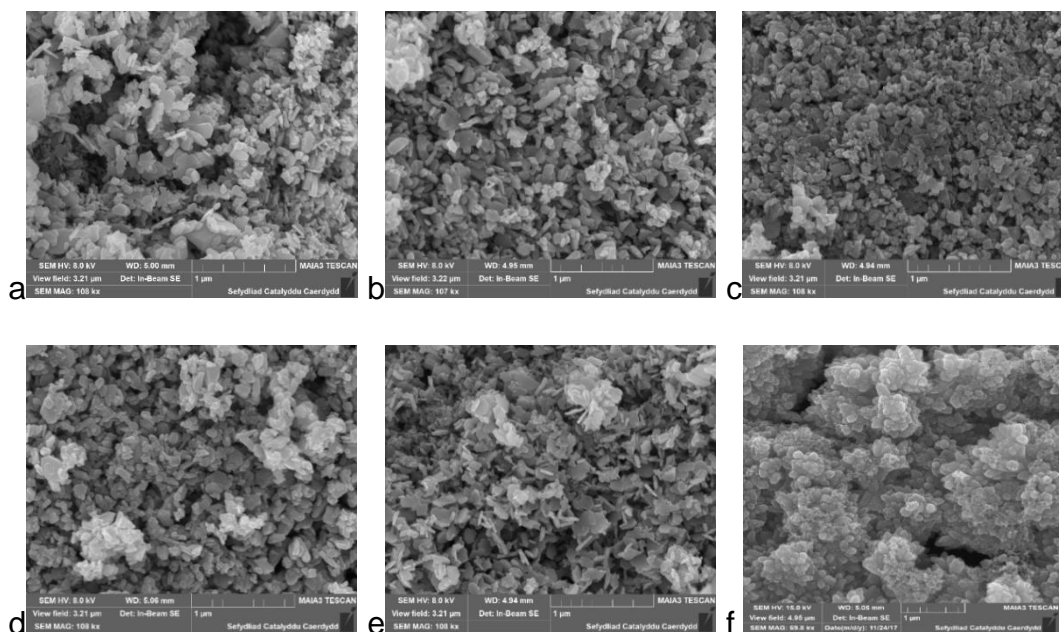


**Figure 4.23: SEM images of the copper manganese samples; (a) crednerite, the calcined samples at (b) 300 °C, (c) 350 °C, (d) 400 °C, (e) 500 °C and (f) co-precipitated calcined at 400 °C.**

## **4.4 Crednerite and spinel derivatives as catalyst for CO oxidation**

### **4.4.1 Carbon monoxide conversion activity of crednerite and spinel derivatives in comparison with co-precipitated hopcalite.**

The crednerite and the spinel derived from heat treatment of the crednerite were used as catalyst for the oxidation of CO in a 4850 ppm CO/air mixture and compared to the co-precipitated materials. The reaction was initially performed at 20 °C to observe the initial activity and any deactivation that might occur in the first 30 minutes of testing. The activity of the catalyst was studied over a temperature range of 20-70 °C (and held at each temperature for 20 minutes) in order to see the increase in activity and to compare the increase in activity of crednerite and its calcined spinel derivatives with the co-precipitated catalysts.

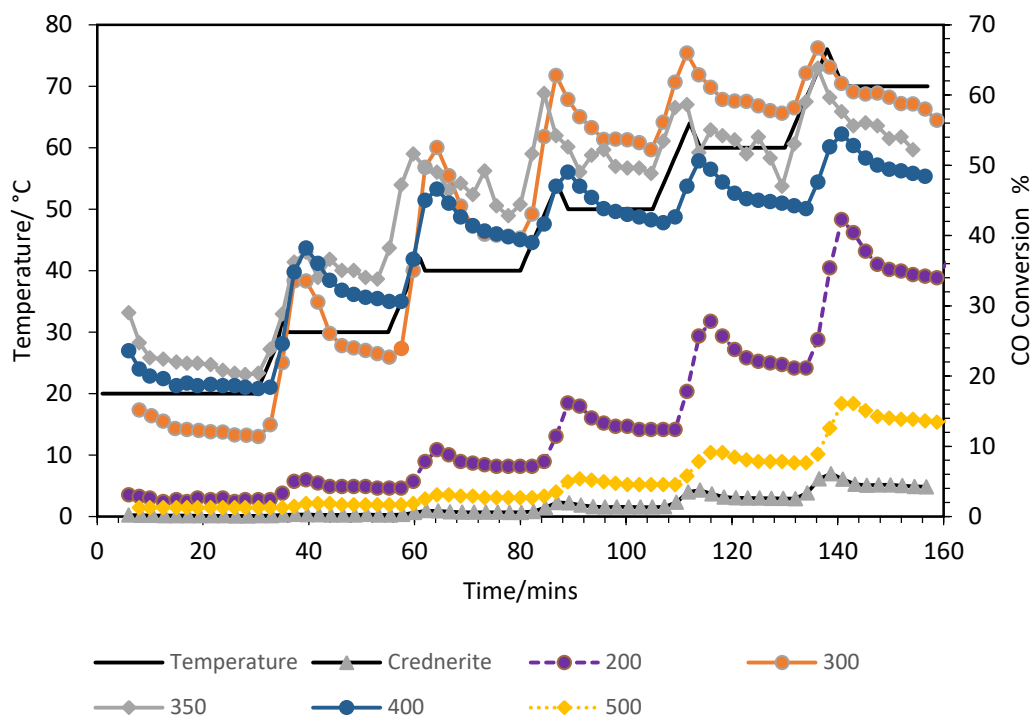


**Figure 4.24: CO oxidation (4850 ppm CO/air) using crednerite and spinel oxides derived from heat treatment of crednerite at 200-500 °C**

The conversion of CO using the crednerite material is very low, showing almost no conversion at room temperature and only approximately 4% at 60-70 °C. This shows that the crednerite is not practically active towards CO oxidation at low temperatures, especially when compared with hopcalite. The reasons for the low activity could be due to the oxidation state of the metal in this phase as all of the copper is present in the +1 oxidation state and manganese is present in the +3 oxidation state. It has been proposed by literature<sup>17, 38</sup> that during CO oxidation hopcalite undergoes a redox cycling between the copper and manganese, with the copper moving between the +1 and +2 and manganese between the +3 and +4 oxidation states. This mechanism would be absent in crednerite, which is locked in the Cu<sup>+</sup> and Mn<sup>3+</sup> oxidation states<sup>38</sup>. The potential for the catalysts to be poisoned by sodium is unlikely since the calcined catalyst had no additional treatment that would have removed residual sodium and these catalysts showed no signs of poisoning.

The crednerite sample that was heat treated to 200 °C (with the bulk still present in crednerite phase) showed a much higher conversion than the

non-heat treated crednerite, with 2% conversion at 20 °C and 34% conversion at 70 °C. The increase in activity of the 200 °C crednerite over the non-heated sample is most likely due to the presence of spinel phase that had formed on the surface of the 200 °C crednerite as observed by XPS. This may have created isolated active sites (possibly spinel phase) on the surface which enhanced the activity of the crednerite.

The spinel oxides derived from crednerite however showed a much more interesting conversion profile in comparison. The crednerite-derived spinel (**Figure 4.24**) calcined between 300-400 °C had a CO conversion of 16-28 % at 20 °C but remained stable at that level. In comparison the co-precipitated catalysts calcined at 400 °C (**Figure 4.25**) had, initially, a higher CO conversion but this rapidly dropped within the first 30 minutes whereas the crednerite derived spinel maintain a consistent level CO conversion within this time frame. This is not also taking into account the lower surface area of the crednerite derived materials over the co-precipitated materials.

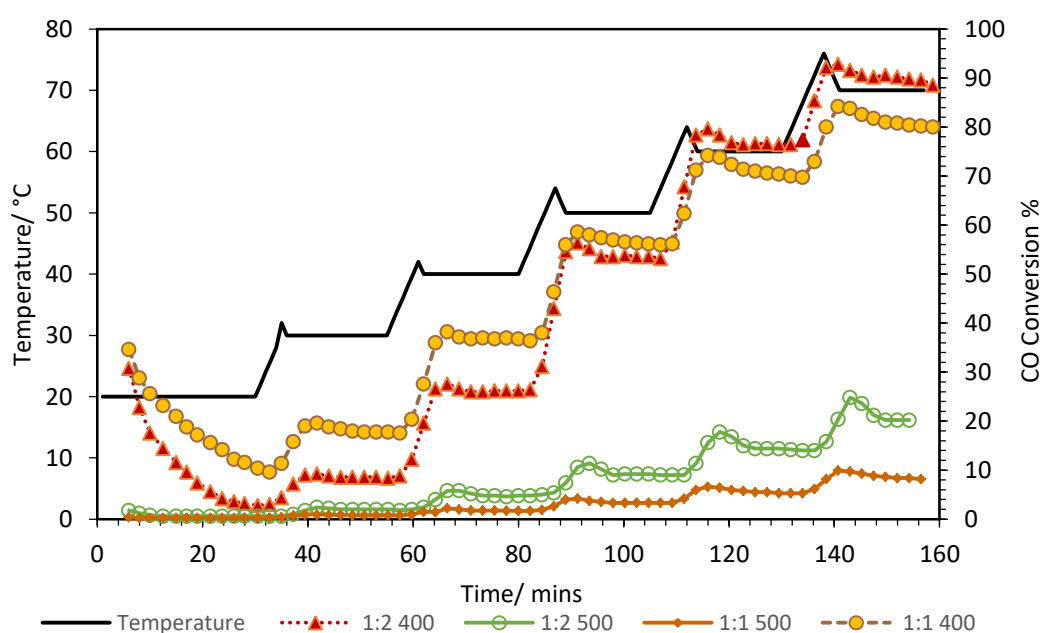


**Figure 4.25: CO-oxidation of the co-precipitated catalysts 1:1 and 1:2 Cu:Mn calcined at 400-500 °C**

However the crednerite derived spinel oxides start to show signs stagnation after 50 °C (80 minutes) while the co-precipitated catalysts continued to increase the amount of CO converted with increasing temperature. This

suggests that the crednerite derived spinel had started to deactivate after 80 minutes which resulted in a decrease in CO conversion after each temperature ramp.

The spinel oxides, prepared from both crednerite and co-precipitation (1:1 and 1:2 Cu:Mn) that were calcined at 500 °C all showed very low CO conversion compared to those calcined 300-400 °C, with this low conversion originating from the increase in crystallinity of the sample and lower surface area.

XPS performed on the post reaction catalyst calcined from crednerite at 300 °C in the Cu 2p region (**Figure 4.26**) showed that a slight increase in the  $\text{Cu}^+$  peak relative to the  $\text{Cu}^{2+}$  compared to the fresh catalyst which is normally a sign of deactivation<sup>37</sup>. While this is only a minor decrease, it does demonstrate a possibility that the catalyst is deactivating due to increased  $\text{Cu}^+$ .

The O 1s region however did show differences between for  $\text{Cu}_{1.5}\text{Mn}_{1.5}\text{O}_4$  calcined at 350 °C pre and post CO oxidation (**Table 4.6**) with the post CO catalysts showing a greater peak at 531.0 eV (adsorbed oxygen) than the fresh catalyst. The catalyst calcined at 300 °C however did not show a difference between the fresh and post CO catalyst in the O 1s region.

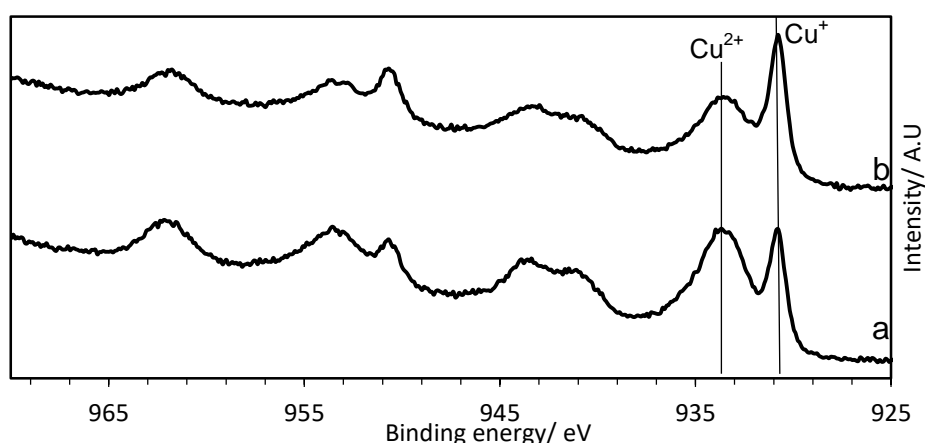


**Figure 4.26:** Cu 2P XPS region of spinel (from crednerite heat treated at 300 °C) a) fresh and b) post reaction

**Table 4.6: Ratio of lattice: surface oxygen ( $\pm 0.1$ ) calculated by XPS of the fresh and post reaction catalysts (crednerite calcined 300 °C and 350 °C)**

Sample	Oxygen Lattice: surface	
	Fresh catalysts	Post reaction
CuMn-300	1:0.5	1:0.6
CuMn-350	1:0.6	1:0.8

#### 4.4.2 Discussion on surface area normalised rates

While the previous sections discussed the activity of each catalyst as a function of CO converted for 50 mg of catalyst, one factor to consider is that the co-precipitated catalysts had a higher surface area than the crednerite derived materials. The fact that the co-precipitated catalyst performed better than crednerite derived materials at higher temperatures may be partly due to the greater number of surface sites present (76 m<sup>2</sup> g<sup>-1</sup> for 1:2 co-precipitated calcined at 400 °C).

The surface area normalised rates were worked out using the equation shown below;

$$\text{Conversion (mol m}^{-2}\text{s}^{-1}) = \frac{(\text{CO mols s}^{-1}) \times (\% \text{ of CO Converted})}{(\text{surface area of catalyst m}^2 \text{ g}^{-1}) \times (\text{catalyst mass g})}$$

**Figure 4.27: Equation for working out surface area normalised activity**

Where *mol* of CO is the amount of CO passing through the catalyst bed per second, which for 4850 ppm CO air at a flow of 20 ml min<sup>-1</sup> worked out as 6.52x10<sup>-8</sup> mol s<sup>-1</sup> (when assuming standard temperature and pressure conditions). For all experiments the catalyst mass was 50 mg and the surface areas are the values derived from 5-point BET (**Table 4.2**).

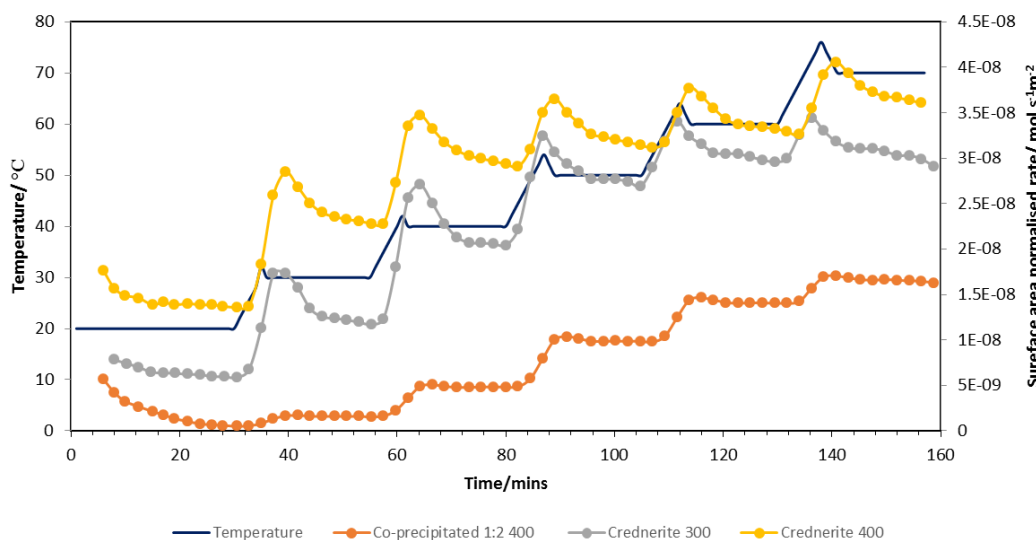


**Figure 4.28: The Surface area normalised CO conversion of the co-precipitated catalyst (400 °C) and crednerite derived spinel (300 °C and 400 °C)**

Normalising the activity per surface area (**Figure 4.28**) has shown that the crednerite derived catalysts have significantly higher rates than the co-precipitated catalysts at nearly all temperatures with the co-precipitated catalyst having a rate of  $1.36 \times 10^{-9} \text{ mol s}^{-1} \text{ m}^{-2}$  at 60 °C compared to the crednerite derived spinel (calcined 400 °C) which had  $1.31 \times 10^{-9} \text{ mol s}^{-1} \text{ m}^{-2}$  at 20 °C. This is even more significant when taking into account that the crednerite derived material is in a 1:1 Cu:Mn ratio whereas the co-precipitated catalysts are 1:2 which has previously been stated as the most activate catalyst for CO oxidation<sup>16</sup>.

#### **4.4.3 The effect of airflow heat treatment methodology on the activity on the CO oxidation activity**

The different methodology used during the heat treatment (at 350 °C) did not affect the catalytic ability of the crednerite derived spinel (**Figure 4.29**), with both the static and flowing air heated copper-manganese having almost the same activity apart from 80 °C when the static showed a slightly higher conversion at 80 °C to the sample calcined under flowing air. Taking surface area normalised rate would make little difference since the two catalysts had the same surface area of  $22 \text{ m}^2 \text{ g}^{-1}$ .

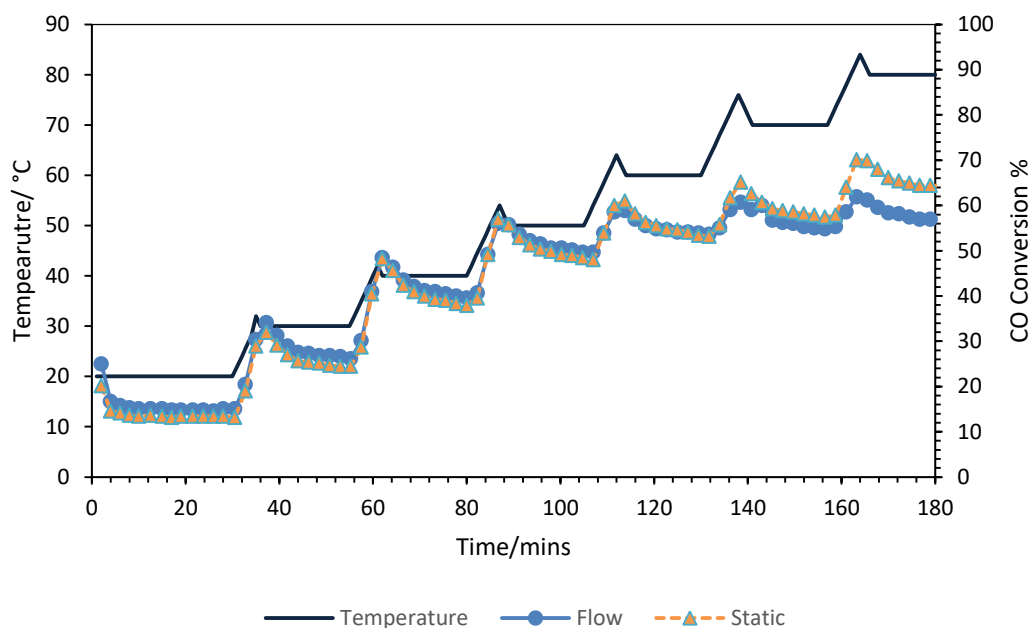


**Figure 4.29: CO conversion of crednerite heat-treated at 350 °C under flow and static air**

The similar CO conversion and the similarities in the XRD data and surface areas show that the airflow over the crednerite had no major effect on its catalytic performance at lower temperatures, especially when taking into account the  $\pm 5\%$  error. Although the two materials formed different amounts of phase separated CuO and spinel phase, the effect on their catalytic activity is very little, especially when compared with the difference in preparation methods and heat treatment temperatures.

#### 4.4.4 Catalyst deactivation and stability

The stability of crednerite derived spinel catalyst was investigated further. As noted in section 4.4.2 the crednerite-derived spinel catalysts deactivated and stagnated in their activity at 50 °C and above. Because of this observation multiple CO oxidation runs were performed to see if the activity recovered in the second run. For this study, the 400 °C spinel sample was used and compared with co-precipitated also calcined at 400 °C (1:1 ratio only). It should be noted the CO oxidation was performed at 20-80 °C and the ramp

rate is  $1\text{ }^{\circ}\text{C min}^{-1}$ . The lower heating rate also had the advantage of giving better control over the temperature set point.

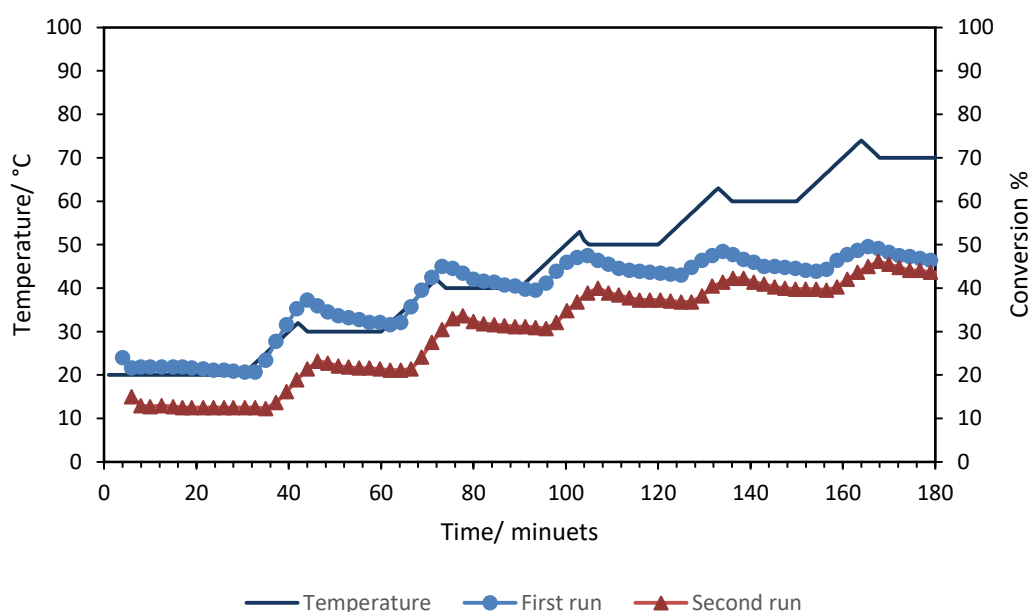


**Figure 4.30: CO oxidation with the crednerite derived catalyst calcined at  $400\text{ }^{\circ}\text{C}$  with the initial/first run and second run**

The initial CO oxidation activity of the sample calcined at  $400\text{ }^{\circ}\text{C}$  (**Figure 4.30**) showed conversion of 21% which plateaued above  $50\text{ }^{\circ}\text{C}$  with CO conversion remaining at 40-46%. When the sample was reused for a second reaction after cooling back down the CO conversion halved at  $20\text{ }^{\circ}\text{C}$ . However, as the temperature increases the difference in CO conversion between the first and second run starts to decrease until  $80\text{ }^{\circ}\text{C}$  where the performance of the catalyst was very similar between the first and second run. The CO conversion on the first run appears to decline after each temperature ramp but on the second run, the activity appears to stabilise shortly after reaching each temperature interval.

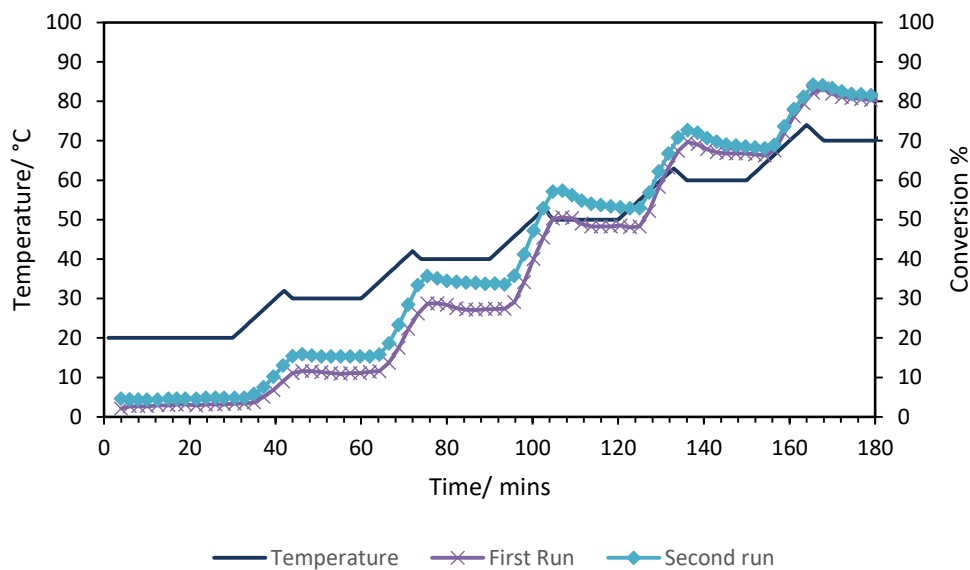


**Figure 4.31: CO oxidation of the co-precipitated catalyst (1:1 Cu:Mn) calcined at 400 °C.**

In comparison, repeat studies of the co-precipitated catalyst (1:1 ratio) also calcined at 400 °C showed a somewhat different trend, with the second CO conversion during the second run oxidation showing very similar conversions although the second run at 40 °C was slightly better than the first, although this difference is within the margin of error.

What is also interesting to note was that there was also no pre-treatment for the spinel phase from crednerite but its conversion remained similar to the sample that was pre-treated with 20% conversion at 20 °C. This would confirm that it had a higher stability towards atmospheric or surface water (at least during the initial run) than the co-precipitated catalysts which showed a rapidly reduced conversion when not pre-treated.

## 4.5 Chapter 4 Conclusions

Copper manganese based delafossite formed from hydrothermal synthesis at 80 °C has been shown to be a poor catalyst for low temperature CO oxidation. The use of crednerite as a precursor to the spinel phase however showed some interesting properties. The spinel phase copper-manganese oxide fully formed at 300 °C with no signs of crednerite phase left while at 200 °C, the phase was still predominately crednerite although XPS studies showed the formation of spinel phase on the surface, which contributed to an enhanced CO conversion compared non heat treated crednerite.

The catalysts despite having a lower surface area of  $<27 \text{ m}^2 \text{ g}^{-1}$ , showed reasonable CO oxidation at room temperature and when compared with co-precipitated catalyst in terms of surface area normalised rates, showed a much better CO oxidation activity per  $\text{m}^2$ , and also showed a lower rate of deactivation in the first 30 minutes of testing. However, these catalysts showed signs of deactivation after heating to higher temperatures and repeat testing showed that CO conversion halved at 20 °C on the second run. XPS showed that there was an increase in the  $\text{Cu}^+:\text{Cu}^{2+}$  between the fresh and post reaction crednerite derived spinel catalyst (calcined 300 °C) that would suggest that a catalyst composition change was partially responsible for this deactivation.

The characterisation of the crednerite-derived spinel oxides showed differences to those prepared by co-precipitations, with XPS analysis on the samples heat treated at 300-400 °C showing a higher  $\text{Cu}^+:\text{Cu}^{2+}$  than the co-precipitated oxides which, along with the TPR profiles, would suggest greater Cu-Mn interaction and mixing in the crednerite derived spinel catalysts than the co-precipitated catalysts.

The formation of crednerite using hydrothermal synthesis rather than a high temperature solid state synthesis demonstrates that hydrothermal synthesis is still a key technique for making materials and catalysts with unique or unusual properties compared to forming oxide through calcination of a precursor salt formed by technique such as co-precipitation.

## 4.6 Chapter 4 Future Work

The use of hydrothermal synthesis to make crednerite and its spinel derivative from heat treatment in air has been shown to produce copper-manganese spinel oxides that behave differently from the conventional hopcalite catalysts. However, further investigation using temporal analysis of products (TAP) reactor is needed to analyse the reaction to see if there are any mechanistic differences between the crednerite derived spinel and the co-precipitated hopcalite samples during CO oxidation.

There has been very little study into the use of crednerite or delafossite in general as supports for precious metals such as gold or platinum for catalysis. The presence of  $\text{Cu}^+$  and the P-type nature of delafossite materials may give properties to supported metal catalysts that may enhance catalytic activity and selectivity, which could be investigated. The spinel phase oxides derived from the crednerite phase, which behave differently from conventional, co-precipitated hopcalite catalysts, may also give different properties and behaviours as supports for precious metal catalysts.

The use of the spinel (derived from crednerite) catalysts could also be used for oxidation of VOCs such as propane, toluene and naphthalene<sup>21, 25</sup> to investigate if these catalysts are viable alternatives to co-precipitated hopcalite and to see if they behave differently for these reactions as well.

The catalysts investigated here were made from one crednerite precursor. Investigation into varying the crednerite preparation methodology (such as temperature during hydrothermal synthesis) and its effects on the spinel derivative is also another avenue that could be investigated.

## 4.7 Chapter 4 References

1. S. Kato, R. Fujimaki, M. Ogasawara, T. Wakabayashi, Y. Nakahara and S. Nakata, *Applied Catalysis B-Environmental*, 2009, **89**, 183-188.
2. R. Gillen and J. Robertson, *Physical Review B*, 2011, **84**, 7.
3. D. O. Scanlon and A. Walsh, *Acta Crystallographica Section B-Structural Science Crystal Engineering and Materials*, 2015, **71**, 702-706.
4. T. I. Draskovic and Y. Y. Wu, *Chemcatchem*, 2017, **9**, 3837-3842.
5. M. S. Prevot, Y. Li, N. Guijarro and K. Sivula, *Journal of Materials Chemistry A*, 2016, **4**, 3018-3026.
6. S. Y. Choi, C. D. Kim, D. S. Han and H. Park, *Journal of Materials Chemistry A*, 2017, **5**, 10165-10172.
7. M. Trari, J. Topfer, J. P. Doumerc, M. Pouchard, A. Ammar and P. Hagenmuller, *Journal of Solid State Chemistry*, 1994, **111**, 104-110.
8. W. C. Sheets, E. Mugnier, A. Barnabe, T. J. Marks and K. R. Poeppelmeier, *Chemistry of Materials*, 2006, **18**, 7-20.
9. M. Poienar, R. Banica, P. Sfirloaga, C. Ianasi, C. V. Mihali and P. Vlazan, *Ceramics International*, 2018, **44**, 6157-6161.
10. S. Mobini, F. Meshkani and M. Rezaei, *Process Safety and Environmental Protection*, 2017, **107**, 181-189.
11. Y. H. Choi, Y. J. Jang, H. Park, W. Y. Kim, Y. H. Lee, S. H. Choi and J. S. Lee, *Applied Catalysis B-Environmental*, 2017, **202**, 605-610.
12. Q. Q. Zhang, D. H. Xiong, H. Li, D. L. Xia, H. Z. Tao and X. J. Zhao, *Journal of Materials Science-Materials in Electronics*, 2015, **26**, 10159-10163.
13. M. Trari, J. Topfer, P. Dordor, J. C. Grenier, M. Pouchard and J. P. Doumerc, *Journal of Solid State Chemistry*, 2005, **178**, 2751-2758.
14. M. Poienar, C. Martin, O. I. Lebedev and A. Maignan, *Solid State Sciences*, 2018, **80**, 39-45.
15. M. A. Sarabia, S. D. Rojas, Z. Lopez-Cabana, R. Villalba, G. Gonzalez and A. L. Cabrera, *Journal of Physics and Chemistry of Solids*, 2016, **98**, 271-279.
16. G. J. Hutchings, A. A. Mirzaei, R. W. Joyner, M. R. H. Siddiqui and S. H. Taylor, *Applied Catalysis A-General*, 1998, **166**, 143-152.
17. Z. R. Tang, S. A. Kondrat, C. Dickinson, J. K. Bartley, A. F. Carley, S. H. Taylor, T. E. Davies, M. Allix, M. J. Rosseinsky, J. B. Claridge, Z. Xu, S. Romani, M. J. Crudace and G. J. Hutchings, *Catalysis Science & Technology*, 2011, **1**, 740-746.
18. T. Biemelt, K. Wegner, J. Teichert, M. R. Lohe, J. Martin, J. Grothe and S. Kaskel, *Applied Catalysis B-Environmental*, 2016, **184**, 208-215.
19. T. K. Liu, Y. Y. Yao, L. Q. Wei, Z. F. Shi, L. Y. Han, H. X. Yuan, B. Li, L. H. Dong, F. Wang and C. Z. Sun, *Journal of Physical Chemistry C*, 2017, **121**, 12757-12770.
20. T. J. Clarke, S. A. Kondrat and S. H. Taylor, *Catalysis Today*, 2015, **258**, 610-615.
21. D. A. Aguilera, A. Perez, R. Molina and S. Moreno, *Applied Catalysis B-Environmental*, 2011, **104**, 144-150.

22. G. J. Hutchings, A. A. Mirzaei, R. W. Joyner, M. R. H. Siddiqui and S. H. Taylor, *Catalysis Letters*, 1996, **42**, 21-24.
23. M. Haruta, N. Yamada, T. Kobayashi and S. Iijima, *Journal of Catalysis*, 1989, **115**, 301-309.
24. T. H. Rogers, C. S. Piggot, W. H. Bahlke and J. M. Jennings, *Journal of the American Chemical Society*, 1921, **43**, 1973-1982.
25. Z. Ye, J. M. Giraudon, N. Nuns, P. Simon, N. De Geyter, R. Morent and J. F. Lamonier, *Applied Catalysis B-Environmental*, 2018, **223**, 154-166.
26. Z. R. Tang, C. D. Jones, J. K. W. Aldridge, T. E. Davies, J. K. Bartley, A. F. Carley, S. H. Taylor, M. Allix, C. Dickinson, M. J. Rosseinsky, J. B. Claridge, Z. L. Xu, M. J. Crudace and G. J. Hutchings, *Chemcatchem*, 2009, **1**, 247-251.
27. K. Wegner, M. Medicus, E. Schade, J. Grothe and S. Kaskel, *ChemCatChem*, 2018, **10**, 3914-3922.
28. M. Kramer, T. Schmidt, K. Stowe and W. F. Maier, *Applied Catalysis A-General*, 2006, **302**, 257-263.
29. D. H. Xiong, Q. Q. Zhang, Z. J. Du, S. K. Verma, H. Li and X. J. Zhao, *New Journal of Chemistry*, 2016, **40**, 6498-6504.
30. A. A. Mirzaei, H. R. Shaterian, R. W. Joyner, M. Stockenhuber, S. H. Taylor and G. J. Hutchings, *Catalysis Communications*, 2003, **4**, 17-20.
31. Y. Bessekhoud, Y. Gabes, A. Bouguelia and M. Trari, *Journal of Materials Science*, 2007, **42**, 6469.
32. L. N. Cai, Z. H. Hu, P. Branton and W. C. Li, *Chinese Journal of Catalysis*, 2014, **35**, 159-167.
33. S. Dey, G. C. Dhal, D. Mohan and R. Prasad, *Bulletin of Chemical Reaction Engineering and Catalysis*, 2017, **12**, 393-407.
34. K. K. Shukla, P. Shahi, S. Gopal, A. Kumar, A. K. Ghosh, R. Singh, N. Sharma, A. Das, A. K. Sinha, A. G. Joshi, A. K. Nigam and S. Chatterjee, *RSC Advances*, 2015, **5**, 83504-83511.
35. Z. X. Li, H. L. Wang, X. X. Wu, Q. L. Ye, X. T. Xu, B. Li and F. Wang, *Applied Surface Science*, 2017, **403**, 335-341.
36. S. A. Kondrat, T. E. Davies, Z. L. Zu, P. Boldrin, J. K. Bartley, A. F. Carley, S. H. Taylor, M. J. Rosseinsky and G. J. Hutchings, *Journal of Catalysis*, 2011, **281**, 279-289.
37. S. Veprek, D. L. Cocke, S. Kehl and H. R. Oswald, *Journal of Catalysis*, 1986, **100**, 250-263.
38. G. M. Schwab and S. B. Kanungo, *Zeitschrift Fur Physikalische Chemie-Frankfurt*, 1977, **107**, 109-120.
39. H. J. Zhao, K. G. Fang, J. Zhou, M. G. Lin and Y. H. Sun, *International Journal of Hydrogen Energy*, 2016, **41**, 8819-8828.
40. W. Luo, L. Sun, Y. Yang, Y. Q. Chen, Z. Zhou, J. H. Liu and F. Wang, *Catalysis Science & Technology*, 2018, **8**, 6468-6477.
41. H. J. Zhao, K. G. Fang, F. Dong, M. G. Lin, Y. H. Sun and Z. C. Tang, *Journal of Industrial and Engineering Chemistry*, 2017, **54**, 117-125.

# Chapter 5 Switchable Solvents for The Preparation of Copper Manganese Oxide Catalysts

## 5.1 Introduction

### 5.1.1 Background on switchable solvents

Switchable solvents as discussed in Chapter 1, are solvents that change their properties, for example, solvent polarity<sup>1</sup>, depending on the atmosphere which they are under. One example is a mixture of 1,8-diazobicyclo[5.4.0]undec-7-ene and an alcohol or amine, which is a non-polar solvent under a nitrogen atmosphere, but becomes a polar solvent under carbon dioxide<sup>2-5</sup>. Switchable systems other than switchable polar solvents (SPS), have since been discovered including switchable hydrophilic-hydrophobicity solvents (SHS) using additives such as triethylamine<sup>6-8</sup>, switchable water additives such as dimethyl ethanolamine which increase the ionic strength of water and induced a salting out affect<sup>9</sup> and switchable surfactants<sup>10-12</sup>.

Such solvent systems have been applied to areas such as metal extraction<sup>13</sup>, recycling homogeneous catalysts<sup>14</sup> as well as reducing the steps and solvents required for purification of products<sup>15</sup>.

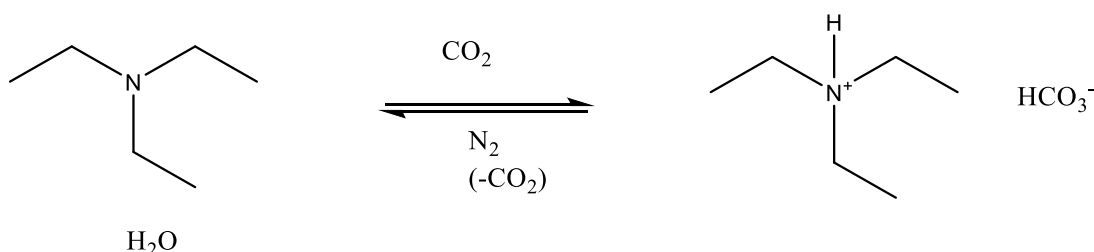


**Figure 5.1: The switchable hydrophobic to hydrophilic system (SHS) using triethylamine and water**

While switchable solvents have been used in a wide range of applications the use of switchable solvents as a medium for the preparation of catalysts or

catalyst precursors has not been explored beyond a few publications. One notable publication was by the group of Saunders *et al.* who used a switchable surfactant as a way of preparing gold supported on silica for use as a catalyst for the reduction of 4-nitrophenol to 4-aminophenol<sup>16</sup>. The role of the switchable surfactant was to control the gold particle size but by having a surfactant that was switchable under different atmospheres, the surfactant (a silylamine) could be removed (by switching the atmosphere) avoiding the use of post synthesis treatments.

Although the carbonated version of the switchable additive triethylammonium carbonate has been reported as a base for the co-precipitation of ceramics including spinel phase oxides<sup>17, 18</sup>, the use of a base in a switchable solvent system has not been reported for the precipitation of metal oxide precursors. The use of a switchable solvent could allow the precipitation of a metal precursor to occur under a carbon dioxide atmosphere or in a nitrogen atmosphere and then switch to a carbon dioxide atmosphere. The use of such a system could potentially be used as a recyclable base system i.e. precipitate the precursor under CO<sub>2</sub> and recover the switchable additive. This system can also allow a co-precipitation route without the use of sodium carbonate and therefore reduce sodium poisoning and the washing required<sup>19</sup>.

### **5.1.2: Choosing the switchable solvent and overview on the switching process for metal carbonate preparation**

Since Jessop published the use of DBU as a switchable solvent in 2005, there has been a wide expansion of research in the area of switchable solvents and investigations into other switchable additives<sup>1</sup>. While the switchable polarity additive DBU is still widely used<sup>3, 20, 21</sup>, it has several disadvantages, most notably its sensitivity to water<sup>22</sup>. The switching occurs due to the formation of an amidinium carbonate salt formed from the DBU and alcohol, which forms an ionic liquid at room temperature. However, the presence of water forms a bicarbonate salt which is more stable than the

carboxylate form. To achieve a proper switchable process with DBU ultra dry conditions are required<sup>22</sup>.

The other consideration when choosing the switchable solvent is the complexity of synthesis and the cost of the switchable additive to synthesise a sufficient amount to be used to make enough catalyst/ precursors for characterisation and catalyst testing.

However, one of the larger influences to consider when choosing the switchable additive is the possibility of residual switchable additive in the catalyst precursor. As seen with the use of choline chloride-oxalic acid deep eutectic solvent in Chapter 3, constituent inorganic or organic substance can be retained in the catalysts even after washing and calcination. Inorganic species as previously seen can poison the catalyst even after excess washing and more complex organic additives such as DBU can also affect the calcination through increasing the calcination temperature and possible exothermic decomposition, potentially increasing the likelihood of carbon formation on the surface, which would restrict active sites and decrease the catalytic activity.

For this reason, simpler and cheaper alternatives to these systems were investigated. In addition, the use of switchable hydrophilic-hydrophobic solvents or switchable water would avoid the issues of posing by water, while the hydrophilic and hydrophobic systems also have a larger polar change in comparison to the DBU systems<sup>23</sup>. The requirements of ultra-dry conditions needed for DBU would further be hampered by the fact that many of the precursor salts are hydrated and would therefore kill the switchable reaction and also may cause the bicarbonate DBU to precipitate with the metal precipitate therefore potentially causing the problems mentioned earlier.

For these reasons triethylamine (TEA) was chosen as the switchable solvent because of its relative broad switching range, commercial availability, and cost as well as the fact that it can be used with water.

### **5.1.3 Aims of Chapter 5**

The aim of this chapter is to use the switchable solvent mixture of triethylamine and water to prepare manganese oxide, copper oxide and mixed copper-manganese oxide catalysts for the use in CO oxidation. The use of switchable solvents for carbon dioxide capture can lead to the formation of metal carbonates, thereby avoiding the use of sodium carbonate which can poison the catalysts and may provide an alternative to the more energy intensive supercritical anti-solvent (SAS) process<sup>24</sup>.

This chapter will compare the physical and catalytic properties of hopcalite made from switchable solvents with those made from supercritical anti-solvent precipitation and co-precipitation, to evaluate the use of switchable solvents for the formation of metal carbonates.

### **5.2 Switchable solvent for single metal carbonate preparation: copper and manganese carbonates**

The first investigation was to see if the technique could be used to make or precipitate single metal oxide precursors. For this manganese and copper was chosen as a starting point since the method was also going to be used for the formation of hopcalite precursors and possibly other mixed copper based catalysts such as copper-zinc oxides (as explored in Chapter 6).

For the formation of manganese carbonate both manganese acetate and manganese nitrate salts were used as the precursor salt. For copper only, the nitrate salt was used. All of the single metal precursors were precipitated under a carbon dioxide atmosphere and left under carbon dioxide for 0.5-1 hour.

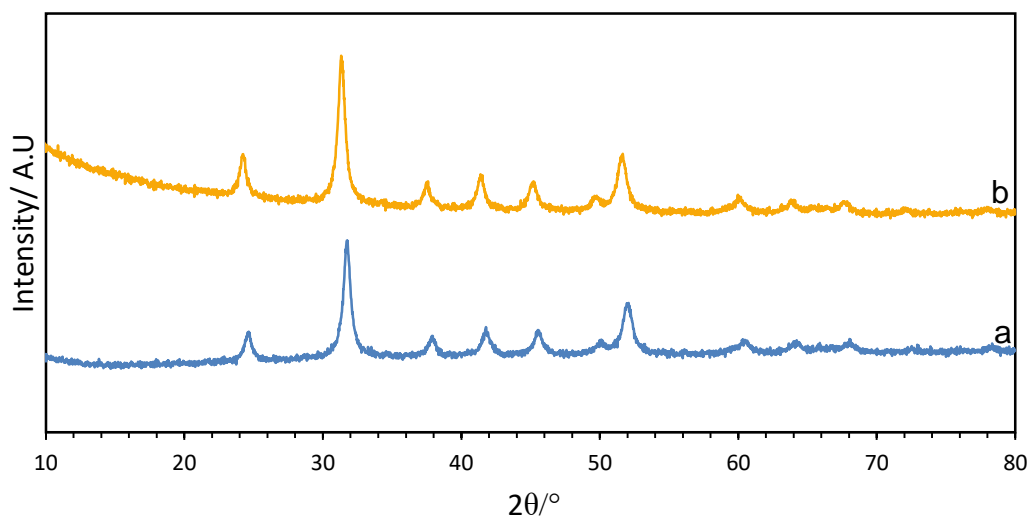


**Figure 5.2: Manganese carbonate formed from switchable solvent triethylamine and water with a) manganese acetate tetrahydrate and b) manganese nitrate tetrahydrate**

The XRD pattern (**Figure 5.2**) confirmed that manganese carbonate was formed when using both manganese salts with the triethylamine and water based switchable solvent with reflections at  $2\theta = 24.3^\circ$  (0 1 2),  $31.4^\circ$  (1 0 4),  $37.6^\circ$  (1 1 0) being associated with the manganese carbonate (rhodochrosite) phase. However infra-red spectroscopy of the samples showed a slight difference between the two samples, with the sample made from nitrates showing two additional peaks at  $1791\text{ cm}^{-1}$  and  $1039\text{ cm}^{-1}$  which could suggest additional impurities not present in the acetate sample that could originate from residual nitrates.

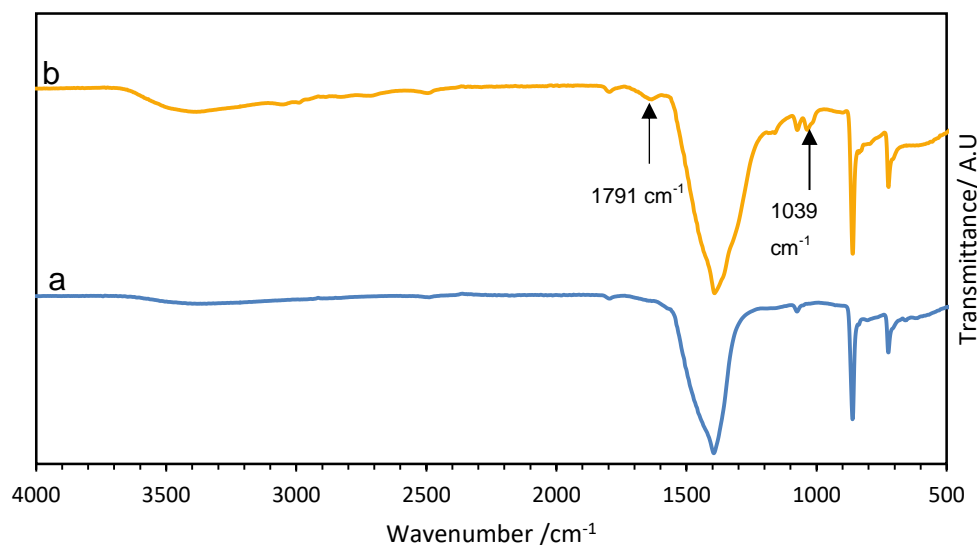


**Figure 5.3: FTIR spectrum of the manganese samples formed in switchable solvents using a) manganese acetate and b) manganese nitrate salts**

The X-ray diffraction pattern of the copper precipitate (**Figure 5.4**) indicates the formation of malachite ( $\text{Cu}_2(\text{CO}_3)(\text{OH})_2$ ) with reflections at  $15.3^\circ$ ,  $18.0^\circ$ ,  $24.5^\circ$ ,  $31.7^\circ$  and  $36.1^\circ$ . The XRD of the sample calcined at  $350^\circ\text{C}$  shows only the reflections of copper oxide with no other crystalline phase observed. This assignment is supported by the FTIR spectrum (**Figure 5.5**) of the sample that shows IR stretches associated with malachite. The stretches at  $3406\text{ cm}^{-1}$  and  $3321\text{ cm}^{-1}$  are associated with the OH stretching while the peaks  $1625\text{ cm}^{-1}$ ,  $1475\text{ cm}^{-1}$ ,  $1326\text{ cm}^{-1}$ ,  $1315\text{ cm}^{-1}$  are associated with the carbonate<sup>25</sup>.

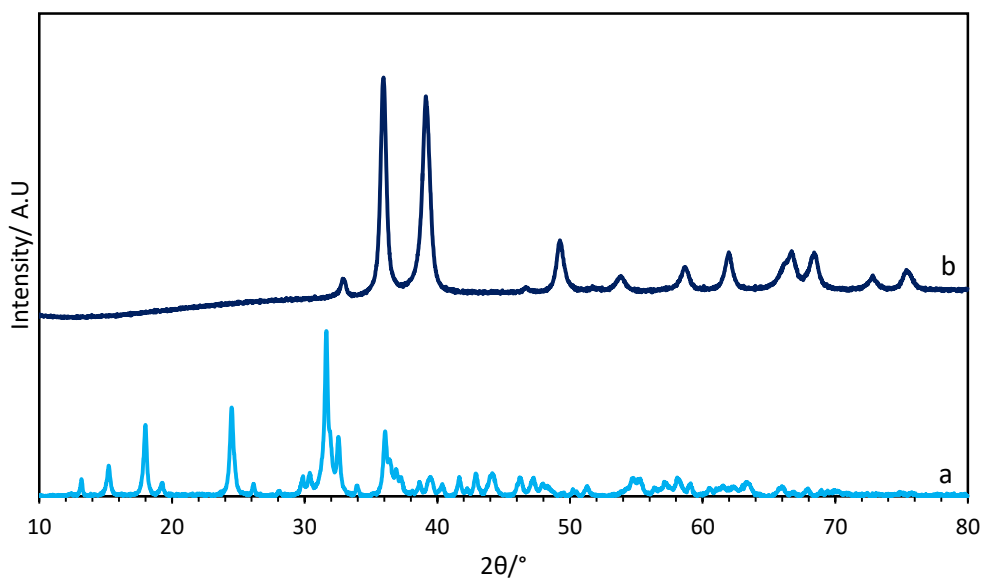


**Figure 5.4: XRD of a) copper carbonate precipitated in switchable solvent under  $\text{CO}_2$  and b) calcined at  $350^\circ\text{C}$  for 3 hours**

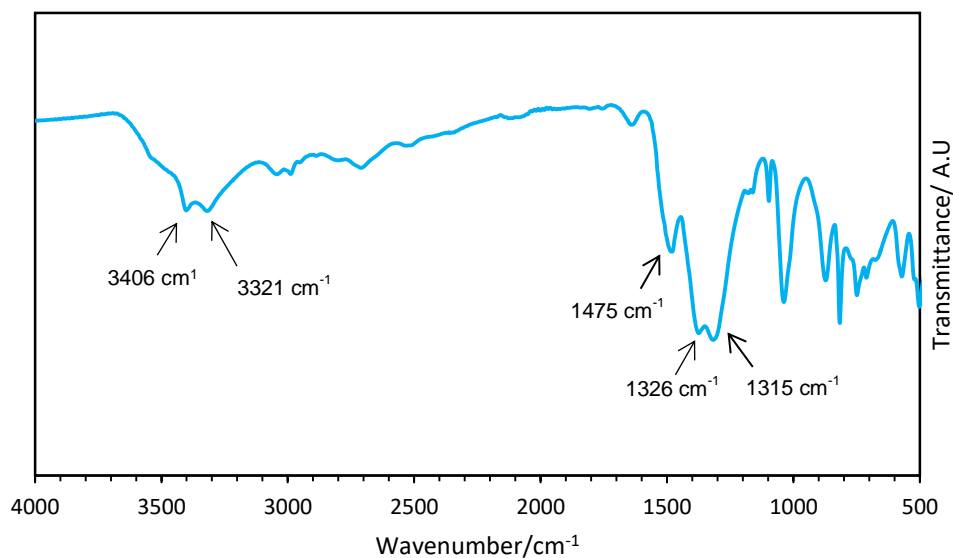


**Figure 5.5: FTIR of copper sample precipitated from switchable solvent showing vibrations associated with malachite**

The thermal gravimetric analysis (Figure 5.6) of the manganese carbonate (acetate sample) shows multiple mass losses in the region of  $50\text{--}550^\circ\text{C}$ . A slow mass loss of 10% occurred between  $50$  and  $150^\circ\text{C}$  followed by a more rapid two-step mass loss at  $170\text{--}350^\circ\text{C}$  before another rapid mass loss at  $550^\circ\text{C}$ . Typically manganese (II) carbonate has been reported to fully decompose at around  $300\text{--}350^\circ\text{C}$ , which corresponds to the second part of

the mass loss, while the final mass loss at 550 °C is caused by the formation of  $\text{Mn}_2\text{O}_3$  from  $\text{MnO}_2$  and the release of oxygen<sup>26</sup>. The first mass loss at 240 °C (too high for water) as well as a minor mass loss at 430 °C are less typical of a manganese carbonate decomposition suggesting that these mass losses are originating from an impurity in the sample (such as residual acetate or amine species). In addition, the weight loss is approximately 36% which is higher than the expected mass loss from the decomposition of a manganese carbonate (non-hydrate) to a manganese oxide of 28-30 %<sup>27</sup> which would support impurities present giving rise to these features.

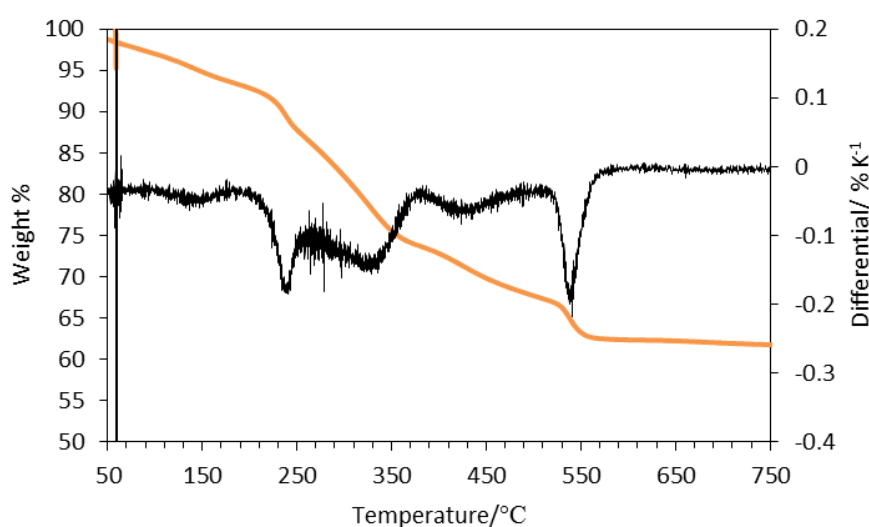


**Figure 5.6: TGA profile of manganese carbonate formed from switchable solvents and manganese acetate**

The malachite sample showed a different TGA profile (**Figure 5.7**) with three weight losses. The first at 100-130 °C most likely being water evolution, followed by a very rapid decomposition at 184 °C and a more gentle decomposition at 300-340 °C. The weight loss at 298-335 °C is more typical range for malachite degrading to copper oxide and malachite usually has no mass loss prior to this temperature<sup>28</sup>. The rapid mass loss at 184 °C could be caused by the degradation of residual nitrates that may cause a rapid decomposition leading to premature degradation of the carbonates at a lower temperature range. It is known from the XRD that copper oxide is the only crystalline phase detected that had formed by this temperature suggesting, along with the TGA, that the precursor material has fully decomposed by this temperature (assuming that the sample is fully crystalline).

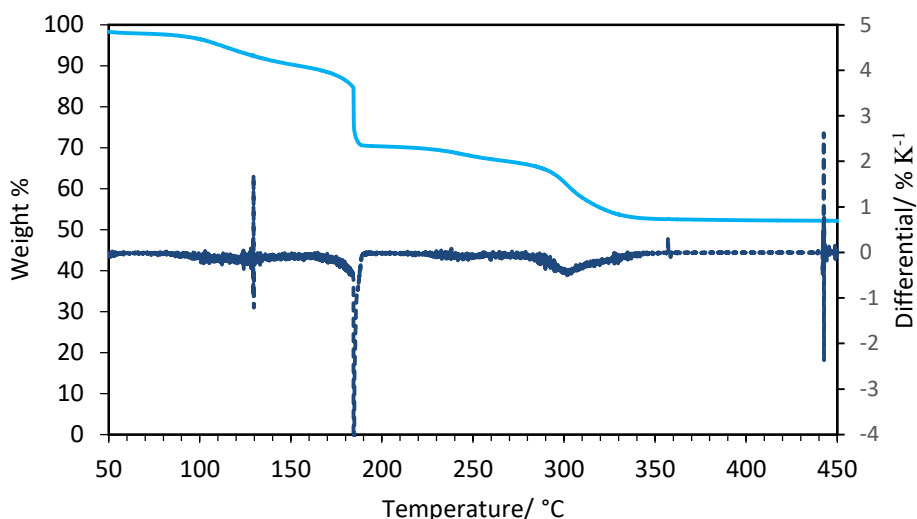


**Figure 5.7: TGA profile and differential of malachite made from switchable solvents**

The SEM images of the carbonates formed from the nitrate solutions show that both copper and manganese formed agglomerates of smaller particles. The manganese carbonate had uniformly formed spherical agglomerates of particle whereas the copper had formed two distinct morphologies, the first being made up of small spherical particles the second forming larger, rectangular particles that appeared to form in separate agglomerates. The formation of two morphologies could suggest that two precipitation mechanisms are happening in the solution, with one occurring over a longer time period than the other. It is also possible that a second undetected compound has been precipitated with the malachite.

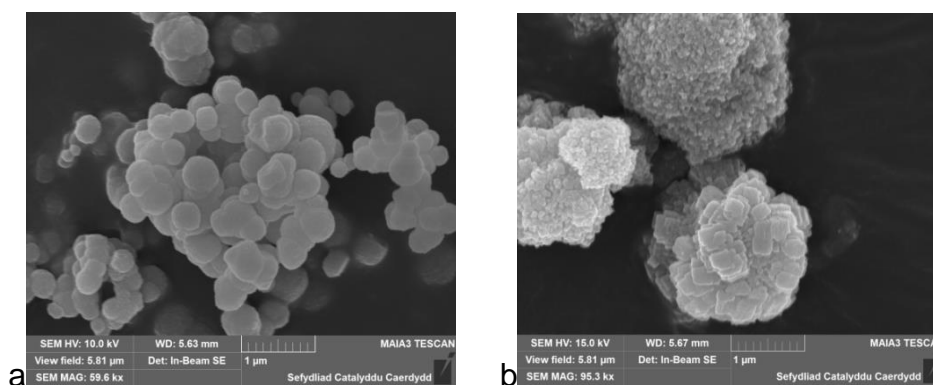


**Figure 5.8: SEM images of the single metal precursors precipitated (from nitrate salts) in switchable solvent under carbon dioxide a) manganese and b) copper**

### 5.3 Switchable solvent for copper-manganese preparation

The previous section demonstrated that the switchable process could be used to prepare single metal carbonates such as manganese and copper carbonate. However, the next step was to make mixed copper-manganese carbonate as a precursor to hopcalite for use as a CO oxidation catalyst.

Catalysts prepared using this technique were then compared to the characterisation and catalytic properties to hopcalite made from other techniques such as co-precipitation and supercritical anti-solvent (SAS).

The initial catalysts were prepared using an amine:water ratio of 1:1.4 (volume) before a series of other catalyst were prepared with variations to the amine: water volume ratios using 1:1 or 1:0.7 (the former is the standard concentration used for switchable solvents) to observe the effect of amine concentration and amine: metal has on the precipitation of the precursor.

The parameters of switchable solvent experiment were then varied to see the effect on the copper-manganese mixing, surface area and catalytic activity. The parameters that were chosen to change were: initial metal salt, the atmosphere ( $\text{CO}_2$  or  $\text{N}_2$ ) during precipitation, the ratio of amine: water and amine: metal and the effect of aging time under different atmospheres.

As a basis for comparison hopcalite precipitated with triethylamine (TEA) was compared with the hopcalite made from both co-precipitation and SAS. The co-precipitated hopcalite which had a Cu:Mn ratio of 1:2 was also used as reference catalyst in Chapter 4.

Previous work looking into the differences between hopcalite made from SAS precipitation and that from co-precipitation has been studied and published by Tang *et al.*<sup>29, 30</sup>. Most notably the SAS precipitated hopcalite was noted for its higher surface area but also its high degree of mixing of the copper and manganese than the co-precipitated catalyst, which were found to form isolated copper oxide<sup>31</sup>.

The conditions chosen for the precipitation of the SAS reference samples was based on the condition that had been noted in previous research to give the optimum surface area and CO oxidation activity<sup>30</sup>. For this reason, the solvent used was 15% water in ethanol, since this gave good surface area and good catalytic activity.

### **5.3.1 Switchable solvent to prepare hopcalite precursor and comparison to SAS and co-precipitated hopcalite**

The initial preparation conditions chosen was the addition of copper-manganese nitrate (in 4 ml of water) to a mixture of 1.4:1 triethylamine: water (volume ratio) under carbon dioxide. This sample was also compared to hopcalite precipitated by SAS.

The XRD pattern of the TEA precipitated material (**Figure 5.9 a**) was identified as the manganese carbonate phase rhodochrosite ( $\text{MnCO}_3$ ), which is also known to appear in the precursor of co-precipitated material (see Chapter 4) and was also the main phase detected in the SAS prepared hopcalite (**Figure 5.9 b**). The XRD also showed weak malachite reflections suggest that not all of the copper mixed with the manganese, resulting in isolated malachite particles although this is also known to occur in other hopcalite preparations such as ball milling<sup>32</sup>. In comparison no separate malachite was detected in the supercritical anti-solvent precipitated sample with the manganese carbonate being the only detectable crystalline phase.

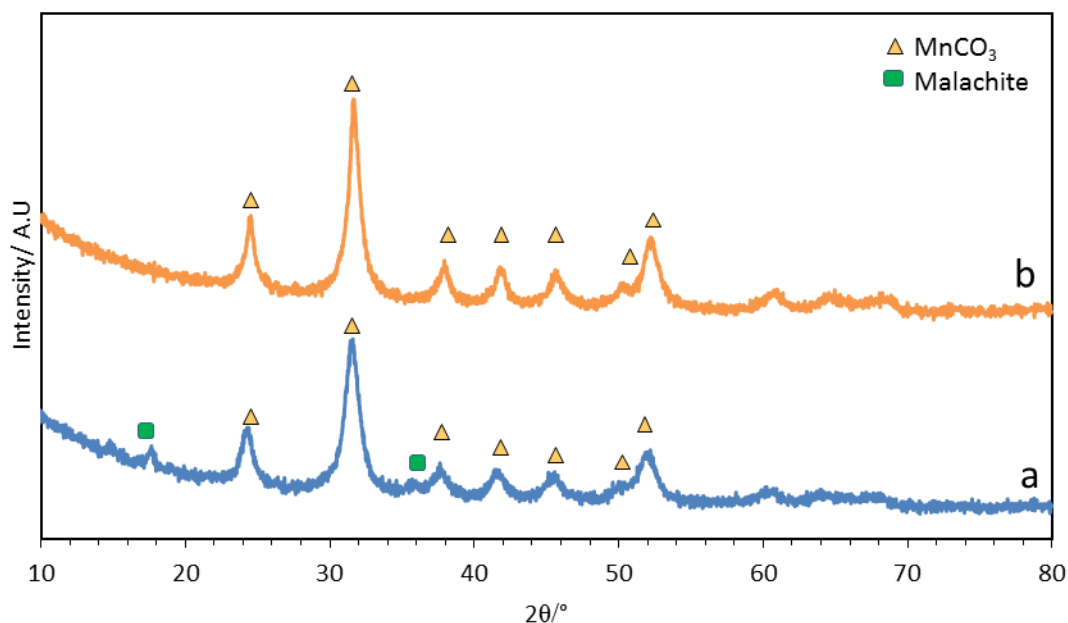


**Figure 5.9:** XRD of the copper-manganese carbonate precipitated using a) switchable solvent under carbon dioxide with 1.4:1 TEA:water and b) supercritical anti-solvent process (15% vol water/ethanol)

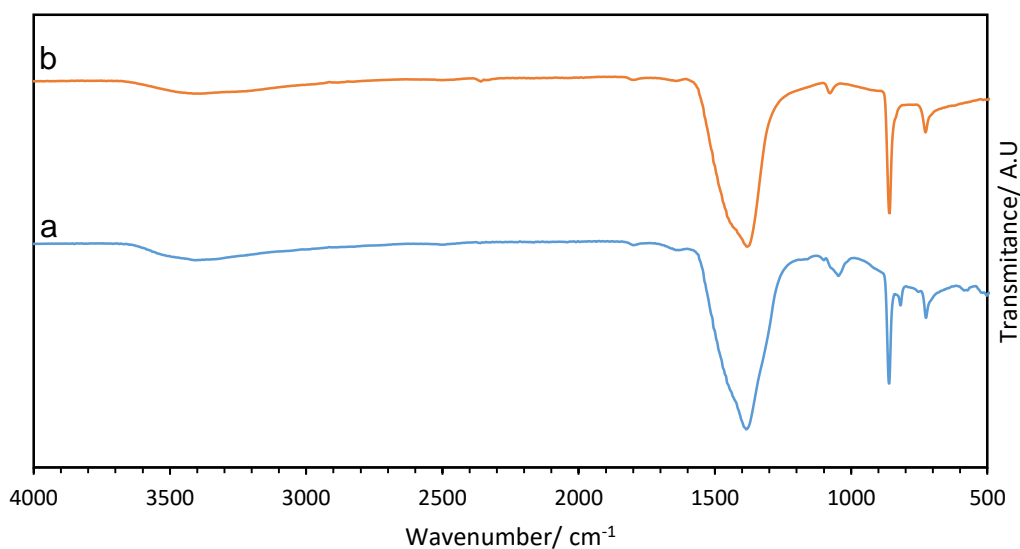


**Figure 5.10:** FTIR of the copper-manganese carbonate precipitated by a) switchable solvent under carbon dioxide with 1.4:1 TEA:water and b) supercritical anti-solvent precipitation (15% vol water/ethanol)

FTIR (**Figure 5.10 a**) of the switchable precursor showed the IR shifts associated with the carbonate at  $1386 \text{ cm}^{-1}$  and hydroxide peaks at  $3350 \text{ cm}^{-1}$ . These were the same IR peaks seen in the SAS precipitated sample (**Figure 5.10 b**). What is notable is that the switchable solvent

prepared sample showed additional vibrational peak at  $819\text{ cm}^{-1}$  as well as a broader, intense vibration at  $1050\text{ cm}^{-1}$ . These correspond to vibrations that were observed with the FTIR of the malachite formed from the switchable solvents, ( $1039\text{ cm}^{-1}$  and  $813\text{ cm}^{-1}$  assigned to OH liberation and  $\text{CO}_3$  asymmetric bending respectively<sup>25</sup>), with the other malachite vibrations (such as  $1380\text{ cm}^{-1}$  or  $1486\text{ cm}^{-1}$ ) being indistinguishable from the carbonate vibrations of both manganese carbonate and mixed copper-manganese carbonate<sup>30</sup>. This, along with the XRD, would suggest that that phase separated malachite had formed during the precipitation in the switchable solvent but not in the SAS sample.

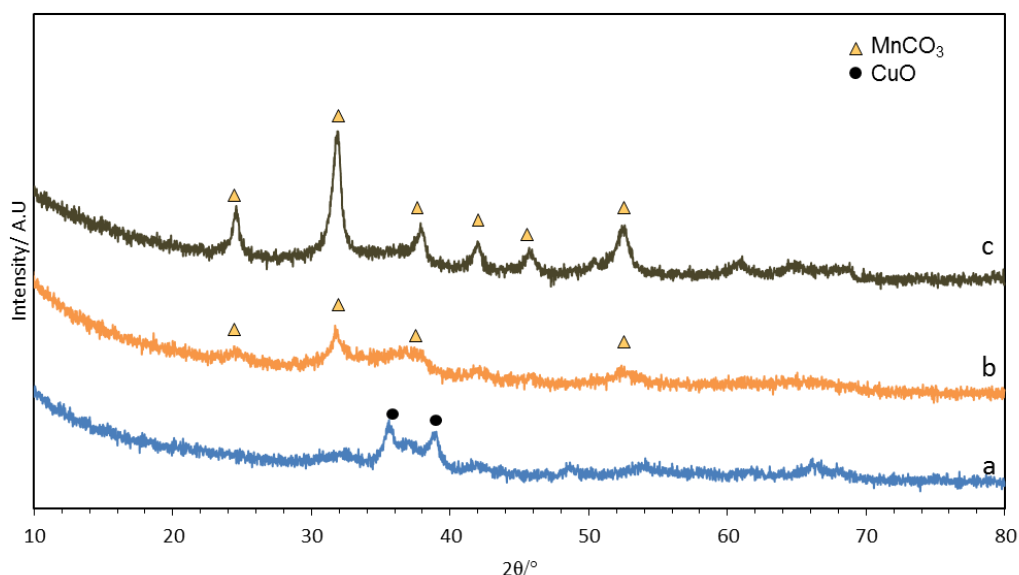


**Figure 5.11: XRD of the calcined  $350\text{ }^{\circ}\text{C}$  copper-manganese carbonates made by a) switchable solvents, b) supercritical anti-solvent and c) co-precipitation**

The XRD of the calcined material (**Figure 5.11**) precipitated in the switchable solvent showed three reflection; two sharper reflections at  $35.5^{\circ}$  and  $39.0^{\circ}$  and a broader reflection at  $37^{\circ}$  which could either originate from a spinel phase  $\text{CuMn}_2\text{O}_4$  or isolated  $\text{CuO}$ . However the reflection at  $2\theta=39.0^{\circ}$  is close to where the (1 1 1) or (2 0 0) of copper oxide is expected so it is likely that these reflections originate from isolated  $\text{CuO}$ .

There is little indication of the carbonate phase in the sample after calcination at  $350\text{ }^{\circ}\text{C}$  other than a weak reflection at  $2\theta=32^{\circ}$ , suggesting that most of the manganese and copper manganese carbonate phase had decomposed

however small amounts of  $\text{MnCO}_3$  may still be present. In comparison the XRD of both the co-precipitated and the supercritical precipitated copper-manganese still shows large manganese carbonate reflections (although much weaker than the precursor XRD pattern) present after calcination at 350 °C which would correspond to the TGA of those samples.

The XRD of the calcined material from supercritical anti-solvent precipitation (**Figure 5.11 b**) show mostly an amorphous pattern. However, the sample calcined at 350 °C shows some reflections (at  $2\theta=31.9^\circ$ ) which could indicate residual manganese carbonate in the sample. Likewise, the co-precipitated sample (**Figure 5.11 c**) (from same batch used in Chapter 4) still showed manganese carbonate reflections after calcination at 350 °C and did not show the formation of amorphous phase until after 400 °C. It should be noted that in comparison the copper-manganese samples precipitated from switchable solvents was already observed to be weakly crystalline phase by 350 °C with no reflections that could be associated with manganese carbonate. This would indicate that the main carbonate phase had degraded by 350 °C (as seen in the TGA) whereas the rhodochrosite phase was still present in co-precipitated sample after heat treatment at 350 °C for 3 hours.

The surface area of both the precursor and final supercritical anti-solvent precipitated catalyst (**Table 5.1**), was shown to be the highest, although this is relatively small increase over the switchable solvent made catalyst, with the final calcined catalysts surface area within  $5 \text{ m}^2 \text{ g}^{-1}$  of each other. The co-precipitated catalyst showed the lowest surface area although this was still mostly in the carbonate phase (**Figure 5.11 c**) at this temperature.

**Table 5.1: Surface area (5 point BET) of the precursor and calcined (350 °C) copper-manganese carbonate made from switchable solvent precipitation, co-precipitation and supercritical anti-solvent precipitation (N/A means not measured).**

	Surface area/ m <sup>2</sup> g <sup>-1</sup>		
	Supercritical anti-solvent	Co-precipitated	Switchable (1.4:1, Nitrate, CO <sub>2</sub> )
Precursor	93 (±10)	N/A	64 (±5)
350 °C	109 (±10)	15 (±2)	102 (±10)

The TPR profile of the hopcalite from supercritical anti-solvent, calcined 350 °C, (**Figure 5.12**) showed a two step reduction with the first step at 215 °C (the preceding broad reduction being caused by residual carbonate)<sup>33</sup> and 260 °C which could suggest good phase integration and copper-manganese interactions<sup>34</sup>. In comparison those formed from switchable solvent precipitation had multiple reduction peaks at 234 °C, 260-280 °C and 311 °C, which would suggest not only a less integrated copper-manganese phase and that some extent of phase separation had occurred<sup>34</sup>.

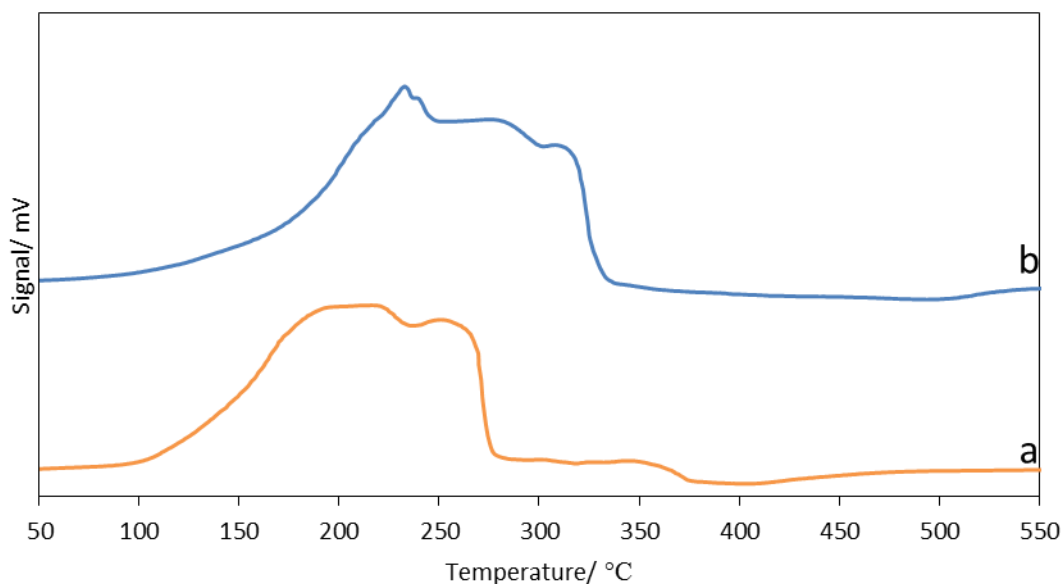


**Figure 5.12: TPR of copper-manganese oxide catalysts (calcined at 350 °C) prepared by a) supercritical anti-solvent and b) switchable solvent**

It should be noted that the catalyst from supercritical anti-solvent precipitation (**Figure 5.12 b**) showed a very small reduction at 340-360 °C that could

possibly originate from a phase separated manganese species, in addition to a reduction between 110-180 °C which would suggest residual carbonate species still present in the sample (partially seen in XRD). In comparison this reduction is not as prevalent in the switchable solvent precipitated sample which would suggest that this precursor had mostly degraded during the calcination process at 350 °C.

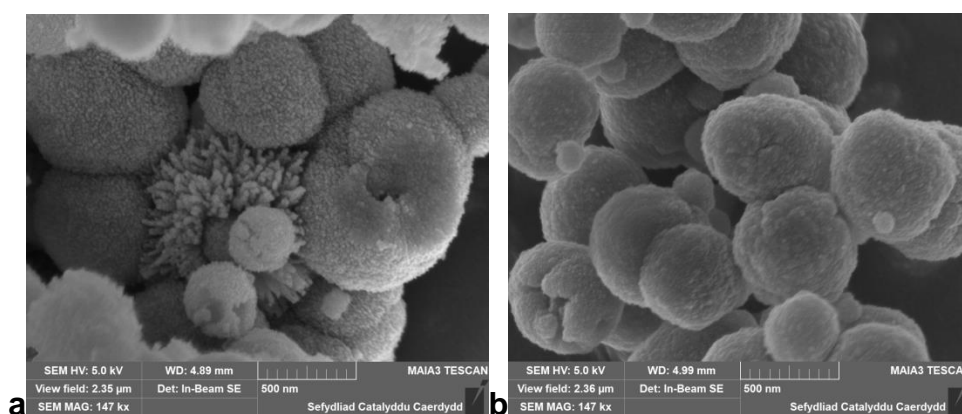


**Figure 5.13: SEM images of the copper-manganese carbonate prepared by a) switchable solvent precipitation and b) supercritical anti-solvent**

The SEM images of the carbonate precipitated from SAS shows spheres made up of agglomerate of smaller spherical particles. The switchable solvent precipitated sample showed a mixture of the spheres along with a second morphology that formed rod shaped crystals. EDX analysis ((**Figure 5.39**), section 5.3.4) showed that these rods are more copper rich and therefore likely originating from the phase separate malachite seen in the XRD and FTIR.

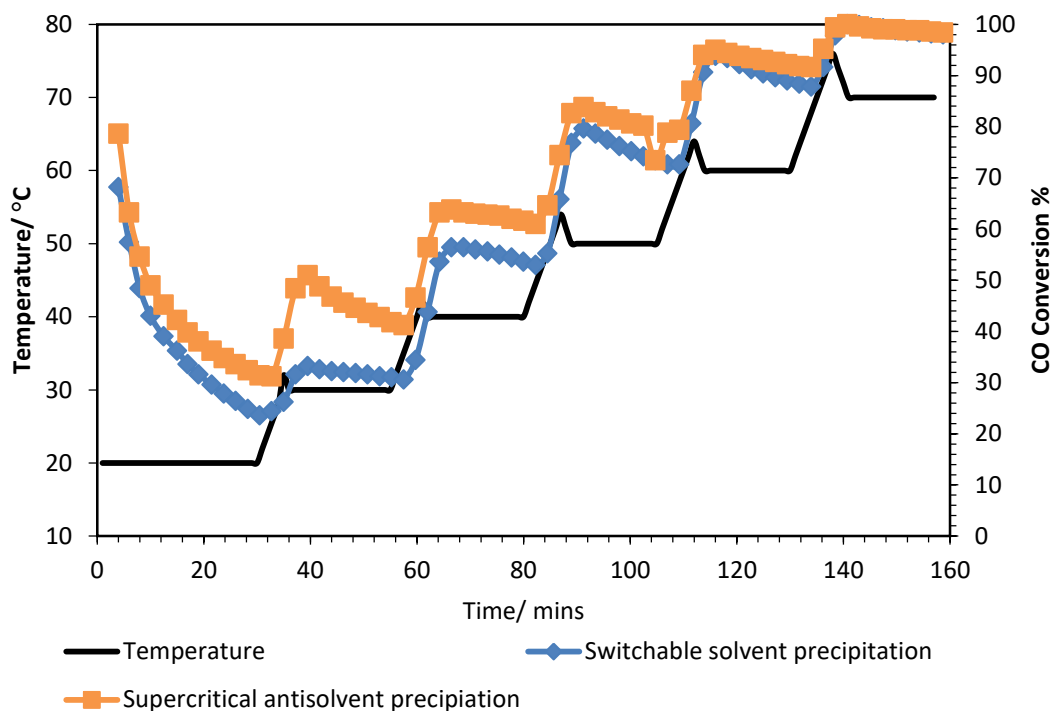


**Figure 5.14: CO oxidation as using copper manganese oxide catalysts prepared by switchable solvent and supercritical anti-solvent precipitated hopcalite calcined 350 °C**

The CO testing of the supercritical anti-solvent precipitated catalyst and the switchable solvent precipitated catalyst (pre-treated under nitrogen at 110 °C) both show a rapid deactivation in the first 30 minutes, which is commonly observed with hopcalite catalysts<sup>30, 35</sup> (see **Section 4.4**). The catalyst prepared by supercritical anti-solvent precipitation was slightly more active than the switchable solvent catalyst, most notably after the first temperature ramp at 30 °C but the switchable catalyst had stabilised after the first temperature ramp and by 40 °C the difference in CO conversion decreased. The higher CO oxidation of the SAS catalyst could owe to the fact that firstly the sample had a slightly higher surface area than the switchable catalyst and secondly the sample had a better copper-manganese mixing which is important in the redox coupling during CO oxidation<sup>36, 37</sup>.

Surface area normalised conversion (**Figure 5.15**) showed that the supercritical anti-solvent precipitated hopcalite was still more active at lower temperatures in this respect, which suggested that the higher activity was more likely owed to better copper-manganese mixing than the higher surface area, although the differences in the normalised activity between the two

catalysts was lower at 20 °C and 40 °C. However by 50 °C both catalysts were showing very similar rates.

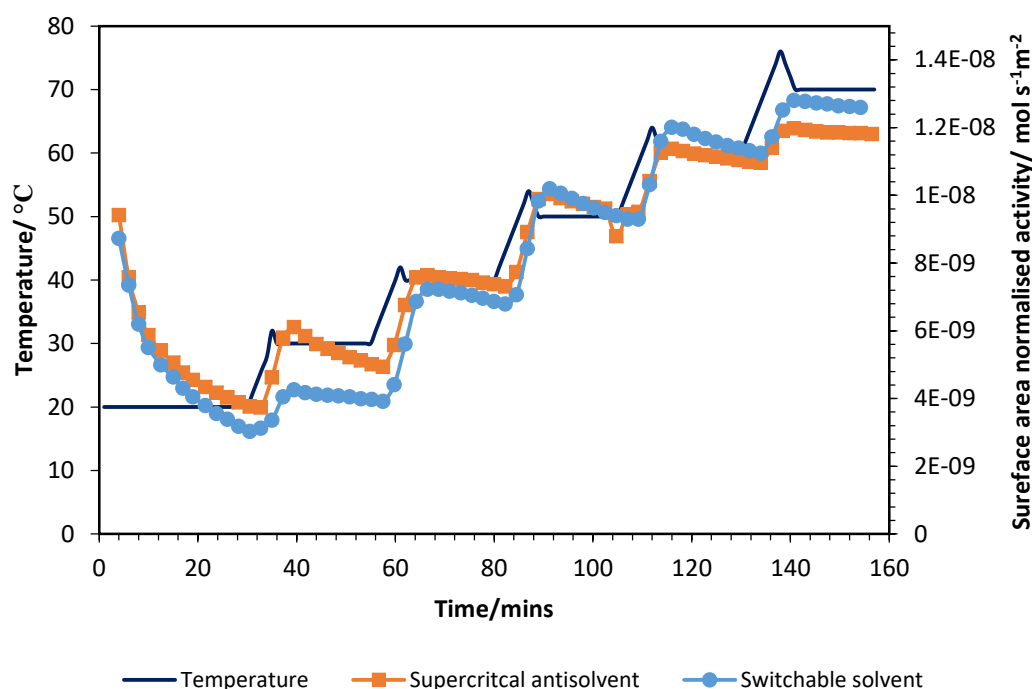


**Figure 5.15: Surface area normalised CO conversion using switchable and SAS precipitated hopcalite calcined 350 °C**

### 5.3.2 Change in precursor salt and precipitation atmosphere

The effect of using different precursor salts and the atmosphere of precipitation on the final catalyst was also investigated. The acetate salt was dissolved in water at the same concentration as the nitrate salt and was precipitated under CO<sub>2</sub> with 1.4:1 TEA:water (the same as the standard sample) and left for 1 hour before centrifuged and washed.

The XRD of the material made from the acetate (**Figure 5.16 a**) only showed the reflections of rhodochrosite with no reflections associated with malachite or any copper containing compound being observed by XRD. This could be due to better mixing but it should be noted from MP-AES analysis later on ((**Table 5.10**) Section 5.3.4) that the acetate sample had a lower copper:manganese ratio of 1:2.5. This would suggest that lack of phase

separate malachite peaks might be due to the lack of copper that precipitated rather than the formation of a more phase pure material. The loss of copper could be due to its failure to precipitate during the addition, resulting in copper being dissolved in the solvent mixture rather than co-precipitating with the manganese carbonate but more investigation would be required to confirm this.

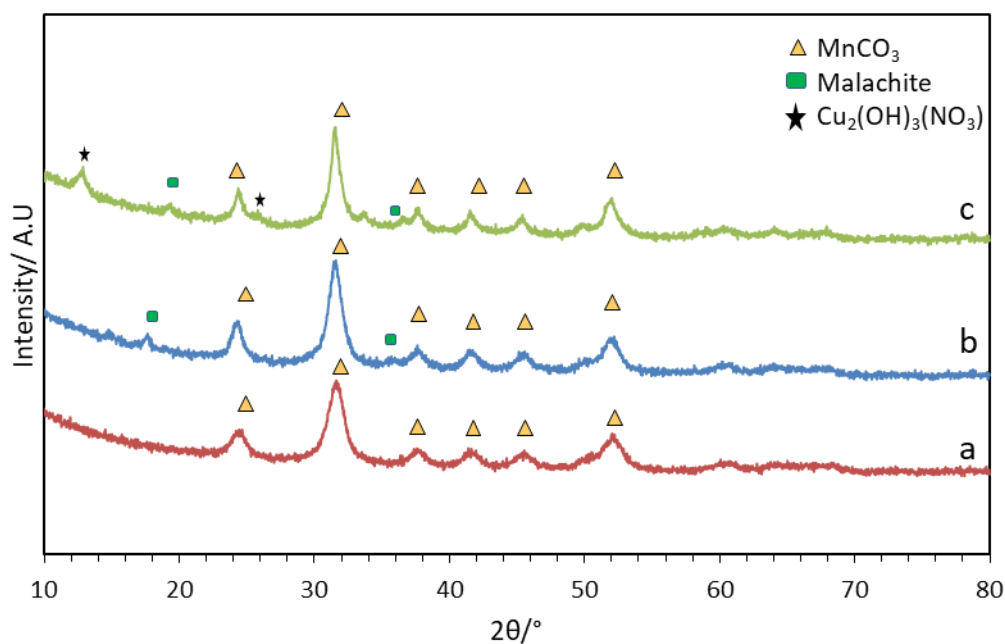


**Figure 5.16:** XRD of the copper-manganese carbonate precipitated under carbon dioxide using a) acetate salts b) nitrate salts and c) precipitated under nitrogen (switched to  $\text{CO}_2$ ) with nitrate salts

XRD of the sample precipitated (**Figure 5.16 c**) under nitrogen showed two small reflections at  $2\theta = 12.8^\circ$  and  $26.3^\circ$  which could be assigned to copper nitrate hydroxide which is known to have two reflections at these angles<sup>38</sup>. This would suggest that not all of the copper nitrates reacted with the TEA during the 1 hour under  $\text{CO}_2$ . Using the Scherrer equation the crystallite size of the manganese carbonate reflection at  $2\theta = 31.6^\circ$  (**Table 5.2**) in the acetate sample was significantly smaller than the material precipitated from the nitrate or the supercritical anti-solvent precipitated precursors.

**Table 5.2: Crystallite size ( $\pm 2$  nm) of the manganese carbonate precursors at  $2\theta=31.6^\circ$  and malachite  $2\theta=17.5^\circ$ . Value of n/a is used for materials that had no malachite reflections.**

Sample	Crystallite size manganese carbonate $2\theta = 31.6^\circ$	Crystallite size malachite $2\theta=17.5^\circ$
1.4:1, CO <sub>2</sub> , Acetates	6.2	n/a
1.4:1, CO <sub>2</sub> , Nitrates	7.9	15.0
1.4:1, N <sub>2</sub> , Nitrates	10.3	10.0
Supercritical anti-solvent	9.3	n/a
Co-precipitated (Na <sub>2</sub> CO <sub>3</sub> pH 8.3)	13.4	n/a

The FTIR of the sample precipitated using the acetate salts (**Figure 5.17 a**) showed the same vibrational shift as the supercritical anti-solvent precipitated sample (**Figure 5.10 b**) but did not show the additional vibrations at  $813\text{ cm}^{-1}$  and  $1050\text{ cm}^{-1}$ , associated with malachite, that was observed in the sample that used nitrate salts (**Figure 5.17 b**). This along with the XRD (**Figure 5.16**) would suggest that separated/isolated copper carbonate predominantly forms with the nitrate salts but was not observed when the acetate salt was used although this could be due to the lack of copper in the acetate sample.

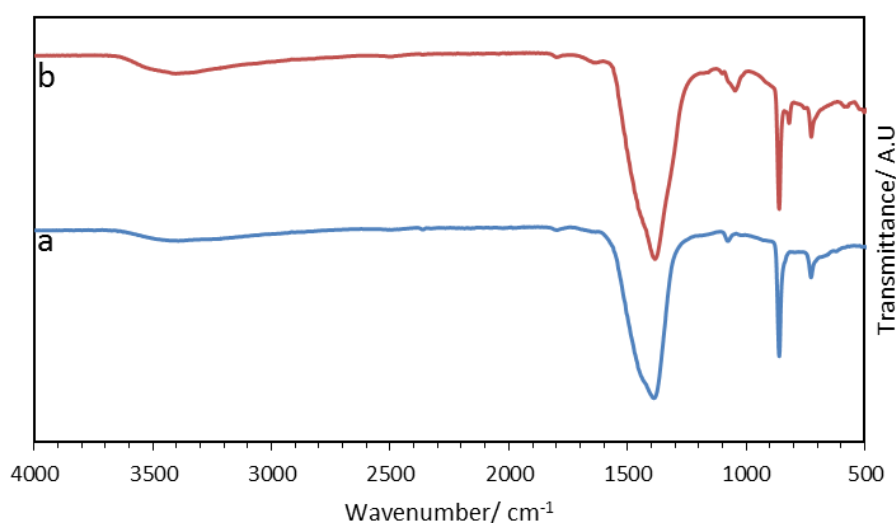


**Figure 5.17: FTIR spectrum of the copper-manganese carbonate precipitated under CO<sub>2</sub> using a) acetate salts and b) nitrate salts**

The XRD profile of the sample precipitated under nitrogen after calcination at 350 °C (**Figure 5.18 c**) showed the same reflections at 35.3° and 38.5° as the sample precipitated under carbon dioxide (**Figure 5.18 a**) which are assigned to isolated copper oxide, along with the broad reflection at 36.4°. In comparison the sample precipitate using acetate salts under carbon dioxide (**Figure 5.18 b**) was mostly amorphous with a broad reflection at 36.2°. The more amorphous nature could be related to the fact that the two reflections at 35.3° and 38.5° originate from isolated CuO which would correspond to the malachite reflections of the precursor and better copper-manganese phase integration seen in both supercritical anti-solvent precipitated and acetate samples. On the whole the reflections at 35.3° and 38.5° are seen in the samples that had malachite in the precursor further justifying the assignment of these reflections to isolated copper oxide.

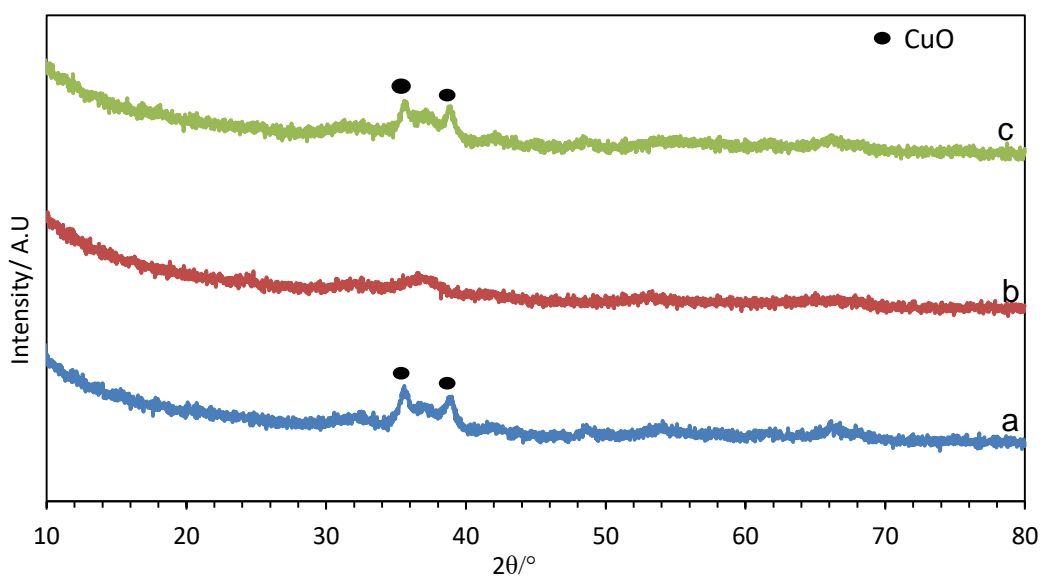


**Figure 5.18: XRD of the calcined (350 °C) copper-manganese samples precipitated in 1.4:1 TEA:water a) nitrate salts CO<sub>2</sub> b) acetate salts CO<sub>2</sub> and c) nitrate salts N<sub>2</sub>**

The surface area of the acetate precursor was generally higher than that of the nitrate salts for the precursor, but the nitrate salt precipitated under the nitrogen atmosphere generally had a higher surface area than either of the two samples precipitated under CO<sub>2</sub>.

**Table 5.3: Surface areas ( $\pm 10 \text{ m}^2 \text{ g}^{-1}$ ) of the precipitated samples (1.4:1 TEA:water) and calcined oxides  $350 \text{ }^\circ\text{C}$ . N/A is used for experiment not performed**

Sample	Surface area/ $\text{m}^2 \text{ g}^{-1}$	
	Precursor	Calcined $350 \text{ }^\circ\text{C}$
Acetate $\text{CO}_2$	92	149
Nitrate $\text{N}_2$	N/A	176
Nitrate $\text{CO}_2$	64	102

The TGA profile of the sample precipitated under nitrogen and carbon dioxide in the 1.4:1 TEA:water (**Figure 5.19**) showed three mass losses at  $220 \text{ }^\circ\text{C}$ ,  $280 \text{ }^\circ\text{C}$  and  $500 \text{ }^\circ\text{C}$ . The mass loss at  $280 \text{ }^\circ\text{C}$  has been associated with the breakdown of the carbonate phase to form the spinel phase while the final mass loss may be attributed to phase separated carbonates. The mass loss was greater for the carbonates that were precipitated under the carbon dioxide atmosphere (38%) than the samples precipitated under nitrogen (33%). This difference might suggest that while XRD showed both samples had formed carbonates, there was possibility that not all of the metals had been carbonated during the aging process under carbon dioxide after the precipitation under nitrogen.

In addition, the mass losses, at  $220 \text{ }^\circ\text{C}$  and  $280 \text{ }^\circ\text{C}$  are more rapid for the carbon dioxide precipitated sample suggesting that the carbonates degraded more rapidly in these samples. The overall profile is very much like the TGA profile observed with manganese carbonate precipitated in TEA, suggesting that the main degradation profile is caused by the manganese carbonate with the copper species degrading in the same temperature range. The rapid decomposition at  $184 \text{ }^\circ\text{C}$  observed in the malachite sample (**Figure 5.7**) is not seen in this sample but the second decomposition at  $300 \text{ }^\circ\text{C}$  would occur in the second decomposition in these samples. The profile also shows that the final weight loss at  $500 \text{ }^\circ\text{C}$  is most likely the formation of phase separated  $\text{Mn}_2\text{O}_3$  from  $\text{MnO}_2$  that is known to occur at this temperature range<sup>27</sup>.

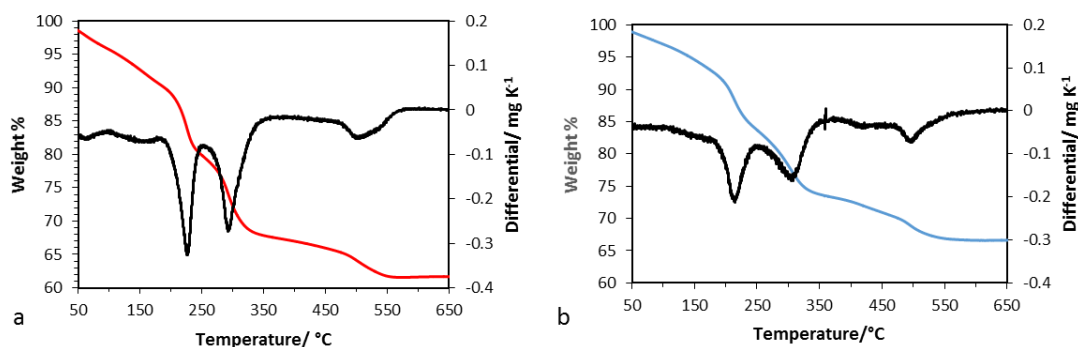


**Figure 5.19: TGA profile under flowing air of copper manganese carbonate precipitated under a) carbon dioxide and b) nitrogen with 1.4:1 triethylamine: water (nitrate salts)**

Temperature programmed reduction was performed on the samples precipitated with nitrates under both atmospheres (Figure 5.20), showed varying reduction profiles between the different the atmospheres. The nitrogen precipitated carbonate showing only two reduction profile at 214 °C ( $\text{Cu}^{2+}$  to  $\text{Cu}^0$ ) (the broad reduction prior to this is due to residual carbonates)<sup>33</sup> and 271 °C which was overall more typical reduction of co-precipitated hopcalite (Chapter 4) and supercritical anti-solvent precipitated samples<sup>30</sup>. The samples precipitated under carbon dioxide using both nitrate and the acetate salts showed similar reduction profile showing multiple reductions the main two at 218 °C and a broad reduction at 251-270 °C, while the sample precipitated using nitrates showed three reductions at 240 °C (with a shoulder reduction at 230 °C), 280 °C and 330 °C. The additional reduction at 330 °C would suggest a phase separate  $\text{MnO}_2$  present in the sample with the multiple reductions suggesting that the copper-manganese was as well integrated as the other materials<sup>34</sup>.

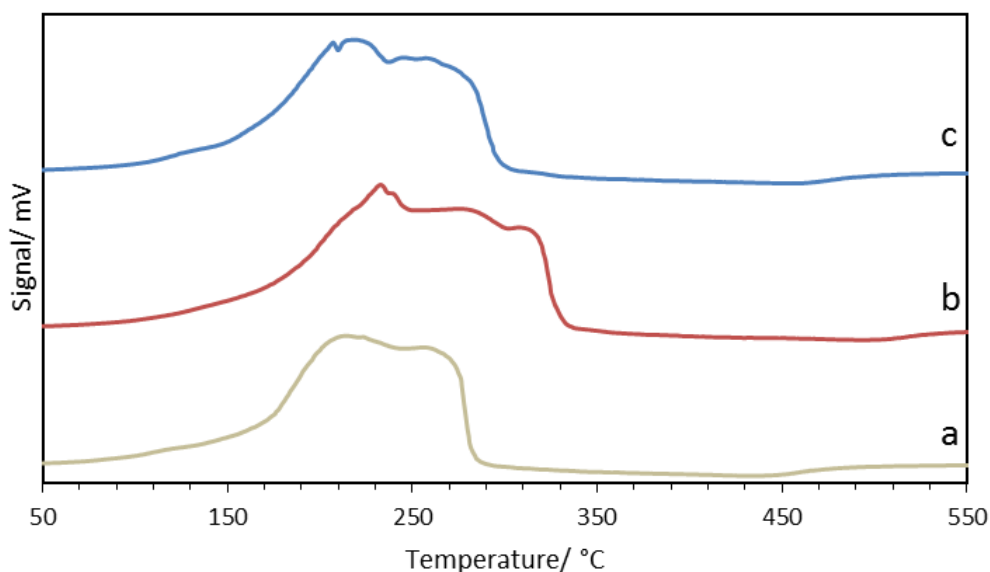


**Figure 5.20: TPR of the copper-manganese oxide calcined 350 °C precipitated from switchable solvents a) 1.4:1 under nitrogen, b) 1.4:1 Carbon dioxide using nitrate salts and c) 1.4:1 carbon dioxide atmosphere acetate salt**

SEM images of the copper-manganese carbonates (**Figure 5.21**) that were precipitated from switchable solvents (using the acetates salts) formed rounded globe shape particles that formed from agglomeration of smaller spherical particles that come together. This type of morphology is also observed with SAS precipitated hopcalite precursors, with the shape and size being very similar suggesting that a rapid precipitation had occurred. The samples retained this morphology after calcination at 350 °C. EDX analysis (**Figure 5.22**) carried out on the acetate sample showed a consistently even distribution of copper and manganese in the sample, showing that the sample had a much better copper-manganese mixing than the nitrate sample. This would also be backed up by the fact that these particles appear more commonly in the samples where phase separated malachite was detected by XRD (**Figure 5.16 b and c**) and do not appear in samples (**Figure 5.21 a and b**) with no phase separated malachite detected by XRD such as the acetate samples (**Figure 5.16 a**).

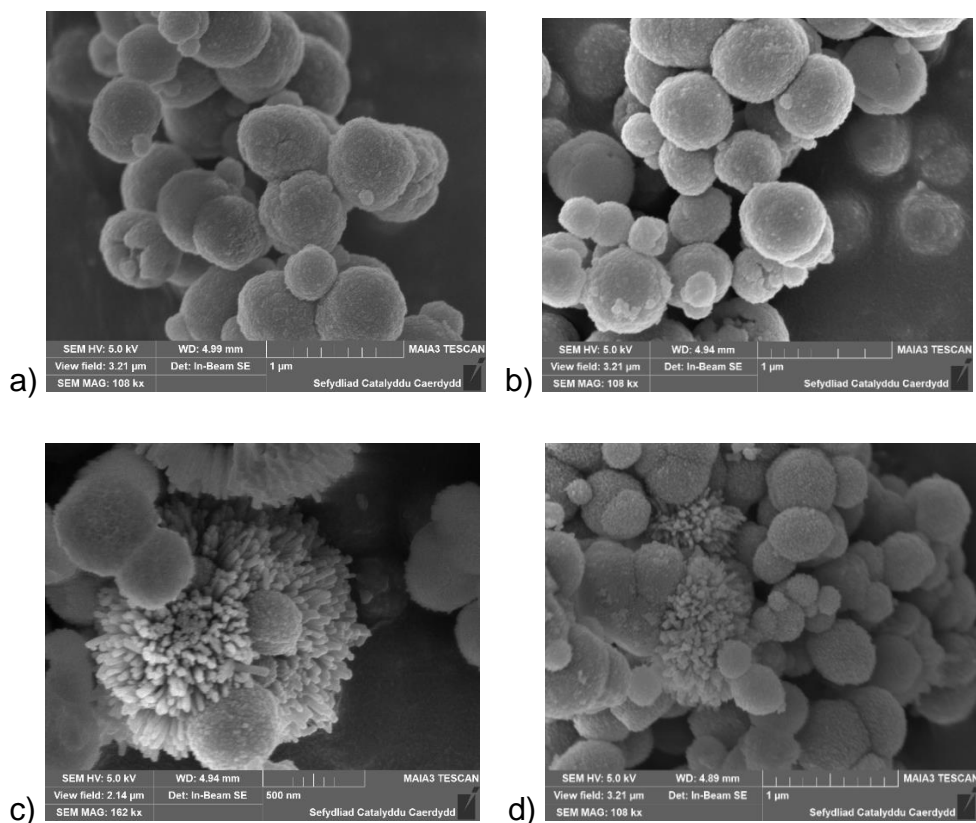


**Figure 5.21: copper-manganese carbonate precipitated from triethylamine (1.4:1) under carbon dioxide using a) acetate salts, and b) calcined at 350 °C and with c) nitrate and d) calcined 350 °C**

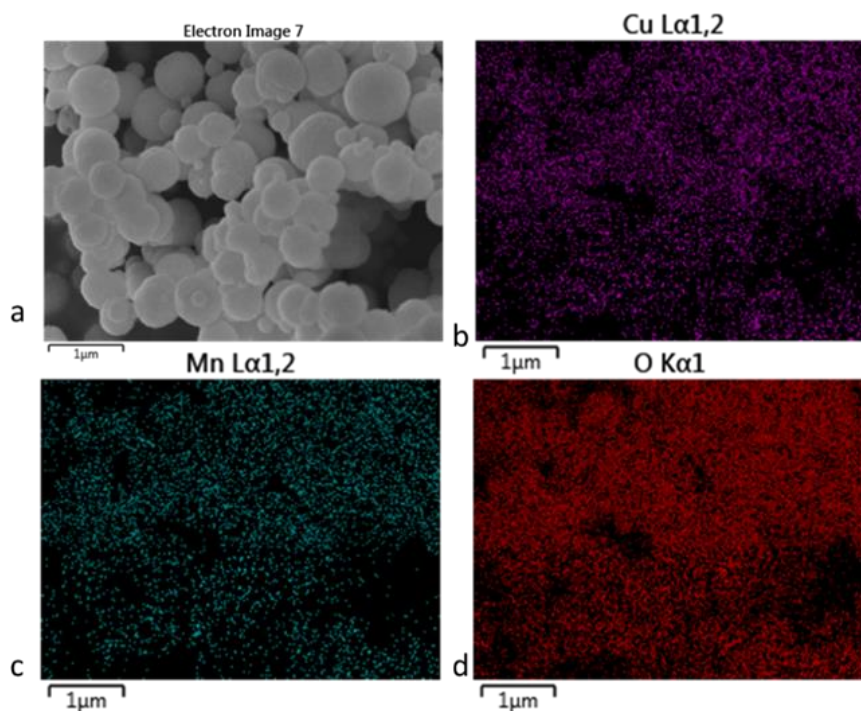


**Figure 5.22: a) SEM image of copper-manganese carbonate from switchable solvent (acetate) and EDX mapping of b) copper, c) manganese and d) oxygen**

The CO oxidation activity of the three catalysts shows large variations. The acetate sample precipitated under carbon dioxide showed the highest activity of the 1.4:1 samples with an initial conversion of 90% although the catalyst was still showing deactivation after the first temperature ramp. This increased CO activity may be related to the better metal mixing and lack of isolated copper clusters. The acetate sample shows greater CO conversion than the supercritical anti-solvent precipitated catalyst (**Figure 5.14**), which is partially due to the higher surface area. The enhanced CO activity of the acetate sample and supercritical anti-solvent precipitated catalyst could be due to the fact that both materials show as mixed copper-manganese oxide compared to the other switchable solvent prepared catalysts that show varying amounts of segregated single oxides.

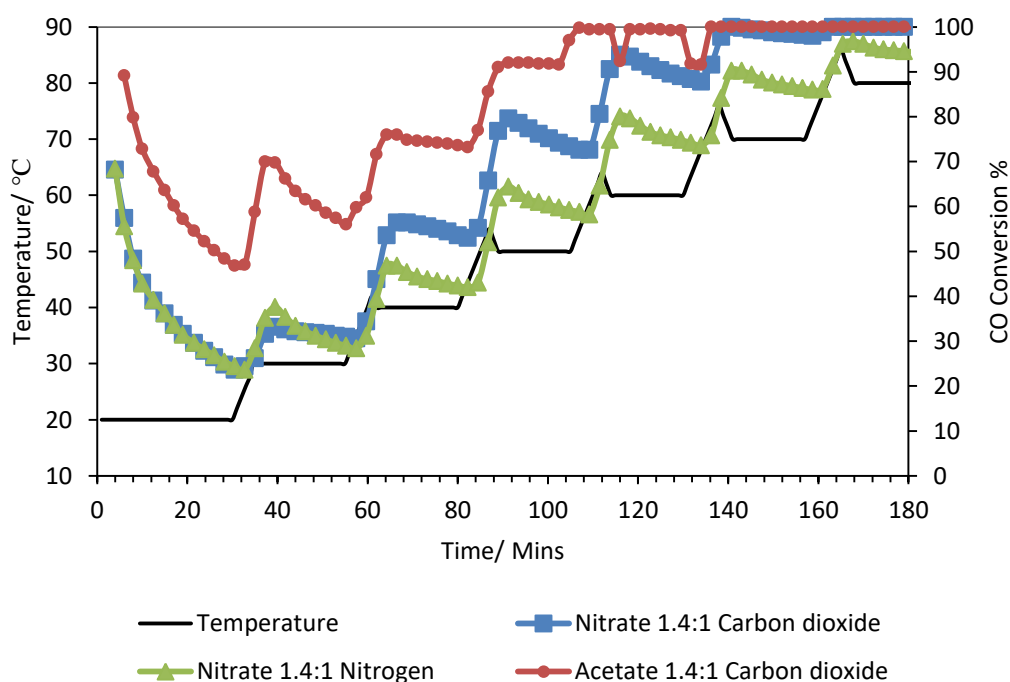


**Figure 5.23: CO oxidation of switchable precipitated hopcalite (calcined 350 °C) made from acetate and nitrate salt (1.4:1 triethylamine: water)**

The nitrate sample precipitated under both atmospheres (with 1.4:1 TEA:water) showed the same initial deactivation curve and have similar conversions. However, the nitrogen precipitated sample showed deactivation after the temperature ramp whereas the carbon dioxide precipitated sample showed a greater degree of stability after the temperature ramp.

### 5.3.3 Effect of varying the amount of triethylamine

In addition to precipitating copper manganese carbonate in 1.4:1 TEA:water, other ratios of 1:1 (standard TEA concentration for switchable solvent) 0.7:1 was also done in order to observe the effect of concentration of TEA on the catalyst and to see how this affects the catalytic activity of the final oxide. The concentration of the TEA would also have an additional affect in that as well as changing the base concentration; the switchable properties would also be changed<sup>15</sup>. The 1:1 amine to water is the standard ratio used for switchable hydrophilic solvent (SHS) system<sup>39</sup>.

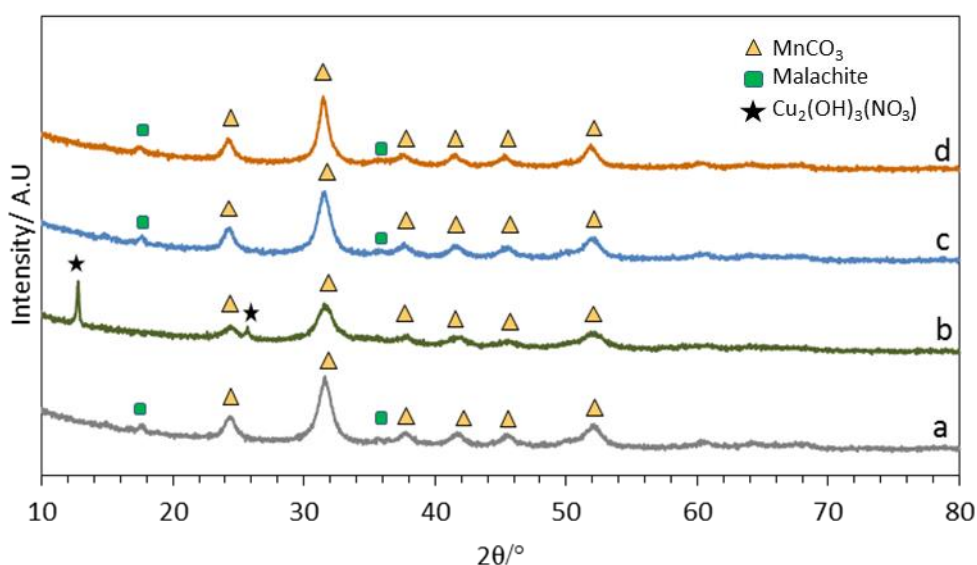


**Figure 5.24: XRD of the copper-manganese carbonates precipitated under  $\text{CO}_2$  with triethylamine: water ratio of a) 0.7:1 b) 1:1, c) 1.4:1 and d) precipitated under nitrogen 1.4:1 TEA:water**

The sample precipitated with 0.7:1 TEA:water did not vary from the 1.4:1 sample, both showing the presence of manganese carbonate and reflections of malachite. In addition the crystallite size of the manganese carbonate ( $2\theta=31.6^\circ$ ) did not vary much between the two samples. The sample precipitated with 1:1 however, was not sufficiently washed and as a result produced two reflections that indicate the large presence of copper nitrate hydroxide. It has been noted however that in conventional co-precipitated catalysts the copper nitrate hydroxide forms initially before redissolving<sup>40</sup>.

There was also no reflection associated with isolated malachite detected in this sample. The sample precipitated under nitrogen with 1:1 TEA:water also showed malachite and rhodochrosite reflections and was more similar to that of the 1.4:1 and 0.7:1 sample precipitated under CO<sub>2</sub>.

There is a correlation between the crystallite size of the manganese carbonate phase of the precursor and the surface area of both the precursor and the final catalysts although the 1:1 TEA:water CO<sub>2</sub> sample does not follow this trend (due to the excess of copper nitrate or copper hydroxy nitrate and reduced overall surface area).

**Table 5.4: Crystallite size of the malachite  $2\theta = 17.5^\circ$  and manganese carbonate  $2\theta=31.6^\circ$  phase of the precursors precipitated in switchable solvent using nitrate salts (error of  $\pm 2$  nm). Value of n/a is used for materials that had no malachite reflection.**

Sample	Crystalline size manganese carbonate $2\theta = 31.6^\circ$	Crystalline size malachite $2\theta = 17.5^\circ$
1:1 CO <sub>2</sub>	8.8	n/a
1:1 N <sub>2</sub>	9.4	15.2
1.4:1 CO <sub>2</sub>	7.9	15.0
1.4:1 N <sub>2</sub>	10.3	10.0
0.7:1 CO <sub>2</sub>	7.7	10

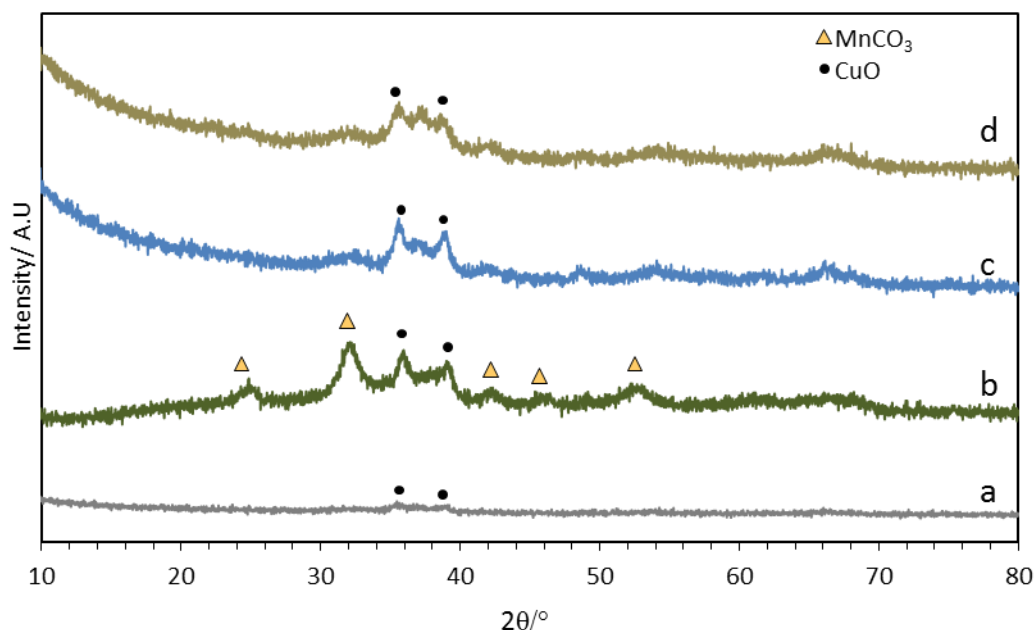


**Figure 5.25:** XRD of the copper-manganese oxide calcined 350 °C precipitated with triethylamine: water ratio of a) 0.7:1 b) 1:1, c) 1.4:1 and d) precipitated under nitrogen 1.4:1

The XRD of the calcined copper-manganese oxides (**Figure 5.25**) shows that the carbonates precipitated with 1.4:1 TEA:water under carbon dioxide and 1:1 TEA:water under nitrogen displayed the same XRD pattern with the two  $\text{CuO}$  reflections at 35.3° and 38.3° as well as the reflection at 36.2°. The sample precipitated with 0.7:1 TEA:water also shows these reflections but they are significantly weaker than those of the copper-manganese oxide precipitated with 1.4:1 TEA:water suggesting a more disordered phase. However, the sample that was precipitated under  $\text{CO}_2$  with 1:1 TEA:water shows distinct reflections at  $2\theta=25.1^\circ$  and  $32.3^\circ$  which would indicate the presence of manganese carbonate which would show that this precursor did not fully convert to the oxide unlike the other samples where the manganese carbonate reflections are either very weak or not present. However, this sample also shows reflections at 35.3° and 37.3° which could indicate presences of  $\text{CuMn}_2\text{O}_4$  or isolated  $\text{CuO}$ . The remaining manganese carbonate is separate and would therefore more likely to form phase separated  $\text{Mn}_2\text{O}_3$  if heated to higher temperatures and that the copper-manganese in this sample was not as homogeneously dispersed as the other samples.

**Table 5.5: Surface area ( $\pm 2 \text{ m}^2 \text{ g}^{-1}$ ) of the precipitated sample (using nitrate salts) using different amine ratios (volume) and precipitation atmospheres**

Sample	Surface area/ $\text{m}^2 \text{ g}^{-1}$	
	Carbonate	Calcined 350°C
1.4:1 $\text{CO}_2$	64	102
0.7:1 $\text{CO}_2$	76	202
1:1 $\text{CO}_2$	9	39
1:1 $\text{N}_2$	37	101

The low surface area of the precursor with 1:1 amine:metal could be associated with the excess  $\text{Cu}_2(\text{OH})_3(\text{NO}_3)$  that was seen by XRD ( $2\theta=12.9^\circ$ ) as this reflection seen in samples that were aged also appears along with a decreased surface area of the precursor. This sample had a low surface area even after calcination at 350 °C, although the material still contains unreacted manganese carbonate (**Figure 5.25**). The copper hydroxyl nitrates have been reported as having an endothermic degradation<sup>41</sup> so this is unlikely to have contributed to the reduced surface area but copper nitrate hydrate has been reported to degrade exothermically<sup>42</sup>, which could have contributed to sintering and reduced surface area if there was unreacted copper nitrate present in the sample.

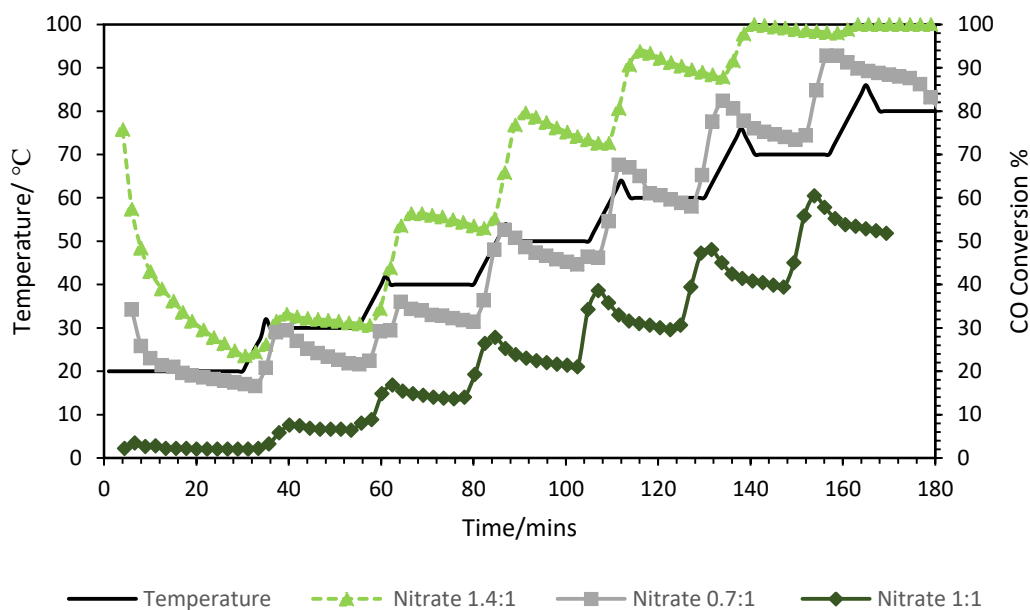


**Figure 5.26: CO oxidation profile of the calcined hopcalite (350 °C) which were precipitated under carbon dioxide with different concentrations of triethylamine (using nitrate salt)**

The activity of the catalyst that was made using the 1.4: TEA:water was shown to be the most active showing an initial conversion of 76% but rapidly deactivating in the first 30 minutes. The sample precipitated with 0.7:1 had a lower conversion despite have almost twice the surface area of the 1.4:1 sample. In addition, this catalyst saw continued deactivation after the first temperature ramp whereas the 1.4:1 TEA:water catalyst exhibited stable performance

The low activity of the catalyst precipitated in 1:1 TEA:water under carbon dioxide with nitrate salts may be related to the excess copper nitrate or copper hydroxyl nitrate that was still present in the sample which resulted in this sample having lower surface area after calcination at 350 °C. The fact that the material had the lowest surface area and the large presence of phase separated manganese carbonate after calcination may be other factors that had decreased CO activity for this catalyst.

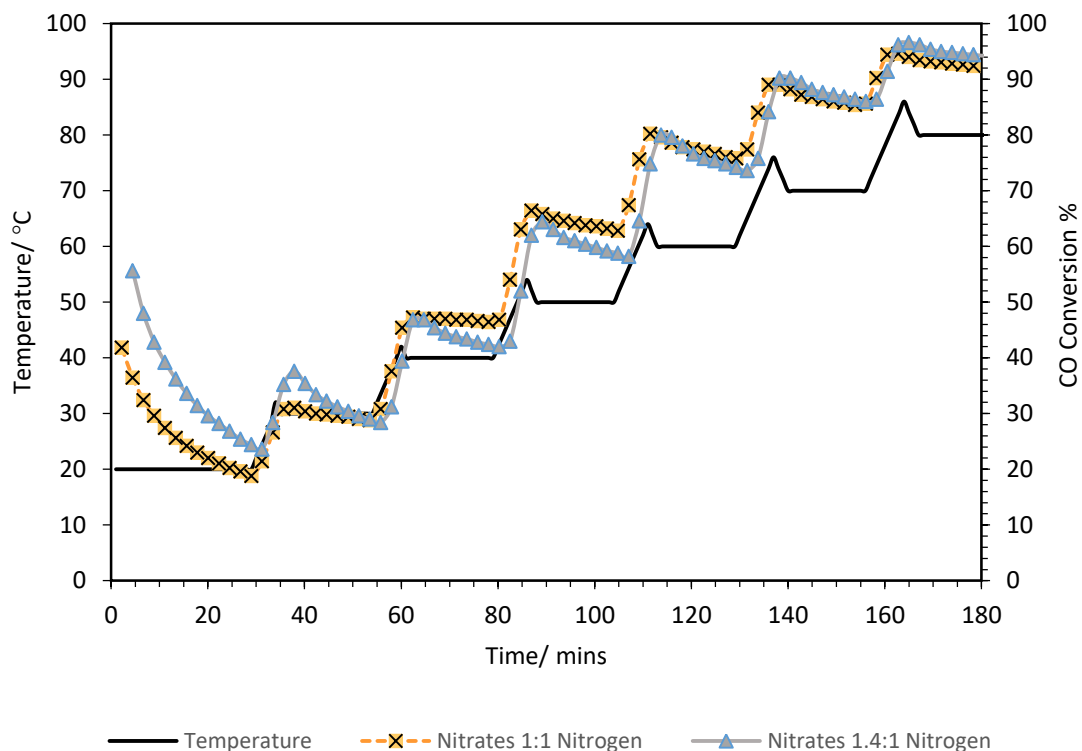


**Figure 5.27: CO oxidation profile of copper-manganese oxides (calcined 350 °C) made from switchable solvents precipitated under nitrogen before being switched to CO<sub>2</sub>**

The catalysts that were made from precursors added under a nitrogen atmosphere and then switched to CO<sub>2</sub> show the same initial CO oxidation activity followed by a large deactivation with the catalysts that was precipitated with 1.4:1 TEA:water.

The CO oxidation activity of the catalyst precipitated under both atmospheres indicated that the catalysts precipitated in 1.4:1 TEA:water were generally more active than those precipitated with 0.7:1 or 1:1. While the increased activity of the 1.4:1 sample over the 1:1 could be due to the increased surface area, the 0.7:1 sample showed a much lower activity despite the higher surface area and similar XRD pattern to that of the 1.4:1 sample.

The copper manganese that was precipitated using 0.7:1 of TEA:water was heat treated at different temperatures (350 °C, 400 °C and 500 °C) to investigate the formation of the crystalline hopcalite phase, as well as to observe the changes in the material (such as surface area and reduction profile).

**Table 5.6: Surface areas ( $\pm 10 \text{ m}^2 \text{ g}^{-1}$ ) of copper-manganese catalyst/precursor made from SAS, co-precipitation and switchable solvents. n/a is used when experiment was not performed**

Calcination temperature	Surface area/ $\text{m}^2 \text{ g}^{-1}$		
	Supercritical anti-solvent precipitation	Co-precipitated	Precipitation 0.7:1 TEA:water under $\text{CO}_2$ using nitrates
(Precursor)	93	n/a	76
350 °C	109	15	202
400 °C	125	73	142
500 °C	n/a	21	30

The XRD of the calcined oxide at 350 °C was very much amorphous, while the samples calcined at 400 °C showed more intense CuO reflections and the sample calcined at 500 °C had formed a crystalline spinel phase but with isolated  $\text{Mn}_2\text{O}_3$  reflections present in the sample (at  $2\theta=33.1^\circ$ ). The CuO reflection at  $2\theta=35.5$  would most likely be masked by the spinel reflection at the same  $2\theta$  but the  $38.5^\circ$  reflection is still visible. The formation of separated  $\text{Mn}_2\text{O}_3$  is likely to have occurred at around 500 °C as observed in the TGA profile for copper-manganese carbonate by the small mass loss in this region being associated with the formation of  $\text{Mn}_2\text{O}_3$ , although co-precipitated hopcalite (1:2 Cu:Mn Chapter 4) also formed phase separate  $\text{Mn}_2\text{O}_3$  at this temperature region as well. The surface area of this hopcalite material dropped rapidly with the increased calcination temperature and formation of a more crystalline material.

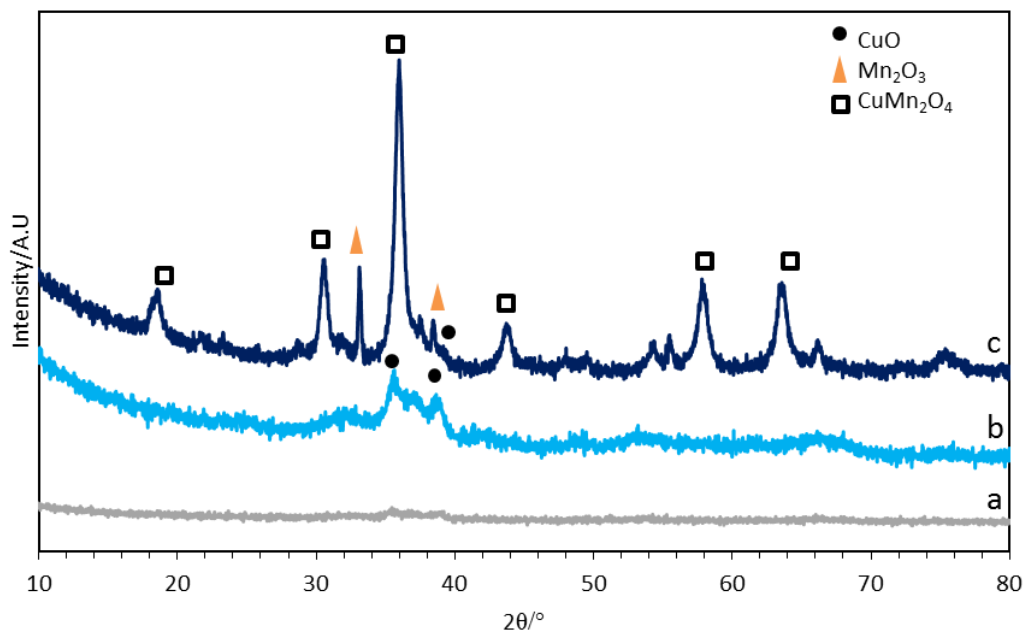


**Figure 5.28: XRD of copper-manganese precipitated in 0.7:1 triethylamine: water and calcined at a) 350 °C, b) 400 °C and c) 500 °C**

The TPR profile of the 400 °C calcined copper-manganese oxide showed very similar reduction profiles to the 350 °C with two reductions at 215 °C ( $\text{Cu}^{2+}$  to  $\text{Cu}^0$ ) and a second reduction at 264 °C ( $\text{Mn}^{3+}$  to  $\text{Mn}^{2+}$ ), which would suggest that the copper-manganese integration did not change much between calcination at 350 °C and 400 °C. The TPR profile of the sample calcined at 500 °C showed a much higher reduction profile as well as multiple reductions which confirmed what was observed with the XRD of phase separation occurring, most likely originating from phase segregated  $\text{Mn}_2\text{O}_3$ .

Overall the change in the calcination conditions (sample precipitate in 0.7:1 TEA:water sample) for the switchable solvent precipitated hopcalite showed that the sample calcined at 400 °C started to show some degree of crystallinity but overall remained mostly amorphous. However, this catalyst showed the same behaviour as co-precipitated catalyst when calcined at 500 °C, becoming more crystalline but with a reduced surface area.

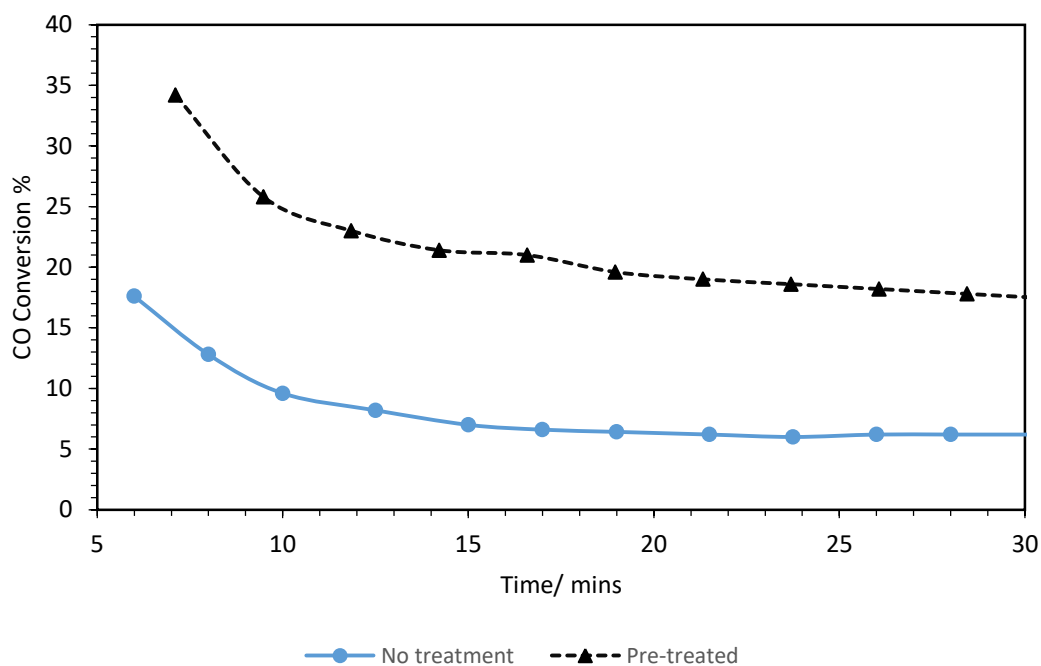


**Figure 5.29: Comparison of CO conversion at 20 °C (30 minutes) with copper-manganese oxide catalyst (0.7:1 sample) with and without pre-treatment at 110 °C for 30 minutes prior to reaction.**

The pre-treatment stage of the catalyst at 110 °C under nitrogen was done in order to remove physisorbed water. It was noted when degassing the switchable solvent precipitated samples for surface area analysis that even after calcination at 350 °C they lost roughly 5-10% weight after the degassing stage. CO oxidation activity of some of these samples showed that the initial conversion (at 20 °C) dropped by 12-15% when the samples were not degassed under nitrogen compared to those that were pre-treated. This suggests that the samples are prone to deactivation by physisorbed species such as water, which affects the initial conversion. It should be noted that supercritical anti-solvent precipitated and co-precipitated prepared hopcalite have similar trends but the effect of pre-treatment shows that these copper-manganese oxides are just as prone to deactivation by water.

### 5.3.4 Effect of aging time and atmosphere

Another important factor to consider is the effect of aging the metal carbonate precursors for different time periods under the different atmospheres to see the effect of leaving the catalyst precursors under these

conditions. It has been previously reported that in conventional co-precipitation of metal carbonates, the atmosphere under which the catalyst precursor is aged does affect its catalytic performance<sup>43</sup>. Since switchable solvent precipitations were carried out under different atmospheres (nitrogen and carbon dioxide) the influence of the atmosphere and how long the catalyst is left to age under these atmospheres is an important factor to consider.

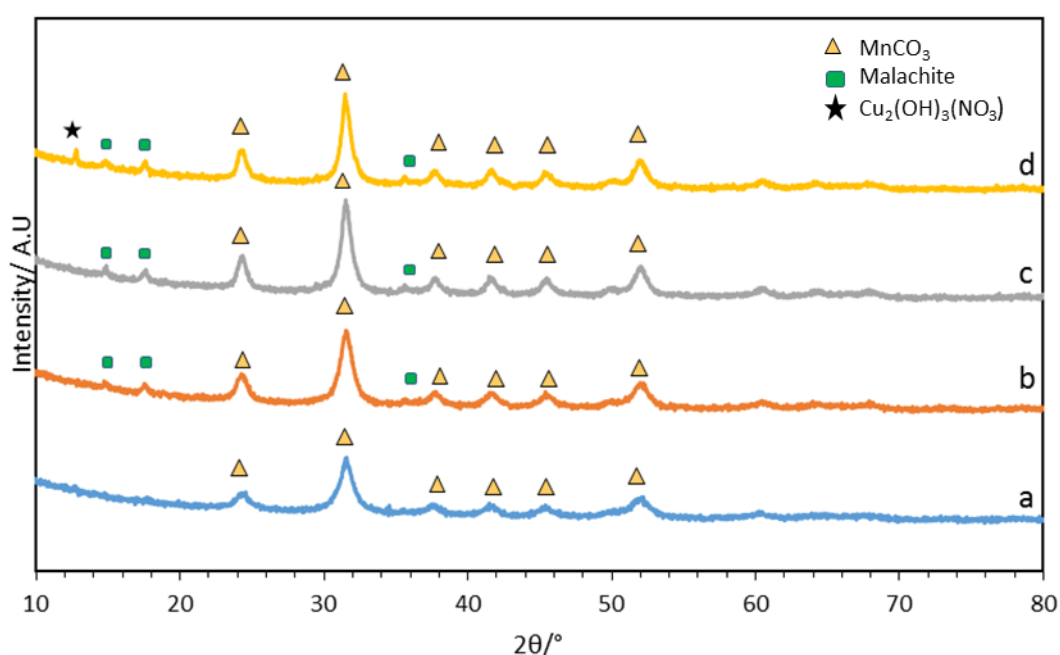


**Figure 5.30: XRD of the copper-manganese carbonate with a) no aging and aging under carbon dioxide atmosphere for b) 0.5 hours, c) 2 hours and d) 5 hours**

The effect of the aging atmosphere and time was performed on copper-manganese carbonates that were precipitated under a carbon dioxide atmosphere and either left to age under either a carbon dioxide atmosphere for 30 minutes, 2 hours and 5 hours, or switched to a nitrogen atmosphere and aged for the same time intervals. For the no aging study, the precipitate was centrifuged and washed immediately after precipitation.

The X-ray diffraction pattern of the copper manganese carbonate precipitated at all aging times showed rhodochrosite phase as the predominant phase in

the sample. With no aging (**Figure 5.30 a**) only the rhodochrosite phase reflections was observed by XRD. However, with aging under a carbon dioxide atmosphere another phase began to appear, in particular the reflections at  $2\theta = 14.6^\circ$ ,  $17.3^\circ$  and  $36.3^\circ$ . These reflections would appear to indicate the presence of malachite that precipitates during the aging process, and increases with increased aging time. It has been noted that other preparation methods of making hopcalite have also seen formation of phase separate malachite in the samples and this observation is not unique to this system<sup>32</sup>. What is also notable is that with increasing aging time under the CO<sub>2</sub> atmosphere, the samples crystallinity appeared to increase after 2 hours, although with the crystallite size initially decreasing for the first 30 minutes of aging. This seems to follow the trend observed with the surface area of the calcined samples (**Table 5.7**).

**Table 5.7: Crystal size of rhodochrosite  $2\theta = 31.6^\circ$  (1 0 4) for the copper-manganese carbonate precipitated and aged under carbon dioxide atmosphere ( $\pm 2$  nm).**

Sample	Crystal size $2\theta = 31.6^\circ$ nm
No aging	12.3
0.5 hour	9.2
2 hours	10.2
5 hours	10.6

Infra-red spectroscopy (**Figure 5.31**) also appears to confirm this observation with the main (very broad) carbonate peak appearing at  $1150-1550\text{ cm}^{-1}$  with the hydroxyl peak appearing (weaker) at  $3580-3500\text{ cm}^{-1}$  which was more predominate after 5 h aging. The FTIR for the sample with no aging did not show the additional vibrations at  $1050\text{ cm}^{-1}$  and  $815\text{ cm}^{-1}$  that are associated with phase separate malachite suggesting that this phase does not form instantly with the manganese phase but precipitates more slowly over the aging time. The FTIR spectrum does not significantly change after 30 minutes aging suggesting that most of the malachite phase forms within the first 30 minutes.

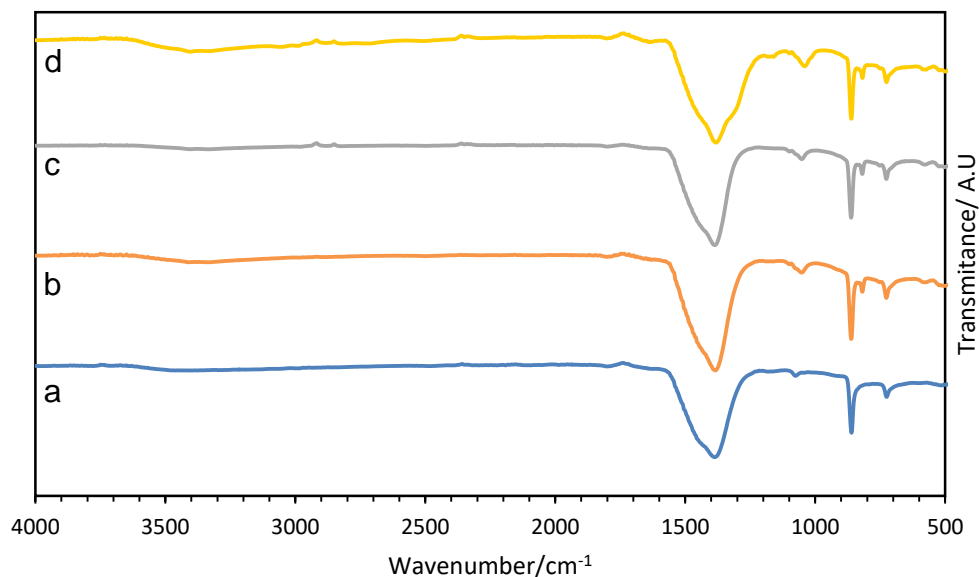


**Figure 5.31: FTIR of the copper-manganese carbonates precipitate with switchable solvent with a) no aging and aging under carbon dioxide for b) 0.5 hours, c) 2 hours and d) 5 hours**

The XRD of the carbon dioxide aged catalysts after calcination shows that the precursors are mostly amorphous with some crystalline phase reflection being present at  $2\theta=32.7^\circ$ ,  $35.8^\circ$ ,  $37.2^\circ$  and  $39.0^\circ$ . These reflections increased in intensity with an increase in the aging time and were not distinguishable in the sample with no aging but more defined after 5 hours aging under  $\text{CO}_2$ . The reflections at  $35.8^\circ$  and  $39.0^\circ$  having been established as isolated CuO, would suggest that the increase in aging time favours the growth of the malachite (as seen in the precursor). The XRD pattern of the non-aged sample resembles the supercritical anti-solvent precipitated catalyst calcined at  $400^\circ\text{C}$ , suggesting that the non-aged sample had better copper-manganese phase mixing and less separated copper carbonate formation in the precursor.

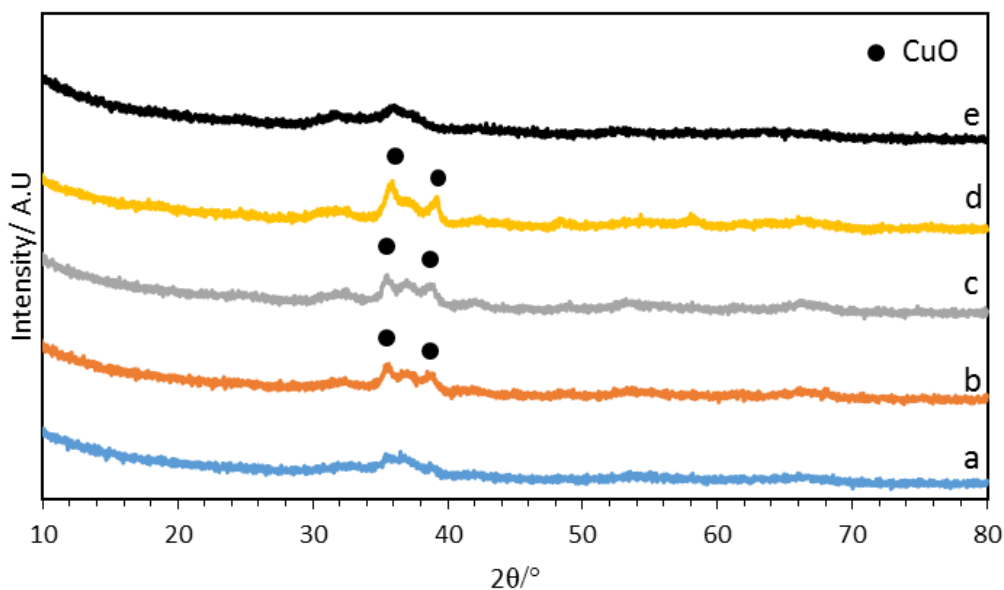


Figure 5.32: XRD of copper-manganese catalyst after calcination at 400 °C with a) no aging of the precursors and aging under carbon dioxide for b) 0.5 hours c) 2 hours d) 5 hours and e) SAS precipitated copper-manganese oxide calcined 400 °C

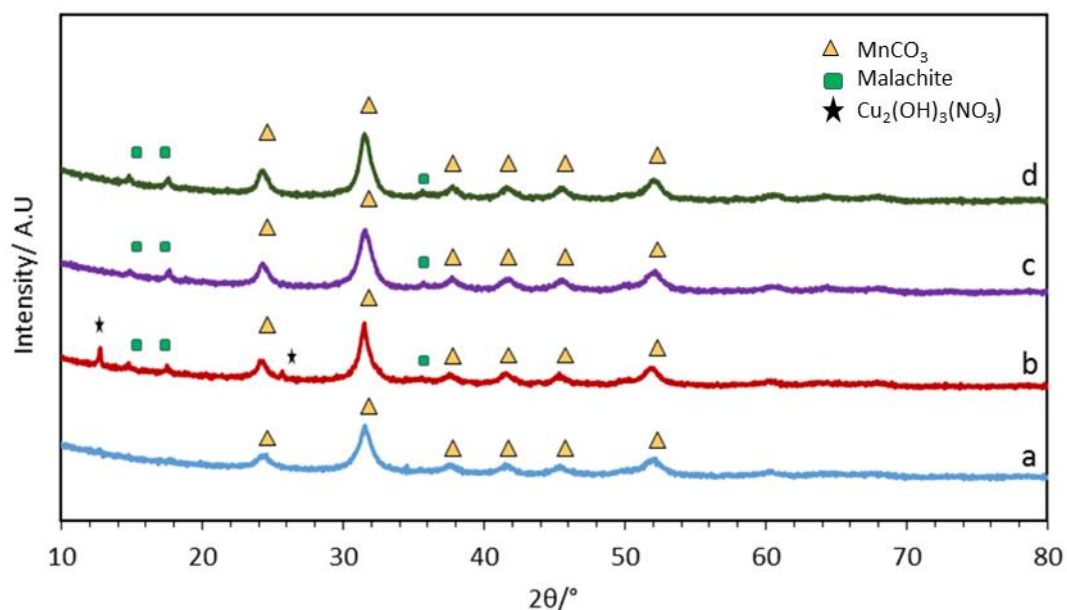


Figure 5.33: XRD of the copper-manganese precipitated in switchable solvents with a) no aging and aging under nitrogen atmosphere for b) 30 mins, c) 2 hours and d) 5 hours

The aging process under nitrogen showed a similar trend in the XRD pattern with the malachite reflections appearing during the aging process. For the sample aging under nitrogen for 30 minutes additional reflections appear at 12.8° and 25.5° which are the reflections associated with copper nitrate

hydroxide. The excess copper-nitrate hydroxide may have been removed during the washing steps but these samples may have not been sufficiently washed to remove this. The fact that there is still copper nitrate hydroxide in the sample even after aging for a short time would suggest that it does not fully dissolve back into the switchable solvent unlike co-precipitation where the copper-nitrate hydroxide initially forms but re-dissolves during the aging process<sup>40, 44</sup>.

**Table 5.8: Crystalline size (rhodochrosite) with different aging times under nitrogen**

Sample	Crystalline size $2\theta=31.6^\circ$
No aging	12.3
0.5 hours	9.9
2 hours	8.7
5 hours	9.5

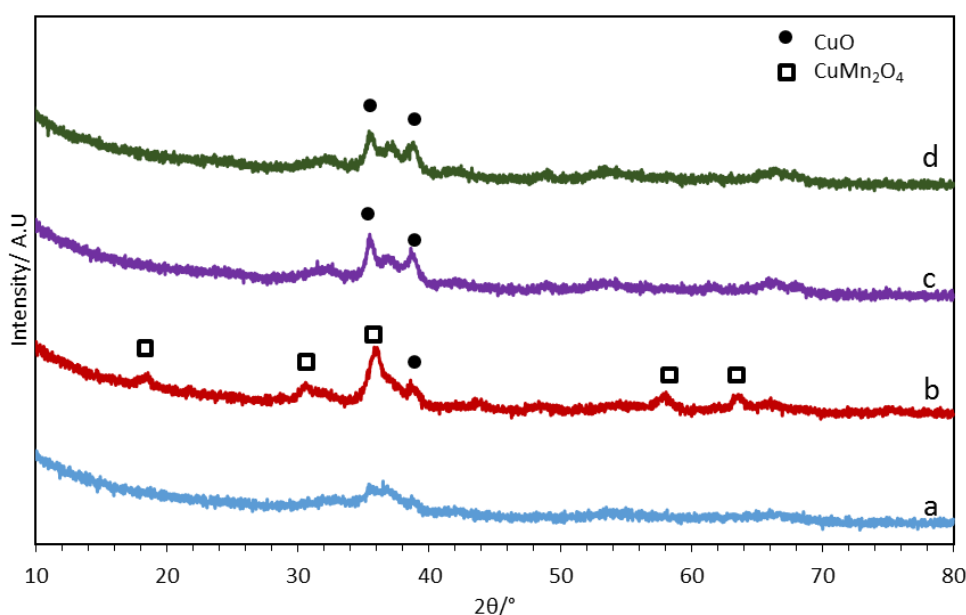


**Figure 5.34: XRD of the copper-manganese catalyst calcined at 400 °C with a) no aging and aging under a nitrogen atmosphere for b) 0.5 hours, c) 2 hours and d) 5 hours**

XRD of the calcined samples that were aged under nitrogen (**Figure 5.34**) showed a similar pattern to those aged under carbon dioxide with three reflections at  $2\theta=32.7^\circ$ ,  $35.8^\circ$  and  $37.2^\circ$  with the  $32.7^\circ$  and  $37.2^\circ$  reflection assigned to CuO. However, the sample aged for 0.5 hours showed

reflections from the spinel phase with reflection at such as 18.5° (1 1 1), 58.6° (5 1 1) and 64.2° (4 4 0), while the broad reflection at 37.2° disappears which suggest that this sample has formed a more crystalline spinel phase than the other aged samples.

The surface areas of the copper-manganese oxides initially increased with aging time under CO<sub>2</sub> at 30 mins and then decreases with increased CO<sub>2</sub> aging time after 30 mins. The aging under nitrogen showed an opposite trend with the surface area initially decreasing but then increasing. Both the nitrogen for 0.5 hours and carbon dioxide aging for 5 hours show significantly lower surface area, which corresponds to the additional Cu<sub>2</sub>(OH)<sub>3</sub>NO<sub>3</sub> peaks observed in the XRD. Aging under nitrogen for 2-5 hours appeared to favour an increase in surface area of both the precursor and the calcined sample compared with the sample aged under carbon dioxide.

**Table 5.9: The BET surface area ( $\pm 10 \text{ m}^2 \text{ g}^{-1}$ ) of the copper-manganese oxides and precursors with different aging times under carbon dioxide and nitrogen atmospheres**

Aging time and atmosphere		Surface area $\text{m}^2 \text{g}^{-1}$	
		Precursor	Calcined 400 °C
No aging		34	118
CO <sub>2</sub>	30 mins	80	128
	2 hours	81	112
	5 hours	12	105
N <sub>2</sub>	30 mins	21	97
	2 hours	107	143
	5 hours	113	145

The TGA of the sample with no aging and aging under both carbon dioxide and nitrogen atmosphere (**Figure 5.35**) all show three main mass losses at 220-240 °C, 300-340 °C and 460-540 °C. The TGA profile for the non-aged sample is very similar to the one seen for manganese carbonate prepared from manganese acetate (**Figure 5.6**), which would suggest that the sample has better Cu-Mn mixing (copper in the manganese carbonate structure and lack of isolated malachite) as seen with the XRD of the precursors.

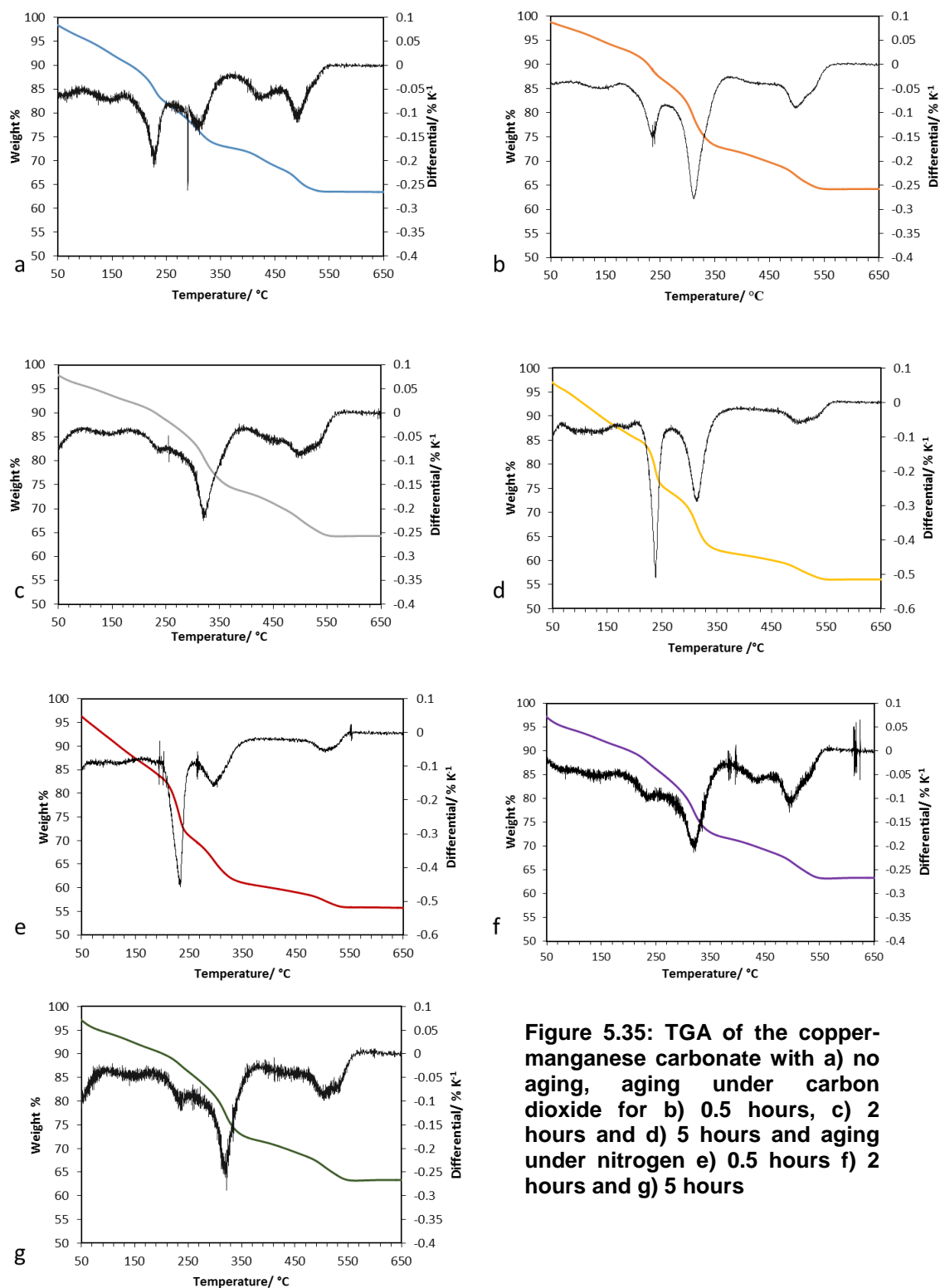


**Figure 5.35: TGA of the copper-manganese carbonate with a) no aging, aging under carbon dioxide for b) 0.5 hours, c) 2 hours and d) 5 hours and aging under nitrogen e) 0.5 hours f) 2 hours and g) 5 hours**

However, as the aging time is increased to 2 hours the most significant mass loss shifts from the 220-240 °C range to the 300-340 °C area. It should be noted that the 5 hours aging under carbon dioxide and the 0.5 hour aging under nitrogen which lack additional washing steps both have a larger mass loss at the initial 220-240 °C range. Both of these samples also had the additional reflection at 12.8° in the XRD, which did not appear in the other samples, suggesting that the copper nitrate hydroxide that appeared at this range also contributed to the initial mass loss at 220-240 °C. This would also suggest that the copper nitrate hydroxide is more likely to be removed with increased aging (assuming standard washing is used). The formation of carbonate over the nitrate hydroxide may be more likely with longer aging time in the switchable solvent. It appears that the mass loss is significantly reduced after 2 hours aging under either atmosphere with the main mass loss shifting to the 310 °C range. It should also be noted that for the sample aged for 5 hours aging under CO<sub>2</sub> had a larger mass loss at 240 °C while the mass loss at 310 °C had also increased (from the differential) compared to the sample aged for 0.5 hour under nitrogen which would suggest that although there were excess nitrates the shift to higher temperature still occurred with increased aging. The final mass loss at 500 °C is the formation of phase separated Mn<sub>2</sub>O<sub>3</sub> from MnO<sub>2</sub><sup>25</sup>.

This shift in mass loss towards 310-320 °C, would suggest that the carbonate phase is more predominate with increased aging time as well as the increase formation of malachite, since this mass loss region is associated with the degradation of the carbonates. This trend is in agreement with the XRD of the precursor phase with the carbonate phase becoming more crystalline and formation of the malachite phase with increased aging time under both atmospheres.

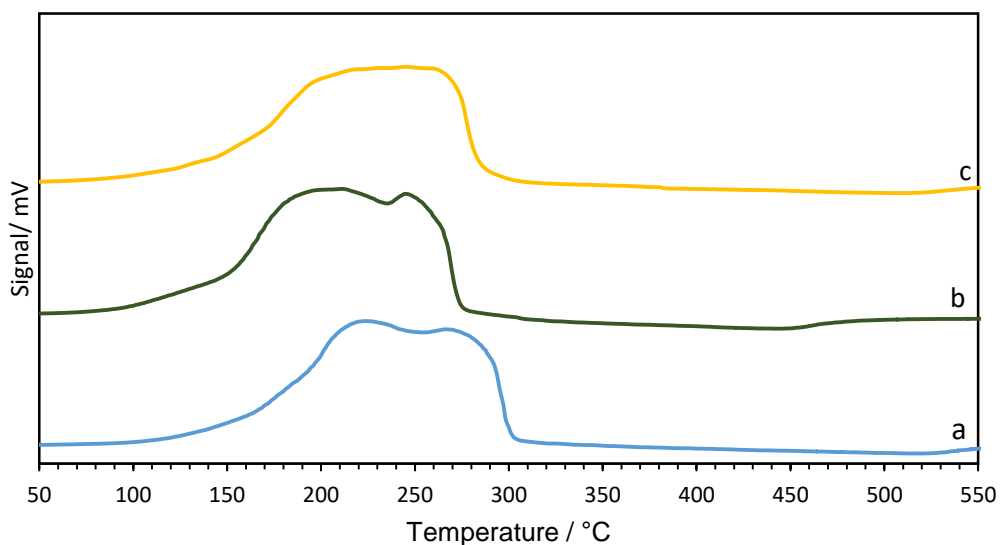


**Figure 5.36: TPR profile of the copper-manganese oxides (calcined 400 °C) made from switchable solvents with a) no aging and aging for 5 hours under b) nitrogen and c) carbon dioxide**

The TPR profile of the samples ( $10\text{ °C min}^{-1}$  heating rate) shows very similar reduction profiles for the catalysts that had no aging and the catalyst that was aged under nitrogen for 5 hours, with two reduction peaks. The sample that was aged under a carbon dioxide for 5 hours also showed a broad reduction at 150-300 °C but the peaks have merged into a broad reduction peak (or at least the two distinct reduction peaks are not visible), the most likely reason being the slightly higher degree of crystallinity observed and possibly better phase integration. The TPR profiles shown here are closer to those of SAS and co-precipitated hopcalite, which shows that the copper-manganese mixing for these samples does not differ from the conventional standards. The aging of the precursors overall seems to have had minor effect on the reduction profile, suggesting that the oxidation state and phase integration is more likely determined by the calcination step.

**Table 5.10: Cu:Mn ratios (in ppm) calculated from MP-AES analysis ( $\pm 0.1$  Mn)**

CuMn <sub>2</sub> O <sub>4</sub> Sample	Cu Average (PPM)	Mn Average (PPM)	Cu:Mn (PPM)	Cu:Mn (Molar ratio)
Acetate	4.0	8.5	1: 2.2	1:2.5
No aging	4.2	7.5	1: 1.8	1:2.1
Aging 5 hours Nitrogen	4.3	7.8	1: 1.8	1:2.1
Aging 5 hours carbon dioxide	7.2	13.0	1: 1.8	1:2.1
Supercritical anti-solvent	4.8	8.1	1 :1.7	1:1.9
Co-precipitation	5.9	10.2	1: 1.7	1:2

MP-AES analysis on the materials showed that there were some differences between the desired ratio and the actual ratio of Cu:Mn, overall there was roughly a 1:2 ratio of copper:manganese precipitated. In addition the ratio of all Cu:Mn did not change with aging for 5 hours under both CO<sub>2</sub> and N<sub>2</sub> atmosphere which means that the increase in malachite reflections and particle size seen in the XRD would be due to a growth in the malachite particles rather than a delayed precipitation. The values however did suggest that there was some small amount of copper loss during the switching process with the acetate system having the most significant loss of copper. This might explain why malachite is not observed in the copper-manganese sample when acetate are used (although they also do not appear in the non-aged sample which has a closer ratio of Cu:Mn of 1:2).

Cu 2p XPS of the non-aged sample (calcined at 400 °C) shows only Cu<sup>2+</sup> peaks present with no indication of the presence of Cu<sup>+</sup> associated with the spinel redox coupling that occurs in hopcalite<sup>35-37</sup>. However, the sample aged under CO<sub>2</sub> for 5 hours showed Cu<sup>+</sup> peaks alongside the Cu<sup>2+</sup> which indicates along with the XRD and TPR that this hopcalite is more crystalline and had a better degree of phase integration. The sample that was calcined at 400 °C with the 5-hour aging under nitrogen showed no Cu<sup>+</sup> peaks either. In comparison both copper manganese oxide prepared by supercritical anti-

solvent precipitation and co-precipitation (Chapter 4) both showed small amounts of  $\text{Cu}^+$  after calcination at  $400\text{ }^\circ\text{C}$ .

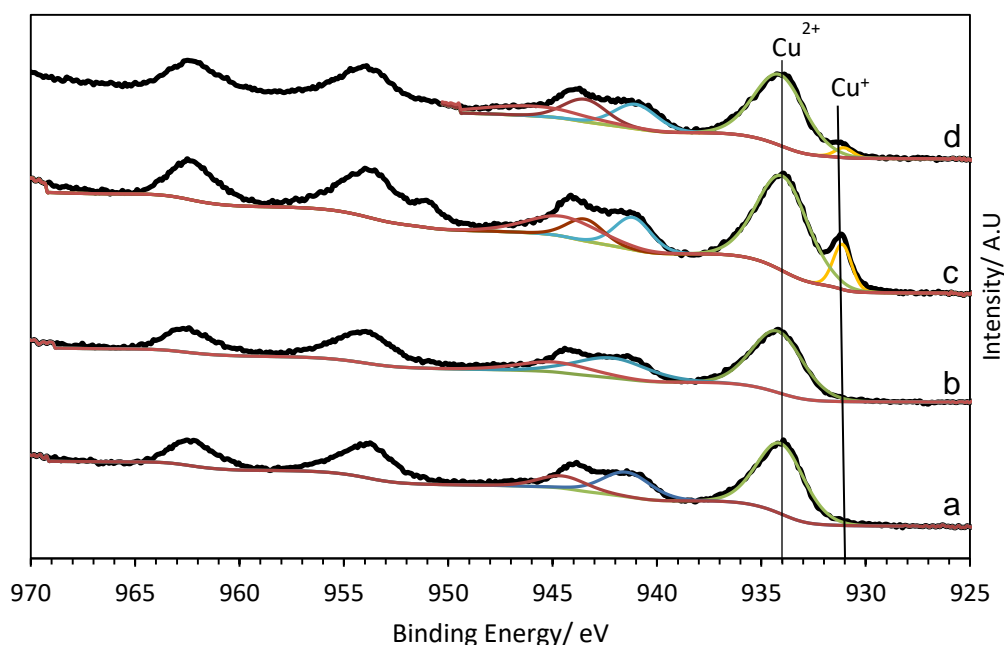


**Figure 5.37:** Cu 2p region of the copper-manganese oxides (calcined  $400\text{ }^\circ\text{C}$ ) with a) no aging b) 5 hours nitrogen, c) 5 hours carbon dioxide and d) SAS precipitated, calcined  $400\text{ }^\circ\text{C}$

The O 1s XPS (**Figure 5.38**) showed a minor increase in the lattice:adsorbed oxygen ratio ( $529.9\text{ eV}$  and  $531.6\text{ eV}$ ) with increased aging time under both atmospheres, with the nitrogen having higher amounts of adsorbed oxygen than the carbon dioxide aged sample.

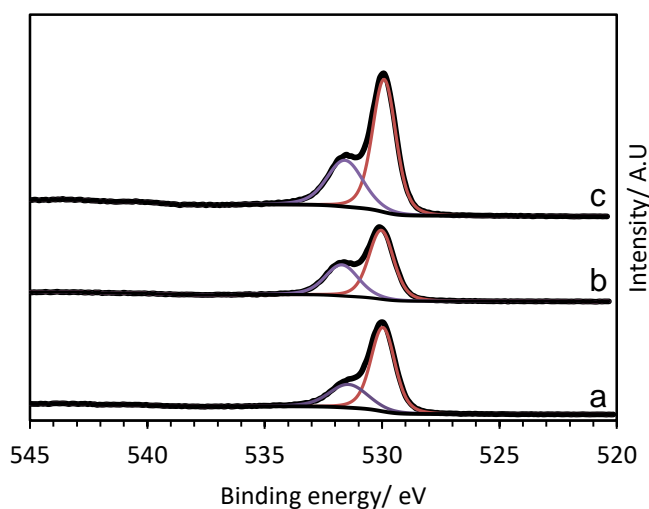


**Figure 5.38:** (left) XPS of the O 1s region of the copper-manganese catalysts with a) no aging, b) 5 hours nitrogen and c) 5 hours carbon dioxide.

Table 5.11: XPS peak area % ( $\pm 5\%$ ) of the O 1s region

Sample	Lattice Oxygen 529.9 eV (%)	Adsorbed oxygen 531.6 eV (%)
No aging	69	31
5 hours Nitrogen	63	37
5 hours Carbon dioxide	65	35

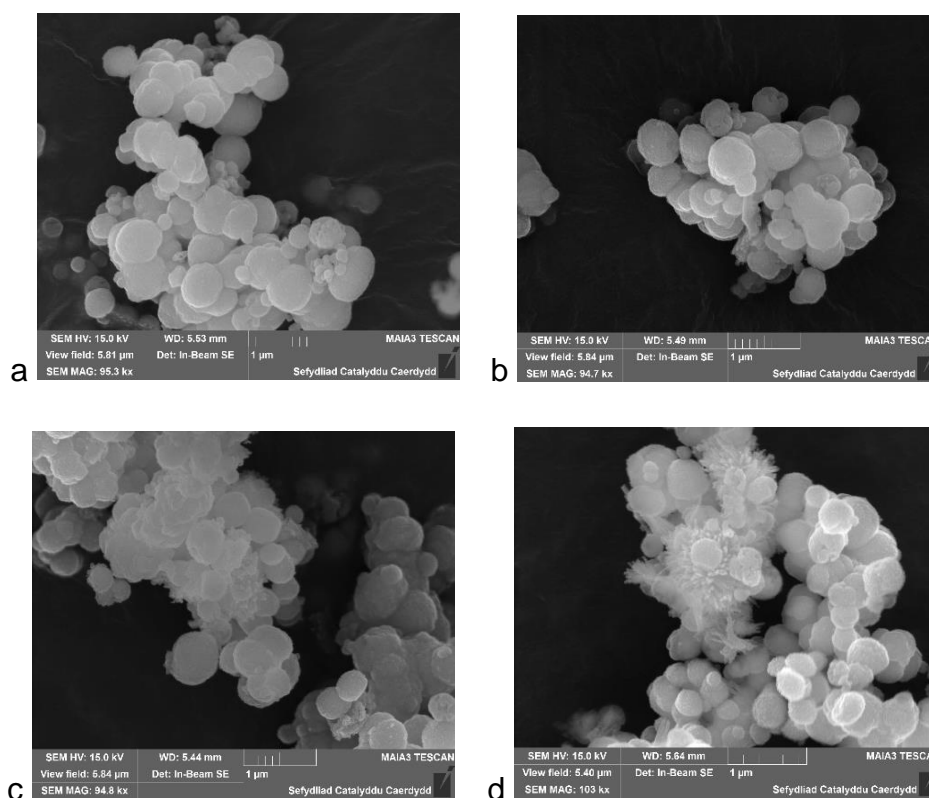
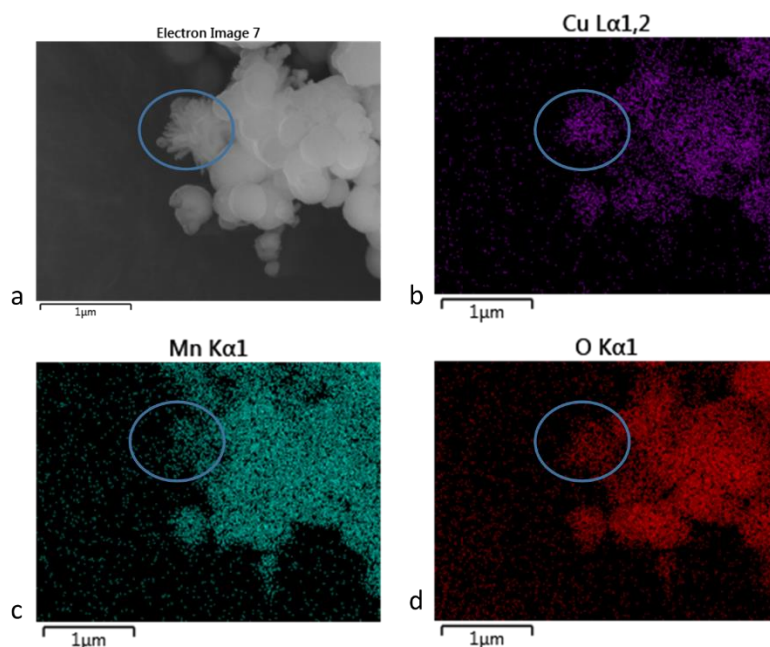


Figure 5.39: SEM images of the copper-manganese oxide (calcined 400 °C) with a) no aging b) 30 minutes CO<sub>2</sub> c) 2 hours CO<sub>2</sub>, d) 30 mins N<sub>2</sub>

SEM images (Figure 5.39) shows an interesting feature of the aging process. The sample without aging showed mostly the single morphology associated with the mixed copper-manganese phase. Upon aging the second rod like morphology associated with the isolated malachite appears. EDX mapping (Figure 5.40) showed this area was relatively Cu rich (and lower manganese) compared to the spherical particles. This would correlate with the XRD

observations of the precursor which showed malachite reflection on the samples that were aged under both atmospheres but was not seen in the non-aged sample.



**Figure 5.40: a) SEM image of copper manganese oxide (calcined 400 °C) from precipitated aged under carbon dioxide for 30 minutes and EDX mapping of b) copper, c) manganese and d) oxygen. The circle shows the mapping of the second morphology**

This would suggest that malachite was precipitating from solution during the aging time but had not precipitated during the initial addition of the nitrate solution, although MP-AES analysis showed the aged and non-aged samples had a similar Cu:Mn ratio. The aging process may have also caused the growth of malachite crystallites, which is supported by observations in both the XRD and the FTIR.

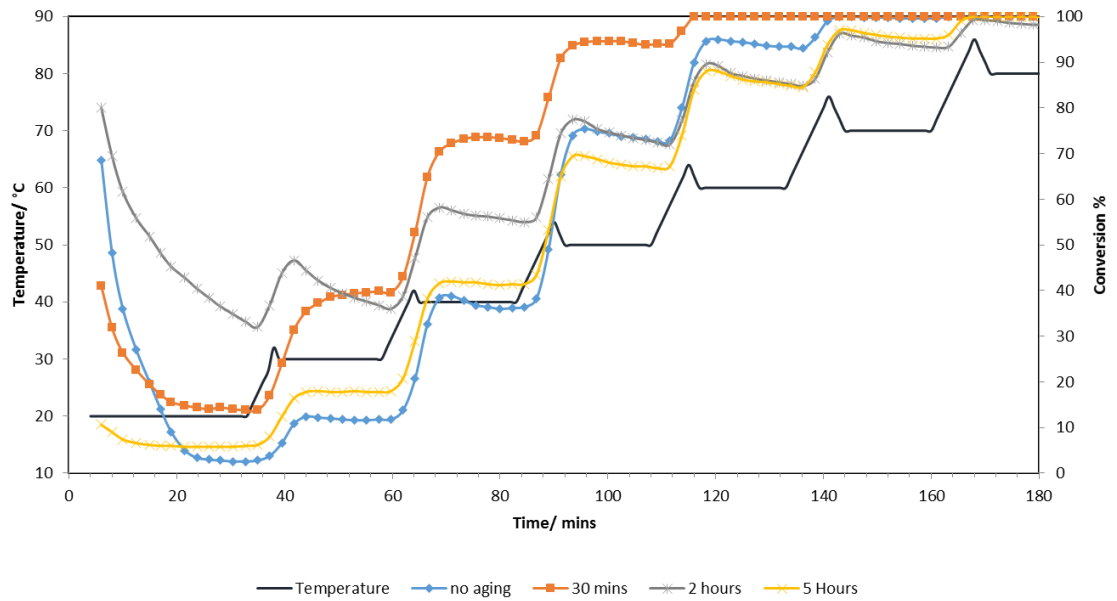


**Figure 5.41: CO oxidation of the copper-manganese with no aging and aged under Carbon dioxide for 0.5, 2 and 5 hours**

The catalyst testing for the sample with no aging showed an initial high CO conversion of 68% at 20 °C but very rapidly deactivated to <3% within the first 20 minutes. The sample aged for 0.5 hours showed a less rapid deactivation stabilising at 14% conversion after 20 minutes. The most notable sample was the 2 hours aging under carbon dioxide had a less rapid deactivation to the extent that the sample had not stabilised after 30 minutes were as the other samples had stabilised after 15-20 minutes. The samples that were aged under nitrogen show a similar trend, with the exception of the 0.5 hour aged sample which could be due to the more crystalline phase that formed or presence of residual copper nitrate hydroxide observed by XRD. It should be noted that the deactivation changes after the first 5 minutes with the initial deactivation curve matching that of the sample with no aging but then the deactivation slows down. The initial deactivation would be due to water, which had been removed from the catalyst surface during the pre-treatment.

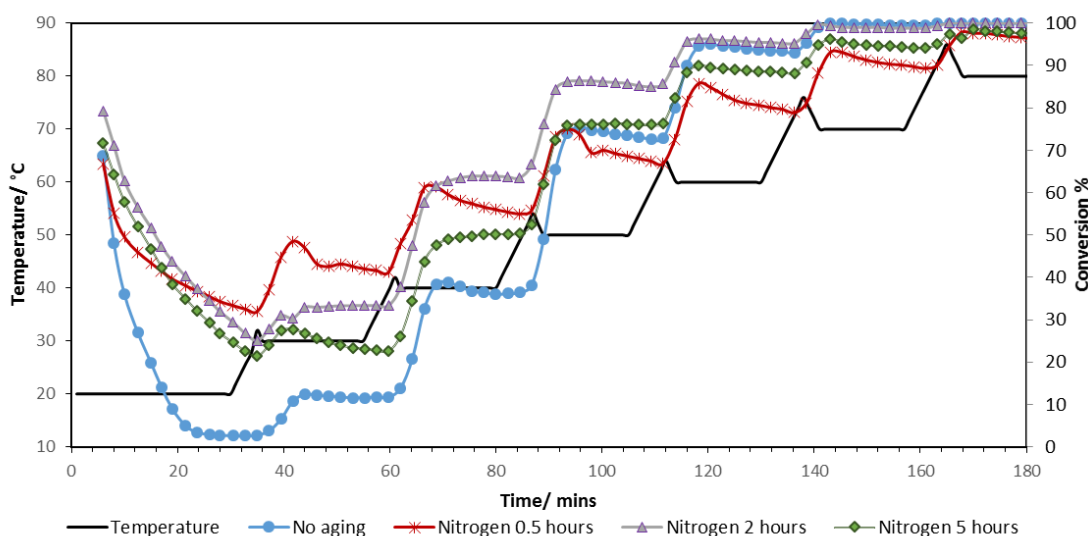


**Figure 5.42: CO oxidation of copper-manganese carbonate with no aging and aging under a nitrogen atmosphere for 0.5 hours, 2 hours and 5 hours**

With the exception of the two samples with residual copper nitrate hydroxide in the precursor (0.5 hour aging nitrogen and 5 hour aging carbon dioxide) the samples seem to show a less rapid deactivation with increased aging time. The sample with no aging and aged under  $\text{CO}_2$  for 30 minutes showed the most rapid deactivation within the first 20 minutes. In comparison the sample aged 2 hours  $\text{CO}_2$  and 2 and 5 hours  $\text{N}_2$  showed a less rapid deactivation (with 20-30 % conversion after 30 minutes) but were continuing to deactivate even after the first temperature ramp at 20-30 °C. These samples were the ones that had the usually higher mass loss at 230 °C in the TGA profile, which shows that the washing and presence of nitrates affect the final hopcalite catalyst and its activity. It should also be noted that for the sample aged for 0.5 hours in nitrogen also was more crystalline than the other samples and this may also contribute to its different CO oxidation activity.

## 5.4 Chapter 5 Conclusions

This chapter showed that the use of switchable solvents could be used not only to prepare single metal oxide precursors such as manganese and copper, but also can be used to make mixed copper-manganese oxide precursors. The change in parameters such as initial metal salt (acetate or nitrate), the atmosphere of precipitation, amine: water ratio and aging time all have a significant effect on the surface area copper-manganese distribution and the catalytic activity. This variation has shown that the method can be tailored to change the properties of both the precursor and the final catalyst. While the method has been used to prepare active hopcalite catalysts, there is some degree of phase separation which occurs in nearly all of the catalysts which may cause some decrease in CO activity and catalyst stability.

However, the method has been shown to produce active copper-manganese catalyst that not only have comparable activity to those of co-precipitated and supercritical anti-solvent precipitation but also in some cases (such as when acetate salts were used) have enhanced catalytic activity. This method is more advantageous as it avoids the potential poisoning from sodium (as in co-precipitation with  $\text{Na}_2\text{CO}_3$ ) as well as producing catalysts with similar morphology and surface area those prepared by the supercritical anti-solvent process without the need for the high pressures which make the process uneconomical for commercial scale up. The use of switchable solvents to precipitate hopcalite precursors demonstrates a greener approach to making highly active metal oxides precursors.

## 5.5 Chapter 5 Future work

The work here has proven that switchable solvents are a viable option for synthesising high surface area hopcalite catalysts with enhanced activity over hopcalite made from other methods. The potential of switchable solvents has been demonstrated to be wide spread and therefore must be investigated further. The use of switchable solvents for hopcalite should be further investigated practically with the improvement of the phase integrations and further investigation using acetate salts.

In addition there are several parameters that can be applied to widen the investigation of switchable solvents for metal oxide preparation.

The first parameters is to investigate whether switchable solvent precipitation can be used to make other single metal oxide precursors such as cobalt, iron and nickel oxides as catalysts for reactions such as VOC combustion as alternatives to supercritical anti-solvent precipitated equivalents<sup>45</sup> to see if these catalyst also have enhanced activity over these conventional catalysts. The use of switchable solvent to prepare other mixed metal oxides, such as cobalt-manganese oxide precursors should also be investigated to see how well the methodology works with other mixed metal oxide systems. The use of switchable solvents for preparation of copper-zinc oxide precursors has also been investigated and the results are given in Chapter 6 of this thesis.

The second parameter that should be investigated is the use of other switchable solvents (switchable hydrophilic-hydrophobic solvents and switchable polar solvents) to prepare metal oxide precursors and to see if these have any improvement over the TEA based switchable hydrophilic-hydrophobic solvents. In addition, the used of mixed solvent systems such as using ethanol to dissolve the metal precursors before addition to the switchable solvent system is also another factor that could change the catalyst precursor and tailor the system to suit different catalyst preparations.

## 5.6 Chapter 5 References

1. P. G. Jessop, D. J. Heldebrant, X. W. Li, C. A. Eckert and C. L. Liotta, *Nature*, 2005, **436**, 1102-1102.
2. T. Yamada, P. J. Lukac, M. George and R. G. Weiss, *Chemistry of Material*, 2007, **19**, 967-969.
3. D. L. Xue, Y. Mu, Y. Mao, T. K. Yang and Z. L. Xiu, *Green Chemistry*, 2014, **16**, 3218-3223.
4. P. G. Jessop, *Aldrichimica Acta*, 2015, **48**, 18.
5. M. C. Ozturk, C. S. Ume and E. Alper, *Chemical Engineering & Technology*, 2012, **35**, 2093-2098.
6. P. G. Jessop, L. Phan, A. Carrier, S. Robinson, C. J. Durr and J. R. Harjani, *Green Chemistry*, 2010, **12**, 809-814.
7. D. Z. Xiong, G. K. Cui, J. J. Wang, H. Y. Wang, Z. Y. Li, K. S. Yao and S. J. Zhang, *Angewandte Chemie-International Edition*, 2015, **54**, 7265-7269
8. L. Phan and P. G. Jessop, *Green Chemistry*, 2009, **11**, 307-308
9. S. M. Mercer, T. Robert, D. V. Dixon, C. S. Chen, Z. Ghoshouni, J. R. Harjani, S. Jahangiri, G. H. Peslherbe and P. G. Jessop, *Green Chemistry*, 2012, **14**, 832-839
10. X. P. Wu, Y. N. Wu, S. Yang, M. W. Zhao, M. W. Gao, H. Li and C. Dai, *Soft Matter*, 2016, **12**, 4549-4556
11. Y. X. Liu, P. G. Jessop, M. Cunningham, C. A. Eckert and C. L. Liotta, *Science*, 2006, **313**, 958-960.
12. Q. W. Tang, Z. Y. Huang, C. C. Zheng, H. S. Lu and D. F. Liu, *Industrial & Engineering Chemistry Research*, 2018, **57**, 13291-13299.
13. E. Yilmaz and M. Soylak, *Analytica Chimica Acta*, 2015, **886**, 75-82.
14. S. M. Mercer, T. Robert, D. V. Dixon and P. G. Jessop, *Catalysis Science & Technology*, 2012, **2**, 1315-1318.
15. J. R. Vanderveen, J. Durelle and P. G. Jessop, *Green Chemistry*, 2014, **16**, 1187-1197.
16. K. Bryant, G. Ibrahim and S. R. Saunders, *Langmuir*, 2017, **33**, 12982-12988.
17. P. Pramanik, S. Biswas, S. Chakrabarti, B. K. Raul and K. L. Chopra, *Materials Research Bulletin*, 1990, **25**, 877-880.
18. A. Pathak and P. Pramanik, *Bulletin of Materials Science*, 1992, **15**, 449-452.
19. A. A. Mirzaei, H. R. Shaterian, R. W. Joyner, M. Stockenhuber, S. H. Taylor and G. J. Hutchings, *Catalysis Communications*, 2003, **4**, 17-20.
20. P. Nanta, W. Skolpap, K. Kasemwong and Y. Shimoyama, *Journal of Supercritical Fluids*, 2017, **130**, 84-90.
21. Y. Xie, R. Parnas, B. Liang, Y. Y. Liu, C. D. Tao and H. F. Lu, *Chinese Journal of Chemical Engineering*, 2015, **23**, 1728-1732.
22. T. Yamada, P. J. Lukac, T. Yu and R. G. Weiss, *Chemistry of Materials*, 2007, **19**, 4761-4768.
23. C. J. Clarke, W. C. Tu, O. Levers, A. Brohl and J. P. Hallett, *Chemical Reviews*, 2018, **118**, 747-800
24. J. Jung and M. Perrut, *Journal of Supercritical Fluids*, 2001, **20**, 179-219.

25. D. Stoilova, V. Koleva and V. Vassileva, *Spectrochimica Acta Part a-Molecular and Biomolecular Spectroscopy*, 2002, **58**, 2051-2059.
26. L. Biernacki and S. Pokrzywnicki, *Journal of Thermal Analysis and Calorimetry*, 1999, **55**, 227-232.
27. K. Qian, Z. X. Qian, Q. Hua, Z. Q. Jiang and W. X. Huang, *Applied Surface Science*, 2013, **273**, 357-363.
28. S. A. Kondrat, P. J. Smith, P. P. Wells, P. A. Chater, J. H. Carter, D. J. Morgan, E. M. Fiordaliso, J. B. Wagner, T. E. Davies, L. Lu, J. K. Bartley, S. H. Taylor, M. S. Spencer, C. J. Kiely, G. J. Kelly, C. W. Park, M. J. Rosseinsky and G. J. Hutchings, *Nature*, 2016, **531**, 83-87.
29. Z. R. Tang, C. D. Jones, J. K. W. Aldridge, T. E. Davies, J. K. Bartley, A. F. Carley, S. H. Taylor, M. Allix, C. Dickinson, M. J. Rosseinsky, J. B. Claridge, Z. L. Xu, M. J. Crudace and G. J. Hutchings, *ChemCatChem*, 2009, **1**, 247-251.
30. Z. R. Tang, S. A. Kondrat, C. Dickinson, J. K. Bartley, A. F. Carley, S. H. Taylor, T. E. Davies, M. Allix, M. J. Rosseinsky, J. B. Claridge, Z. Xu, S. Romani, M. J. Crudace and G. J. Hutchings, *Catalysis Science & Technology*, 2011, **1**, 740-746.
31. S. A. Kondrat and S. H. Taylor, in *Catalysis*, eds. J. J. Spivey and K. M. Dooley, The Royal Society of Chemistry, 2014, Volume 26, pp. 218-248.
32. T. J. Clarke, T. E. Davies, S. A. Kondrat and S. H. Taylor, *Applied Catalysis B-Environmental*, 2015, **165**, 222-231.
33. T. J. Clarke, S. A. Kondrat and S. H. Taylor, *Catalysis Today*, 2015, **258**, 610-615.
34. F. C. Buciuman, F. Patcas and T. Hahn, *Chemical Engineering and Processing-Process Intensification*, 1999, **38**, 563-569.
35. S. A. Kondrat, T. E. Davies, Z. L. Zu, P. Boldrin, J. K. Bartley, A. F. Carley, S. H. Taylor, M. J. Rosseinsky and G. J. Hutchings, *Journal of Catalysis*, 2011, **281**, 279-289.
36. S. Veprek, D. L. Cocke, S. Kehl and H. R. Oswald, *Journal of Catalysis*, 1986, **100**, 250-263.
37. G. M. Schwab and S. B. Kanungo, *Zeitschrift Fur Physikalische Chemie-Frankfurt*, 1977, **107**, 109-120.
38. B. Liu, *Nanoscales*, 2012, **4**, 7194-7198.
39. P. G. Jessop, L. Kozycz, Z. G. Rahami, D. Schoenmakers, A. R. Boyd, D. Wechsler and A. M. Holland, *Green Chemistry*, 2011, **13**, 619-623.
40. G. J. Hutchings, A. A. Mirzaei, R. W. Joyner, M. R. H. Siddiqui and S. H. Taylor, *Applied Catalysis A-General*, 1998, **166**, 143-152.
41. I. Schildermans, J. Mullens, B.J Van der Veken, J. Yperman, D. Franco and L. C. Van Poucke, *Thermochimica Acta*, 1993, **224**, 227-232.
42. Z. Ding, W. Martens and R. L. Frost, *Journal of Materials Science Letters*, 2002, **21**, 1415-1417.
43. S. H. Taylor, G. J. Hutchings and A. A. Mirzaei, *Chemical Communication*, 1999, 1373-1374.
44. G. J. Hutchings, A. A. Mirzaei, R. W. Joyner, M. R. H. Siddiqui and S. H. Taylor, *Catalysis Letters*, 1996, **42**, 21-24.
45. R. P. Marin, S. A. Kondrat, R. K. Pinnell, T. E. Davies, S. Golunski, J. K. Bartley, G. J. Hutchings and S. H. Taylor, *Applied Catalysis B-Environmental*, 2013, **140**, 671-679.

# Chapter 6 Deep Eutectic Solvent and Switchable Solvents for The Preparation of Copper-Zinc Oxides.

## 6.1 Introduction

### 6.1.1 Background

In the previous chapters, deep eutectic solvents (DES) and switchable solvents have both been demonstrated as viable, alternative methods for the preparation of single and mixed metal oxides such as cobalt oxide, manganese oxide and copper-manganese oxide as catalysts for CO oxidation or total oxidation of volatile organic compounds (VOC). These two preparation methods were shown to have advantages and disadvantages over the conventional method for making metal oxide catalysts for these reactions. However the potential of the use of DES and switchable solvents beyond CO and VOC oxidation is an avenue that has yet to be explored.

Copper-zinc oxide catalysts are widely used by industry for various reactions, most notably for methanol synthesis and low temperature water gas shift reaction<sup>1-4</sup>. Despite having been used as the industrial standard catalyst for methanol synthesis since the 1960s<sup>5</sup>, Cu/ZnO are still widely studied in academia and industry, with the focus on improvement on the performance of copper zinc catalysts through the preparation methods<sup>3, 6</sup>.

Co-precipitation is still the most common method of preparing Cu/ZnO or Cu/ZnO/Al<sub>2</sub>O<sub>3</sub> methanol synthesis and water gas shift catalysts<sup>7</sup>. The catalysts are usually precipitated from a nitrate solution using sodium carbonate and are precipitated as hydroxyl carbonate most commonly as a zincian malachite or other phases such as rosasite and aurichalcite<sup>7, 8</sup>. These hydroxyl carbonate precursors are then calcined to the CuO/ZnO and are reduced *in situ* to the active Cu/ZnO catalyst.

In recent years it was demonstrated that a copper-zinc carbonate precursor known as georgeite, which is naturally unstable and difficult to synthesise by

conventional methods, aging to form zincian malachite during co-precipitation<sup>9</sup>, could be prepared through supercritical anti-solvent precipitation<sup>8</sup>. Copper-zinc catalysts derived from supercritical anti-solvent precipitated georgeite were found to have highly disperse Cu and a higher Cu surface area. This resulted to have formed Cu/ZnO that were highly active for methanol synthesis<sup>8, 10</sup>. The supercritical anti-solvent process also had the advantage over co-precipitation as the process avoided the use of sodium carbonate as a precipitating agent, thereby eliminating poisoning by sodium<sup>3</sup>.

These publications on georgeite prepared by supercritical anti-solvent precipitation demonstrates how alternative techniques can be used to make catalyst precursors that are not only difficult to prepare but also enhances the catalytic properties of the metal oxide catalyst compared to those derived from conventional methods.

However, supercritical anti-solvent is an energy intensive process with an operating pressure of 100-150 bar at 40 °C and as such its application and scale up to industrial level is often not applied for catalyst preparation, even if the resulting catalyst is more active than the conventional co-precipitated catalysts<sup>11</sup>. As a result, co-precipitation remained the most common and the industrial standard method for the preparation of Cu/ZnO catalysts as it is a more easily scalable and optimised process<sup>3, 12</sup>.

The work in Chapter 5 demonstrated that not only could copper-manganese oxide (hopcalite) catalysts be prepared using switchable solvents but were also in some cases, found to be more active CO conversion catalysts than those synthesised by supercritical anti-solvent precipitation. This is important since switchable solvents process only required 1 bar pressure compared to the 100-150 bar for supercritical anti-solvent precipitation, therefore providing a greener alternative to prepare these catalysts.

Choline chloride based deep eutectic solvents (DES), although containing chlorine, have been shown to be excellent templates for synthesising metal oxide and/or metal oxide precursors with controllable morphologies. It had been demonstrated that the addition of water could be used to DES make

metal oxide with rod like morphologies with examples including ceria<sup>13</sup> or the use of water as an anti-solvent to form zinc oxide needles<sup>14</sup>. Chapter 3 also demonstrated that the use of other choline chloride-oxalic acid based DES with an anti-solvent could be used to tailor the morphology of the catalyst precursor and final oxides.

An early publication on deep eutectic solvents by Abbott *et al.* showed different metal oxides including zinc oxide could be dissolved by choline chloride based DES. Zinc oxide could be dissolved in choline chloride-urea based DES with a concentration of 1800-90000 ppm depending on the temperature of the DES solution<sup>15-17</sup>. It was later demonstrated by Dong *et al.* that zinc oxide could also be precipitated out of the DES through an anti-solvent<sup>18</sup> method, primarily with water, and that different rates of addition of the anti-solvent to the choline chloride-urea based DES could change the morphology of the precipitated zinc oxide. If the zinc oxide was allowed to precipitate slowly from the DES, it would form long needles compared to elliptical shaped ZnO particles if a rapid precipitation occurred<sup>18</sup>. This method later showed that if a copper salt such as copper nitrate was added to the anti-solvent then the copper would co-precipitate onto the zinc oxide during the anti-solvent process, resulting in a Cu<sup>2+</sup> doped onto ZnO<sup>19</sup>.

### 6.1.2 Aims of chapter

The aim of this chapter was to apply the DES anti-solvent and switchable solvent methodologies described in the previous chapters of this thesis to prepare precursors of Cu/ZnO methanol synthesis catalysts. This chapter will look into variations in both the DES method and switchable solvent method to see variations in the precursor surface area, decomposition temperature and morphology. Some of these catalysts were tested for methanol synthesis to see how they perform and to assess whether these are viable methods of preparing Cu/ZnO catalysts.

Making copper-zinc oxide catalysts using deep eutectic solvents and switchable solvents presents more of a challenge than preparing single

oxides or mixed metal oxide for CO/VOC oxidation. For this reason, only bimetallic Cu/ZnO was prepared during this work to assess the methods with Al<sub>2</sub>O<sub>3</sub> not being added to the catalysts shown in this chapter.

## 6.2 Deep eutectic solvent preparation

Although the use of choline chloride-urea has been established for the preparation of single and mixed metal oxides, one important factor that most likely will cause problems with this method is the use of a chlorine-based solvent. The work in Chapter 3 did demonstrate that for some metal oxide precursors such as cobalt oxalate, the choline could be sufficiently removed and the resulting oxide would contain little chlorine. However, the presence of chlorine was still present in iron oxide after washing and calcination and as such poses a potential problem.

The preparation to make the mixed Cu/ZnO was based on the method used by Hsu *et al.*<sup>19</sup> however to make enough catalyst the concentration of the ZnO in the choline chloride-urea DES was increased from 2400 ppm to 28000 ppm. Deionised water was used as the anti-solvent. For rapid precipitation 1500 ml of water was used in order to rapidly breakup the eutectic and precipitated ZnO (with co-precipitation of the copper). In addition, the precursor was washed with additional 1500 ml of water and 600 ml of ethanol to remove the choline species from the precursor.

### 6.2.1 Effect of the Cu:Zn ratio

The first step was to see what Cu:Zn ratios were possible for this technique and the effect on the properties of the material with increased ratios. The group of Hsu *et al.* only synthesised up to 10% (atomic) loading of Cu on the ZnO, which would be too low for a methanol synthesis or water gas shift catalyst therefore higher ratios, were prepared. To see the effect on the phase a series of Cu:Zn loadings of 0.01:1 to 2:1 were prepared. The volume

of anti-solvent was kept the same with the concentration of copper acetate in the anti-solvent increased for higher copper loadings.

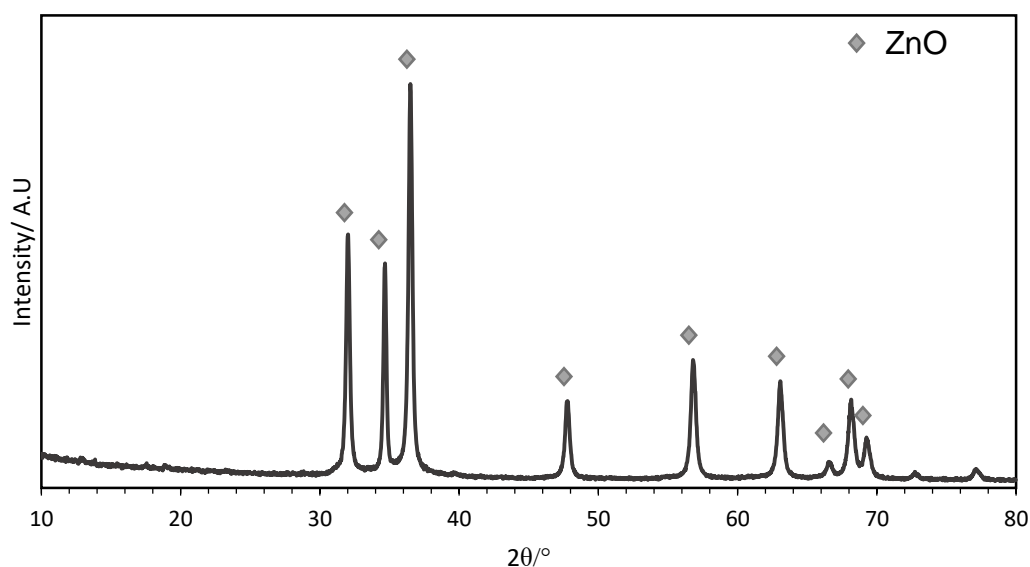


**Figure 6.1: XRD of ZnO precipitated from the DES solution in 1500 ml of water**

The XRD patterns of the zinc oxide precipitated from choline chloride-urea without copper (**Figure 6.1**) showed reflections of zinc oxide at  $32.0^\circ$  (1 0 0),  $34.6^\circ$  (0 0 2) and  $36.5^\circ$  (1 0 1) along with the  $47.7^\circ$  (1 0 2),  $56.8^\circ$  (1 1 0) and  $63.1^\circ$  (1 0 3). There were no additional reflections that would indicate any crystalline impurities in this sample. Other publications on the precipitation of ZnO from DES have noted that zinc carbonate can form as a result of a reaction of zinc oxide with urea during the anti-solvent process<sup>14</sup>, but the XRD pattern (**Figure 6.1**) did not show any indication of this in this sample, as only ZnO reflections were detected.

The XRD patterns of the samples that were co-precipitated with the copper-acetate (**Figure 6.2**) showed for 0.01:1 Cu:ZnO some of the zinc oxide reflections were still viable. With the increase in copper loading the zinc oxide reflections start to disappear and the XRD shows a less crystalline phase with some reflections such as  $2\theta = 36.9^\circ$ ,  $59.4^\circ$  remaining the same intensity while the reflection at  $12.5^\circ$  became more visible at higher Cu loadings (0.2:1-1:1 Cu:Zn loading (**Figure 6.2 e-g**)). The patterns ( $12.5^\circ$ ,  $24.6^\circ$  (weak more visible in **Figure 6.8**)  $33.2^\circ$   $35.3^\circ$  and  $60.1^\circ$ ), particularly at higher loadings indicate that the copper-zinc precipitated as a (hydrotalcite-like)

layered double hydroxide (LDH) phase<sup>20, 21</sup>. It is notable that the LDH reflections appeared when copper was added and are more prevalent at higher loading. This suggests that the LDH formation is caused by the addition of copper acetate in the anti-solvent. In addition, the disappearance of zinc oxide peaks above 0.01:1 Cu:Zn suggest the formation of a mixed phase material although it should be noted that LDH have been reported to form during ionothermal synthesis with choline chloride-urea after the addition of water<sup>22</sup>.

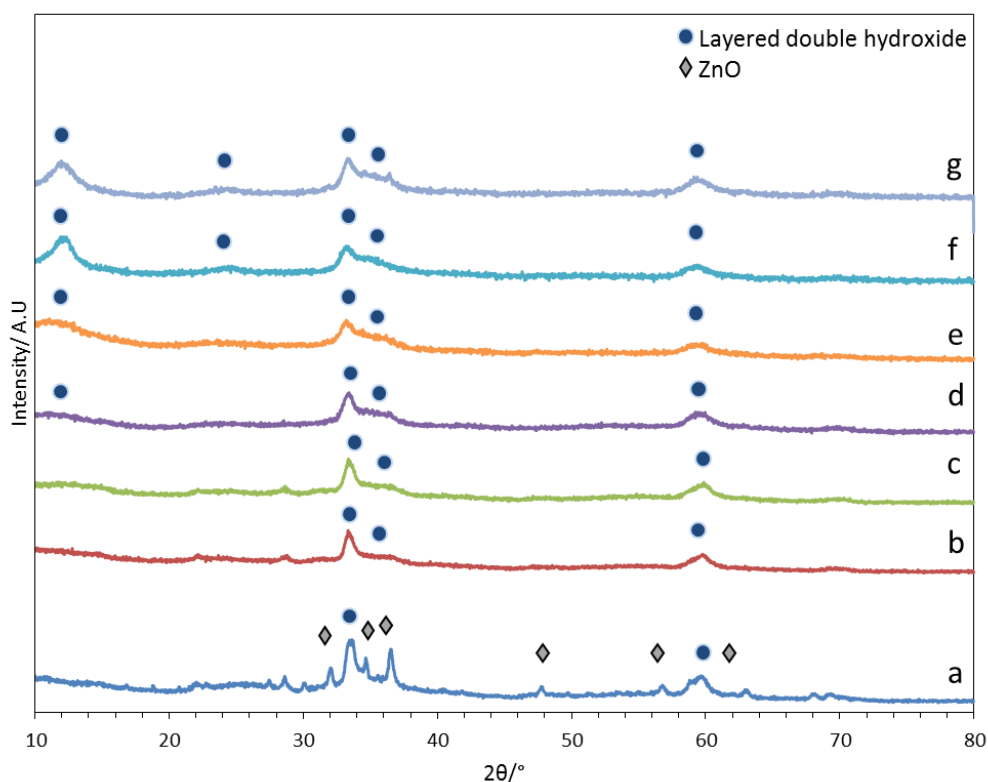


**Figure 6.2** XRD of the copper-zinc precursors precipitated out of the DES with a Cu:Zn ratio of a) 0.01:1 b) 0.02:1 c) 0.05:1 d) 0.01:1 e) 0.02:1 f) 0.04:1 and g) 1:1

The FTIR of the precipitated sample (**Figure 6.3**) showed variations at  $3350\text{ cm}^{-1}$  (possible O-H)  $2200\text{ cm}^{-1}$  (not to be confused with the  $\text{CO}_2$  peak at  $2350\text{ cm}^{-1}$ )  $1623\text{ cm}^{-1}$  (C-O),  $1473\text{ cm}^{-1}$ ,  $1387\text{ cm}^{-1}$ ,  $1049\text{ cm}^{-1}$  and  $840\text{ cm}^{-1}$ . What is notable is the strong band at  $2200\text{ cm}^{-1}$ . This band would indicate a possible urea-metal coordination bond, which is known to occur in metal salt-urea, based DES<sup>23</sup>. In addition, a weaker vibration at  $1635\text{ cm}^{-1}$  (C=O of urea) would confirm that some of the urea from the DES was precipitated and

retained in the structure of the precipitate. It should be noted that ZnO when dissolved in the DES is complex with urea<sup>15</sup> and its possible that urea was still bound to the zinc when it precipitated, which gave rise to the metal-urea bond vibration seen in the FTIR. In addition, there are several peaks, notably at  $1473\text{ cm}^{-1}$  that might originate from residual choline chloride.

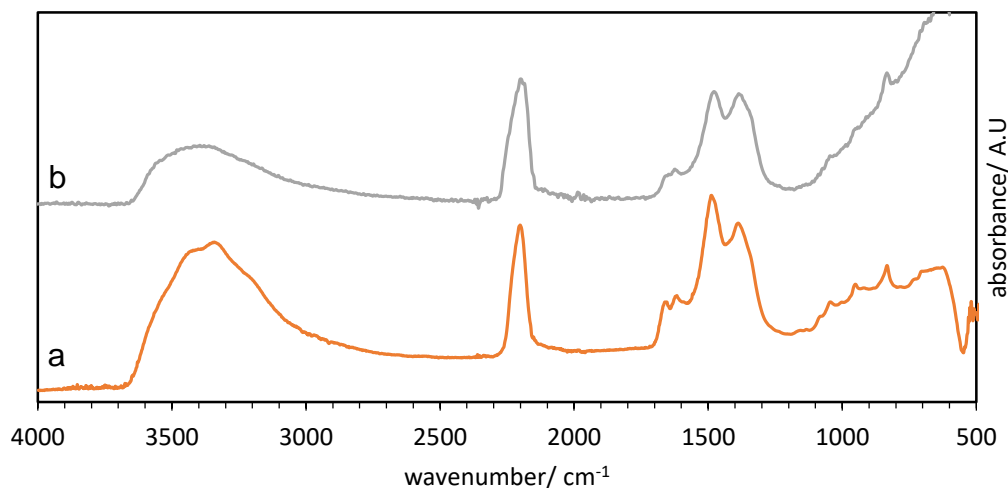


**Figure 6.3:** FTIR of the copper-zinc precursor precipitated by DES with a Cu:Zn ratio of a) 0.05:1 (baseline corrected) and b) 0.4:1

The TGA/DSC (**Figure 6.4**) of the precipitate (0.4:1) (heating rate  $1\text{ }^{\circ}\text{C min}^{-1}$ ) shows two minor mass losses at  $74\text{ }^{\circ}\text{C}$  and  $180\text{ }^{\circ}\text{C}$  followed by a large mass loss at  $265\text{ }^{\circ}\text{C}$ . The sample remained at 69% of original mass after  $300\text{ }^{\circ}\text{C}$  suggesting that the precursor and residual DES had mostly decomposed by this temperature.

What was interesting to note was the DSC scan showed that the mass loss at  $220\text{--}280\text{ }^{\circ}\text{C}$  (peaking at  $265\text{ }^{\circ}\text{C}$ ) was an endothermic decomposition rather than an exothermic decomposition that would occur with an acetate. This endothermic decomposition would suggest that the copper was no longer present as an acetate<sup>1</sup>.

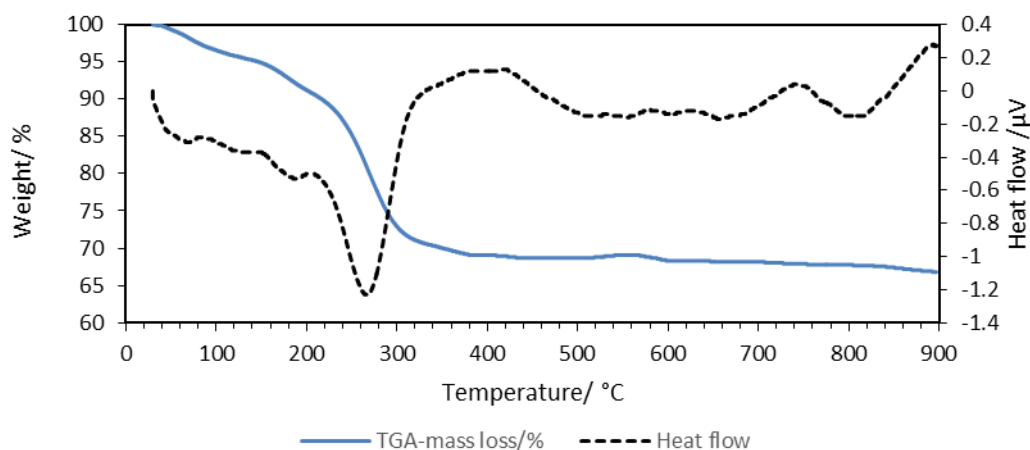


**Figure 6.4** TGA and DSC profile of the 0.4:1 Cu:Zn precursor precipitated by DES anti-solvent

XRD patterns of the calcined samples (**Figure 6.5**) confirmed the formation of CuO/ZnO after calcination at 350 °C for 3 hours and the CuO reflections (notably at  $2\theta = 38.6^\circ$ ) becoming larger with increased copper loading as would be expected. **Table 6.1** shows a general increase in surface area of the calcined sample when the copper: zinc ratio is increased from 0.02:1 to 0.4:1 ( $40 \text{ m}^2 \text{ g}^{-1}$ ) although 0.2:1 is the exception with a surface area of  $52 \text{ m}^2 \text{ g}^{-1}$ . However, at higher loadings the total surface area rapidly decreases.

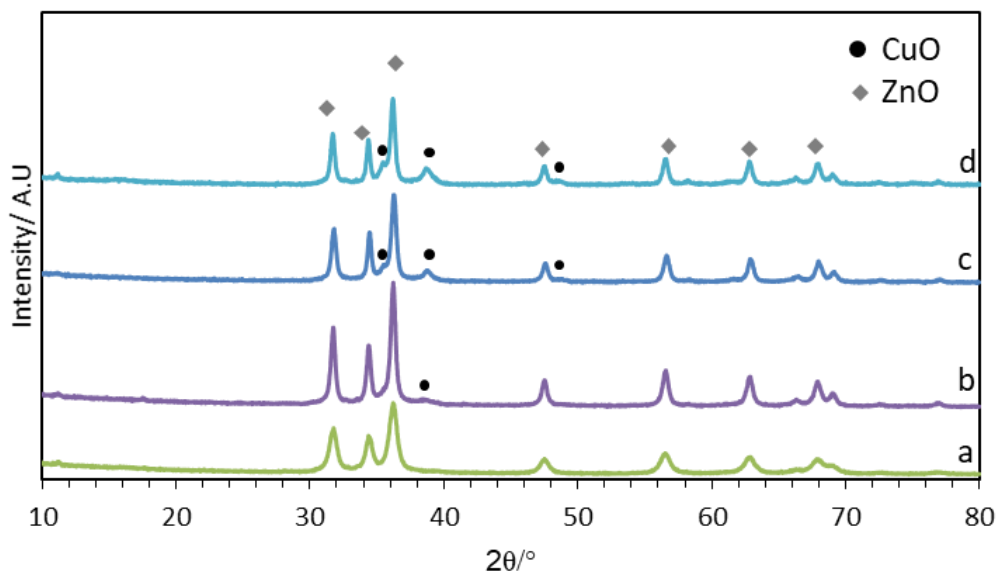


**Figure 6.5:** XRD of CuO/ZnO calcined at 350 °C with a Cu:Zn ratio of a) 0.05:1, b) 0.1:1, c) 0.2:1 and d) 0.4:1

However, MP-AES analysis on the sample precipitated by DES (**Table 6.1 and Figure 6.6 a and b**) showed that the target ratio of Cu:Zn was achieved with ratios between 0.01:1 to 0.4:1 within a reasonable range (10-16%) of the expected ratio as well as linear to the expected concentration. However, when the target ratio of Cu:Zn was increased to 1:1 the MP-AES showed that the ratio that precipitated was 3.6:1 which means that at least 72% of the zinc failed to precipitate out (assuming that all of the copper precipitated). Cu:Zn with a target of 2:1 was off by a more substantial amount of 31:1. This means that the higher copper loading is preventing the zinc oxide from precipitating out of the DES during the anti-solvent process or reacting with the zinc to form a water-soluble compound. One notable fact was that the anti-solvent volume was constant (1500 ml) while the concentration of the copper acetate in the solution was changed.

**Table 6.1: Surface area of the final oxide materials calcined at 350 °C and the copper: zinc ratio determined by MP-AES**

Sample (target ratio) Cu:Zn	Actual ratio (error ±2%)	BET Surface area $\text{m}^2\text{g}^{-1}$ ( $\pm 2 \text{ m}^2\text{g}^{-1}$ )
0.01:1	0.016:1	15
0.02:1	0.023:1	4
0.05:1	0.059:1	31
0.1:1	0.11:1	37
0.2:1	-	52
0.4:1	0.46:1	40
1:1	3.6:1	9
2:1	31:1	16

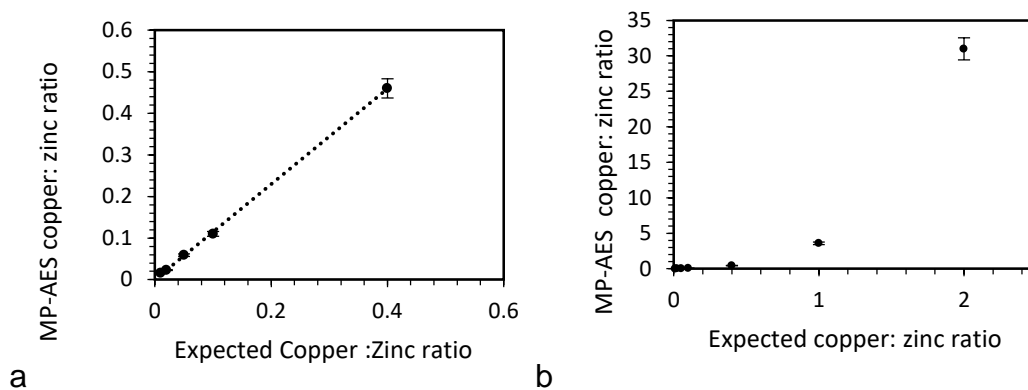


**Figure 6.6: Aimed Cu:Zn ratio plotted against the actual Cu:Zn ratio a) 0.01:1 to 0.4:1 Cu:Zn and b) 0.01:1 to 2:1 Cu:Zn**

XPS analysis of the Cl 2p region of the calcined CuO/ ZnO (0.05:1, 0.2:1 and 0.4:1) (**Figure 6.7**) showed that there was a significant amount of chlorine left on the surface of the catalyst even after calcination. 0.05:1 showed the highest amount of chlorine with approximately 12% (**Table 6.2**) of the surface being chlorine while the 0.2:1 and 0.4:1 had around 5%. This amount of chlorine would most likely cause these catalysts to be inactive. The binding energy of the chlorine from the Cl 2p region showed peak with binding energies of 198.7 eV, which would indicate that the surface chloride, is in the form of a metal chloride rather than residual organic chloride.

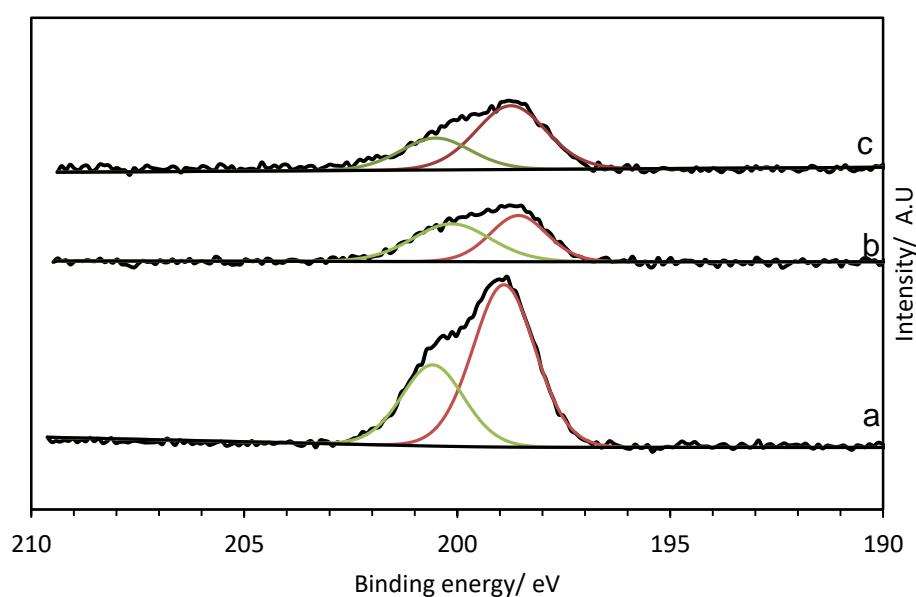


**Figure 6.7: XPS of Cl 2p region for the CuO/ZnO prepared by DES (calcined 350 °C) a) 0.05:1, b) 0.2:1 and c) 0:4**

**Table 6.2: Surface chlorine (atomic %) derived from XPS (error  $\pm 1\%$ )**

Cu:ZnO	Surface Cl (%)
0.05:1	12
0.2:1	5
0.4:1	5

### **6.2.2 Effect of the rate of precipitation and the precursor salt.**

As with the Chapter 3 and previous work on the use of DES-anti-solvent, the rate of precipitation from the DES can have a major effect on the morphology and surface area of the precursor<sup>18</sup>. The initial investigation of preparing copper-zinc oxide precursors using a rapid precipitation method (i.e. adding the DES to 1500 ml of deionised water). The rate of precipitation was controlled by adding the copper/water anti-solvent mixture at a controlled rate of 1 ml min<sup>-1</sup> for 100 ml followed by 600 ml of deionised water (similar to the setup described in Chapter 3).

Another factor that was considered was the effect of the copper salt used in the anti-solvent. Changing the metal salt may have an effect on how the zinc oxide co-precipitates (when the DES is broken up) with the previous section using copper acetate.

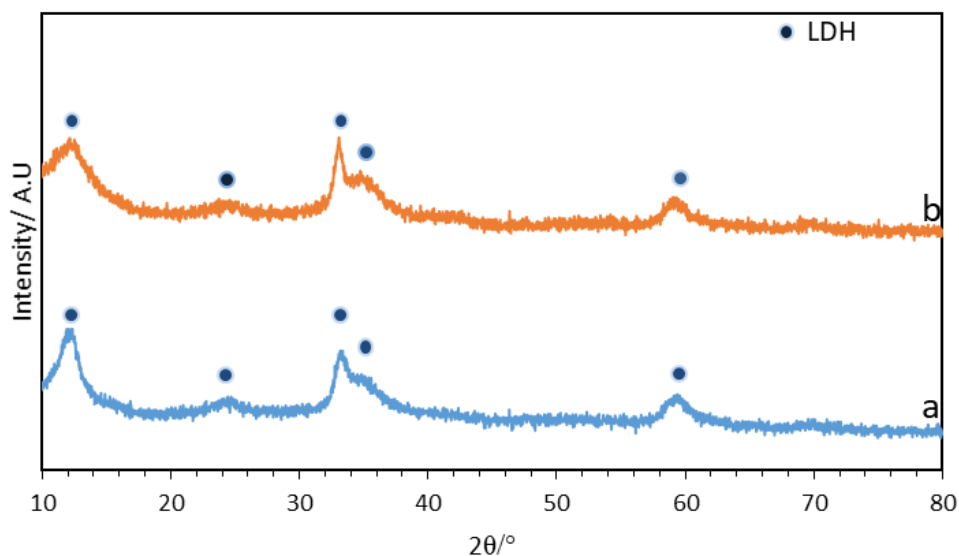


**Figure 6.8:** XRD of the 0.4:1 Cu:Zn precursor with a) rapid precipitation and b) slow injection of anti-solvent

The XRD (**Figure 6.8**) of the precursor that was formed with a slow addition of the copper acetate water anti-solvent showed the same reflection pattern that were identified as a LDH like phase ( $2\theta=12.5^\circ$  (0 0 3),  $24.6^\circ$  (0 0 6),  $33.5^\circ$ ,  $35.2^\circ$  and  $60.1^\circ$ ), which matched those of the precipitated by rapid addition, showing that the rate of addition did not alter the phase of the material.

FTIR (**Figure 6.9**) also confirmed that the same precursor was produced with the different rates of precipitation, both showing the hydroxyl peak ( $3380\text{ cm}^{-1}$ ) the metal-urea shift ( $2187\text{ cm}^{-1}$ )<sup>23</sup> the CO shift at  $1630\text{-}1650\text{ cm}^{-1}$  from urea and carboxy shifts  $1380\text{ cm}^{-1}$ . The slow precipitated copper-zinc precursor will still have some DES retained in the sample so it is likely that the precursor and the final Cu/ZnO catalyst would still have large amounts of chlorine present.

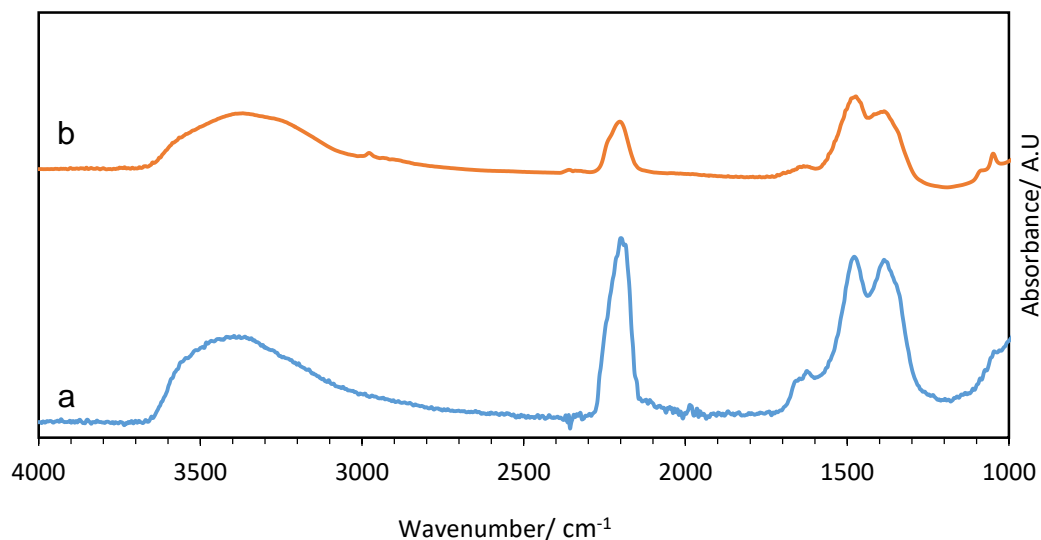


**Figure 6.9: FTIR (absorbance) of the copper-zinc precursors (0.4:1) precipitated from DES using a) fast injection and b) slow injection of the anti-solvent**

While the XRD and FTIR showed little difference between the two rates of addition, BET analysis (**Table 6.3**) of the precursors showed a rapid increase in the surface area from  $59 \text{ m}^2 \text{ g}^{-1}$  to  $212 \text{ m}^2 \text{ g}^{-1}$  demonstrating that the rate of addition of the anti-solvent to the DES had an impact on precursor morphology, without altering the phase.

**Table 6.3 BET surface area of the precursor 0.4:1 Cu:ZnO with rapid and slow precipitation**

Sample Cu:Zn	Surface area $\text{m}^2 \text{ g}^{-1}$
Fast precipitation 0.4:1	$59 (\pm 5)$
Slow precipitation 0.4:1	$212 (\pm 20)$

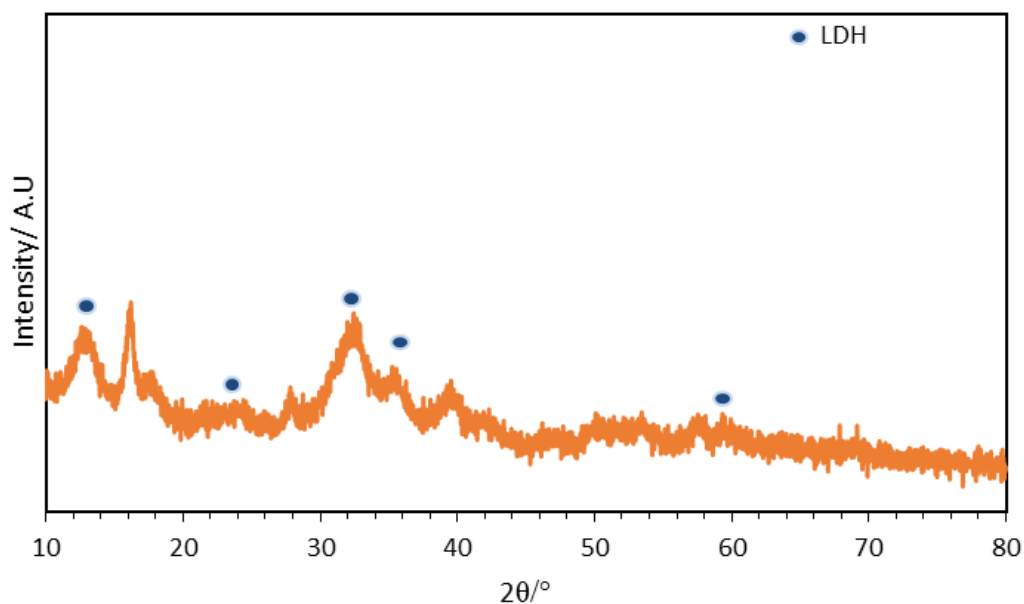


**Figure 6.10: XRD of the Cu/ZnO precursor precipitated from DES in water with copper nitrate with as Cu:Zn ratio of 1:1**

The XRD pattern of the 1:1 nitrate precursors (**Figure 6.10**) showed a pattern similar to that of the acetate precursors with the reflections that had been associated with a LDH like phase, although there is an additional reflection at  $16.2^\circ$  that is not in the acetate samples.

The XRD pattern (**Figure 6.11**) of the calcined nitrate precursor (Cu:Zn 1:1) showed a different profile from the XRD pattern seen with the calcined acetate precursors. Firstly, the CuO reflections are more intense which would suggest that like the acetate, the target ratio of Cu:Zn was not achieved at higher copper loadings. Secondly there was a higher degree of impurities indicated by the appearance of a reflection at  $2\theta=11.3^\circ$ . There had been a very weak reflection that appeared in the acetate sample in this region but is more intense in this sample which would suggest that this reflection originates from a copper based compound.

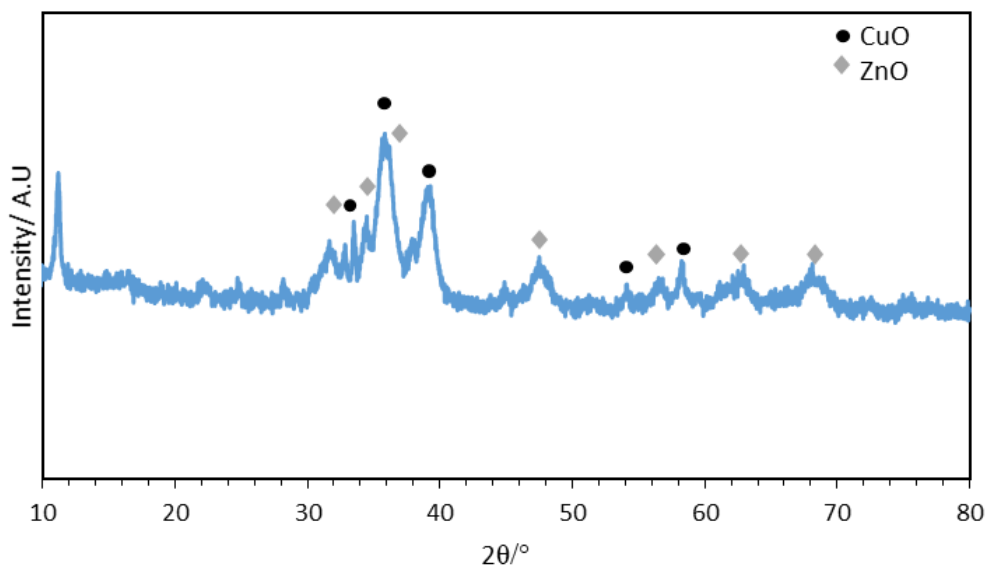


**Figure 6.11: XRD of the calcined (350 °C) CuO/ZnO (target ratio 1:1) precipitated from DES with copper nitrate**

SEM images of the precursor material (**Figure 6.12**) shows a change in the morphology between the two rates of precipitation with the slow precipitation showing flake like sheets whereas the fast precipitation formed large clusters. Since XRD and FTIR identified the two precipitates as the same phase, the difference in morphology must therefore originate with the rate of precipitation. The clustered morphology that had formed would have most likely been caused by the rapid addition/exposure to the anti-solvent whereas the slow addition of the anti-solvent allowed the formation of the flake like morphology. This rapid change in morphology reflected the BET surface area (**Table 6.3**)

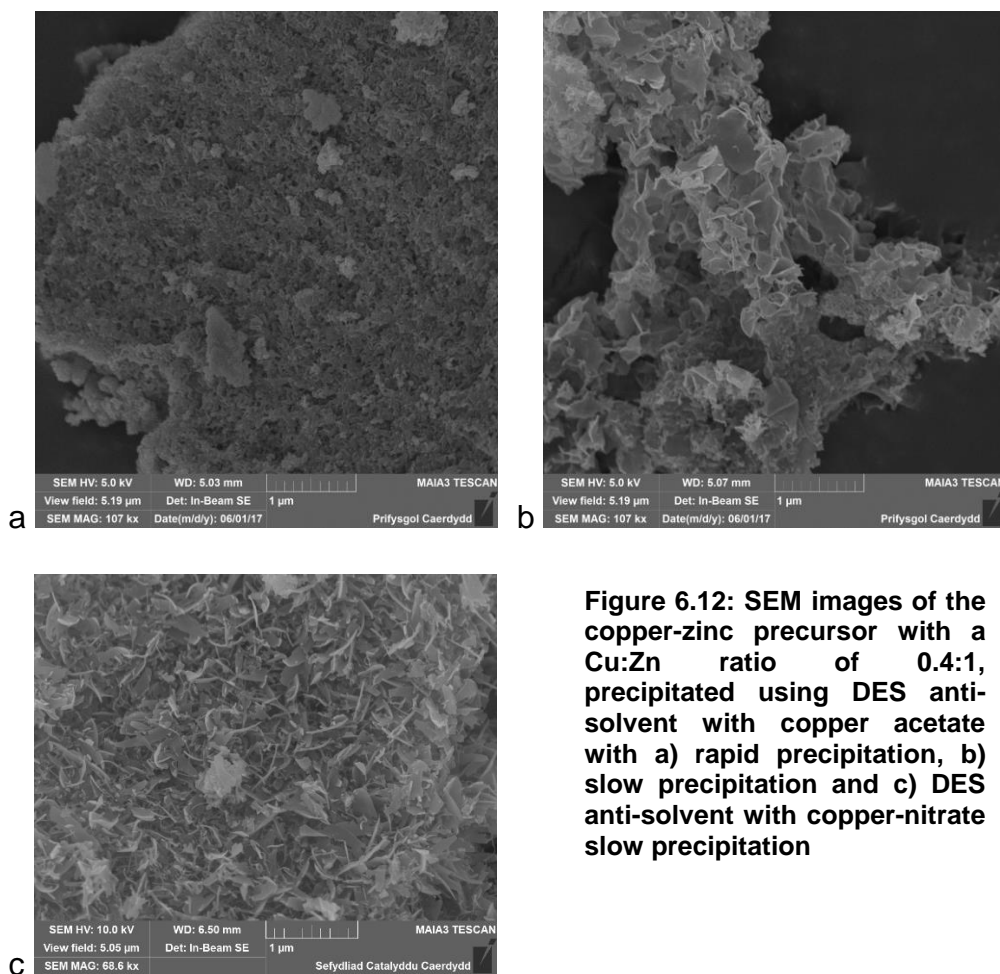


**Figure 6.12: SEM images of the copper-zinc precursor with a Cu:Zn ratio of 0.4:1, precipitated using DES anti-solvent with copper acetate with a) rapid precipitation, b) slow precipitation and c) DES anti-solvent with copper-nitrate slow precipitation**

The slow precipitated precursor had a flake like morphology similar to the platelets that hydrotalcite type materials form, which supports the XRD observation (**Figures 6.2, 6.8 and 6.10**) that these materials, resembled a hydrotalcite. The nitrates also formed a flake like morphology similar to the acetate although this may be due to the nature of a slow precipitation.

The total surface areas of the materials calcined at 350 °C (nitrate and acetate) were the same ( $43 \text{ m}^2 \text{ g}^{-1}$ ), possibly owing to a collapse in the precursor structure during calcination which means that any increase in the surface area of the precursor (**Table 6.3**) was lost. When the slow precipitated catalyst (acetates) had a lower heating rate of  $1 \text{ }^\circ\text{C min}^{-1}$  (from  $5 \text{ }^\circ\text{C min}^{-1}$ ) the surface area increased from  $43 \text{ m}^2 \text{ g}^{-1}$  to  $71 \text{ m}^2 \text{ g}^{-1}$ , which may also confirm that the precursor structure collapsed during the calcination step and lowering the heating rate would control that process resulting in an enhanced surface area. However the 1:1 Cu:Zn with the nitrate salt had a higher total surface area after calcination than the 0.4:1.

**Table 6.4: BET surface areas ( $\pm 5 \text{ m}^2 \text{ g}^{-1}$ ) of the Cu:ZnO prepared by DES anti-solvent**

Cu:Zn (target ratio)	Copper-salt precipitation rate and heating rate	BET Surface area calcined 350 °C/ $\text{m}^2 \text{ g}^{-1}$
0.4:1	Slow precipitation $1 \text{ }^\circ\text{C min}^{-1}$	71
0.4:1	Slow precipitation $5 \text{ }^\circ\text{C min}^{-1}$	43
0.4:1	Nitrate Slow precipitation $5 \text{ }^\circ\text{C min}^{-1}$	43
1:1	Nitrate slow precipitation $1 \text{ }^\circ\text{C min}^{-1}$	112

However, copper surface area of these catalyst was poor with the 0.4:1 acetate and nitrates showing,  $<1 \text{ m}^2 \text{ g}^{-1}$  of copper. Even with low copper loading these are very low values for copper surface area. The very low copper surface area might have been caused by the high concentration of chlorine present in the calcined sample, resulting in sintering during the reduction.

**Table 6.5: Copper surface area determined by  $\text{N}_2\text{O}$  chemisorption of the 0.4:1 Cu/ZnO prepared by DES (error  $\pm 0.1$ )**

Sample	Cu SSA / $\text{m}^2 \text{ g}^{-1}$
0.4:1 slow precipitation acetate	0.3
0.4:1 Fast precipitation acetate	0.2
1:1 Slow nitrate	0.6

### 6.2.3 Catalytic testing

The catalysts that were tested were the 0.4:1 Cu/ZnO from the acetate salt and 1:1 slow precipitation with copper nitrate. The catalysts prepared by the DES anti-solvent process showed low methanol yield of 0.1% and 0.1-0.25% CO<sub>2</sub> conversion (**Table 6.6**). This showed that the catalytic activity of these catalysts was very poor, even if considering the low copper loading and 100 mg of catalyst used. The most likely reason is down to two factors; firstly the presence of chlorine still present in the sample and secondly the  $<1 \text{ m}^2 \text{ g}^{-1}$  copper surface area which for methanol synthesis is an important factor. The high selectivity is generally due to the low conversion of the CO<sub>2</sub>.

Overall, despite the variation in morphology and surface area that can be achieved with DES anti-solvent, the presence of chlorine and the limitations in copper loading is too much of an issue for this method to be a viable route for the preparation of Cu/ZnO. Even using different salts and different Cu:Zn ratios did not dramatically improve catalytic performance. In fact, at lower temperatures the nitrate catalyst (with higher copper loading) performed worse than the acetate Cu/ZnO.

**Table 6.6: CO<sub>2</sub> conversion, methanol selectivity and methanol yield after 200 minutes for the Cu/ZnO (0.1 g) catalyst precipitated using DES anti-solvent method, calcined at 350 °C. Reaction performed by Dr James Hayward**

<b>Catalyst</b>	<b>Reaction temperature / °C</b>	<b>CO<sub>2</sub> conversion %</b>	<b>Methanol selectivity/ %</b>	<b>Methanol yield/ %</b>
<b>0.4:1 Cu/ZnO Acetate slow</b>	200	0.16	29.6	<0.1
	225	0.25	26.6	0.1
	250	0.05	100	0.1
<b>1:1 Cu/ZnO Nitrates slow</b>	200	0.02	100	<0.1
	225	0.04	100	0.1
	250	0.14	100	0.1

### 6.3 Switchable solvent preparation

In addition to investigating the hopcalite systems as presented in Chapter 5, the use of triethylamine-water switchable solvents was also investigated for the synthesis of other mixed metal oxide catalyst precursors to see how widely this technique could be used. The copper-zinc system was also used to investigate the use of switchable solvents for a broader range of metal oxide precursors. One advantage of using the switchable solvent system to precipitate the Cu/ZnO precursors is that it avoids the use of sodium based precipitating agents (i.e. sodium carbonate) which is commonly used in co-precipitation. Sodium is a known poison for copper-zinc oxide methanol synthesis catalyst as it increases sintering and copper size during calcination<sup>3</sup>, so the use of a system that avoids sodium is advantageous.

Two copper-zinc precursors were prepared; one precipitated in triethylamine-water under nitrogen and the other under carbon dioxide. The same basic method used for the copper-manganese precursors in Chapter 5 was used with copper-zinc precursors with an amine: water ratio of 1.14:1. Both samples were aged under carbon dioxide for 1 hour.

### 6.3.1 Characterisation

The XRD of the precursors (**Figure 6.13**) that were precipitated under both carbon dioxide and nitrogen showed reflections at  $12.8^\circ$ ,  $25.6^\circ$ ,  $32.8^\circ$ ,  $35.4^\circ$ . The reflections at  $2\theta=12.8^\circ$  and  $25.6^\circ$  (and possibly  $36.6^\circ$ ) could be assigned to a nitrate-hydroxide which shows reflections at these angles of similar intensities. Pure zinc or copper hydroxyl carbonate would show a much higher intensity around  $30-40^\circ$  than those shown here. This would suggest that the copper zinc oxide did not form a carbonate species, unlike the copper-manganese carbonate from Chapter 5 which showed the formation of malachite and manganese carbonate. Copper was known (from Chapter 5) to form a copper nitrate hydroxide when unaged and not fully washed, although the copper zinc precursor had the same washing (with water and ethanol) and aging (1 hour  $\text{CO}_2$ ) steps as per the standard copper manganese preparation.

The XRD pattern of the sample precipitated under nitrogen contained most of the reflections of the sample precipitated under carbon dioxide but also notably contained additional reflections which suggest a separate second phase that formed under the nitrogen precipitation but not the carbon dioxide precipitation. Some of these reflections such as  $2\theta=17.8^\circ$  and  $24.4^\circ$  could indicate the possible formation of a copper carbonate hydroxide. It might be the case that the sample precipitated quickly as a copper-zinc hydroxide but when precipitated under nitrogen (and switched to  $\text{CO}_2$ ) some of the copper had a delayed precipitation resulting in the formation of malachite under the  $\text{CO}_2$  atmosphere.

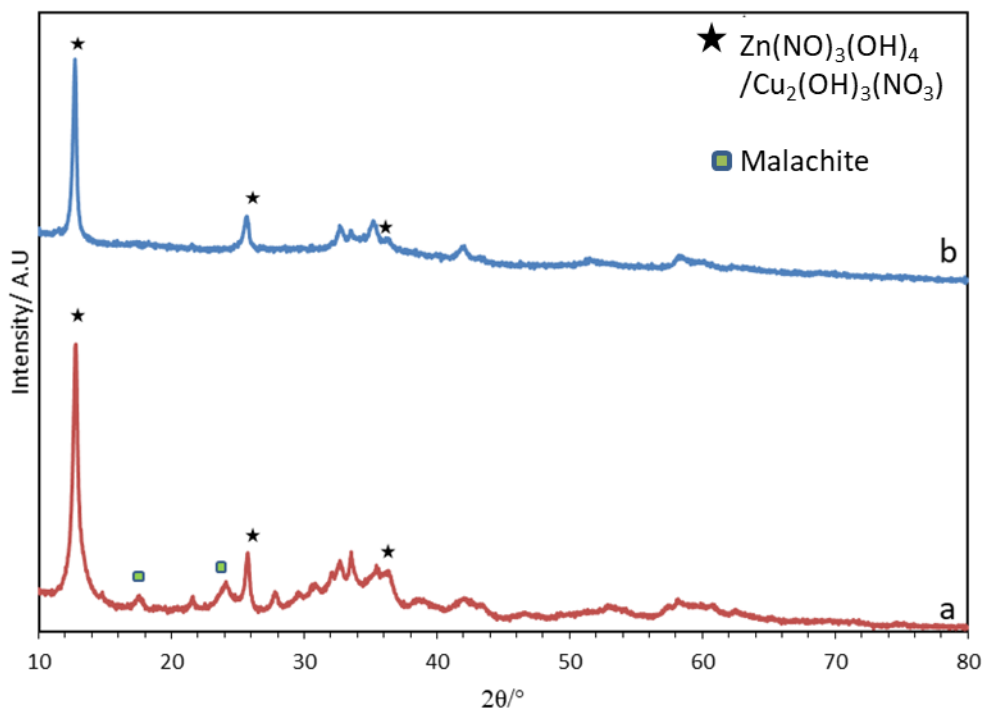


**Figure 6.13: XRD of the precursor precipitated in the switchable solvent under a) nitrogen and b) carbon dioxide**

The FTIR of the two precipitates (**Figure 6.14**) showed matching peaks at  $3330\text{ cm}^{-1}$  (O-H),  $1033\text{ cm}^{-1}$  and  $831\text{ cm}^{-1}$ , although the sample precipitated under carbon dioxide showed a broad vibration at  $1382\text{ cm}^{-1}$  and a smaller vibration at  $1471\text{ cm}^{-1}$ . The sample precipitated under nitrogen showed multiple vibrational peaks in this region at  $1340\text{ cm}^{-1}$ ,  $1350\text{ cm}^{-1}$  and  $1512\text{ cm}^{-1}$ . These additional vibrational shifts match those seen in the FTIR of malachite formed from copper nitrate in the switchable solvent (**Figure 5.5** in Chapter 5).

The FTIR and XRD results both suggest the formation of phase separated copper (possibly in the malachite form) and zinc nitrate during precipitation under the nitrogen atmosphere and a more phase integrated copper zinc precursor under carbon dioxide precipitation.

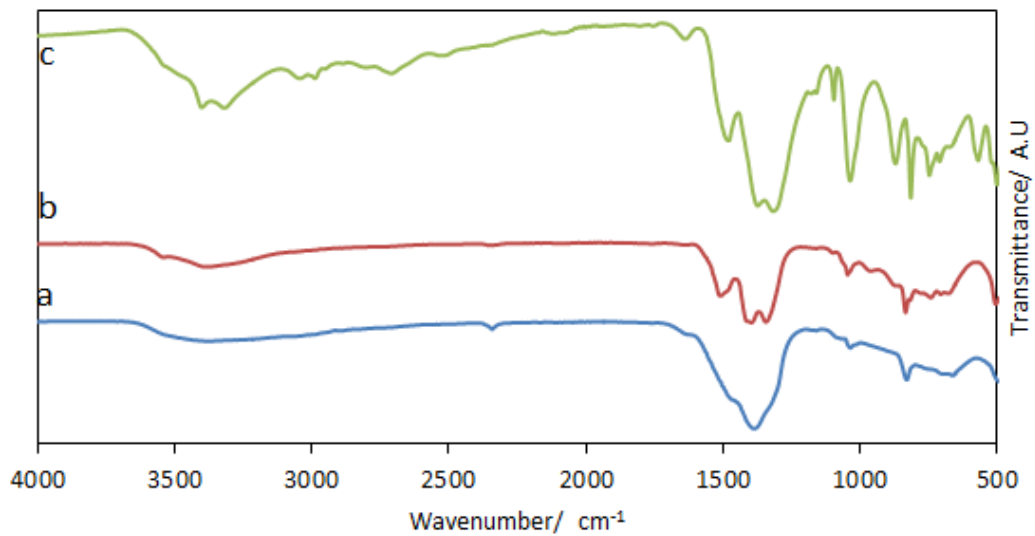


**Figure 6.14:** FTIR of the copper-zinc precipitate formed using switchable solvent under a) carbon dioxide, b) nitrogen atmosphere and c) copper carbonate precipitated under carbon dioxide

The TGA analysis both of the copper-zinc precursors (**Figure 6.15**) showed a different profile between the two precipitation atmospheres. The sample precipitated under carbon dioxide showed three mass losses; a minor mass loss at 160 °C followed by a large mass loss at 220 °C and a minor mass loss at 400-450 °C. The sample precipitated under nitrogen showed only two large mass losses at 160 °C and 250 °C. There was also a difference in the final mass of the two samples, with the carbon dioxide precipitated sample having 46 % mass loss after 500 °C compared to the 36 % for nitrogen precipitated sample.

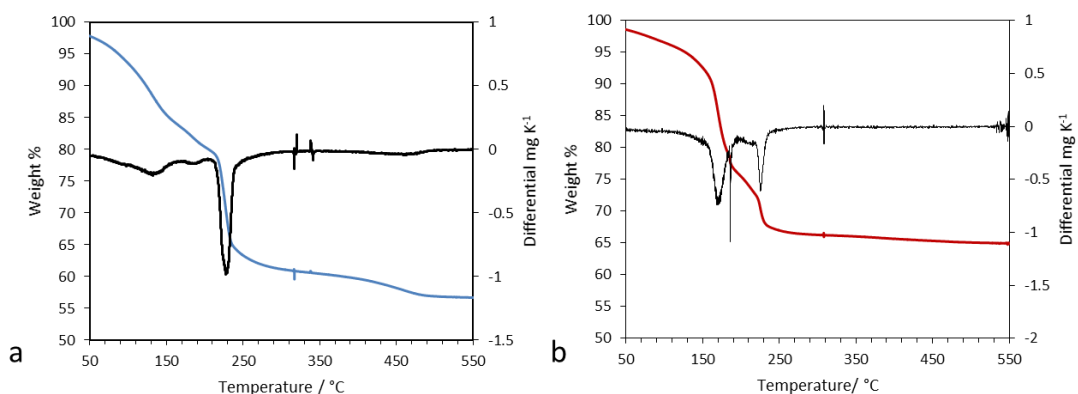


**Figure 6.15:** TGA profile for copper-zinc precursors precipitated under a) carbon dioxide and b) nitrogen

This difference in mass loss between the precipitates formed under CO<sub>2</sub> and N<sub>2</sub> suggests along with the XRD and FTIR data that the precursors are somewhat different. The sample precipitated under nitrogen showing a larger mass loss at 168 °C which had also been observed with the hopcalite samples (Chapter 5) that still had nitrate species present. This would corroborate with the nitrate hydroxide reflections observed in the XRD patterns. The two-part decomposition of the nitrogen precipitated sample compared to the one-part decomposition of the carbon dioxide precipitated sample would support the formation of two species in the precursor formed under nitrogen. In addition the temperature of range of the first mass loss (160-185 °C) is in the same temperature range as the pure copper precursor (Figure 5.5 in Chapter 5).

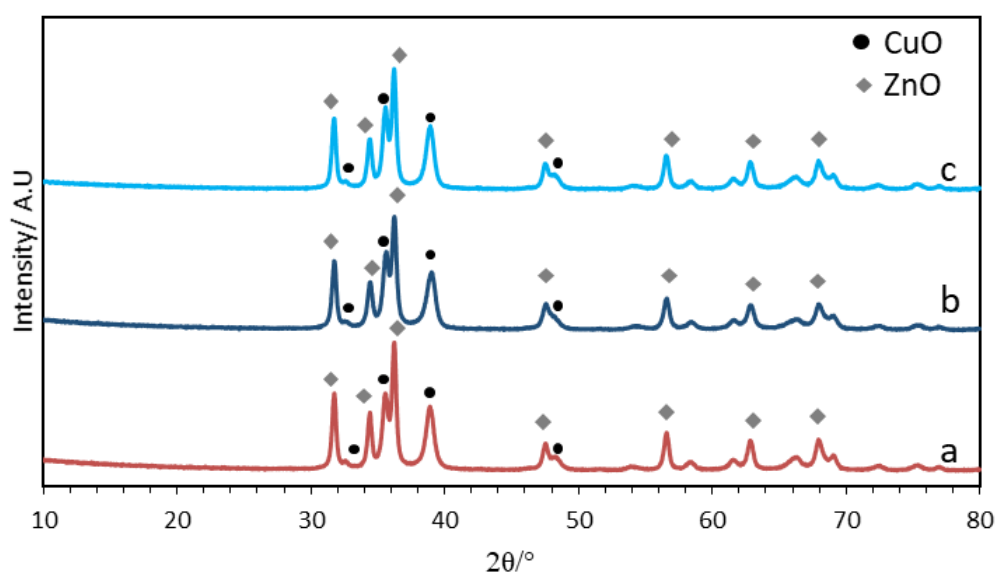


**Figure 6.16:** XRD of the calcined copper-zinc oxides a) precipitated under nitrogen calcined 250 °C, b) precipitated under carbon dioxide calcined 250 °C and c) carbon dioxide calcined 350 °C

The XRD pattern of the samples (Figure 6.16) after calcination at both 250 °C and 350 °C showed the reflections for both copper oxide and zinc oxide. The samples were shown to form crystalline CuO and ZnO phases as low as 250 °C, although the nitrogen precipitated sample was shown to have a higher ZnO crystallite size (Table 6.7) at 250 °C than the carbon dioxide precipitated samples calcined at 250 °C or 350 °C.

**Table 6.7: BET surface areas and crystallite size of the CuO/ZnO precipitated using switchable solvent (calcined at 250-350 °C)**

Sample	Surface area / $\text{m}^2 \text{g}^{-1}$ ( $\pm 2 \text{ m}^2 \text{g}^{-1}$ )	Crystallite size copper at $2\theta=38.96^\circ / \text{nm}$ ( $\pm 2 \text{ nm}$ )	Crystallite size zinc at $2\theta=56.52^\circ / \text{nm}$ ( $\pm 2 \text{ nm}$ )
Carbon dioxide calcined 250 °C	23	12.1	17.9
Carbon dioxide calcined 350 °C	19	12.4	22.1
Nitrogen calcined 250 °C	26	12.2	24.1

The SEM of the sample precipitated under carbon dioxide (**Figure 6.17 a**) showed that this sample has a somewhat different morphology from the sample previously seen with the DES anti-solvent precipitates or the copper manganese carbonate formed by switchable solvents. A more random and jagged structure was formed with some areas showing what appear to be small needles. The variations of shapes in this sample showed that the morphology was not homogeneous throughout.

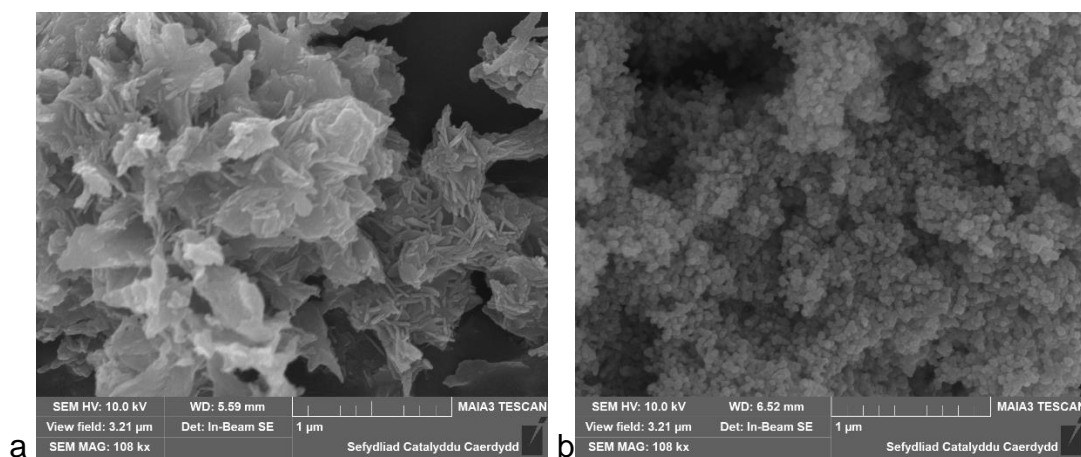


**Figure 6.17: SEM of the a) copper-zinc precursor precipitated by switchable solvents under carbon dioxide and b) calcined at 350 °C to form the CuO/ZnO**

However, the SEM of the sample after calcination (**Figure 6.17 b**) showed that this structure had collapsed and formed small rounded crystallites like those seen with the DES precipitated CuO/ZnO calcined at the same temperature. EDX mapping (**Figure 6.18**) of the sample (calcined 350 °C) showed that the

copper and zinc were evenly distributed with no sign of isolated zinc or copper clusters. This is in contrast to the EDX mapping of the copper-manganese oxide catalyst in Chapter 5, which showed clusters of isolated copper as well as mixed copper manganese.

EDX analysis determined a Cu:Zn ratio (by mass) of 38:33 which would give a molar ratio of 1.16:1 Cu:Zn which suggest a slight excess of copper formation but close to the target ratio, unlike the DES 1:1 Cu:Zn samples which had a massive excess of copper at this ratio. Another region showed 0.92:1 Cu:Zn showing that at least from surface analysis the Cu:Zn ratio is close to the target value but the distribution of copper and zinc may vary within the bulk sample.

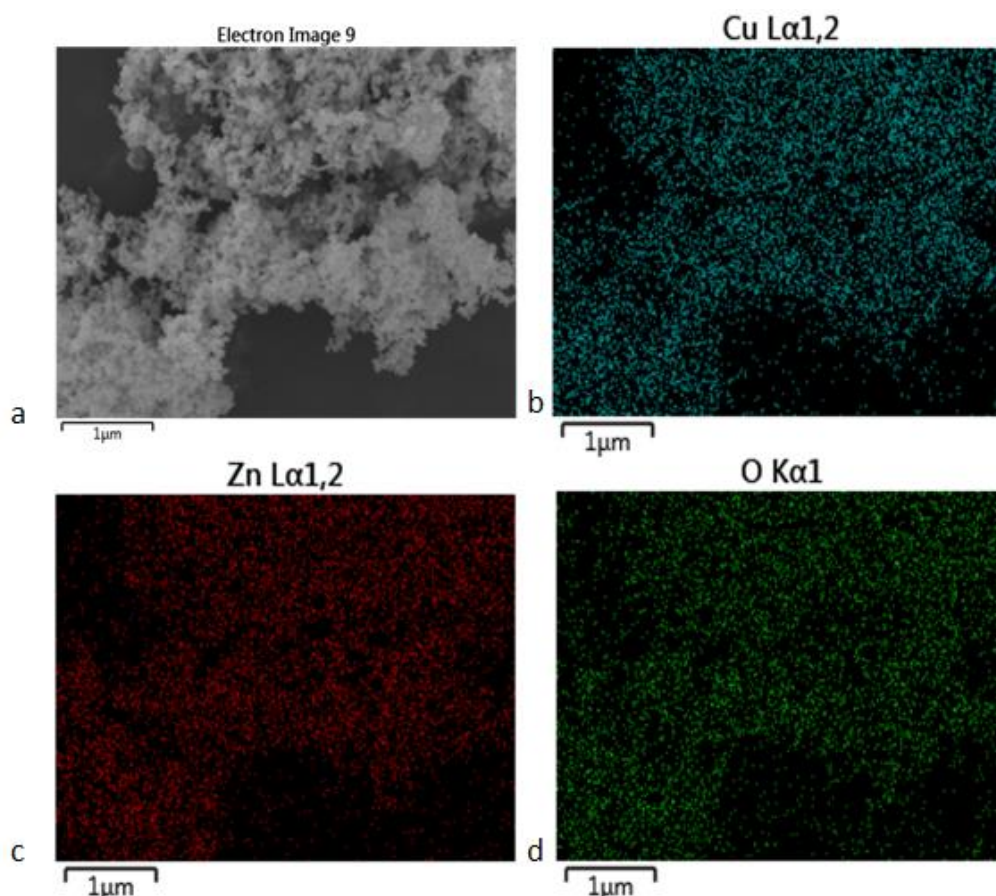


**Figure 6.18:** a) SEM scan of the CuO/ZnO calcined at 350 °C from the sample precipitated under carbon dioxide and EDX mapping of b) copper, c) zinc and d) oxygen

### 6.3.2 Catalyst testing

The Cu/ZnO precipitated using switchable solvents were shown to be active for methanol synthesis, unlike the DES sample which showed near very little conversion and 0.1% methanol yield at 250 °C. All products observed were methanol or CO with no other side products being detected.

The switchable solvent precipitated catalyst showed (**Table 6.8**) a reasonable methanol yield of up to 2.1 %. Out of the three catalysts the CO<sub>2</sub> precipitated catalyst calcined at 350 °C was shown to be the least active, which was expected as this was calcined at a higher temperature and sintering would have occurred. The nitrogen precipitated sample appeared to have a slightly better CO<sub>2</sub> conversion and methanol yield but lower selectivity (at 200 °C and 225 °C) than the carbon dioxide precipitated sample, although the decrease in selectivity would be an effect of increased activity of the catalyst (forming CO as a by-product).

Otherwise, the two catalysts (precipitated under carbon dioxide and nitrogen and aged for 1 hour) calcined at 250 °C showed similar performance at all three temperatures after 200 minutes. In terms of stability the catalyst precipitated under CO<sub>2</sub> did show a slight deactivation between 25 and 200 minutes at 200 °C while the catalyst precipitated under nitrogen showed a higher degree of stability at all temperatures with no drop in the methanol yield with time, although there was a decrease in methanol selectivity with a slight increase in CO<sub>2</sub> conversion after 20 minutes. At 225 °C and 250 °C the nitrogen precipitated catalysts showed higher CO<sub>2</sub> conversion, methanol yield and selectivity after both 25 and 200 minutes compared to the CO<sub>2</sub> precipitated catalysts.

In comparison to published results<sup>3</sup> using copper zinc catalysts prepared by supercritical anti-solvent, the catalyst prepared by switchable solvents had a slightly lower conversion and methanol yield than the supercritical anti-solvent (SAS) precipitated catalysts. Notably sodium free SAS Cu/ZnO had a methanol yield of 2.9% with MeOH selectivity of 67% compared to yield of 2.2% and MeOH selectivity of 43-45% with the switchable catalysts.

However it should be noted that the switchable catalysts only had 1:1 Cu:Zn ratio compared than 2:1 Cu:Zn of the SAS catalysts as well as having a higher flow rate (25 ml min<sup>-1</sup> used with switchable solvents compared with 6.25 ml min<sup>-1</sup> with SAS catalysts). In addition these catalysts have not been optimised, opening the possibility of making more active catalysts in future studies.

**Table 6.8: CO<sub>2</sub> conversion, methanol selectivity and methanol yield after 25 and 200 minutes (after each temperature ramp) for the Cu/ZnO (0.1 g) catalyst precipitated using switchable solvents (calcined 250-350 °C). Reaction performed by Dr James Hayward**

Catalyst	Reaction temperature / °C	CO <sub>2</sub> conversion / % (±1 %)		Methanol selectivity/ % (±1 %)		Methanol yield/ % (±0.1)	
		25 mins	200 mins	25 mins	200 mins	25 mins	200 mins
Cu/ZnO	200	2.9	3.2	68.6	62.2	2.0	2.0
	225	5.2	5.2	43.1	42.1	2.2	2.2
Nitrogen 250 °C	250	10.7	10.7	19.3	19.6	2.1	2.1
Cu/ZnO  Carbon dioxide 250 °C	200	2.8	2.6	71.0	68.5	1.9	1.8
	225	4.6	4.6	45.8	45.3	2.1	2.1
	250	9.3	10.8	20.8	18.2	1.9	2.0
Cu/ZnO  Carbon dioxide 350 °C	200	2.3	2.1	56.4	60.0	1.3	1.3
	225	3.8	3.5	43.5	44.0	1.6	1.5
	250	6.9	7.1	21.3	24.2	1.5	1.7

## 6.4 Chapter 6 Conclusions

This chapter looked into the use of DES and switchable solvents to prepare Cu/ZnO catalysts for methanol synthesis. The DES anti-solvent method was shown to be able to prepare Cu/ZnO precursors with different morphologies and in some cases a high BET surface areas, although there was a limit in the Cu:Zn target ratio that could be achieved.

Although the copper zinc oxide could be formed with high surface area precursors the amount of choline present in the sample even after washing and the limitation on the copper loading before massive amount of zinc loss, make this method not viable for copper-zinc oxide preparation at least as a catalyst. Variations to improve the method including different salts and Cu:Zn ratios did not result in an improvement in the poor catalytic performance. The use of at least 3 litres of deionised water did not remove the chlorine. The use of choline chloride-urea DES for anti-solvent Cu/ZnO catalyst preparation is hard to justify further research. In addition, the process resulted in very low Cu surface area which would make any additional washing (after calcination) useless as these catalysts would generally be inactive.

However, the switchable solvent precipitated copper-zinc oxide catalysts have shown some degree of promise. These catalysts showed reasonable methanol yield, despite the process not being fully optimised. Like the hopcalite catalysts shown in Chapter 5, changing the atmosphere of precipitation had some effect on the precursor material with precipitation under a nitrogen atmosphere resulting in a slightly more active catalyst.

## 6.5 Chapter 6 Future work

The work here has demonstrated that, while choline chloride-urea DES can be used to prepare Cu/ZnO precursor the amount of residual chlorine as well as a breakdown in the Cu:Zn ratio at higher copper loadings, makes this method not viable for the preparation of copper-zinc catalysts. However, this does not mean that DES should be avoided or even to that matter choline chloride based DES. In fact, Chapter 3 had previously demonstrated that some precipitates such as cobalt oxalate could be prepared with no or very little chlorine present even though choline chloride oxalic acid was used. There are also a wide variety of DES that do not contain choline chloride<sup>24</sup> and could be used as alternative to prepare Cu/ZnO.

This chapter has shown that switchable solvents can be used to make Cu/ZnO catalysts that are active for methanol synthesis. However, this was only a preliminary study to demonstrate that it was possible to use the technique to prepare these catalyst and as such the condition have not been optimised. There are a number of parameters that can be altered that can improve the technique to prepare more active catalysts.

Another factor that should be considered when preparing these catalysts with switchable solvents is the aging. Aging had been shown to be an important parameter for the preparation of copper-zinc carbonate precursors in co-precipitation<sup>25</sup> and the use of different aging times should be performed to see the effect on the catalyst. Chapter 5 showed that the aging time affected the copper-manganese carbonate under the switchable solvents and therefore the effect on copper-zinc carbonate could be another area of investigation that could potentially increase the activity of these catalysts.

As well as the aging time, the aging atmosphere could also be investigated as it was in Chapter 5. Previous research into aging of copper-zinc carbonates under different atmospheres showed a change in catalytic activity for CO oxidation<sup>26</sup> and therefore investigation of copper-zinc under different atmospheres should be investigated with the switchable solvents.

## 6.6 Chapter 6 Reference

1. P. J. Smith, S. A. Kondrat, J. H. Carter, P. A. Chater, J. K. Bartley, S. H. Taylor, M. S. Spencer and G. J. Hutchings, *ChemCatChem*, 2017, **9**, 1621-1631.
2. P. Kowalik, K. Antoniak-Jurak, W. Prochniak, P. Wiercioch, M. Konkol, R. Bicki, K. Michalska and M. Walczak, *Catalysis Letters*, 2017, **147**, 1422-1433.
3. S. A. Kondrat, P. J. Smith, J. H. Carter, J. S. Hayward, G. J. Pudge, G. Shaw, M. S. Spencer, J. K. Bartley, S. H. Taylor and G. J. Hutchings, *Faraday Discussions*, 2017, **197**, 287-307.
4. S. S. Dang, H. Y. Yang, P. Gao, H. Wang, X. P. Li, W. Wei and Y. H. Sun, *Catalysis Today*, 2019, **330**, 61-75.
5. M. J. L. Gines, N. Amadeo, M. Laborde and C. R. Apesteguia, *Applied Catalysis A-General*, 1995, **131**, 283-296.
6. M. Behrens, *Angewandte Chemie - International Edition*, 2014, **53**, 12022-12024.
7. G. Prieto, K. P. de Jong and P. E. de Jongh, *Catalysis Today*, 2013, **215**, 142-151
8. S. A. Kondrat, P. J. Smith, P. P. Wells, P. A. Chater, J. H. Carter, D. J. Morgan, E. M. Fiordaliso, J. B. Wagner, T. E. Davies, L. Lu, J. K. Bartley, S. H. Taylor, M. S. Spencer, C. J. Kiely, G. J. Kelly, C. W. Park, M. J. Rosseinsky and G. J. Hutchings, *Nature*, 2016, **531**, 83-87.
9. M. S. Spencer, *Catalysis Letters*, 2000, **66**, 255-257.
10. S. A. Kondrat, P. J. Smith, L. Lu, J. K. Bartley, S. H. Taylor, M. S. Spencer, G. J. Kelly, C. W. Park, C. J. Kiely and G. J. Hutchings, *Catalysis Today*, 2018, **317**, 12-20.
11. P. Kowalik, K. Antoniak-Jurak, R. Bicki, W. Prochniak, P. Wiercioch and K. Michalska, *International Journal Hydrogen Energy*, 2019, **44**, 913-922.
12. M. Behrens, D. Brennecke, F. Girgsdies, S. Kissner, A. Trunschke, N. Nasrudin, S. Zakaria, N. F. Idris, S. B. Abd Hamid, B. Kniep, R. Fischer, W. Busser, M. Muhler and R. Schlogl, *Applied Catalysis A-General*, 2011, **392**, 93-102.
13. O. S. Hammond, K. J. Edler, D. T. Bowron and L. Torrente-Murciano, *Nat. Commun.*, 2017, **8**, 7.
14. J. Y. Dong, W. H. Lin, Y. J. Hsu, D. S. H. Wong and S. Y. Lu, *Crystengcomm*, 2011, **13**, 6218-6222.
15. A. P. Abbott, G. Capper, D. L. Davies, K. J. McKenzie and S. U. Obi, *Journal of Chemical Engineering Data*, 2006, **51**, 1280-1282.
16. A. P. Abbott, G. Capper, D. L. Davies, R. K. Rasheed and P. Shikotra, *Inorganic Chemistry*, 2005, **44**, 6497-6499.
17. A. Abo-Hamad, M. Hayyan, M. A. AlSaadi and M. A. Hashim, *Chemical Engineering Journal*, 2015, **273**, 551-567.
18. J. Y. Dong, Y. J. Hsu, D. S. H. Wong and S. Y. Lu, *Journal of Physical Chemistry C*, 2010, **114**, 8867-8872
19. Y. H. Lu, W. H. Lin, C. Y. Yang, Y. H. Chiu, Y. C. Pu, M. H. Lee, Y. C. Tseng and Y. J. Hsu, *Nanoscale*, 2014, **6**, 8796-8803.

20. F. D. Velazquez-Herrera, G. Fetter, V. Rosato, A. M. Pereyra and E. I. Basaldella, *Journal of Environmental Chemical Engineering*, 2018, **6**, 3376-3383.
21. D. L. Li, Y. B. Cai, Y. Y. Ding, R. L. Li, M. M. Lu and L. L. Jiang, *International Journal of Hydrogen Energy*, 2015, **40**, 10016-10025.
22. X. Ge, C. D. Gu, X. L. Wang and J. P. Tu, *Journal of Colloid and Interface Science*, 2015, **454**, 134-143.
23. Q. Wang, X. Q. Yao, Y. R. Geng, Q. Zhou, X. M. Lu and S. J. Zhang, *Green Chemistry*, 2015, **17**, 2473-2479
24. Y. T. Dai, J. van Spronsen, G. J. Witkamp, R. Verpoorte and Y. H. Choi, *Journal of Natural Products*, 2013, **76**, 2162-2173.
25. C. Baltes, S. Vukojevic and F. Schuth, *Journal of Catalysis*, 2008, **258**, 334-344.
26. A. A. Mirzaei, H. R. Shaterian, S. H. Taylor and G. J. Hutchings, *Catalysis Letters*, 2003, **87**, 103-108.

## **Chapter 7 Overall Conclusions and Future Work**

The aim of this thesis was to find alternative methods of preparing metal oxides or metal oxide precursors to the energy intensive supercritical anti-solvent process, to produce highly active catalysts with properties such as tailored morphology or high surface areas that cannot easily be achieved through conventional methods. This work explored switchable solvents, hydrothermal synthesis and deep eutectic solvents as possible alternatives.

### **7.1 Conclusions**

#### **7.1.1 Deep eutectic solvents for metal oxide preparation**

The use of choline chloride based deep eutectic solvent (DES) with different anti-solvents mixtures was explored as a novel method to prepare cobalt, manganese and iron oxalates, with the aim of using the technique to tailor the morphologies of these materials to enhance their catalytic activity. This method comprised of dissolving the metal salt/precursor in the choline chloride-oxalic acid DES and then precipitating the metal oxalate through a controlled anti-solvent precipitation.

For cobalt oxalate, anti-solvent mixtures such as water and water-alcohol resulted in the formation of 1-D rod like morphologies. When using the ethanol-water anti-solvent the cobalt oxalate needles were longer and thinner compared to when a pure water anti-solvent was used. The requirement of water in the anti-solvent process was shown to be an important factor when precipitating the cobalt oxalate from the DES as demonstrated when using pure ethanol or methanol.

The cobalt oxides derived from the DES route were shown not to be as active for propane oxidation as cobalt oxide made from supercritical anti-solvent (SAS) precipitation, but were shown to be more active than calcined cobalt

acetate. The use of different anti-solvents was demonstrated to make some difference to the surface area, crystallinity and propane oxidation activity of the sample, although this was not as significant as the calcination temperature and conditions used to make the oxide from the oxalate.

This method showed differences in the precipitation when other metals were added which resulted with alternative morphologies being observed. It was also shown that the precursor salt caused variations in morphology and activity. The use of the technique to prepare iron oxalate was shown to result in iron oxides with a linear rod-like formation as observed for cobalt although the iron oxides had a higher surface area of up to  $221 \text{ m}^2 \text{ g}^{-1}$ .

The method was also viable for making mixed metal oxide precursors as demonstrated with cobalt-manganese and iron-manganese oxalate. The characterisation of these materials using X-ray diffraction and temperature programmed reduction showed that there was some extent of phase integration which contributed to the increase in propane oxidation at lower temperature compared to the single metal oxides.

However, it should be noted that there are several downsides to this technique. Firstly, it relies on the metal that is being precipitated with some metals (cobalt and iron) precipitating as linear needles or rods but manganese oxalate forming different morphology. This may be due to the possibility that the nature of the DES may be changed when larger concentrations of metal salts are dissolved, but further studies would be required to prove this.

Secondly some metal oxides such as iron oxide were shown by X-ray photoelectron spectroscopy to have retained the chlorine after calcination and therefore would require more washing steps to remove this. However it should be noted that cobalt and manganese showed no indication of chlorine after precipitation and calcination.

However, despite these disadvantages the method has been demonstrated as a novel route to make metal oxalate precursors and the few parameters that were changed were shown to have an impact on the morphology and

surface area of the metal oxide catalysts. This, therefore, demonstrates a novel route for making metal oxalates that can be tailored and is an avenue that should be further explored beyond this work.

The use of DES for copper-zinc oxide preparation, however, showed the major disadvantage of using DES for preparation of catalyst. The method had problems in several areas, notably loss of zinc at higher Cu:Zn ratios and excess chlorine in the catalysts even after calcination, which resulted in catalysts with very low Cu surface area and almost completely inactive.

### **7.1.2 Crednerite as a hopcalite precursor**

Chapter 4 had demonstrated that while crednerite is a poor CO oxidation catalyst it does provide an interesting alternative as a precursor to the spinel phase copper-manganese oxide. The crednerite based spinel catalysts were different to conventionally prepared hopcalite in that hopcalite materials are usually prepared from soluble metal salt. It has been shown that the non-crystalline hopcalite is the most active but all of the crednerite derived catalysts were all crystalline since crednerite itself was a crystalline phase. Although these catalysts had a lower initial CO conversion at 20 °C they retained a stable activity in the first 30 minutes compared to co-precipitated catalysts, which rapidly dropped in activity. However, they showed possible deactivation at higher temperatures and longer time periods with CO conversion halved in repeat tests, possibly owing to change in surface composition seen by XPS. However, these catalysts showed the same CO conversion whether or not they were pre-treated under N<sub>2</sub> before the reaction.

The use of crednerite as a hopcalite precursor was shown to not only be a viable alternative to make spinel phase copper-manganese oxides but also produced hopcalite catalyst that differed in behaviour from the conventional co-precipitated catalysts as well as taking a somewhat different approach to what has previously been taken with preparation of hopcalite material by using

a crystalline phase as a precursor. This demonstrated that, although hydrothermal synthesis has been around for a long time, it still has major advantages and uses as a method for the preparation of metal oxides compared to precipitation based methods.

### **7.1.3 Switchable solvents for hopcalite and copper zinc oxide**

It was demonstrated that the switchable solvent mixture of triethylamine and water, could be utilised to precipitate both single copper and manganese carbonate and mixed copper-manganese carbonate and copper-zinc carbonate precursors. The calcined copper-manganese oxides had a high surface area, CO oxidation activity and morphology similar to the precursor/catalyst prepared by SAS precipitation and in some cases was shown to have a superior surface area and CO oxidation activity than the SAS prepared catalyst. It was also showed that variations in the method including amine: water ratio (volume), metal salt and aging all had an effect on the elemental mixing, surface and catalytic activity of the final catalyst.

Like co-precipitation the use of triethylamine required both washing and drying steps to remove nitrates and triethylamine. It was observed that residual metal nitrates were present in the precursor when the washing step was not performed which resulted in a lower surface area copper-manganese oxide catalyst that had a lower CO oxidation activity. It should be considered that SAS precipitation, although an energy intensive process, does eliminate the use of a precipitating agent (such as sodium carbonate)<sup>1, 2</sup>, which reduces the possibility of poisoning and the need for washing steps. Switchable solvents however offered a potential alternative without the need for high pressure and that hinders the potential for scale up.

The method also worked for copper-zinc oxide preparation and although this was only an initial investigation, the catalysts formed using the switchable solvent methodology were shown to have reasonable methanol production activity. This is despite only having 1:1 Cu:Zn ratio and not being fully

optimised, especially when compared to those prepared by the DES anti-solvent method. This shows that the switchable solvent methodology can be used not only for hopcalite but for other catalysts was well.

As well as the requirement of washing step and drying steps needed to remove excess nitrates there are several disadvantages with the technique. There is a possibility of the loss of triethylamine due to its high vapour pressure during the degassing of  $N_2/CO_2$  during the switching. The method used created a lack of control in the precipitation or the pH of the solution. However, like the DES methodology this was an initial investigation and further development could improve and eliminate these problems, and the method overall has shown to be a viable alternative to supercritical anti-solvent for the application in metal oxide preparation.

#### **7.1.4 Overall conclusions**

This thesis has looked into a diverse range of methods for preparing different catalysts, each one with its merits and disadvantages. The key points outlined in the introduction and aims was to investigate these methods for the application in preparing catalyst that have equally or ideally superior catalytic activity to those prepared by supercritical anti-solvent and co-precipitation. To this extent, switchable solvents have achieved this goal, notably, when used for the preparation of copper-manganese oxide catalysts which were shown to have equal or superior ambient temperature CO oxidation activity than the reference supercritical anti-solvent precipitated catalysts. While deep eutectic solvents did not fully achieve this, it was demonstrated that they can be utilised as a method for making metal oxides with tailorable morphologies and is a method that, with further expansion has the potential of making highly active metal oxide catalysts. However, there are some DES and metal combinations such as the preparation of Cu/ZnO where this method is not viable.

The key factors that were highlighted for the solvent systems in this work were the effect of residual solvent present after the formation of the metal precursor precipitated. This factor was prevalent when using choline chloride based deep eutectic solvents since the residual chlorine was found from XPS to be retained in some catalysts even after calcination, most notably in the Cu/ZnO catalysts in Chapter 6 prepared by choline chloride-urea. This resulted Cu/ZnO with very poor catalytic activity although other problems associated with this method also contributed to this.

Likewise, iron oxide prepared by DES-oxalate method was found to have retained chlorine although in this case it was found to have not been as much of a problem as Cu/ZnO. However, cobalt oxide prepared with choline chloride-oxalic acid did not show signs of residual chlorine in the final catalysts, demonstrating that not all choline chloride-based DES methods retain chlorine in the final catalyst. This problem was not found to be an issue with the triethylamine switchable solvents, with little indication of residual switchable additive, although some metal nitrates could be retained if the precipitate was not extensively washed. The possibility of retaining residual solvent was one of the factors considered when choosing a switchable additive and the requirement of extensive washing. This is often a factor that is not fully considered or mentioned by research publications on the use of these solvents for novel preparation but it is none the less a highly important one.

## 7.2 Future work expansion of deep eutectic solvent, hydrothermal and switchable solvent systems

This work has shown that a number of different metal oxide catalysts could be prepared using alternative techniques such as switchable solvents or deep eutectic solvents. However, some of the methods used for preparing metal oxides with these techniques, notably the switchable solvent and DES-oxalate based methods were novel preparation methods and as such this work only explored the initial preparation and testing for a few selected metal oxides, suitable reactions and limitations in the parameters that were varied.

Variations in the DES oxalate method such as temperature at which the DES-oxalate mixture was maintained at or the use of other anti-solvent mixtures (such as ethylene glycol) as well as applying this method under hydrothermal conditions in an autoclave are parameters that could have an impact on the morphology and surface area of the cobalt oxalate precursor which could increase their activity.

Application of these DES-oxalate derived oxides as supports is a possible area where the tailorable morphology properties may be more advantageous, as well as the high surface area iron oxide that resulted from this preparation could make a good support for gold nanoparticles<sup>3</sup>.

While the use of choline chloride-urea deep eutectic solvent resulted in inactive Cu/ZnO catalysts, this does not mean that all DES are problematic for the application in Cu/ZnO preparation. There are a whole variety of deep eutectic solvents and choline based ionic liquids already published in the literature. Examples of DES that eliminate choline chloride that could be utilised as a solvent or as soft templating include dimethylurea-citric acid mixture. In addition, there are other choline based ionic liquids notably choline carboxylates that could eliminate the problem of choline chloride and these ionic liquids have much simpler preparation techniques compared to the imidazolium based ionic liquids. These alternatives could be useful solvents for metal oxide preparation<sup>4</sup>.

The use of hydrothermal synthesis to make crednerite as a precursor formed a copper-manganese oxide catalyst with properties that differed from that of conventional hopcalite. Although this work demonstrated that the use of  $\text{CuMnO}_2$  as an interesting precursor to spinel phase  $\text{Cu}_{1.5}\text{Mn}_{1.5}\text{O}_4$  catalysts, there are a variety of copper based delafossites that could also be applied to CO oxidation or other reactions. In fact, there has recently been publication in the application of copper based delafossite in heterogeneous catalysis most notably  $\text{CuFeO}_2$  as a precursor to a Fischer-Tropsch catalyst<sup>5</sup>.

In addition, the use of gold and cobalt doped on co-precipitated hopcalite has been reported to enhance these catalysts for CO oxidation<sup>6, 7</sup> and doping these metals onto crednerite derived hopcalite would be another area to investigate how these differ from conventional co-precipitate hopcalite.

The synthesis of metal oxides with switchable solvents is perhaps the area that has both the largest potential and the area that has been used the least in the field of metal oxide preparation and therefore the area with the greatest potential for expansion. While the use of TEA-water based switchable hydrophilic-hydrophobic solvents can be used for other single and mixed metal oxides such as cobalt, iron and nickel, there are a whole variety of switchable solvents that had been discovered<sup>8</sup>, some of which may provide better Cu/Mn mixing and eliminate the problems of excess nitrates being retained in the precursor. In addition, it had already been demonstrated that using a metal nitrate or a metal acetate salt had an impact on the final catalyst and more investigation into using different copper-manganese salts would prove interesting as well as eliminating the problem of residual nitrates being retained in the precursor.

There are a large variety of novel solvent systems as well as expanding knowledge on the nature of systems such as ionic liquids and deep eutectic solvents that have allowed us to understand how these systems could be used as potential alternatives to the conventional systems and this thesis is only a small part of a much larger area, which is only just becoming mainstream in the field of heterogeneous catalyst preparation.

### 7.3 Chapter 7 References

1. S. A. Kondrat, P. J. Smith, J. H. Carter, J. S. Hayward, G. J. Pudge, G. Shaw, M. S. Spencer, J. K. Bartley, S. H. Taylor and G. J. Hutchings, *Faraday Discussions*, 2017, **197**, 287-307.
2. Z. R. Tang, S. A. Kondrat, C. Dickinson, J. K. Bartley, A. F. Carley, S. H. Taylor, T. E. Davies, M. Allix, M. J. Rosseinsky, J. B. Claridge, Z. Xu, S. Romani, M. J. Crudace and G. J. Hutchings, *Catalysis Science and Technology*, 2011, **1**, 740-746.
3. L. W. Hou, Q. H. Zhang, F. Jerome, D. Duprez, F. Can, X. Courtois, H. Zhang and S. Royer, *ChemCatChem*, 2013, **5**, 1978-1988.
4. N. Muhammad, M. I. Hossain, Z. Man, M. El-Harbawi, M. A. Bustam, Y. A. Noaman, N. B. M. Alitheen, M. K. Ng, G. Hefter and C. Y. Yin, *Journal of Chemical and Engineering data*, 2012, **57**, 2191-2196.
5. Y. H. Choi, Y. J. Jang, H. Park, W. Y. Kim, Y. H. Lee, S. H. Choi and J. S. Lee, *Applied Catalysis B-Environmental*, 2017, **202**, 605-610.
6. K. Morgan, K. J. Cole, A. Goguet, C. Hardacre, G. J. Hutchings, N. Maguire, S. O. Shekhtman and S. H. Taylor, *Journal of Catalysis*, 2010, **276**, 38-48.
7. C. Jones, S. H. Taylor, A. Burrows, M. J. Crudace, C. J. Kiely and G. J. Hutchings, *Chemical Communications*, 2008, 1707-1709.
8. P. G. Jessop, *Aldrichimica Acta*, 2015, **48**, 18-21.